HYDROGEN DESORPTION AND ABSORPTION FOR ACTIVATED

MAGNESIUM HYDRIDE

by

James William Prendergast

A thesis submitted to the University of Birmingham for the degree of
Doctor of Philosophy

School of Chemistry

The University of Birmingham

October 2010

UNIVERSITY OF BIRMINGHAM

University of Birmingham Research Archive

e-theses repository

Abstract

The interaction between MgH_2 and $LiBH_4$ was studied to determine the resultant effects on hydrogen desorption and absorption kinetics for potential use as a hydrogen storage material. It is found that the addition of $LiBH_4$ in small molar ratios results in improved kinetics of the same order as those observed for mechanically milled magnesium. The mixture of MgH_2 + $LiBH_4$ in ratios at and below 4:1, once reacted, is a highly reversible material at 300°C and it is observed that the kinetics improve upon the process of hydrogen cycling. This improvement is partially attributed to a refinement in microstructure that results in highly porous particle agglomerates and it is this feature that is likely to have a large effect on the kinetics of hydrogenation due to the rate limiting step of the reaction being hydrogen diffusion into the particles of Mg which can be coated in MgH_2 phase, through which H_2 does not diffuse easily. Additionally it is observed via Raman spectroscopy that a new bonding structure exists in the H_2 cycled and reacted mixture upon desorption which might also improve the rehydrogenation of the sample and reduce the enthalpy of decomposition by providing an intermediate pathway that has a lower energy barrier. This intermediate possibly has its origins in the decomposition intermediates of $LiBH_4$, recently reported to be $Li_2B_{12}H_{12}$ and $Li_2B_{10}H_{10}$, that are formed above 150°C once $LiBH_4$ begins to partially dehydride.

Thermodynamic measurements were conducted in a variety of methods that determined that there was either no change in the enthalpy of formation or a very slight reduction that might indicate that the mixture is less stable than standard MgH_2. DSC measurements show that MgH_2 + $LiBH_4$ (90:10) absorb hydrogen faster than MgH_2 and Mg and that it has a complex desorption exothermic reaction that is as-yet unidentified.

Finally, multiple samples were exposed to suspected contamination from the IGA measurement apparatus. While their kinetics are slower than uncontaminated samples with the same stoichiometry, they are still kinetically improved over as-received MgH_2 and perhaps point to a good resistance to contamination for the mixture.

Acknowledgements

Table of contents

1.   Introduction

In the latter part of the 20th century two topics central to the current stability of our civilisation were brought to the fore by researchers, politicians and the media: energy reserves and climate change. Both issues potentially affect all levels of human behaviour on the planet from individual lives to the actions and profitability of multinational corporations.

1.1 Climate change

Climate change is a broad term that covers many effects and processes within the ecosphere. Global warming is arguably the most politically-charged environmental process that has an influence on all aspects of nature and has been shown to be directly impacted by human activity. Part of the controversy surrounding this phenomenon is due to the fact that the average temperature of the Earth fluctuates naturally over short periods, though trends of long-term temperature increase and decrease can be in the region of thousands of years[1]. This leads some to conclude that the recent observed increase in average global temperature over the last 100 years is merely a facet of this natural variation.

There are several factors affecting global temperature trends but the three main contributors are solar activity, aerosol levels and climatic activity. Solar variation has a large impact on the climate though it can be heavily limited by the amount of reflection from the atmosphere[2] and the Earth itself. The amount of solar variance can be estimated from ground temperature measurements[3] and short wave irradiance measurements[4], although this data is restricted to the last century or so. Inferring the solar activity over longer periods of history can be achieved by analysing the ^{14}C and ^{10}B content of ice cores and tree rings[5], however, there is a level of uncertainty in the accuracy of the relationship between these isotope concentrations and solar activity. Crucial to being able to understand the relative effect of solar variation on global temperature fluctuations has been space exploration whereby the magnitude and overall trends of solar radiative variability can now come to be understood[6] and applied to modelling programmes that attempt to address their impact on global warming

and the interactive forces on other processes that affect global temperatures[7]. Work is still on-going in this field as models are constantly refined to better reflect available data and understanding of the processes involved[8].

Aerosol levels are important when considering global temperature variations due to the fact that their presence in the atmosphere affects solar radiation penetration as well as preventing radiation from the Earth escaping into space. The coefficients of absorption for terrestrial and solar radiation for a particular particle, along with possible reflection and scattering of light due to particle size, will determine whether there is a net increase, decrease or no change in radiation reaching the Earth when that particle interacts with radiation[9]. This means that effects from global warming via other mechanisms can be masked if there is a cooling effect from particle build-up in the upper atmosphere – specifically the stratosphere. It has been shown that particle build up from volcanic eruptions can reduce ground temperature during the day and increase it in the night over the short term directly after an eruption[10] and that volcanic particles can take from 1 to 3 years to reach the troposphere where their descent is expedited by winds and precipitation[9].

Greenhouse gases affect the mean temperature of the planet in a similar fashion to aerosols – they absorb infrared wavelengths emitted by the Earth's surface and in turn emit their own long wavelength radiation, effectively reducing the amount of heat lost through the atmosphere. There are several naturally occurring greenhouse gases including CO_2, CH_4 and N_2O which have helped stabilise global temperatures in the past, however, anthropogenic influences on the concentration of these[11] and artificial greenhouse gases such as chlorofluorocarbons(CFCs), perfluorocarbons (PFCs) and hydrofluorocarbons (HFCs) have lead to an enhanced greenhouse effect[12]. The impact of these gases is determined by their relative concentrations in the atmosphere, radiative efficiency, atmospheric lifetimes and the impact of the gas molecules on atmospheric chemistry. Naturally occurring greenhouse gases have quite short atmospheric lifetimes in comparison to halogenated species that have been introduced into the atmosphere by human activity[13] as shown in Table 1. As such, their effect on global temperatures is lower for the same concentration.

Gas Species	Radiative efficiency (Wm^{-2}ppb^{-1})	Lifetime (years)
CO_2	0.01548	N/A
CH_4	3.7×10^{-4}	12
N_2O	3.1×10^{-3}	114
CCl_3F	0.25	45
$CClF_3$	0.25	640
$CHClF_2$	0.20	11.9
CHF_3	0.16	260
C_2F_6	0.26	10000
CF_4	0.08	50000

Table 1 : Greenhouse gas species and their radiative efficiency and lifetime relative to carbon dioxide[13]

Certain greenhouse gases (e.g. CH_4 and CO) also have a secondary effect on global warming by reacting with other molecules in the atmosphere, reducing the amount of stratospheric ozone and increasing the concentrations of CO_2, stratospheric H_2O and tropospheric O_3 – all of which contribute a warming effect. There is also an observed decrease in OH radicals which are a decomposition pathway for CH_4 and other hydrocarbons in the atmosphere – leading to the exacerbated effect of compounds with even longer lifetimes[13].

Nitrogen compounds, N_2O, NO_x and NH_3 also play an important role in the atmospheric chemistry surrounding global warming[14]. N_2O has a long atmospheric lifetime and is a large contributor to positive radiative forcing (increasing retention of heat) while NO_x gases (NO and NO_2) have lifetimes of hours to days. However, the main effect of these oxides is in the production of tropospheric ozone which is also a large contributor to positive radiative

forcing. They also contribute to the decomposition of CH_4 leading to shortened atmospheric lifetimes for this compound[15]. NH_3 contributes an indirect negative radiative forcing effect (cooling effect) due to the formation of nitrate aerosols[11] which have been shown, along with other aerosols, to increase cloud lifetimes and thus increase the amount of reflected solar radiation by their presence[16].

1.2 Feedback Effects

While the above contributions to global warming are the primary factors involved, there are various sinks of greenhouse gases that can be released with increased temperature along with process feedback loops resulting from the above effects.

Increased water vapour content in the upper troposphere can result from a rise in temperature resulting in increased radiative forcing effect. If the water vapour is in an area at a temperature that is lower than the ground temperature, then the emitted long-wave radiation from the ground is blocked from escaping the atmosphere. Increasing this temperature gradient will also increase the blocking effect of the water vapour[17].

Clouds absorb and emit both solar and emitted long-wave radiation from the ground providing both positive and negative radiative feedback effects in the atmosphere. The strengths of these depend on the cloud height and thickness as well as the radiative properties of the clouds. These features depend on the amount of water vapour, ice particles and aerosols as well as water droplet size within the clouds. With a higher overall humidity from raised global temperatures, more clouds would form and so could potentially radiate more energy back towards the earth – but could also deflect more solar radiation, meaning that at the moment there is no definitive answer as to the feedback effects of increasing cloud coverage[17].

Oceans provide sinks for heat and also radiative gases such as CO_2, they also transport the stored heat around the globe via large-scale flows. The majority of these flows head towards

the poles, decreasing the temperature gradient between the equatorial regions and the poles, though there is one exception to this rule in the Atlantic ocean. Due to the large volume of water and the related capacity for storing heat, oceans provide a time delay to climatic changes in heat and can mask heating and cooling trends over short periods (decades) in this manner. Carbon dioxide is water soluble but the uptake of this gas is dependent on the vertical mixing rate of the body of water and also the temperature of the water. Deep vertical mixing takes place on a seasonal timescale, with a maximum during winter months and a minimum during summer months where the shallow mixing near the surface effectively isolates deeper water from the atmosphere[18]. The deep vertical mixing during winter months is aided by ice-melt and precipitation meaning that, in the short term, as the global temperature increases ice melt will also increase throughout the year leading to a larger effect on deep convection mixing, however, as available ice at the poles is reduced along with the ocean temperature gradient it is possible that less convection will take place. A reduction in convection could result in less nutrient supply to the surface where various photosynthetic marine life forms help sequester CO_2[11]. This would affect both carbon sequestering and also the surface reflectance and absorption of solar radiation from the presence of these biota.

Increased CO_2 in the atmosphere can result in increasingly acidic oceanic conditions due to an increase of the CO_2 concentration gradient forcing transfer from the atmosphere to the sea[19]. An increase in global temperature would result in less carbon being sequestered in the ocean and after a certain temperature boundary there lies a possibility of emission of CO_2, leading to a global increase in CO_2 concentration and thus accelerated global warming. These changes could lead to ecosystem structure further reinforcing a negative or positive effect on CO_2 sequestration or emission.

Land masses also affect global warming feedback through several processes. An increased amount of CO_2 in the atmosphere is predicted to also increase the uptake of CO_2 by plants[20] though the extent of this uptake with increasing CO_2 concentration is unknown and the ability of plants to take advantage of a larger source of carbon tends to be limited by nutrients[21]. This could provide a small stabilising effect on atmospheric carbon dioxide levels. However,

global temperature rises could lead to an overall increased chance of naturally occurring wild fires – releasing CO_2 into the atmosphere[22]. Deforestation also contributes to the release of and reduction in ability to sequester CO_2. Counter to this effect is the re-coverage and growth of plant mass – specifically forests[23] – which have a greater ability to sequester carbon than grasslands or croplands. These factors have been greatly aided by human endeavours to replenish previously exploited woodlands during the latter half of the 20th century, though the effects of these projects will only be realised over the mid-to-long term.

A further feedback effect is the albedo of the surface of the earth – i.e. the reflectance of received radiation. As the temperature of the planet increases, areas that are normally covered by highly reflective ice or snow will decrease leading to increased absorption of radiation by the ground and biomass and to increased global warming. Forested areas have a low surface albedo due to the higher absorption of radiation by the canopy and even snowfall tends to have little effect in comparison with open ground[24]. It has been observed that, in general, agricultural areas have only a slightly higher albedo than forested areas and thus little is gained or lost in reflectance when considering only this aspect. Further factoring into the albedo effects of snow or other lighter landscapes are soot particles from human activities which have been shown to reduce the reflectance of the materials[25].

1.3 Effects of global warming on society

Regardless of the causes of global temperature trends, these temperature rises have an effect on the stability of the economies and societies of the various countries in the world. One way global warming is likely to affect society is through diseases and vermin. If the mean temperature of the latitudes nearer the poles grows warmer then there will be a change and probable migration of the ecosystem from equatorial latitudes. Already disease-spreading vermin such as cockroaches and mosquitoes are being observed at higher latitudes in Europe in increasing quantities due to the relatively small rises in temperature.

Along with this migration of disease vectors, it has been predicted that animal/human diseases will spread throughout areas where they were previously absent[26, 27] due to their hosts surviving for longer periods at elevated latitudes. The potential effects on societies previously unused to dealing with these maladies could be highly disruptive and expensive in terms of treatment and education.

Plant populations will also shift or expand as local climates that were previously unsuitable (for example frosts during early spring and late autumn) for growth become available. One repercussion is that if a certain degree of warming is achieved then crop species may become viable at higher latitudes but unsustainable nearer the equator or more arid regions[28]. Water availability near the equator may also cause a shift in farming preferences to alternate crop varieties. These factors will place pressure on the availability of certain varieties of 'staple' crops and while intensification and improvement in productivity of northern crops may take place due to increased atmospheric CO_2[29] content and the ability to provide the crops with sufficient nitrate for nutrition, reduced productivity in Mediterranean areas could lead to more land being used to alleviate crop shortages resulting in possible increased feedback effects on local soil moisture content due to evaporation and nutrient depletion from over-farming[30].

Changes in plant physiology and morphology from increased CO_2 levels can cause disease epidemiology to be affected which, in some cases, can result in increased disease potency[31]. It was also observed that increased amounts of fungicide would be required in certain circumstances due to improved environments for fungal growth, leading to escalating costs to produce certain crops. These factors all impact the economic viability of crops due to increased crop failure[32] though the effects can be mitigated somewhat with improved bioengineering of crop strains and crop management policies.

Effects of extreme events on society have been recorded with increasing frequency over recent years[33, 34]. While average temperatures and rainfall are slowly increasing, the upper and lower limits of these scales are increasingly further apart. However, the effects of climate

change are not universal – with some areas of Europe expected to record higher levels of precipitation and heat-waves but other areas expecting less both during winter and summer though those countries will still experience higher average temperatures. Computer modelling studies show that, in the Mediterranean, daily maximum and minimum temperatures will increase throughout the year with the maximum values increasing by a greater amount than the minimum values[35]. Thus the average temperature in the equatorial regions is predicted to increase slightly and decreased precipitation is also expected in the Mediterranean area. These predictions contrast with latitudes that are further from the equator where there would be a decrease in snow cover and sea ice and as a consequence, the temperatures in the northern hemisphere are predicted to increase more than in the southern hemisphere[36]. These effects also increase the cost of producing crops as well as placing pressure on social structure with increased costs for living through electricity, food/water and heating.

1.4 Alternative energy supplies

EIA (Energy Information Administration) studies predict that energy demand will increase by up to 44% over the period 2006-2030[37] and that fossil fuels will still cover the majority of this requirement. These studies predict that by 2020 the percentage of the total global energy requirement for oil will drop slightly while dependence on natural gas and coal will remain about the same (Figure 1.1). Overall, nuclear and renewable resources are expected to replace the reduction in oil usage in their percentage of the total energy fulfilment. The cost per barrel of oil is uncertain over this period: best-case scenarios predict that by 2015 barrel prices will have stabilised at around $50 until 2030, whereas worst-case scenarios reach $200 per barrel by 2030 with these prices being heavily affected by demand for use in the transport sector. While estimates in the total remaining oil reserves have increased slightly and production is predicted to increase over the period until 2030, alternative fuel sources are expected to become viable as the price of petroleum increases. Linked into these

estimates is the fact that there is a more limited amount of oil and natural gas than coal in developing countries; whose energy demand is expected to more than double.
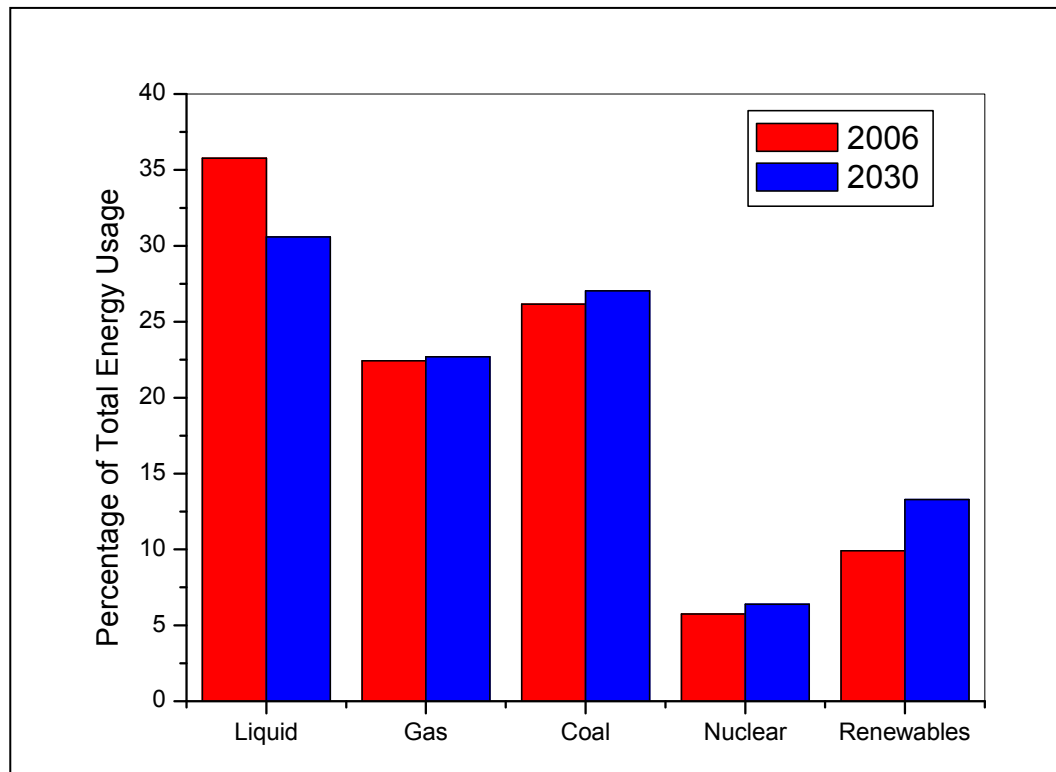
Figure 1.1 : Chart displaying percentage energy usage by resource for 2006 and predicted usage in 2030[37]

In order to reduce our dependence on fossil fuels for power, various alternate energy resources have been researched and piloted to differing degrees. Solar, wind, hydro, geothermal and biomass/biocrops are all alternate, renewable resources available to be utilised. Most of these technologies rely on solar energy to operate either directly, such as solar cells, or indirectly as in the case of wind- or wave- powered turbines - even fossil fuels are derived indirectly from solar energy, being formed from plant matter over millions of years.

Non-renewable resources such as nuclear fission and fusion are also championed as being the solution to the world's potential energy crisis due to their relatively high energy production. However, the solutions to various problems such as disposal of radioactive waste

and, in the case of fusion, the ability to maintain and harness the energy output are currently insurmountable in a near timeframe[38]. Whichever energy source provides the solution to our future energy requirements there is a broad consensus that moving away from an over-reliance fossil fuels is in the best interests of the human race[39, 40].

Geothermal energy is another viable alternative but its application is also severely limited due to reliance on the thickness of the Earth's crust at the point of use and thus cannot be considered as an alternative global energy resource.

Biomass technologies have been present and in use since the early 1800s in the form of gasifiers[41] to produce usable methane and hydrogen from crops and other waste. These were primarily in use in rural areas were there was ease of access to these materials. Other biomass technologies rely on bacteria in a process called anaerobic digestion (AD)[42]. While useful energy is derived from these processing techniques there are some downsides to the widespread adoption of biomass. Gasifiers require energy to function – reducing the overall energy output – and produce waste such as CO_2, tar and ash, all of which have to be scrubbed from the produced gas in order to be more efficient when combusted in an engine. The design of a gasifier also determines which materials can be converted due to tar and ash amounts. Some digesters also require energy input to increase the efficiency of the bacteria during decomposition of the materials along with 'feed' – solutions of sugar or analogous chemicals – to allow the bacteria to function. Digesters are also vulnerable to changes in pH and contamination by other bacteria strains.

Further complications with a move to widespread biomass use is the source of these materials. While biogas production on a small scale is easily maintained from waste materials on site, larger scale production and distribution of the gas/energy obtained is more difficult due to siting of conversion plants and farms[43]. The use of land to produce the required amount of crops in the form of plantations is also a worry if a reduction of usable arable land takes place with global warming and competition with food crops begins to take place[44]. All

of these factors diminish the appeal of biomass as a widespread solution to global energy demands.

Solar technologies cover broad segments of the energy market from simple water heaters, complex mirror and lens arrays that can drive steam turbines, to direct solar collection through photovoltaic cells[45]. Though these technologies tend to be expensive to implement, the implementation and operation costs of solar technology are lowering constantly[46]. One of the problems for photovoltaic technology is the lifetime of the cells depending on the particular cell type – for example, amorphous Si-based cells are prone to degradation. Taking these into consideration along with the general efficiency of a photovoltaic cell being quite low outside of laboratory conditions (<50%), photovoltaic technology remains promising but falls short of current requirements for large-scale energy production but is almost guaranteed to fulfil a major role in the future energy landscape once it has matured[47]. However, the greatest roadblock to widespread solar technology adoption is availability of solar radiation.

Wind power generation also suffers from this caveat. While wind turbine farms are similarly expensive to install in comparison with solar plants[46] the areas where these farms can efficiently be placed is limited. There are also environmental and military impacts to be considered when installing wind farms as there has been some evidence that their placement can affect bird migratory patterns and radar equipment[48, 49].

By comparison with most renewable resources, hydroelectric power plants are well-established throughout the world. Developing countries such as China are increasing the amount of energy generated by hydroelectric projects and as of 2007 hydroelectric energy accounted for 6% of the world's total energy consumption[50] which, though small in comparison with 35% for oil, is a larger portion than other renewables.

It is likely that the energy sources mentioned above will all find widespread use throughout the world depending on which application is appropriate for the area in question in the coming decades, however, there are some problems with implementing some of these solutions in the short term besides costs and efficiencies of conversion. Global warming is

predicted to change the weather patterns of the world and will therefore affect any technology that is dependent on these natural patterns. It is predicted that there will be possible reductions in wind availability for wind turbine farms if global warming passes a certain point[51] resulting in reduced power output from these systems and if cloud coverage is affected by climate change then solar powered solutions may also be placed in sub-optimal positions. The difficulty lies in the fact that if these solutions are not implemented, it is possible that we will hasten and increase in magnitude any climate change we are already facing.

1.5 Energy storage

Production of electricity via renewable resources is already a reality even if the efficiencies of the current technologies are below expectations and ideal values, however, matching this production to the demand of communities and countries is incredibly difficult thus storage of this energy is needed so that when production outstrips demand the extra energy is not wasted and can be used to cover the gap when demand outstrips production[52]. Currently, the only large-scale storage of energy is achieved through pumped-water hydroelectric plants that lift water to an upper reservoir to store the energy and then when the energy is required sluice gates are opened and the water flows through the turbines to the lower reservoir. This technique is severely limited in availability and total storage amount and as such cannot be applied across all energy markets[53]. Instead, it is suggested that smaller scale local storage is the more viable route which also bypasses the problems of having all renewable resources and related energy stores connected to the national power grid.

Battery technology is one of the options available for storage of energy from fluctuating resources and these are routinely used in conjunction with wind and solar arrays[52]. There are two types of commercially viable large-scale batteries: lead-acid and alkaline. Both are well established forms of energy storage though alkaline batteries are less cost effective while lead-acid batteries tend to suffer from the need to occasionally refill them with water. They

are also already used extensively in nuclear power plants as a means of ensuring safe operation[54]. One problematic aspect of battery technology is currently the storage limits, efficiencies of conversion and also operational lifetimes,[55] which tend to be shorter than predicted when implemented in conjunction with renewables[56]. However, battery technology is improving steadily and is continually being implemented in new developments.

An alternative energy storage option is hydrogen. Hydrogen is a versatile energy storage medium and its level of implementation can be tailored to the specific application. It can be formed from water on-site and recombined with oxygen to reclaim the stored energy. Notably, this stored hydrogen can also be transferred from the site of production which can result in little energy lost (via transportation) as opposed to battery technologies which are considered stationary and hydrogen is also appealing due to the fact that there is no energy loss over the period spent in storage – unlike in battery-based systems.

1.6 The hydrogen economy

The backing for a hydrogen economy began in the 1970s when the International Association for Hydrogen Energy was formed[57]. Since that time many technological advancements in the fields of hydrogen production, storage and conversion have taken place, however, widespread hydrogen adoption is still a fair way off.

Hydrogen has been used as a fuel for many years in the space industry as well as the petrochemicals industry and is considered a 'clean' fuel in comparison with the hydrocarbon alternative, the only product of combustion being water. It can be obtained via various sources whether from electrolytic splitting of water[58, 59], steam reformation from methane and methanol[52] or evolution of hydrogen from biomass reactors[60], and can be used in combustion engines or to generate electricity by direct combination with O_2 in fuel cells.

Taking these facts into account, hydrogen has the potential to play a major part in energy systems from future electricity grids to vehicular fuels[61, 62]. However, hydrogen has some

major hurdles to clear in relation to its implementation in the transport sector. The relative immaturity of many hydrogen technologies and the expense in comparison with intermediate fuel technologies (e.g. hybrid vehicles) are limiting factors along with the cost of implementing a unified nation-wide infrastructure to support the change from petroleum- to hydrogen-powered machinery[63]. In fact, there is no one hydrogen delivery system to be considered for integration into the current energy infrastructure and as such any possible progress towards including hydrogen is hindered by lack of a clear vision - though some potential roadmaps have been laid out[63, 64].

1.7 Storage of hydrogen

The major obstacle to uptake of hydrogen as an energy carrier is storage[60, 65, 66]. Due to hydrogen being gaseous at standard temperatures and pressures, a way for it to become more energy dense must be determined. Traditionally there have been two methods of doing this:

- High pressure compressed hydrogen gas cylinders

- Liquid hydrogen

Both of these techniques are energy intensive, specifically the liquefaction of hydrogen which requires a substantial amount of energy to cool the gas down to 20 K. Liquid hydrogen has a very low critical temperature (33 K) and so boil-off is inevitable, resulting in loss of stored energy. The size of the containers and the energy density contained therein is a major issue for the viability of these storage techniques: liquid H_2 has a volumetric density of 70.8 kg/m^3 while compressed gas cylinders are available in 20 and 80 MPa varieties which have volumetric densities of 9 and 36 kg/m^3, respectively[66]. In comparison, the volumetric density of petroleum is 737 kg/m^{3}[67]. The hydrogen content of petrol is 17.3 wt%[65] which gives a total H_2 volumetric density of 127 kg/m^3 for petrol. These storage methods are currently employed by the major car manufacturers in their hydrogen powered cars but unfortunately

come at a cost of space within the cars – either seating or luggage space - due to their relatively large volumes.

To overcome the problem of volumetric storage of hydrogen various political entities have laid out requirements for storage that, if fulfilled, would allow commercial use of hydrogen for the transport sectors. The US Department of Energy (DoE) has five requirements that are predicted to enable the use of hydrogen technologies to be officially adopted as a fuel for transport[65] and these are good benchmarks for any endeavours in this area of research:

- A minimum 6.5 wt% or 65 kg/m^3 H$_2$ capacity

- Temperature of operation between 60-120 °C with a plateau pressure of a few bar in this range

- Reversible – to facilitate recharging with H$_2$

- Low cost

- Low toxicity and non-explosive

Comparing liquid and compressed stores of hydrogen to this list shows that they will most likely never be adopted on a large scale. However, there is a third option for storage of hydrogen: solid state storage.

1.   Hegerl G.C., Zwiers F.W., Braconnot P., Gillett N.P., Luo Y., Marengo Orsini J.A., Nicholls N., Penner J.E., and Stott P.A., *Understanding and attributing climate change*. Climate Change 2007: The Physical Science Basis. Contribution of Working Group I to the Fourth Assessment Report of the Intergovernmental Panel on Climate Change, ed. S. Solomon, D. Qin, M. Manning, Z. Chen, M. Marquis, K.B. Averyt, M. Tignor and H.L. Miller. 2007, Cambridge, United Kingdom and New York, NY, USA: Cambridge University Press.

2.   Stanhill G. and Cohen S., *Global dimming, a review of the evidence for a widespread and significant reduction in global radiation with a discussion of its probable causes and possible agricultural consequences*. Agric. Forest Meteorol., 2001. **107**: p. 255.

3.   Jones P.D., New M., Parker D.E., Martin S., and Rigor I.G., *Surface air temperature and its changes over the past 150 years.* Rev. Geophys, 1999. **37**(2): p. 173.

4.   Gilgen H., Wild M., and Ohmura A., *Means and trends of shortwave irradiance at the surface estimated from global energy balance archive data.* J. Clim., 1998. **11**: p. 2042.

5.   Muscheler R., Joos F., Beer J., Muller S.A., Vonmoos M., and Snowball I., *Solar activity during the last 1000 yr inferred from radionuclide records.* Quaternary Sci Rev, 2007. **26**: p. 82.

6.   Fröhlich C. and Lean J., *Solar radiative output and its variability: evidence and mechanisms.* The Astron Astrophys Rev, 2004. **12**: p. 273.

7.   Ammann C.M., Joos F., Schimel D.S., Otto-Bliesner B.L., and Tomas R.A., *Solar influence on climate during the past millennium: Results from transient simulations with the NCAR Climate System model.* P NATL ACAD SCI USA, 2007. **104**(10): p. 3713.

8.   Stott P.A., Jones G.S., and Mitchell J.F.B., *Do models underestimate the solar contribution to recent climate change?* J Climate, 2003. **16**: p. 4079.

9.   Humphreys W.J., *Volcanic dust and other factors in the production of climatic changes and their possible relation to the ice ages.* J FRANKLIN I, 1913. **CLXXVI**(2): p. 131.

10.   Mass C. and Robock A., *The Mount St. Helens volcanic eruption 18 May 1980: Large short-term surface temperature effects.* Science, 1982. **216**: p. 628.

11.   Denman K.L., Brasseur G., Chidthaisong A., Ciais P., Cox P.M., Dickinson R.E, Hauglustaine D., Heinze C., Holland E., Jacob D., Lohmann U., Ramachandran S., da Silva Dias P.L., Wofsy S.C., and Zhang X., *Couplings between changes in the climate system and biogeochemistry.* Climate Change 2007: The Physical Science Basis. Contribution of Working Group I to the Fourth Assessment Report of the Intergovernmental Panel on Climate Change, ed. Q.D. [Solomon S., Manning M., Chen Z., Marquis M., Averyt K.B., Tignor M., Miller H.L. (eds.)]. 2007: Cambridge University Press, Cambridge, United Kingdom and New York, NY, USA.

12.   Ehhalt D., Prather M., Dentener F., Derwent R., Dlugokencky E., Holland E., Isaksen I., Katima J., Kirchhoff V., Matson P., Midgley P., and Wang M., *Atmospheric chemistry and greenhouse gases.* In: Climate Change 2001: The Scientific Basis. Contribution of Working Group I to the Third Assessment Report of the Intergovernmental Panel on Climate Change, ed. J.T. [Houghton, Y. Ding, D.J. Griggs, M. Noguer, P.J. van der Linden, X. Dai, K. Maskell, and C.A. Johnson (eds.)]. 2001: Cambridge University Press, Cambridge, United Kingdom and New York, NY, USA, 881pp.

13.   Ramaswamy V., Boucher O., Haigh J., Hauglustaine D., Haywood J., Myhre G., Nakajima T., Shi G.Y., and Solomon S., *Radiative forcing of climate change.* In: Climate Change 2001: The Scientific Basis. Contribution of Working Group I to the

Third Assessment Report of the Intergovernmental Panel on Climate Change, ed. J.T. [Houghton, Y. Ding, D.J. Griggs, M. Noguer, P.J. van der Linden, X. Dai, K. Maskell, and C.A. Johnson (eds.)]. 2001, Cambridge University Press, Cambridge, United Kingdom and New York, NY, USA, 881pp.

14.   Holland E.A., Braswell B.H., Sulzman J., and Lamarque J.F., *Nitrogen deposition onto the United States and Western Europe: synthesis of observations and models.* Ecol. Appl., 2005. **15**: p. 38.

15.   Prather M.J., *Lifetimes of atmospheric species: integrating environmental impacts.* Geophys. Res. Lett., 2002. **29**(22): p. 2063.

16.   Kaufman Y.J. and Koren I., *Smoke and pollution aerosol effect on cloud cover.* Science, 2006. **313**: p. 655.

17.   Stocker T.F., Clarke G.K.C., Le Treut H., Lindzen R.S., Meleshko V.P., Mugara R.K., Palmer T.N., Pierrehumbert R.T., Sellers P.J., Trenberth K.E., and Willebrand J., *Physical climate processes and feedbacks.* In: Climate Change 2001: The Scientific Basis. Contribution of Working Group I to the Third Assessment Report of the Intergovernmental Panel on Climate Change, ed. J.T. [Houghton, Y. Ding, D.J. Griggs, M. Noguer, P.J. van der Linden, X. Dai, K. Maskell, and C.A. Johnson (eds.)]. 2001: Cambridge University Press, Cambridge, United Kingdom and New York, NY, USA, 881pp.

18.   Marshall J. and Schott F., *Open-ocean convection: observations, theory and models.* Rev. Geophys., 1999. **37**: p. 1.

19.   Prentice I.C., Farquhar G.D., Fasham M.J.R., Goulden M.L., Heimann M., Jaramillo V.J., Kheshgi H.S., Le Quéré C., Scholes R.J., and Wallace D.W.R., *The carbon cycle and atmospheric carbon dioxide.* Climate Change 2001: The Scientific Basis. Contribution of Working Group I to the Third Assessment Report of the Intergovernmental Panel on Climate Change, ed. J.T. [Houghton, Y. Ding, D.J.

Griggs, M. Noguer, P.J. van der Linden, X. Dai, K. Maskell, and C.A. Johnson (eds.)].
2001: Cambridge University Press, Cambridge, United Kingdom and New York, NY,
USA, 881pp.

20.   Oren R. et al., *Soil fertility limits carbon sequestration by forest ecosystems in a CO2-enriched atmosphere.* Nature, 2001. **411**(6836): p. 469.

21.   Koerner C. et al., *Carbon flux and growth in mature deciduous forest trees exposed to elevated CO2.* Science, 2005. **309**(5739): p. 1360.

22.   Flannigan M.D., Stocks B.J., and Wotton B.M., *Climate change and forest fires.* Sci. Total Environ., 2000. **262**: p. 221.

23.   Pacala S.W. et al., *Consistent land- and atmosphere-based US carbon sink estimates.* Science, 2001. **292**: p. 2316.

24.   Forster P., Ramaswamy V., Artaxo P., Berntsen T., Betts R., Fahey D.W., Haywood J., Lean J., Lowe D.C., Myhre G., Nganga J., Prinn R., Raga G., Schulz M., and Van Dorland R., *Changes in atmospheric constituents and in radiative forcing*. Climate Change 2007:The Physical Science Basis. Contribution of Working Group I to the Fourth Assessment Report of the Intergovernmental Panel on Climate Change, ed. Q.D. [Solomon S., Manning M., Chen Z., Marquis M., Averyt K.B., Tignor M., Miller H.L. (eds.)]. 2007: Cambridge University Press, Cambridge, United Kingdom and New York, NY, USA.

25.   Hansen J. et al., *Global warming in the twenty-fi rst century: An alternative scenario.* Proc. Natl. Acad. Sci., 2000. **97**: p. 9875.

26.   Ogden N.H., Maarouf A., Barker I.K., Bigras-Poulin M., Lindsay L.R., Morshed M.G., O'Callaghan C.J., Ramay F., Waltner-Toews D., and Charron D.F., *Climate change and the potential for range expansion of the Lyme disease vector Ixodes scapularis in Canada.* Int. J. Parasitol., 2006. **36**: p. 63.

27.   Peterson A.T. and Shaw J., *Lutzomyia vectors for cutaneous leishmaniasis in Southern Brazil: ecological niche models, predicted distributions and climate change effects.* Int. J. Parasitol., 2003. **33**: p. 919.

28.   Olesen J.E. and Bindi M., *Consequences of climate change for European agricultural productivity, land use and policy.* Eur. J. Agron., 2002. **16**: p. 239.

29.   Rosenzweig C. and Parry M.L., *Potential impact of climate change on world food supply.* Nature, 1994. **367**: p. 133.

30.   Rabbinge R. and van Diepen C.A., *Changes in agriculture and land use in Europe.* Eur. J. Agron., 2000. **13**: p. 85.

31.   Hibberd, J.M., R. Whitbread, and J.F. Farrar, *Effect of 700 mmol per mol CO_2 and infection of powdery mildew on the growth and partitioning of barley.* New Phytol., 1996. **1348**: p. 309.

32.   Chakraborty S., Tiedemann A.V., and Teng P.S., *Climate change: potential impact on plant diseases.* Environ. Pollut., 2000. **108**: p. 317.

33.   Goodness C., W.R., Ribalaygua J., Schuepbach E., Plaut G., Cacciamani C.,Tosi E., Schmith T., Schmidli T., Caspary H., Bardossy A., Maheras P., *STARDEX: STAtistical and Regional dynamical Downscaling of EXtremes for european regions, EVK2-CT-2001-00115, 5th Framework European programme project.* (2002-2005).

34.   Christensen J.H., *PRUDENCE (Prediction of Regional scenarios and Uncertainties for Defining EuropeaN Climate change risks and Effects, EVK2-CT2001-00132), 5th Framework European programme project.* (2002-2005).

35.   Sanchez E., Gallardo C., Gaertner M.A., Arribas A., and Castro M., *Future climate extreme events in the Mediterranean simulated by a regional climate model: a first approach.* Global Planet. Change, 2004. **44**: p. 163.

36. Cubasch U., Meehl G.A., Boer G.J., Stouffer R.J., Dix M., Noda A., Senior C.A., Raper S., and Y. K.S., *Projections of future climate change*. In: Climate Change 2001: The Scientific Basis. Contribution of Working Group I to the Third Assessment Report of the Intergovernmental Panel on Climate Change, ed. J.T. [Houghton, Y. Ding, D.J. Griggs, M. Noguer, P.J. van der Linden, X. Dai, K. Maskell, and C.A. Johnson (eds.)]. 2001: Cambridge University Press, Cambridge, United Kingdom and New York, NY, USA, 881pp.

37. Conti J.J., Doman L.E., Smith K.A., Mayne L., Staub J., Yucel E., Barden J., Fawzi A., Martin P., Mellish M., Kearney D., Kette S., Murphy B., LaRiviere M., Vincent K., Kapilow-Cohen B., and Lindstrom P., *International energy outlook*, E.I. Administration, Editor. 2009.

38. Llewellyn Smith C., *The need for fusion.* Fusion Eng. Des., 2005. **74**: p. 3.

39. Wuebbles D.J. and Jain A.K., *Concerns about climate change and the role of fossil fuel use.* Fuel Process. Technol., 2001. **71**: p. 99.

40. van der Zwaana B. and Gerlagh R., *Climate sensitivity uncertainty and the necessity to transform global energy supply.* Energy, 2006. **31**: p. 2571.

41. Rajvanshi A.K., *Alternative energy in agriculture*, ed. Goswami D.Y. Vol. Vol. II. 1986: CRC Press. 83-02.

42. Marchaim U., *Biogas processes for sustainable development*. 1992: Publications Division, Food and Agriculture Organization of the United Nations, Viale delle Terme di Caracalla, 00100 Rome, Italy.

43. van der Horst D., *The benefits of more spatial detail in regional bioenergy models and the problems of disaggregating agricultural census data.* Options Mediterraneennes, Serie A, 2002. **48**: p. 131.

44.   Berndes G., Hoogwijk M., and van den Broek R., *The contribution of biomass in the future global energy supply: a review of 17 studies.* Biomass and Bioenergy, 2003. **25**: p. 1.

45.   Call P.J., *Overview of solar energy conversion technologies: Quantum processes and thermal processes.* Mater. Sci. Eng., 1982. **53**: p. 7.

46.   McConnell R., *Concentrator photovoltaic technologies.* ReFocus: Renewable Energy Focus, 2005. **6**(4): p. 35.

47.   Goetzberger A., Hebling C., and Schock H., *Photovoltaic materials, history, status and outlook.* Mater. Sci. Eng., 2003. **40**: p. 1.

48.   Marsh G., *WTs: beaming in on the radar issue.* ReFocus: Renewable Energy Focus, 2007. **8**(5): p. 36.

49.   Kikuchi R., *Adverse impacts of wind power generation on collision behaviour of birds and anti-predator behaviour of squirrels.* J. Nature Conservation, 2008. **16**: p. 44.

50.   *BP Statistical Review of World Energy June 2008*. 2008: The Editor, BP Statistical Review of World Energy, BP p.l.c.,1 St. James's Square, London, SW1Y 4PD, UK.

51.   Sailor D.J., Smith M., and Hart M., *Climate change implications for wind power resources in the Northwest United States.* Renew Energ, Article in Press.

52.   Dell R.M. and Rand D.A.J., *Energy storage - a key technology for global energy sustainability.* Journal of Power Sources, 2001. **100**: p. 2.

53.   Ibrahim H., Ilinca A., and Perron J., *Energy storage systems - Characteristics and comparisons.* Renew. Sust. Energ. Rev., 2008. **12**: p. 1221.

54.   Gagnol P., *Industrial batteries in the electric power system of 'Electricité de France'.* J. Power Sources, 1997. **64**: p. 203.

22

55.   Rydh C.J. and Sandé B.A., *Energy analysis of batteries in photovoltaic systems. Part II: Energy return factors and overall battery efficiencies.* Energ. Convers. Manage., 2005. **46**: p. 1980.

56.   Kaiser R., *Optimized battery-management system to improve storage lifetime in renewable energy systems.* J. Power Sources, 2007. **168**: p. 58.

57.   Veziroglu T.N., *Twenty Years of the Hydrogen Movement: 1974-1994.* Int. J. Hydrogen Energ., 1995. **20**(1): p. 1.

58.   Momirlan M., Muresan L., Sayigh A.A.M., and Veriroglu T.N., *The use of solar energy in hydrogen production.* Renew. Energ., 1996. **9**(1-4): p. 1258.

59.   Ni M., Leung M.K.H, and Leung D.Y.C, *Technological development of hydrogen production by solid oxide electrolyzer cell (SOEC).* Int. J. Hydrogen Energ., 2008. **33**: p. 2337.

60.   Conte M., Iacobazzi A., Ronchetti M., and Vellone R., *Hydrogen economy for a sustainable development: state-of-the-art and technological perspectives.* J. Power Sources, 2001. **100**: p. 171.

61.   Keith D. and Farrell A., *Rethinking hydrogen cars.* Science, 2003. **301**: p. 315.

62.   Turton H., *Sustainable global automobile transport in the 21st century: An integrated scenario analysis.* Technol. Forecast. Soc., 2006. **73**: p. 607.

63.   McDowall W. and Eames M., *Forecasts, scenarios, visions, backcasts and roadmaps to the hydrogen economy: A review of the hydrogen futures literature.* Energ. Policy, 2006. **34**: p. 1236.

64.   Winter C., *Into the hydrogen energy economy - milestones.* Int. J. Hydrogen Energ., 2005. **30**(681).

65.   Grochala W. and Edwards P.P., *Thermal decomposition of the non-interstitial hydrides for the storage and production of hydrogen.* Chem. Rev., 2004. **104**: p. 1283.

66.   Zuttel A., *Hydrogen storage methods.* Naturwissenschaften, 2004. **91**: p. 157.

67.   http://www.simetric.co.uk/si_liquids.htm, *Density of Petrol (vehicle)*.

2. Solid state hydrogen storage methods

2.1 Properties of solid state hydrogen storage

Unlike compressed gas and liquid storage, solid state storage is not reliant solely on the properties of hydrogen gas. Instead the principle of utilising materials to 'sequester' hydrogen by chemical reaction or van der Waals forces is applied. This approach can have several advantages: a high percentage weight of H_2, high volumetric density of H_2, and stable forms of storage – allaying fears of safety and providing the ability to easily control the evolution of hydrogen as and when it is needed. It is important to note that no known compound satisfies the five requirements set out in the introduction but it is equally important to acknowledge that those five criteria are guidelines to a best-case scenario. Economic and social pressures would allow the use of materials that fell short of these guidelines and as such, research has continued in earnest on improving these materials in parallel with the search for the ideal solid state storage medium.

There are two methods for storing hydrogen in solid state materials: physisorption and via chemical interaction. Physisorption is the process of attracting and holding a molecule to a surface through van der Waals interactions. These weak, intermolecular forces are caused by electrostatic interactions and result from both permanent and induced poles in the electronic field of an atom or molecule. This force is composed of both an attractive and repulsive component which diminish from an atom or surface by r^{-6} and r^{-12} respectively, resulting in a potential energy minimum at a distance of about one molecular radius of the adsorbed species[1] from the surface. Once a surface has been completely covered by a layer of the adsorbed phase (a monolayer) any further adsorption of the species must interact with the adsorbed phase and not the surface itself and therefore the binding energy is similar in magnitude to the heat of sublimation/vaporisation of the adsorbed species. Thus, at any given pressure, if the temperature is equal to or greater than that of the boiling point the adsorbed phase is effectively limited to a monolayer[2].

Hydrogen has two electrons and as such has a very low polarisability which results in weak induced dipole moments[3]. Adding to the weak van der Waals forces, H_2 is supercritical past 33 K[4] which means that it behaves as a gas at all temperatures greater than this (Figure 2.1) and thus will always form a monolayer at these higher temperatures.
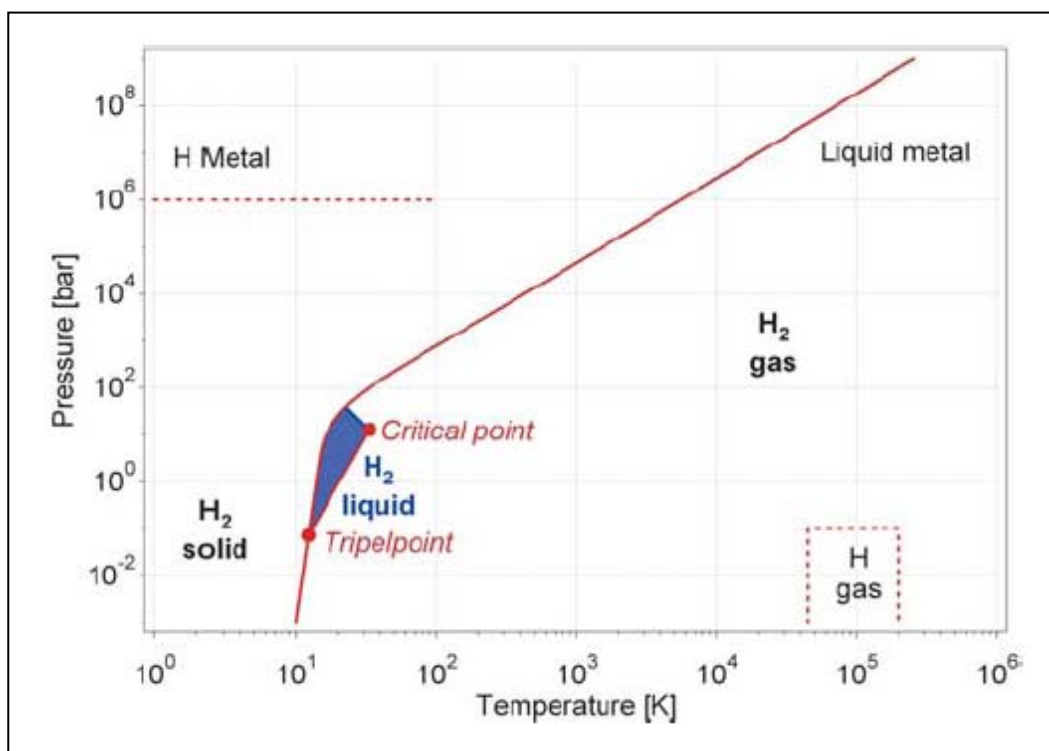
Figure 2.1 : A simple phase diagram for H_2. Liquid H_2 exists between 21.2 and 32 K, beyond which hydrogen is supercritical (67)

In contrast, chemical interaction consists of two processes: chemisorption and chemical reaction. Chemical reaction is the process of bonding hydrogen to another element, forming a new compound with a recognisably different crystal structure, and is defined as absorption through ionic or covalent interactions with the host material. The absorbed hydrogen is largely immobile due to the strength of the bond that is formed and therefore hydrogen can only be reclaimed by breaking the bond through the input of energy – usually in the form of heat. Chemisorption is the process whereby a compound binds hydrogen at interstitial sites throughout the crystal lattice, incorporating the hydrogen in vacant sites without largely altering the overall structure of the compound.

2.2 Porous materials

It is possible to increase the binding energy for hydrogen at a site on a surface by having a second (or multiple) surfaces near the adsorption site – offering increased interaction. Alternatively, a similar method may be used to trap H_2 molecules by forcing them into nano-sized pores and then encasing them in the structure by lowering the temperature[3, 4], effectively ignoring the low binding energies for the H_2 molecule. This has resulted in the low-temperature ($\geq$ 77 K) study of several types of porous material for the storage of hydrogen.

2.2.1 Zeolites

Zeolites are hydrophilic porous materials that consist of an alumino-silcate framework derived from corner-linked $[SiO_4]^{4-}$ and $[AlO_4]^{5-}$ polyhedra[5, 6]. This framework consists of tunnels and cavities of sufficient size for molecules to enter. The zeolite framework is anionic due to a charge imbalance upon substitution of Si^{4+} with Al^{3+} and is stabilised by cations which are loosely bound and have a high degree of mobility in the tunnels and cavities[7] (Figure 2.2). Zeolites can have various configurations based on some simple building blocks and will vary depending on the Si to Al ratio and the cation present. This allows for effective tailoring of the material to store the maximum amount of hydrogen possible. It has been noted that zeolites could be used to encapsulate other gases once degassed[8-10] and as such they were considered to be good candidates for hydrogen storage[11, 12].

Fraenkel et al. established that an ion-exchanged zeolite A would adsorb and encapsulate hydrogen from pressures of 24 bar at elevated temperatures[11]. However, hydrogen encapsulation capacity was low: 0.6 wt% at 917 bar for a partially exchanged Cs-A (Cs ions per cage = 5.4). It was observed that the radii of the ions determined the efficiency of encapsulation by blocking hydrogen release at room temperature and pressure; smaller ions allowed higher and easier inclusion of hydrogen into the framework but larger ions retained more of this H_2 content once the pressure and temperature were returned to RTP.
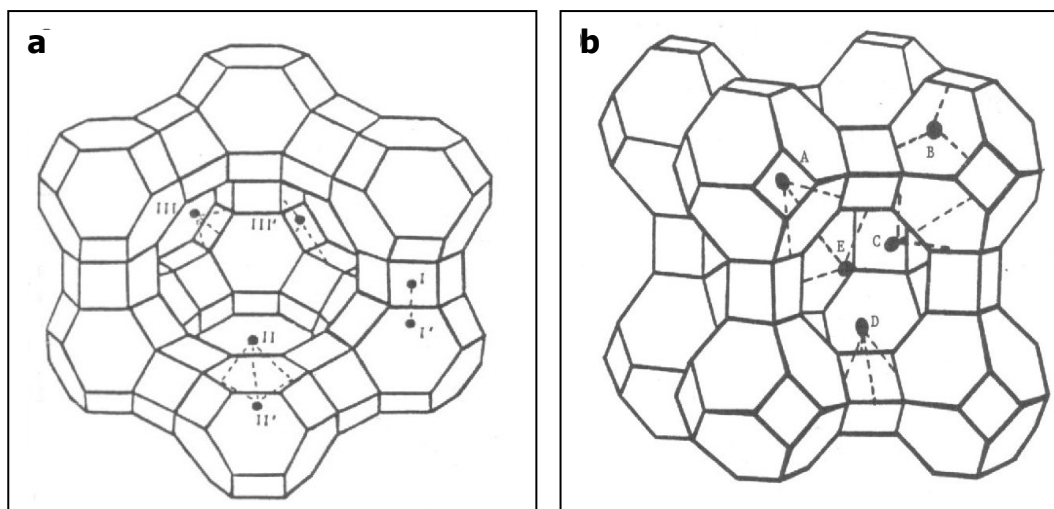
Figure 2.2 : Diagram depicting the structure of a) Zeolite X/Y and b) Zeolite A with cation sites highlighted[74]

Low temperature studies on adsorbed hydrogen were first performed to determine its interaction with the surface as a means to better understand the electrostatic forces for solid-state catalysts and other surface-driven mechanisms[13]. Later it was discovered that, in zeolites, hydrogen formed a stronger affiliation with the cations present and was used to determine the positions of sodium in zeolite X[14, 15]. Kazansky et al. reported that although the particular cation present at the adsorption site was important, at low temperatures isothermal data showed the uptake of H_2 for LiX, NaX and CsX to be almost identical leading them to suggest that the framework also had an effect on H_2 adsorption[16, 17]. Hydrogen adsorption in zeolites had also been utilised for applications in gas purification and separation[18, 19] though no direct link to storage of hydrogen was made from the research.

A study by Langmi et al. which focused purely on the storage aspects of zeolitic materials reported a slightly higher wt% H_2 uptake to Kazansky (1.2 wt% at 77K, 0.2 bar H_2[16]) with an observed 1.79 wt% at 77K, 15 bar H_2 for NaX[20]. Of the numerous zeolites studied NaY adsorbed the highest amount of H_2 with an observed 1.81 wt% at 77K, 15 bar H_2. Elevated and room temperatures yielded very poor results for all materials involved. It was also noted that increased BET N_2 surface area measurements correlated with H_2 uptake as observed by

Nijkamp et al. – though this trend does not apply to materials with pore sizes that are too small to be 'seen' by the N_2 molecule but that will allow passage of H_2.[20, 21].

In an attempt to increase the hydrogen storage potential of zeolites a broad range of ion exchanges has been investigated. Exchange of Na with other alkali and alkaline metals resulted in mixed results; Na, K and Ca ion-exchanged zeolites proved to have the highest hydrogen storage potential for zeolites X and Y, with CaX achieving 2.19 wt% H_2 uptake at 77K[22]. An alternative route is to replace the metal ions with organic 'ions' to promote hydrogen adsorption at higher temperatures[23]. Bae et al. substituted the cations for pyridine complexes in NaY and HY. This resulted in H_2 uptake of 0.29 (± 0.05) wt% for a pyridinium chlorochromate exchanged NaY and 0.34 (±0.08) wt% for the equivalent HY exchanged sample at 298K under 10 bar H_2. Earlier literature suggests that no significant H_2 uptake is observed for NaY[12, 20] and so the authors' attempts to synthesise an 'organic-inorganic hybrid-zeolite' provide an interesting addition to potential zeolite hydrogen stores.

Overall, there are aspects that make zeolites appealing for non-mobile storage of hydrogen:

- they are not flammable in hydrogen or air

- their synthesis has a low carbon footprint and they are cheap to produce

- potentially operate at near-room temperature conditions

However, there are problems with zeolitic hydrogen stores that make them unlikely to achieve widespread acceptance:

– they are sensitive to atmospheric water content – though this can be reversed

– they have very low gravimetric densities

– low heat of adsorption for H_2 in most cases

2.2.2 Nano-structured carbon

Nano-structured carbon materials are a diverse collection of non-planar carbon structures ranging from single- and multi-walled carbon nanotubes (SWNT/MWNT) to nanofibers and nanohorns. MWNTs were discovered first during fullerene synthesis[24] and consist of multiple concentric layers of graphite sheets. SWNTs are similar, in that they are formed from graphite sheets[25] though they also have the ability to self-arrange into ropes via van der Waals forces[26]. Graphite sheets are themselves not ideal hydrogen adsorbents as the ΔH_{ads} for H_2 is small, however, due to the curvature and the diameter of the SWNTs or the area between graphene layers in MWNTs being small, the potential fields of the surfaces overlap providing a stronger binding energy than that of a flat surface. This is due to the reduced overlap of the π electrons in the double bonds resulting in localised fields[3].

Despite the increased surface area and electrostatic interactions between H_2 molecules and carbon nanotubes over graphite sheets, there is little evidence that substantial amounts of adsorption can take place. At 1 bar and 77K, unaltered SWNTs have been reported to take up between 0 - 2.5 wt%[21, 27] H_2 whereas unaltered MWNTs take up between 0 - 0.25 wt%[28]. These values are of the same order as steam activated carbons at 77K, 1 bar H_2, which range from 0 - 1.5 wt% although one particular activated carbon achieved 2 wt%[21]. Increasing the H_2 pressure results in increased wt% value at the same temperatures, as observed by Chen et al.[29] with 2.9 wt% H_2 at 50 bar and 77 K.

There are two processes for uptake of hydrogen in carbon materials – physisorption of hydrogen molecules onto the surface or cavities of the material or chemisorption on the carbon to form C-H bonds (Figure 2.3)[30].

As with zeolitic materials, the potential adsorption of hydrogen on carbon materials is directly linked to the surface area[21, 27] and as such, much research has concentrated on the production of carbons with this aspect. However, carbon materials can also chemisorb hydrogen through bonding to 'dangling' carbon atoms at defect sites after partially damaging
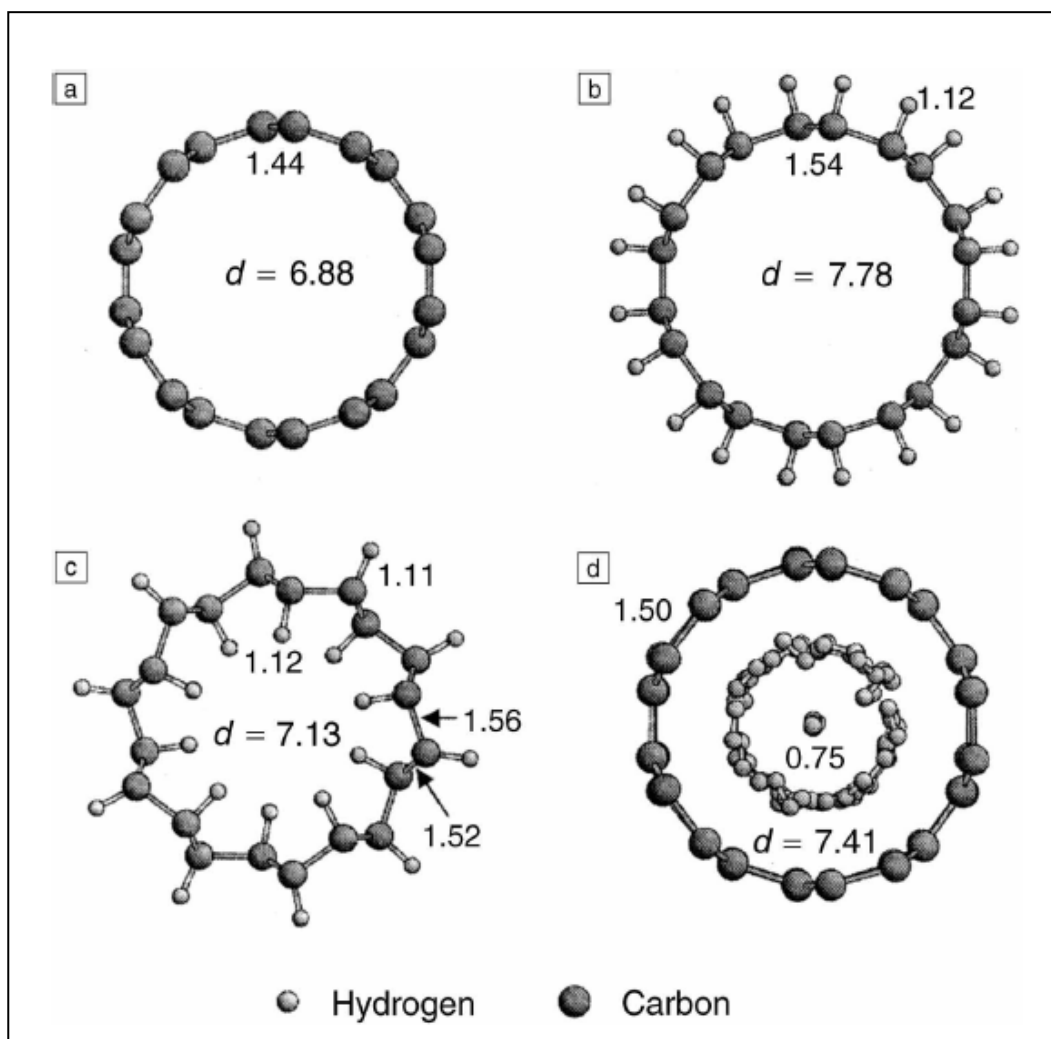
Figure 2.3 : A diagram depicting a) clean carbon SWNT, and various sorption mechanisms: b) arch type (H atoms chemisorbed on the exterior), c) zigzag type, (H atoms chemisorbed on both the interior and exterior), d) molecular hydrogen situated within the nanotube[97]

the nanotubes through acid treatments that are used to remove metals[31]; excessive washing with acid can potentially decompose the nanotubes and form hydrocarbons. Acid-treated SWNTs exhibit higher surface areas and thus higher hydrogen adsorbing properties, achieving 1.8 wt% H_2 at 1 bar, 77 K in comparison to the same sample before acid-treatment which had an uptake of 0.8 wt% at the same temperature and pressure[32].

Mechanical milling of graphite has been shown to introduce defects[33] and thus increase surface area for nano-structured carbon. It has also been shown that if milling is performed under a pressure of hydrogen that absorbed (bonded) hydrogen will form[34] with desorption

occurring at ~600 and 950 K[35]. This technique saw an uptake of 7.4 wt% H_2 though it was determined that this was primarily from C-H bonding rather than physisorption and after treatment at high temperatures the authors were unable to re-hydrogenate the sample.

Residual metals that are incorporated into carbon nanotubes, while able to block access to inner surface areas, can also have a positive effect on hydrogen uptake. Yang investigated the effects of doping Li and K onto MWNTs and discovered that their adsorption properties were increased to 2.5 and 1.8 wt% under 1 atm H_2 and 500°C, respectively[36]. This work was in response to erroneous data from Chen et al. who observed higher wt% values due to contamination of the sample by water vapour from the high pressure cylinder supplying the hydrogen[37].

Zhong et al. doped Ni and Co into amorphous carbon via an electric arc method – successfully increasing the H_2 storage capacity to 2.3 wt% for a 20 wt% Ni-containing sample at 35 bar and 500°C which decreased upon subsequent hydriding / dehydriding cycles to 1.6 wt% due to migration of the Ni atoms out of the carbon matrix[38]. Co-containing samples exhibited similar behaviour, absorbing 1.6 wt% H_2 at the same temperature and pressure. C-H bond stretches were observed with IR spectroscopy and as such the authors attributed the high temperature H_2 uptake to chemisorption – aided by the presence of Ni and Co. The same Ni-containing sample was also investigated at 77K and it was observed that H_2 uptake increased with pressure – with a maximum measured value of 2.7 wt% at 70 bar and 77K though this is not attributed directly to the presence of Ni.

The mechanism of hydrogen transport from metal centres onto nearby carbon was coined the 'spillover effect' by Boudart et al.[39, 40] though the effect was studied before[41, 42]. Pt metal centres doped in carbon were observed to ease diffusion of hydrogen atoms onto the surface of the carbon through a process of migration from the Pt interstitial sites to the carbon surface – increasing the maximum uptake above the un-doped carbon and Pt – though this effect was not observed for other materials such as alumina[41]. Sancier et al. also reported a diffusion of H_2 from Pt and Pd metal centres in alumina, silica and Na/Ca zeolite Y – observed

during ESR experiments[42] – through a reduction mechanism involving iron oxide. Lueking et al. have since utilised this effect to increase the hydriding potential of MWNTs by providing diffusion sites from a $Ni_{0.4}Mg_{0.6}O$ catalyst[43]. It was found that the highest H_2 uptake was observed when synthesising the MWNTs in situ with the catalyst (0.65 wt% 1 bar H_2, 25°C) and was determined to promote more linkages between the catalyst and the carbon nanotubes. It is important to note that the $Ni_{0.4}Mg_{0.6}O$ catalyst is commonly used to decompose methane for the production of MWNTs and the spillover effect could potentially have affected H_2 uptake results gained from this synthetic process[36, 37]. In subsequent experiments it was found that MWNTs with catalytic $Ni_{0.4}Mg_{0.6}O$ could adsorb up to 3.7 wt% H_2 with 1.3 wt% absorbed by the catalyst to form a hydride of the form $H_xNi_yMg_{1-y}O$ at 69 bar, 298°C[44] and that carbon nanotubes benefited the most from spillover when compared to nanofibers and activated carbons[45].

Carbon materials are a promising area of research, however they suffer from similar drawbacks to zeolitic materials: namely the volumetric density of the hydrogen incorporated within and the low temperatures for physisorption to take place. Their dependence on extremely high pressures of H_2 gas to operate efficiently is also a drawback especially when considering compressed gas storage has a higher volumetric density under these conditions.

2.2.3 Metal organic frameworks (MOFs)

In an attempt to obtain large surface area materials specifically designed to adsorb hydrogen at low temperatures, a bottom-up approach (using known starting structures to direct the assembly of larger structures that maintain similar properties) has been undertaken to discover the attributes required for direct synthesis of these ideal materials. There are some attributes that are preferred for a MOF[46]:

- Geometric rigidity

- Chemical functionality

- Simple and cheap scalable syntheses with high yields

- Lightweight composition

- High surface area

MOFs utilise polymerisation techniques to form ordered structures from relatively simple building units comprised of metal centres and organic linking units. These units define the structure of the resulting compound (e.g. width of channels or pores for adsorption) and thus a certain amount of prediction is involved in the selection of and reaction between these building blocks. This process is termed 'reticular synthesis' by Yaghi et al.[47].

The most attractive feature of MOFs is their generally high surface area of >1000 m^2/g [48]. However, the geometry of this internal surface is also important in the physisorption of hydrogen and unlike zeolites or carbon, a higher surface area does not necessarily equate to increased H_2 sorption. For example, MOF-177 has a surface area of 4526 m^2/g and an H_2 uptake of ~1.2 wt% in comparison with IRMOF-11 with an area of 1911 m^2/g and uptake of ~1.6 wt% at 77 K[49]. Uptake of H_2 can be affected by the polarities of the surface area from the linking units and metal centres and occupancy of the binding sites by solvents[46]. It is therefore possible to discern favourable H_2 binding sites and then tailor the properties of the

surfaces of a MOF to more effectively physisorb H_2 molecules and release solvent molecules by varying the organic linking units[50].

One problem for the formation of MOFs is interpenetration of the crystal lattice of the product(s) which takes place when the reagents polymerise around each other[51]. This can reduce the available internal pore volume but increase the overall surface area per m^3 though the result of these effects on hydrogen sorption within the materials cannot be predicted beforehand when designing a MOF system. Interweaving of frameworks is a similar process that also can occur during MOF synthesis[52], however, in this case the frameworks are identical – one encased in the other – and there is little loss of pore or channel volume (Figure 2.4). An attractive effect of this process is that the structure is strengthened – resisting decomposition at higher temperatures as well as dissolution in solvents.

Impregnation or intercalation of a different compound – such as a carbon structure - is another method that can increase the potential surface area interactions for H_2 sorption and thus improve the uptake capacity of the material[53]. However, all three of these methods decrease the gravimetric density of H_2 storage in these frameworks due to the incorporation of a larger number of heavier elements within the same volume.

It is possible to produce MOFs with metal centres that have free metal coordination sites after removal of ligands (such as water) at temperature. In certain compounds these ligands provide structural integrity and removal results in collapse. However, it is possible to select metal centres which form frameworks that retain their porosity once de-ligated[54]. These metal centres are attractive due to the possibility of direct interaction with H_2 molecules or atoms – thus increasing binding energies from charge interactions or through chemisorption. Typically, only a fraction of these metal centres are occupied when at full capacity.
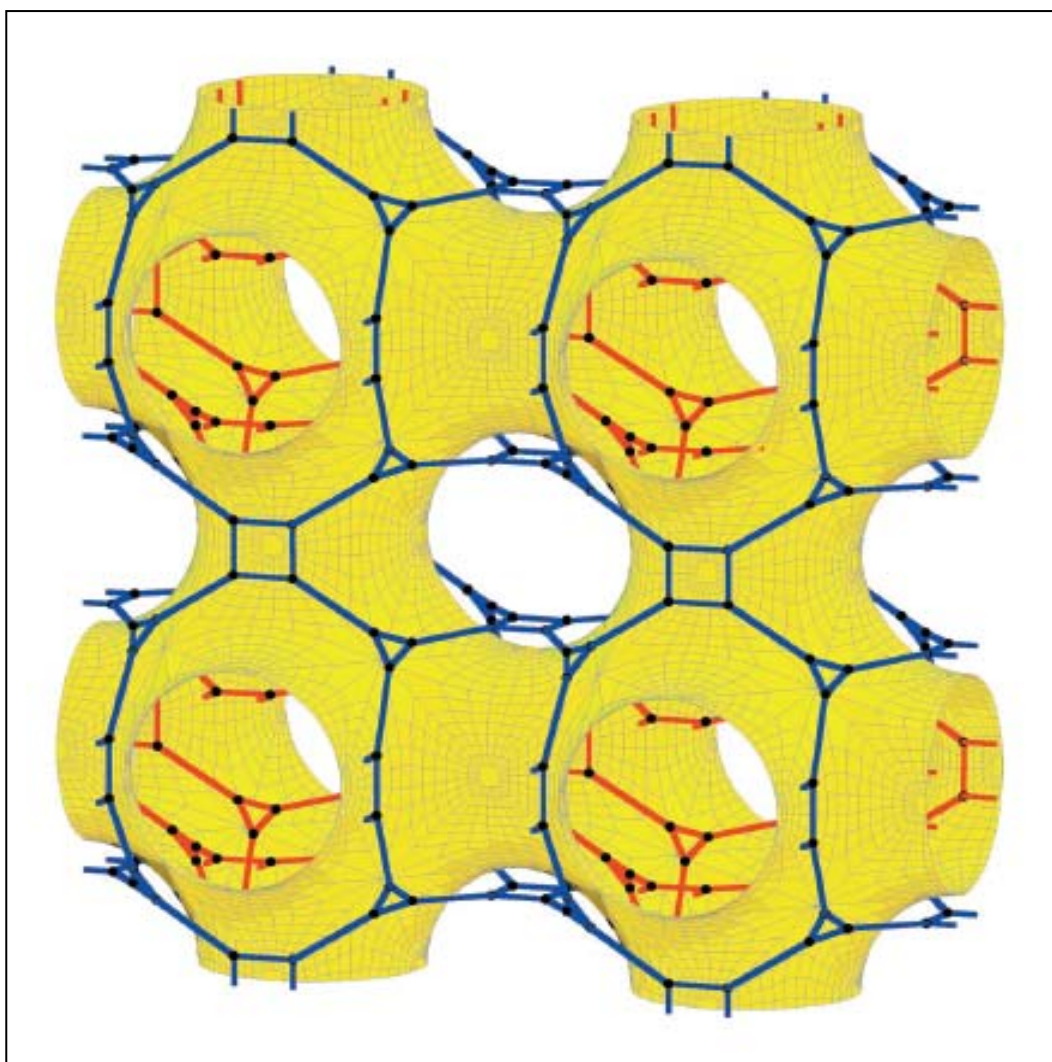
Figure 2.4 : A schematic of two interwoven MOF-14 frameworks – the red and blue structures are identical but formed one inside the other and rotated 90 degrees. The lines and dots are simplified structures representing linked square 'paddle-wheel' and triangular BTB building units linked by copper ions.
The yellow structure is a virtual P-minimal surface that defines the separation between them – a partition that neither structure crosses[52]

MOFs hold some promise as possible stores for hydrogen: they are cheap and easy to produce with high yields and they have high surface areas and numerous options for the organic linkers, allowing customisation towards H_2 sorption[50]. There are some barriers to overcome in the form of low gravimetric and volumetric densities as well as operational temperatures – though their H_2 uptakes at room temperature are more promising than those of zeolites and on a par with carbon.

2.2.4 Microporous polymers

With MOFs providing low gravimetric density for hydrogen storage due to their inclusion of metal centres several research initiatives have removed metals and their ions from a synthetic standpoint and instead have concentrated on the polymerisation of organic compounds. These polymers of intrinsic microposity, PIMs, are designed to be tailored towards optimum hydrogen uptake by incorporating the maximum number of micropores per unit volume for H_2 physisorption[55].

Most polymers are not suited as hydrogen storage mediums as, due to their flexibility and space-filling tendencies, little to no microporosity is observed. PIMs, however, are rigid macromolecules synthesised from two monomers composed of fused-ring components that are unable to contort into different configurations, ensuring that inefficient packing takes place[56]. For microporosity to be achieved there must be at least one site of contortion in a monomer's structure that will not allow free rotation of part of the molecule. These can take the forms of spiro-centres and non-planar rigid molecules (Figure 2.5). This inefficient packing results in an amorphous material that has a porous microstructure that is not reduced over time by relaxation/minimisation of the structure.
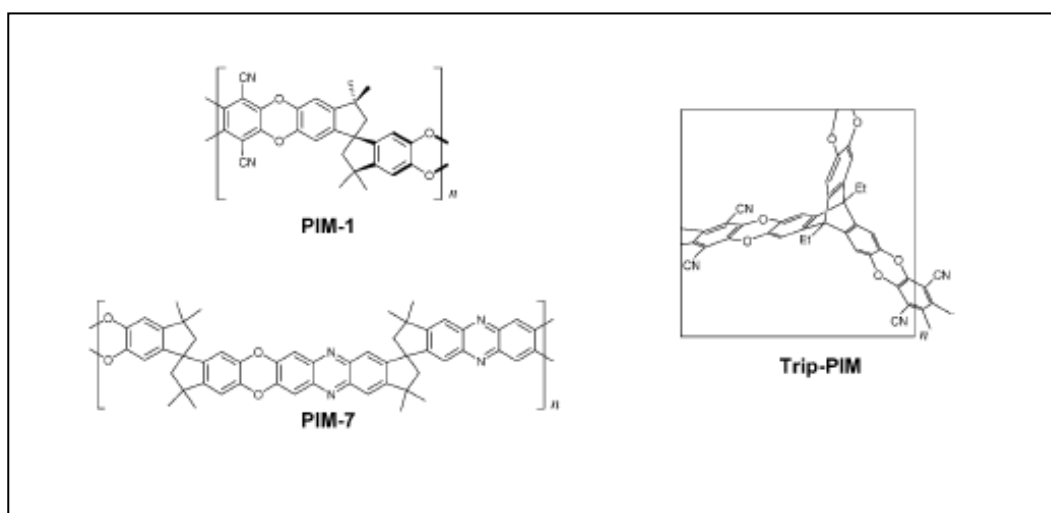

Figure 2.5 : Molecular structures of PIMs 1, 7 and a triptycene-based PIM showing spiro and rigid non-planar structural elements that are vital to micropore formation[55]

Inclusion of π-bonded aromatic components can also encourage favourable van der Waals interactions through partial polarisation of the H_2 molecule and it has been shown that H_2 is preferentially adsorbed where the contortion sites are situated[56, 57]. Due to the amorphous nature of PIMs there is no defined porous structure, however pore size measurements have shown that the smallest pores range from 0.5 to 1.5 nm across a range of polymer materials[55] with 1.4 to 3 wt% hydrogen sorption observed at 15 bar H_2, 77K. PIMs 1, 7 and the triptycene-based PIM adsorbed H_2 in accordance with their calculated relative surface areas in the same fashion as carbon materials: 1.5, 1.4 and 2.8 wt% respectively at the same temperature and pressure.

Similar results have been reported for polymers featuring multiple cross-links between the monomers[58, 59] created by first forming the polymer then swelling it by occluding a suitable solvent within the structure. This swelled structure is then cross-linked via a Friedel-Crafts reaction, creating a nanoporous structure. In this manner, materials with surface areas greater than 1000 m^2/g are achievable; displaying H_2 uptakes equal to and exceeding those of the currently reported PIMs: Lee et al. synthesised a cross-linked polymer with a surface area of 1466 m^2/g and an H_2 uptake of 3 wt% at 15 bar, 77K[59].

Polymer materials designed for the storage of hydrogen are interesting possible storage solutions and benefit from being relatively undeveloped when compared with the alternatives. They display the same relationship between increasing surface area and H_2 adsorption as carbons while retaining a relatively lightweight composition when compared to metal-containing frameworks and the possibility of much higher surface areas combined with nano-porous structure which facilitates H_2 uptake could result in even higher adsorption values. However, their development can be difficult and though self-forming units are useful in theory, in practice the structure that is formed is highly dependent on more that just the reactants present in the mixture[51]: small changes in reaction conditions such as interactions with solvent molecules and counterions can result in various alternative structures being formed as well as defects and malformations that affect and reduce the porous nature and stability of the structures.

2.2.5 Porous materials conclusions

While development of porous materials as potential hydrogen storage materials has increased in recent years resulting in increased storage capacity per unit volume, their viability has not improved appreciably.

Low temperatures are still required to store and maintain storage of hydrogen as well as constant high pressures. While some porous materials display H_2 uptake values approaching the DoE requirements, these are at hundreds of bars of pressure. The materials are also vulnerable to atmospheric interference as many are hygroscopic or will preferentially adsorb other molecules within their structures meaning that stores must be kept in a sealed state at all times. These factors increase the cost of building and maintaining stores based on these materials and at the present time it is unlikely that any of these particular solutions will be adopted on any scale.

2.3 Metal hydrides and alloys

The premise of using metals and alloys as hydrogen storage materials is a relatively recent development considering when the knowledge of hydrogen combining with metals was discovered. During the initial phase of the 'hydrogen movement' in the 60s and early 70s metal hydrides and their alloys were targeted as a possible solution to the problems of liquid and pressure containment, especially for applications in the transport sector[60]. While still requiring energy to effectively add and remove H_2 from each solid state store, depending on the compounds used, the risk of fire and explosion is greatly reduced in comparison to both liquid and compressed gas stores.

In contrast, the process of alloying metals has been known for many centuries – dating back, at least, to the Bronze Age. Traditionally, this alloying process is conducted by melting the constituents together to facilitate mixing and thus the formation of a new phase, though more recently reactive mechanical milling techniques have been developed that also yield

alloys through less demanding syntheses[61]. In fact, due to the forces present in mechanical milling syntheses, it is possible to form phases and compounds that are unachievable through melting under non-reactive atmospheres[62].

2.3.1 Transition metal alloys

The storage of hydrogen in transition metal alloys has been well documented[63-65]. There are different known combinations of metals that produce hydrogen storage materials of the forms AB, AB_2 and AB_5 (where A and B represent different metallic elements, though partial substitution with one or more transition metals is also possible). Hydrogen is generally stored in an interstitial manner[66] (Figure 2.6) in these crystalline structures rather than through direct insertion into a crystal structure which results in a lower threshold for absorbing and desorbing H_2.

Figure 2.6 : Depiction of the octahedral and tetrahedral interstitial sites in a face-centred-cubic crystal structure[(131)]
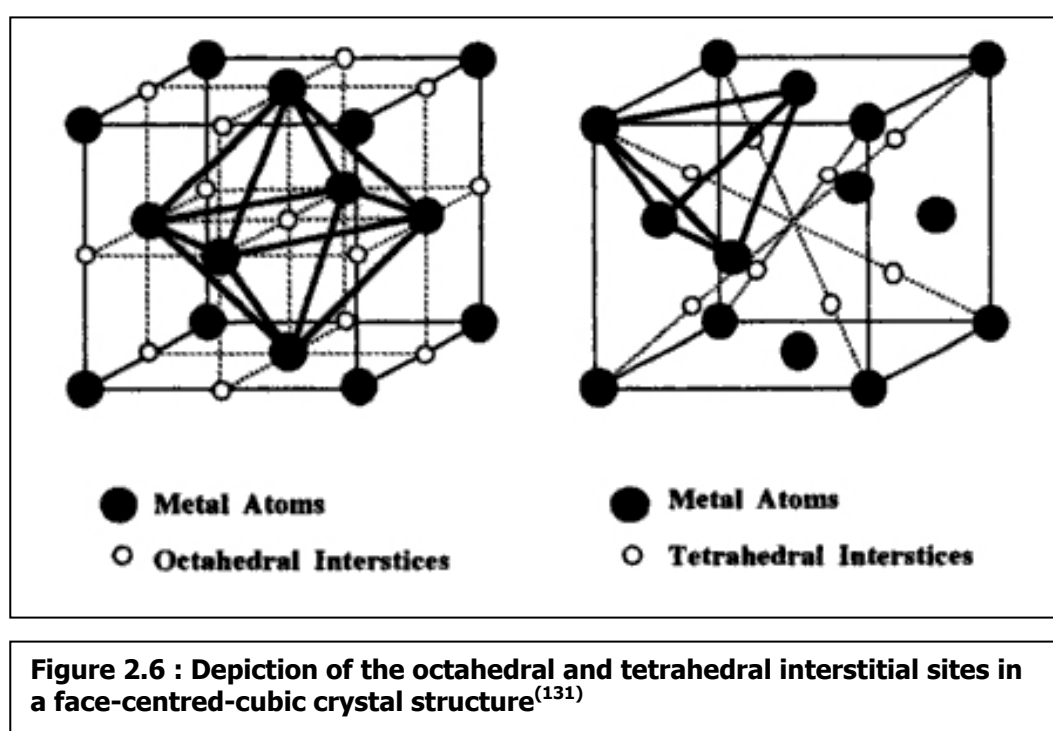
One of the main drawbacks to the use of transition metal alloys (TM) alloys is the cost of the materials: many are composed of expensive elements such as the lanthanides and actinides. (for example pure La costs ~$233 per 100g[67]). On top of this cost, most TM alloys usually require activation to allow storage of hydrogen to take place due to 'dirty' surfaces through

which hydrogen is unable to pass through – which usually takes the form of oxide or hydroxide layers of the compound in question. This problem can be alleviated through mechanical milling techniques which reduce the overall particle size and increase the defects along grain boundaries which provide a clean surface for H_2 interaction with the alloy[68, 69].

Decrepitation – caused by repeated hydrogenation and dehydrogenation – also results in reduced particle size which increases the kinetics of those two processes. A further aspect of using TM elements is the reduction in percentage weight of H_2 stored in the alloy which is a consideration for small and mobile applications with many TM alloys (FeTi, Mg_2Ni, $LaNi_5$, $MmNi_5$ and $TiCr_2$) capable of storing less than 3-4 wt% H_2 at temperatures below 300°C. It has been shown that kinetics of hydrogenation and dehydrogenation can be improved by addition of impurities through alternative synthetic routes and composition through addition of selected elements[70, 71].

Unlike most of the porous and basic metal hydride materials TM alloys can be resistant to the effects of poisoning from the atmosphere and can be relatively easily regenerated via the same high temperature annealing processes used to activate them[72-74], though usually at a loss of total H_2 capacity. However, gases such as CO and H_2S are highly poisonous to the materials even at low concentrations[75].

Transition metal alloys are unlikely to be widely adopted for storage of hydrogen due to their expense and weight (and low weight percent H_2 storage), though specific application of these materials might become established due to their reliability and low operating temperatures.

2.3.2 Metal hydrides

In comparison to the complex transition metal alloys and their hydrides, metal hydrides consist primarily of chemical compounds that are ionic- and covalently-bonded with their hydrogen content rather than storing the hydrogen interstitially[53]. There are two types of metal hydride: those that are reversible at relatively low temperatures and pressures and those that are more stable and thus require more extreme conditions in order to re- or dehydride. In long term applications of metal hydride stores irreversible or unfavourably reversible compounds and processes such as hydrolytic generation of H_2 can be ruled out due to the high cost of maintaining these systems[76]. Reversible hydrides must also have a high weight percent and volumetric content of H_2, fast de/hydrogenation kinetics at reasonably low pressures (<50 bar) and low cost with preferably a 1 bar equilibrium pressure at 25°C. These requirements reduce the available elements for storing hydrogen to the light weight alkali metals, alkali earth metals, transition metals and non-metals. Of this list of desirable elements three main elements can be picked out as targets for prospective hydrogen storage compounds: lithium, sodium and magnesium.

2.3.3 Lithium compounds

Lithium is the lightest metal and as such is desirable as a component in a solid state hydrogen store from a gravimetric viewpoint. Prospective lithium compounds for use as a storage material are LiH, $LiNH_2$, $LiBH_4$ and $LiAlH_4$ corresponding to 12.7, 8.8, 18.5 and 10.6 wt% H_2 content respectively. However, due to its highly ionic nature lithium tends to form strong bonds with hydrogen that are not easily dissociated and these four compounds all have relatively high decomposition temperatures: 720, 374, 380 and 180°C, respectively[53, 77].

a) Lithium aluminium hydride

Despite the low decomposition temperature of $LiAlH_4$, the compound is not practically reversible, requiring high temperatures and pressures of H_2 to be successfully reconstituted. However, following on from work performed by Bogdanović at al. on doping sodium aluminium hydrides with compounds containing Ti and Fe[78, 79], Chen J. et al. demonstrated that doping with $TiCl_3/AlCl_3$ greatly enhanced the kinetics of the decomposition and reformation of $LiAlH_4$[80] via the following pathway:

$$3LiAlH_4 \longrightarrow Li_3AlH_6 + 2Al + 3H_2$$

$$Li_3AlH_6 \longrightarrow 3LiH + Al + \frac{3}{2}H_2$$

$$3LiH \longrightarrow 3Li + \frac{3}{2}H_2$$
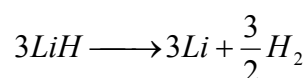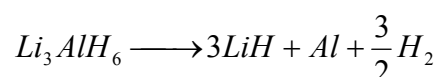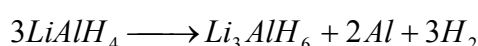
The $TiCl_3$ is reduced by $LiAlH_4$ resulting in Ti acting as an electron donor and acceptor – as had been predicted by density functional band calculations[81] – though the total amount of H_2 stored each cycle reduced with time.

b) Lithium amide

$LiNH_2$ is also an unfavourable hydrogen store due to its decomposition products including ammonia and lithium nitride[82] which result in reduced H_2 storage capacity through loss of nitrogen and borderline irreversibility due to the thermodynamic stability of Li_3N. Similarly, LiH is also thermodynamically stable: requiring above 600°C to completely dissociate making the compound unattractive as a hydrogen storage material. Chen et al. discovered that the presence of LiH during the decomposition of $LiNH_2$ greatly reduced the evolution of NH_3 in favour of increased H_2 desorption[77, 83]. It was observed that the onset temperature of desorption was decreased to ~ 100°C for a 1:1 mixture, from ~ 200°C for pure $LiNH_2$, with a mass loss of 6 wt% at 200°C under dynamic vacuum. A 1:2 $LiNH_2$, LiH mixture showed more promising results with ~ 6.5 wt% produced at ~190°C under vacuum with full decomposition

at ~430°C resulting in 9.6 wt% mass loss. Analysis of the products at each of these two stages showed Li_xNH_{3-x} (with some unreacted LiH) and Li_3N respectively. Furthermore, it was shown that this reaction was reversible above 150°C under a pressure of H_2[77, 84] and Chen et al. and proposed the following reaction scheme:

$$LiNH_2 + 2LiH \longleftrightarrow Li_{1+x}NH_{2-x} + xH_2 + (2-x)LiH \longleftrightarrow Li_3N + 2H_2$$
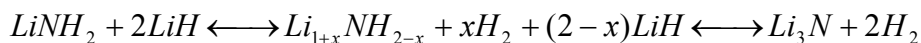
It was shown by Hu and Ruckenstein that the reaction proceeded via the interaction of NH_3, released from $LiNH_2$, and LiH to form $LiNH_2$ and H_2[85] which is thought to be near instantaneous upon contact at 300°C[86]. This diffusion of NH_3 has been determined to be the rate limiting step for dehydriding and that the overall surface contact between LiH and $LiNH_2/Li_2NH$ is important for continued reversibility of the reaction[87]. The combined possible H_2 stored in this system is ~ 10.4 wt%. However, due to a lower negative enthalpy change, it is thermodynamically easier (and thus more energy efficient) to store hydrogen in the amide/imide part of the system, which equates to 6.5 wt% H_2, than proceed to full desorption of H_2 to form the nitride. It is also kinetically faster to hydride Li_2NH to form $LiNH_2$ than it is to hydride Li_3N to form Li_2NH due to the porous nature of the Li_2NH compound which allows diffusion of hydrogen and ammonia during absorption and desorption[87].

c) Lithium borohydride

Lithium borohydride has the highest H_2 content by weight though only begins to desorb well above its melting point (~275°C) at around 600°C to produce H_2, LiH and B under 10 bar H_2. The process is reversible under extreme conditions: 600°C, 350 bar[88] H_2 – both of which are undesirable for hydrogen storage compounds for use in commercial and non-commercial applications. At room temperature $LiBH_4$ has orthorhombic symmetry (space group Pnma) with the tetrahedral anions, which are aligned in two orthogonal directions, under strong distortion with respect to their B-H bond lengths and angles (Figure 2.7)[89]. Each Li is coordinated to nine H atoms: three pairs from three of the four surrounding BH_4^- units with the last three bonded to the fourth BH_4^- unit. The compound undergoes a structural phase transition at ~108°C to a hexagonal symmetry (space group $P6_3mc$) that is closely related to
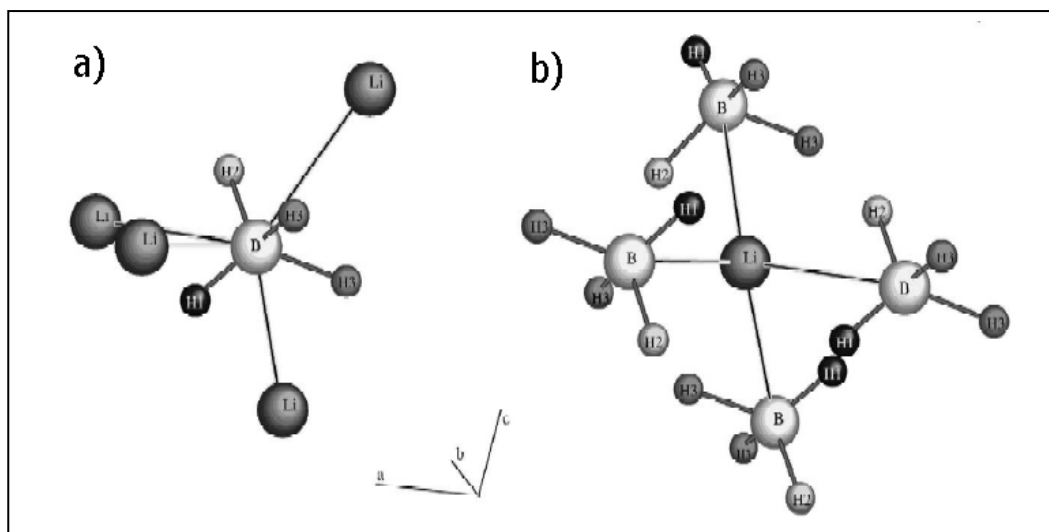
Figure 2.7 : Diagram showing the coordination of a) boron and b) lithium in orthorhombic LiBH₄ at room temperature[89]. Boron is the large light gray balls and lithium is the large dark gray balls with the remainder being hydrogen atoms

the orthorhombic room temperature polymorph. The transformation of the unit cell retains the arrangement of the Li^+ and BH_4^- units with a contraction of the orthorhombic a axis and an associated expansion of the orthorhombic b and c axes which results in a density increase for the compound. This high temperature phase has less distortion with respect to the B-H bond lengths and angles. These bonds are no longer orthogonal but point in the same direction, changing the hydrogen coordination for each Li atom; thirteen H atoms: three triplets of three H atoms from the nearest BH_4^- units and one from a fifth, more distant BH_4^- unit[89]. It has also been shown that this high temperature phase evidences rapid lithium ion diffusion throughout the structure whereas H atom diffusion is very slow[90, 91]. The diffusion of hydrogen throughout the structure is limited by their association in the BH_4^- unit, however, it has been calculated that the main process for H diffusion might proceed via the formation of interstitial H_2 in low concentrations which can move through channels in the $LiBH_4$ lattice. These interstitial H_2 molecules would slowly exchange with other BH_4^- units[92].

Although $LiBH_4$ requires >400°C to desorb H_2, theoretical calculations have suggested that destabilisation of the compound through donation of an electron to a surface-doped catalyst

could reduce the temperature for dehydrogenation by lowering the activation barrier[93]. It was also suggested that such a catalyst might support the formation of the theorised orthorhombic phase LiBH (space group Pnma) during dehydrogenation that would liberate 13.1 wt% H_2 and that this phase would enable relatively facile rehydrogenation. Mosegaard et al. observed two intermediate phases during decomposition of $LiBH_4$ via a constant heating rate of 5°C in synchrotron radiation powder XRD experiments[94]. The first phase (I) evolved between 200-300°C was indexed to a hexagonal unit cell and appeared to be marginally more stable than the high temperature hexagonal $LiBH_4$ phase which is seen to melt at 275°C. The second new phase (II) was observed between 300-400°C which was indexed to an orthorhombic unit cell. These phases were synthesised in lab conditions by heating samples of $LiBH_4$ to between 245-265°C in sealed quartz tubes: with longer annealing times (of the order of 5 hours) leading to the formation of phase II presumably through the transformation or evolution of phase I during extended exposure to elevated temperatures. Both phases were stable at room temperature and it was suggested that they were partially dehydrided forms of $LiBH_4$ with phase I desorbing H_2 to form phase II.

Orimo et al have reported the presence of monoclinic $Li_2B_{12}H_{12}$ during the decomposition of $LiBH_4$ between 427-457°C as determined by Raman spectroscopy and thermogravimetric analysis and in agreement with theoretical calculations that predicted its formation[95]. The decomposition follows the following reaction scheme:

$$LiBH_4 \longleftrightarrow \frac{1}{12}Li_2B_{12}H_{12} + \frac{5}{6}LiH + \frac{13}{12}H_2 \longleftrightarrow LiH + B + \frac{3}{2}H_2$$
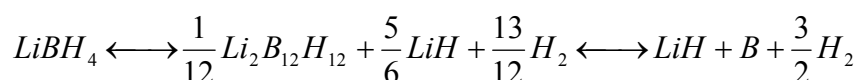
The first step corresponds to a loss of 10 mass% whilst the second step corresponds to a loss of 4 mass%. $Li_2B_{12}H_{12}$ displayed additional and altered B-H bending and stretching modes between 600-1000 cm^{-1} and 2500 cm^{-1} though no XRD diffraction peaks which implies a lack of long-range order at elevated temperatures. Building on this, Friedrichs et al. reported $Li_2B_{12}H_{12}$ was formed above 150°C via the reaction of $LiBH_4$ with diborane (B_2H_6); the reaction also produced an amorphous phase, $Li_2B_{10}H_{10}$ which was formed above 200°C, discovered via

NMR and identified via comparison with the similar phase $K_2B_{10}H_{10}$[96]. $Li_2B_{10}H_{10}$ is thought to form through the following reaction scheme:

$$LiBH_4 + 2B_2H_6 \longrightarrow \frac{1}{2}Li_2B_{10}H_{10} + \frac{11}{2}H_2$$
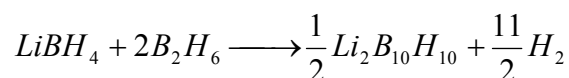
The authors postulate that desorption of $LiBH_4$ at elevated temperatures (>600°C) leads to the release of diborane. Diborane decomposes at temperatures higher than 400°C to B and H_2 though some of the diborane gas (or speculated higher borane species) react with $LiBH_4$ to form the two compounds reported above. This process is also thermodynamically more favourable than the decomposition to LiH, B and H_2: approximately 20 $kJmol^{-1}$ smaller[95]. However, the rehydrogenation process in a hydrogen environment would not carry this benefit and this perhaps explains why such high pressures (155-350 bar H_2) must be used. If such a process did occur then the $LiBH_4$ would not be completely rehydrided as reaction of LiH with B_2H_6 and other analogous boranes results in a passivation layer of $LiBH_4$ on the surface of each LiH grain, hindering diffusion to the centre[97].

The rehydrogenation reaction between LiH and B proceeds slowly, even at elevated temperatures and pressures. However, Remhof et al. observed that the hydrogenation of pre-annealed LiB (using atomic Li and B at 327°C for 60 hours) to form $LiBH_4$ proceeds at much lower temperatures and pressures (150 bar H_2). LiB was observed to partially decompose above 200°C, forming LiH in the presence of H_2, which then reacted with B and H_2 above 350°C to form $LiBH_4$[98].

In 1980, Muller et al. demonstrated that the desorption temperature of $LiBH_4$ could be reduced to as low as 200°C by the addition of 10% aluminium powder[99]. This method, while producing pure H_2 with no gaseous boron compounds, was only reversible at high temperature and pressure (>300°C, >100 bar) and was therefore also impractical as a H_2 storage method. Various other additives have been tested to reduce the absorption and desorption conditions though most result in irreversible reactions or required high temperature and pressure to proceed. Zuttel et al. observed that with the addition of SiO_2 the

desorption temperature was reduced to 200°C[100], while Orimo noted that addition of 10% Mg resulted in a 30°C reduction to desorption and absorption temperatures[88], though these experiments were carried out at 600°C and pressures of 350 bar H_2 upon rehydriding.

Au et al. observed that addition of transition metal oxides (TiO_2, ZrO_2, V_2O_3, SnO_2) and chlorides ($MgCl_2$, $TiCl_3$) through mechanical milling reduced the hydrogen abs/desorption temperatures of $LiBH_4$[101]. However these compounds react with the $LiBH_4$ to produce TiB, LiCl and Li_3BO_3 resulting in reduced storage capacity over successive hydrogenation cycles. Yu et al. also observed improved H_2 absorption and desorption temperatures with the addition of Fe_2O_3, V_2O_5, Nb_2O_5 and TiO_2 via mechanical milling, with hydrogen evolution starting below 100°C and reaching a total of 6 wt% by 200°C for the sample containing Fe_2O_3[102]. It was suggested that the improvement in dehydrogenation was due to a redox reaction between the metal oxide and $LiBH_4$.

It has also been reported that addition of aluminium to $LiBH_4$ in a ratio of 1:2 also results in improved desorption properties with operating temperatures and pressures of 400°C, 100 bar for absorption and 450°C, 10 mbar for desorption of H_2[103]. However, it was observed that the total H_2 capacity (theoretical 8.5 wt%, observed 7.2 wt% 1st absorption, 3 wt% 4th absorption) during hydrogen cycling diminished as a function of each cycle which was thought to be due to loss of boron-containing species during dehydrogenation. Further analysis showed that at these low temperatures the reaction was not complete and that the formation of LiH and AlB_2 via the decomposition of $LiBH_4$ with Al continues above 450°C where LiH and Al react to form LiAl, releasing H_2[104]. Friedrichs et al. reported that the hydrogenation reaction between LiH and AlB_2 can proceed at pressures as low as 13 bar H_2 at 450°C[105] though loss of H_2 capacity was still a problem. This loss of capacity was also observed for mixtures of $LiBH_4$ and silica-gel and was attributed to the production of diborane that accompanied H_2 evolution[106]. The addition of silica to $LiBH_4$ reduced the H_2 desorption temperature under vacuum from 170°C to a maximum around the melting point at 275°C – a second desorption was also observed between 350-500°C.

Various groups have also reported that LiBH$_4$ is destabilised by the introduction of carbon, specifically carbon nanotubes[107, 108]. Superior desorption capabilities compared to LiBH$_4$ were observed when carbon nanotubes were added via mechanical milling. Absorption of H$_2$ took place at 400°C, 100 bar H$_2$ whilst desorption occurred between 250-600°C under 1 bar Ar though the kinetics of the system were very poor[107]. Fang et al. reported improved kinetics with SWNTs (Single-walled carbon Nanotubes) for LiBH$_4$ milled with 30 wt% SWNT for 1h, with 11.4 wt% H$_2$ desorbed within 50 minutes at 450°C, 10 mbar H$_2$. 6 wt% H$_2$ was rehydrided at 400°C, 100 bar H$_2$ over a period of 10 hours though H$_2$ capacity was also decreased over successive dehydrogenation and hydrogenation cycles[108]. Addition of 10 wt% carbon-supported Pt catalyst to the LiBH$_4$ system via milling was also reported to improve hydrogenation and dehydrogenation kinetics[109]. While capacity reduction is also observed, it stabilised at ~4 wt% after successive H$_2$ cycling.

Vajo et al. noted that the reaction of MgH$_2$ with LiBH$_4$ resulted in a partial dehydrogenation to form MgB$_2$ under static vacuum conditions whereby the sample was desorbed into a previously evacuated chamber whilst undergoing heating at a rate of 2°C/min to 450°C and which resulted in the production of 8-10 wt% H$_2$[110] in the presence of 2-3 mol% TiCl$_3$ via the following reaction:

$$LiBH_4 + \frac{1}{2} MgH_2 \longrightarrow LiH + \frac{1}{2} MgB_2 + 2H_2$$
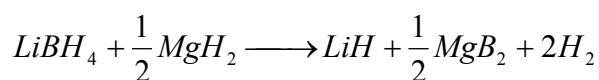
The reverse reaction can be achieved at 350°C at 100 bar H$_2$ with relatively fast kinetics – the reaction and its reverse complete within a few hours – which improve with subsequent hydrogen cycles. It was noted that, on dehydrogenation, a pressure of H$_2$ was required for the formation of MgB$_2$ otherwise Mg metal formed and there was a subsequent loss of H$_2$ capacity upon rehydriding. This was possibly due to the loss of boron-containing gases though these were not observed through residual gas analysis (RGA). Wan et al. confirmed that 8.3 wt% H$_2$ was absorbed over a period of 7 hours for a 120h milled mixture of LiH and

MgB$_2$ to form LiBH$_4$ under similar conditions (265°C, 90 bar H$_2$) though desorption proceeded very slowly at this temperature, only achieving 2 wt% H$_2$ in 7 hours under a vacuum of 10^{-3} bar [111]. Shaw et al. elucidated the hydrogenation mechanism at 265°C and observed that it was driven primarily by rehydriding the Mg phase[112]. It was also observed that the use of liquid nitrogen temperature mechanical milling reduced the presence of particle 'caking' which reduces hydrogen diffusion into the particles of the material through a process of cold welding LiBH$_4$ onto the surface of MgH$_2$ particles during the normal room temperature mechanical milling procedure. Caking was removed altogether via the addition of 5 vol% graphite and was presumed to control the process due to its inherent lubricating properties[113]. The addition of 5 vol% C greatly improved the dehydriding kinetics, releasing 4 wt% H$_2$ in 7 hours at 10mbar H$_2$, 265°C compared to a sample of 2LiBH$_4$ + MgH$_2$ that released 0.5 wt% in the same time period. However, samples containing the graphite were observed to kinetically degrade over subsequent hydrogen cycles; this was attributed to grain and particle growth and loss of defects in the microstructure while held at constant temperature.

The stoichiometric effects of combining LiBH$_4$ and MgH$_2$ were investigated by Price et al. who reported that a ratio of 03:1 had faster kinetic properties than for the previously reported 2:1 under dynamic vacuum for desorption and 100 bar H$_2$ for absorption at a heating rate of 1°C/min from room temperature to 550°C[114]. It was observed that the 0.3:1 ratio system decomposed via the formation of Mg-Li alloys[115, 116] whereas the 2:1 system decomposed via a proposed intermediate species similar to that observed by Orimo et al. during the decomposition of LiBH$_4$[95].

The LiBH$_4$-rich system pioneered by Vajo et al. has also been modified by the addition of TM dopants. Crosby et al. noted that the addition of 0.05 mol% vanadium via mechanical milling improved the desorption kinetics of the 2LiBH$_4$+MgH$_2$ system though it had no effect on the absorption kinetics of the sample, which has a lower overall H$_2$ capacity upon H$_2$ cycling than the unmodified mixture of LiBH$_4$ and MgH$_2$[117]. It was also observed that addition of 0.05 mol% Mn resulted in faster absorption kinetics of the same system but that it had no effect

on the desorption kinetics. This was explained through Mn promoting lattice distortion in the decomposition product, MgB_2 which improved the diffusion of Mg vacancies allowing more facile uptake of H_2. In comparison, addition of V improved dehydrogenation due to the formation of $VH_{0.81}$ which promotes formation of H_2. Other groups have also had success improving the kinetics of the $2LiBH_4$-MgH_2 system through addition of TiF_3 and Pd – both of which reduced desorption temperatures. 0.01 mol% TiF_3 was observed to reduce the desorption peaks observed by DSC for the system to 309°C and 388°C which are reduced from the unaltered mixture by 56°C and 106°C respectively[118]. This improvement was observed to occur due to the reaction of LiH with TiF_3 to form TiH_2 and LiF though the exact mechanism was unclear. This sample also had superior hydriding kinetics, completing hydrogenation within 4 hours at 350°C – three times faster than the unaltered $2LiBH_4$+MgH_2 mixture. Weng et al. improved the dehydrogenation of $2LiBH_4$+MgH_2 through the addition of 10 wt% Pd nanoparticles which reduced the desorption temperature from 350°C to 260°C[119]. The addition of Pd results in the formation of the Mg_6Pd alloy through reaction with Mg which appeared to catalyse the reaction between $LiBH_4$ and MgH_2 to form MgB2 at below 400°C.

It has also been shown that $LiBH_4$ can be destabilised through the reaction with $LiNH_2$[120]. Aoki et al. predicted through first principle calculations that the mixture would have a much lower enthalpy of dehydrogenation than pure $LiBH_4$. It was shown that a mixture of the ratio 1:2 resulted in the production of 7.8 wt% H_2 at 250°C under vacuum and was predicted to proceed via the following reaction pathway:

$$LiBH_4 + 2LiNH_2 \longrightarrow Li_3BN_2 + 4H_2$$
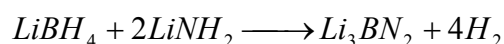
However, after mechanical milling for 1 hour and after heat treatment at 100 bar H_2 at 250°C a new, unidentified cubic phase was observed via X-ray diffraction that was indexed with a lattice parameter a = 10.67 Å, with no trace of the starting materials. This phase decomposed to a Li_3N•BN complex (possibly related to Li_3N•3BN[121]) and Li_3BN_2 and was

determined to be $Li_3BN_2H_8$ by Pinkerton et al. who also observed its formation with a lattice parameter of a = 10.76 Å under similar conditions, though they observed the production of ~11.5 wt% H_2 along with some mass loss due to evolution of NH_3[122]. Later, Chater et al. provided a detailed structural analysis of this phase and determined that the actual composition was $Li_4BN_3H_{10}$[123]. Though this compound achieves a high hydrogen content, thus far it does not appear to be reversible under reasonable conditions.

It has been shown that lithium containing compounds could be used as hydrogen storage materials at moderately high temperatures and reasonable pressures. However their reactive nature with atmospheric components such as oxygen and water and the need to reduce the pressures and temperatures at which these compounds are able to quickly absorb and desorb hydrogen means that they are unlikely to be used outside of the more complex multicomponent systems mentioned above and those yet to be discovered.

2.3.4 Magnesium compounds

Magnesium is a relatively abundant element, making up approximately 2.09% of the Earth's crust, meaning that it is also fairly cheap to acquire. It is also relatively light and is known to form alloys with many of the metallic elements and is therefore ideal for using in a hydrogen storage material. Prospective compounds for use as a storage material are MgH_2, $Mg(AlH_4)_2$, $Mg(NH_2)_2$ and $Mg(BH_4)_2$ which provide 7.8, 9.3, 7.1 and 14.9 wt% H_2 respectively. All of these compounds are reactive with the atmosphere though MgH_2 has the least vigorous reaction and although the aluminium hydride and borohydride have desirably high hydrogen content neither are easily synthesised or purified, with samples from both usually containing NaCl or LiCl as a by-product of their syntheses.

a) Magnesium borohydride

$Mg(BH_4)_2$ was synthesised by Wiberg et al. in 1950 and found to have a decomposition temperature of between 260 – 280°C though this included some bound solvent[124]. More

recent work has shown that the decomposition is a two step process resulting in the formation of MgH_2 and B in the first step and Mg in the second step[125]. The first step was found to be irreversible at temperatures up to 350°C and 100 bar and therefore the use of magnesium borohydride as a reversible hydrogen store would appear to be redundant in favour of the lighter MgH_2 system, though $Mg(BH_4)_2$ would be ideal for single-use disposable systems which utilise thermodynamically favourable reactions between compounds with a high density of H_2.

b) Magnesium aluminium hydride

$Mg(AlH_4)_2$ was also first synthesised by Wiberg et al., however it was only recently that a more accurate decomposition temperature was found[126]. Magnesium aluminium hydride decomposes via two steps: the first at 115 – 150°C corresponding to formation of MgH_2, Al and H_2 and the second at 240 – 290°C which corresponds to the breakdown of MgH_2 to form Al_3Mg_2 which explains the significantly lower desorption temperature for MgH_2. Similarly to $Mg(BH_4)_2$, $Mg(AlH_4)_2$ does not easily recombine and thus is not currently suitable for reversible storage solutions. However, thin films of $Mg(AlH_4)_2$ with a Ti catalyst layer have been shown to be reversible at temperatures below 100°C[127].

c) Magnesium amide

Magnesium amide decomposes via loss of ammonia until ~500°C through the following reaction pathway[128]:

$$3Mg(NH_2)_2 \xleftrightarrow{\;320^oC\;} 3MgNH + 3NH_3 \xleftrightarrow{\;500^oC\;} Mg_3N_2 + NH_3$$
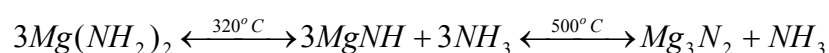
Leng et al. showed that, through a similar process to the reaction between $LiNH_2$ and LiH, it was also possible to reversibly react $Mg(NH_2)_2$ and LiH which proceeds via the reaction pathway:

$$3Mg(NH_2)_2 + 8LiH \longleftrightarrow Mg_3N_2 + 4Li_2NH + 8H_2$$
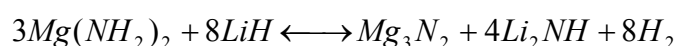
This leads to almost exclusively H_2 desorption – though a small amount of NH_3 is observed – beginning at 140°C with a peak at 190°C and completing by 300°C which resulted in production of ~7 wt%. Leng et al. also observed that MgH_2 could be substituted for LiH in this reaction[129] reducing the onset temperature of desorption to 80°C though increasing the completion temperature to 450°C, with a peak at 415°C which resulted in 7.3 wt% H_2. The reason given for this is the difference in enthalpy of formation between $LiNH_2$ and $Mg(NH_2)_2$ (and thus their relative stability), which form on the surface of LiH and MgH_2 particles respectively from the reaction with NH_3 before further decomposing to the imide.

It has also been observed that, due to the relatively similar size of Mg and Li, mixtures of MgH_2 + $LiNH_2$ and $Mg(NH_2)_2$ + LiH can result in Mg-Li phases due to substitution within one or other lattice[130-132], and these phases possibly provide a lower energy pathway to the formation of the fully hydrided and dehydrided products by allowing an intermediate phase whereby the H_2 can be easily absorbed and transferred. This Li-Mg-N-H phase has a relatively high H_2 plateau pressure (above 10 bar) but relatively slow kinetics at 180°C, and thus desirably the operating temperature and pressure for this system would need to be above this range for absorption[133].

d) Magnesium hydride

MgH_2 is one of the promising possible hydrogen storage compounds. While having a high H_2 content it is also easily reversible at temperatures around 300°C and has a plateau pressure of 1 bar at 280°C. Thermodynamically, hydride formation is favoured with the enthalpy of formation being -75 kJmol^{-1} H_2 which denotes that the formation of MgH_2 is exothermic[134]. The kinetics of hydrogenation and dehydrogenation are relatively slow and they are highly dependent on the overall surface area with which the H_2 can react as well as the diffusion into the inner material of each particle. Oxide layer formation can also impede hydrogen diffusion into the grains and particles and to reduce this effect MgH_2 must be cycled at temperatures above 400°C at vacuum and pressures up to 30 bar[135]. However, it has been shown that thin oxide layers can actually improve the kinetics of hydrogenation by providing

nucleation points for the MgH$_2$ phase[136]. The pressure of H$_2$ also affects the kinetics of absorption and desorption – increasing pressure leads to an increase in kinetics up to ~30 bar above which the kinetics are reduced due to over-saturation of the outermost layer of a given Mg particle leading to a shell of MgH$_2$, blocking access to the inner core of Mg[137]. These factors result in the fact that it is very difficult to completely hydride magnesium and often there will be residual, unreacted metal in a given sample.

At room temperature MgH$_2$ has a tetragonal crystal structure (Rutile type, Figure 2.7), which is referred to as the β-phase (labelled α in the crystallographic nonmenclature), with hydrogen bound to magnesium atoms via a primarily ionic bond. Noritake et al. have shown through synchrotron experiments that the hydrogen atoms also have a weak covalent nature to their bonding between both their Mg and H neighbours and suggest that one route to improvement of the dehydrogenation performance of MgH$_2$ is through the weakening of the
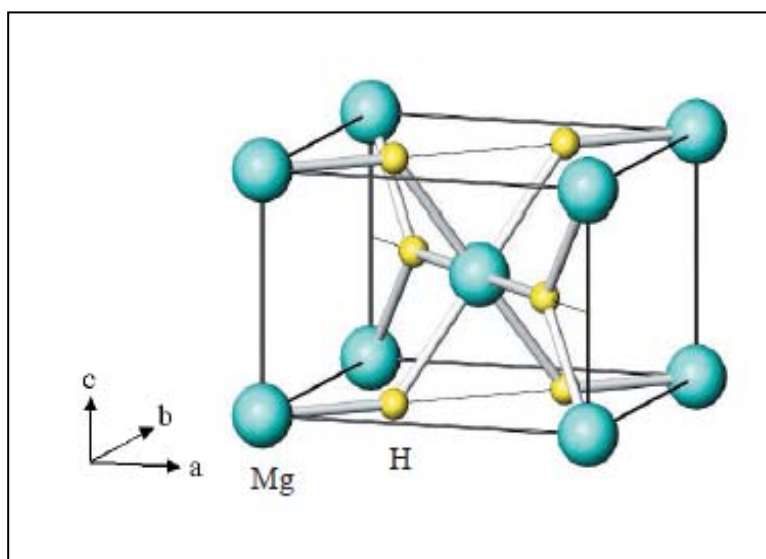
Figure 2.8 : Diagram depicting the crystal structure of MgH$_2$: Tetragonal, Rutile type (Space group P4$_2$/mnm)(138)

ionic interactions between Mg and H atoms[138]. MgH$_2$ can also form various high temperature and/or pressure phases[139] though only the orthorhombic (space group Pbcn) phase is observed to be formed through the process of high energy mechanical milling. This γ-phase of MgH$_2$ is metastable at room temperatures and pressures and is usually formed

between 5.5 – 9.5 GPa at 25°C. The α- and γ-phases of MgH_2 are structurally similar due to the Mg atoms forming edge-linked octahedral in one direction and via corners in the other two directions – possessing the same packing type and coordination number. However, these octahedral are strongly distorted in the γ-MgH_2 phase compared to the α-MgH_2 phase due to the structural rearrangement caused by the $\alpha \rightarrow \gamma$ phase transition[140]. γ-MgH_2 is observed to reconvert to α-MgH_2 at ~300°C under 1 bar H_2 and will not reform under relatively low temperatures and pressures (300°C, $\leq$ 50,000 bar/5 GPa) upon hydrogenation if first dehydrided to Mg.

d) (i) Mechanical milling

One method of increasing the kinetics of hydrogenation and dehydrogenation is via mechanical milling. It has been discovered that hydride layers > 50 μm cannot be penetrated by H_2[137] and as such, ideally, Mg particles would have to have a radius less than 50 μm. Zaluska et al. discovered that milling has several converging effects that improve the overall kinetics of a sample:

- A reduction in particle size

- A reduction in grain size

- An increase in defects via strain mechanisms

These three factors allow for hydrogen diffusion into a particle along defects and grain boundaries – of which there are more in a given particle. The reported kinetic improvement was quite large and extended milling times resulted in further improvements with times below 60 minutes for full absorption and desorption at 300°C and 10 bar in comparison to hours for unmilled MgH_2[134]. Zaluska also states that there is no observed grain growth up to 400°C meaning that this microstructure is left intact and that the kinetics will not reduce with successive hydrogen cycling as there is little to no grain agglomeration. It should be noted that changing particle and grain size has no effect on the thermodynamics of the system[141]

and, while small grain and particle sizes result in fast kinetics, a large variation in particle size can result in 'dual' desorption peaks or 'shoulders' as reported by Varin et al.[142], and this feature is purely a result of some particles being relatively kinetically efficient at diffusing H_2 molecules and others constrained by the diffusion of H_2.

The exact effects and magnitudes of a reduction in particle and/or grain size have long been studied and contested. Zaluska et al. reported that reduction in grain size via mechanical milling, whilst keeping particle size relatively the same, resulted in improved hydrogen absorption kinetics[134] – their results confirming that hydrogen mainly diffuses through the grain boundaries or imperfections inside the hydride phase[137]. However, it was also reported by Varin et al. and other authors that the reduction in particle size is the more important factor regarding kinetic improvements in MgH_2 as this reduction can facilitate diffusion of H_2 through very small particles, bypassing the rate-limiting step caused by diffusion of H_2 though a surface layer of MgH_2[143-145]. It was observed that, while grain size is reduced very quickly with short milling times (~10nm for 10-20 hours of milling[143, 146, 147]) and then plateaus, longer milling times are required to attain a more homogenous particle size (< 1µm at ≥ 50 hours milling time). This reported behaviour determined that the onset temperature (T_{onset}) of desorption during a DSC measurement was reduced further as a function of particle size reduction than grain size reduction[143, 146]. However, in both studies there appeared to be a large reduction in particle size between 10 and 20 hours milling time which then experienced a plateau until after 50 hours milling time. The improvement of the 1st desorption properties during these milling times was suggested to be due to not only the reduction in particle size but also the formation of the γ-MgH_2 phase of which the smaller particles primarily consisted.

As noted above, mechanical milling of MgH_2 can result in the formation of the metastable orthorhombic γ-MgH_2 phase; possible at lower pressures and temperatures due to the high energy impact of the balls to create deformations and structural defects in the sample which overcome the activation energy to form the phase[141]. γ-MgH_2 can be formed in as little as 2 hours of milling time, though this can take longer depending on the synthetic route[146, 148].

Varin et al. reported that formation of γ-MgH$_2$ from elemental Mg under a pressure of 7 bar did not take place until ~150 hours of milling time[146] and that combination with a sufficient quantity of other metallic elements could also suppress its formation[149].

During dehydrogenation, γ-MgH$_2$ is observed to desorb H$_2$ at slightly lower temperatures than β-MgH$_2$, resulting in a double peak during DSC measurements[141, 148]. It is also speculated that the gamma phase has a synergetic effect on the desorption of the alpha phase whereby desorption of γ-MgH$_2$ results in volume contraction, causing stress within the attached β-MgH$_2$ clusters, that facilitates β-MgH$_2$ decomposition[148]. This introduction of strain through interaction with the metastable γ-MgH$_2$ helps destabilise β-MgH$_2$ and highlights the importance of introducing structural impurities into the system in order to improve the properties of hydrogenation and dehydrogenation. Though it should be noted again that γ-MgH$_2$ does not reform upon hydrogen cycling of the material at lower pressures and temperatures and the improved sorption characteristics for the onset temperature trend towards the as-received material for pure MgH$_2$[143]. It is also observed that the H$_2$ cycling procedure (MgH$_2$ → Mg → MgH$_2$) reduces the stresses and anneals defects introduced during mechanical milling because the whole sample undergoes a phase transition. Since the kinetic improvement of milled MgH$_2$ is retained in subsequent H$_2$ cycles this also suggests that the reduction in particle size is more important than the reduction in grain size[145].

MgH$_2$ is sensitive to atmospheric gases such as O$_2$ and H$_2$O and will degrade if exposed to either one. Impurities introduced from the milling process can also have a negative effect on the kinetics of the material as well. Ares et al. discovered that impurities such as Fe or Zr can increase particle agglomeration, which in turn reduces overall surface area and increases H$_2$ diffusion distances[150]. However, there has been much research into introducing beneficial impurities in the form of potential additives or catalysts.

Various catalysts that have been linked with improving H_2 sorption kinetics for MgH_2 include Pd[134], V[151] and Ni[152]. Transition metal (TM) oxides have also been widely tested with mechanically milled MgH_2 such as Nb_2O_5[152, 153], Cr_2O_3[154], Fe_2O_3 and Fe_3O_4[155], and almost all show some improvement in the base kinetics of MgH_2 milled for an identical time, with the exception of a Mo catalyst additive which resulted in slower kinetics[156]. It is difficult to differentiate between different mechanisms taking place in previous research and thus derive which factors are the most important. Factors that can affect hydrogenation and dehydrogenation in compounds include exposure to atmosphere/oxygen or addition of impurities during the milling process. There are also instances where the additive oxide has been reduced, as is the case with niobium and iron oxides, and the effect of the additive in these cases can be difficult to separate from the effect of adding in a small amount of oxide that might increase nucleation sites by reducing the E_a or conversely, over-oxidise an already partially oxidised sample, reducing H_2 diffusion kinetics. Borgschulte et al. have reported that addition of TM oxides during the milling process (including Fe_2O_3, ZrO_2 and Nb_2O_5) results in the formation of a destabilised intermediate and slightly hydrogen deficient phase of MgH_2 that has a larger unit cell and through which hydrogen diffusion and desorption at the MgH_2 grain boundary takes place[157]. Zaluska et al. reported that various transition metals milled with an electronegative compound created surprisingly effective catalysts that displayed none of the expected structure from the initial compounds[158]. The catalysts were briefly milled with Mg and then exposed to 10 bar H_2 pressure at room temperature ~25°C which resulted in 6.5 wt% H_2 absorption; 3.3 wt% of this was absorbed within 15 minutes. Hanada et al. also reported H_2 absorption at room temperatures (~20°C) and 10 bar H_2 pressure from milling 1mol% Nb_2O_5 with MgH_2 which experienced rapid absorption; 4.5 wt% in 15 seconds[159]. This reaction appeared to be catalysed by a form of Nb that had been reduced to NbO by MgH_2 during milling[160]. In comparison, H_2 desorption of this material required elevated temperatures (~160°C) under a helium flow, therefore a zero hydrogen partial pressure existed. It was observed that this ultrafast material had improved kinetics at lower temperatures due to a localised temperature effect of the exothermic formation of MgH_2 at elevated reaction conditions (>150°C) that increased the local temperature of MgH_2 to

approach 400°C, which is the equilibrium pressure of this material at 10 bar[161]. An increase in H_2 pressure from 10 to 30 bar at ~20°C resulted in both improved absorption kinetics and H_2 capacity from 4.5 wt% to 5 wt% in 15s. Reactions carried out at 0°C showed similar effects and it has been suggested that this material could be utilised in H_2 capture of boil-off from liquid and other sub-273K H_2 stores.

One further effect is of the addition to the MgH_2 itself. Some researchers note that addition of a suitably harder substance to the milling mixture will result in drastically smaller particle sizes for a set milling time and regime and also affect surface defects. Interestingly, MgO has been reported to provide an improvement of the same order as some of the above catalysts and oxides[162], which might suggest that the majority of effects could be down to a smaller, more homogenous particle size.

d) (ii) Chemical modification

Due to the close atomic size of magnesium to lithium, it is possible to not only react these compounds to form new chemical phases but to also substitute Mg atoms for Li in their respective compounds and vice versa. This has the added benefit of possibly reducing the $\Delta H_{formation}$ of a given compound and can decrease the thermodynamic barrier. It is also possible to increase kinetics for a given temperature through this doping method, forming defect sites within the crystal lattice of the host compound and allowing propagation of H_2 within a grain or particle.

In 2004, Vajo described the destabilisation of MgH_2 with Si via reaction to form Mg_2Si[163]. The relatively stable magnesium silicon alloy drives the reaction at temperatures as low as 150°C and the system has a plateau pressure of 7.5 bar at that temperature for small samples in contrast with the plateau pressure for MgH_2 being 1 bar at ~ 280°C. However, as Vajo points out, rehydriding is a problem as any temperature above 150°C would require a very high pressure H_2 environment to force the reformation of MgH_2 and at temperatures below 150°C the reaction kinetics are so slow that it is impractical to use this system as a reversible storage solution. Other systems that rely on chemical modification of the initial hydride

system include reactions that provide a stable alloy phase to drive the reaction. MgH_2 was shown to be destabilised by reaction with $MgCu_2$ to reversibly form Mg_2Cu[164].

Johnson et al. reported that MgH_2 chemically reacted with 10% $LiBH_4$ at 300°C, 10 bar H_2 resulted in absorption kinetics that were of the same order as 15hr milled MgH_2: the mixture also improved upon successive cycling[165]. Interestingly, while absorption kinetics were equivalent to the milled material, the desorption kinetics were faster at 300°C, 10 mbar H_2. X-ray diffraction, NMR and IR techniques could not detect the presence of $LiBH_4$ after reaction and hydrogen cycling when the sample was hydrided thus it is not known what happens to the $LiBH_4$ species. The microstructure also evolved with hydrogen cycling, becoming finer with each successive cycle. Walker et al. expanded on this system and reported that a sample of MgH_2 + 25% $LiBH_4$ desorbed H_2 in three steps: at 360, 405 and is completed by 580°C which correspond to decomposition of MgH_2, $LiBH_4$ and LiH, respectively[115]. He posits that alloys $Li_{0.184}Mg_{0.816}$ and $Li_{0.30}Mg_{0.7}$ are formed at those higher temperatures and that the whole system provides 8.5 wt% H_2 in comparison with the 6.5 wt% of Johnson's system.

Mao et al. verified the enhanced kinetics in the MgH_2 + 10% $LiBH_4$ system and also reported that the similar MgH_2 + 10% LiH system also had improvements over standard milled MgH_2 at 300°C[166], though these experiments were carried out at 30 bar. It was postulated that since there is no evidence from X-ray diffraction for Li or B doping in the Mg or MgH_2 lattices that either Li^+ or H^- ions from LiH or $LiBH_4$, were catalysing the de- and re-hydrogenation of MgH_2. However, reflections for an unidentified phase were observed at 24.7° and 26.1° 2θ that are thought to be indicative of oxidation of the $LiBH_4$ though it is possible that this phase could be indicative of oxidation of $LiBH_4$.

Chemical modification remains a viable way to improve and adjust chemical systems that lie outside of the desired properties of hydrogen stores for applications within the hydrogen industry. While most of these chemical systems are currently too sensitive to the effects of environmental factors (such as exposure to oxygen), expensive to implement on a large scale (due to engineering solutions required to allow heat and gas transfer throughout a H_2 store)

or too energy or time intensive (either through high thermodynamic stability or kinetic stability), there lies the hope of discovering a revolutionary compound or system of compounds that could change the status quo and start the hydrogen economy.

1.   Zuttel A., *Hydrogen storage methods.* Naturwissenschaften, 2004. **91**: p. 157.

2.   Brunauer S., Emmett P.H., and Teller E., *Adsorption of gases in multimolecular layers.* J Am Chem Soc, 1938. **60**: p. 309.

3.   Fichtner M., *Nanotechnological aspects in materials for hydrogen storage.* Adv. Eng. Mater., 2005. **7**(6): p. 443.

4.   Zhao X., Xiao B., Fletcher A.J., Thomas K.M., Bradshaw D., and Rosseinsky M.J., *Hysteretic adsorption and desorption of hydrogen by nanoporous metal-organic frameworks.* Science, 2004. **306**: p. 1012.

5.   Dyer A., *An introduction to zeolite molecular sieves*. 1988.

6.   Sun T. and Seff K., *Silver clusters and chemistry in zeolites.* Chem. Rev., 1994. **94**(4): p. 857.

7.   Bae D. and Seff K., *Extensive intrazeolitic hydrolysis of Zn(II): partial structures of partially and fully hydrated Zn(II)-exchanged zeolite X.* Micro. Meso. Mat., 2000. **40**(1-3): p. 233.

8.   Breck D.W., *Crystalline molecular sieves.* J. Chem. Educ., 1964. **41**: p. 678.

9.   Barrer R.M. and Vaughan D.E.W, *Trapping and diffusion of rare gases in Phillipsite, zeolite K-M and other silicates.* Trans. Faraday Soc., 1971. **67**: p. 2129.

10.   Barrer R.M. and Vaughan D.E.W., *Trapping of inert gases in sodalite and canrinite crystals.* J. Phys. Chem. Solids, 1971. **197**(32): p. 731.

11.   Fraenkel D. and Shabtai J., *Encapsulation of hydrogen in molecular-sieve zeolites.* J. Am. Chem. Soc., 1977. **99**(21): p. 7074.

12.   Weitkamp J., Fritz M., and Ernst S., *Zeolites as media for hydrogen storage.* 1995. **20**(12): p. 967.

13. Sheppard N. and Yates D.J.C., *Changes in the Infra-red spectra of molecules due to physical adsorption.* Proc. R. Soc. Lon Ser-A, 1956. **238**(1212): p. 69.

14. Forster H. and Schuldt M., *Infrared active fundamentals of deuterium, nitrogen, and oxygen in zeolitic matrices.* J Chem. Phys., 1977. **66**(11): p. 5237.

15. Kazansky V.B., Borovkov V.Y., and Karge H.G., *Diffuse reflectance IR study of molecular hydrogen and deuterium adsorbed at 77 K on NaA zeolite.* J. Chem. Soc. Faraday Trans., 1997. **93**(9): p. 1843.

16. Kazansky V.B., Jenoft F.C., and Karge H.G., *First observation of vibration-rotation drift spectra of para- and ortho-hydrogen adsorbed at 77 K on LiX, NaX and CsX zeolites.* J. Chem. Soc. Faraday Trans., 1998. **94**(9): p. 1347.

17. Kazansky V.B., Borovkov V.Y., Serich A., and Karge H.G., *Low temperature hydrogen adsorption on sodium forms of faujasites: barometric measurements and drift spectra.* Micro. Meso. Mat., 1998. **22**: p. 251.

18. Basmadjian D., *Adsorption equilibria of hydrogen, deuterium, and their mixtures.* Can. J. Chem., 1960. **38**: p. 141.

19. Ruthven D.M. and Farooq S., *Concentration of a trace component by pressure swing adsorption.* Chem. Eng. Sci., 1994. **49**(1): p. 51.

20. Langmi H.W., Walton A., Al-Mamouri M.M., Johnson S.R., Book D., Speight J.D., Edwards P.P., Gameson I., Anderson P.A., and Harris I.R., *Hydrogen adsorption in zeolites A, X, Y and RHO.* J. Alloy. Compd., 2003. **356-357**: p. 710.

21. Nijkamp M.G., Raaymakers J.E.M.J., van Dillen A.J., and de Jong K.P., *Hydrogen storage using physisorption - materials demands.* Appl. Phys. A, 2001. **72**: p. 619.

22.   Langmi H.W., Book D., Walton A., Johnson S.R., Al-Mamouria M.M., Speight J.D., Edwards P.P., Harris I.R., and Anderson P.A., *Hydrogen storage in ion-exchanged zeolites.* J. Alloy. Compd., 2005. **404-406**: p. 637.

23.   Bae D., Park H., Kim J.S., Lee J., Kwon O., Kim K., Song M.K., and No K.T., *Hydrogen adsorption in organic ion-exchanged zeolites.* J. Phys. Chem. Solids, 2008. **69**: p. 1152.

24.   Iijima S., *Helical microtubules of graphitic carbon.* Nature, 1991. **356**: p. 56.

25.   Iijima S. and Ichihashi T., *Single-shell carbon nanotubes of 1-nm diameter.* Nature, 1993. **363**: p. 603.

26.   Thess A., Lee R., Nikolaev P., Dai H., Petit P., Robert J., Xu C., Lee Y.H., Kim S.G., Rinzler A.G., Colbert D.T., Scuseria G.E., Tomanek D., Fisher J.E., and Smalley R.E., *Crystalline ropes of metallic carbon nanotubes.* Science, 1996. **273**: p. 483.

27.   Schimmel H.G., Kearley G.J., Nijkamp M.G., Visser C., de Jong K., and Mulder F.M., *Hydrogen adsorption in carbon nanostructures: comparison of nanotubes, fibers, and coals.* Chem. Eur. J., 2003. **9**: p. 4764.

28.   Wu X.B., Chen P., Lin J., and Tan K.L., *Hydrogen uptake by carbon nanotubes.* Int. J. Hydrogen Energ., 2000. **25**: p. 261.

29.   Chen X., Haluska M., Dettlaff-Weglikowska U., Hirscher M., Becher M., and Roth S., *Pressure isotherms of hydrogen adsorption in carbon nanostructures.* J. Mater. Res. Soc. Symp. Proc., 2001. **706**: p. Z9.11.

30.   Zuttel A. and Orimo S., *Hydrogen in nanostructured, carbon-related and metallic materials.* Mat. Sci. Eng. B - Solid, 2004. **108**(1-2): p. 9.

31.   Monthioux M., Smith B.W., Burteaux B., Claye A., Fischer J.E., and Luzzi D.E., *Sensitivity of single-wall carbon nanotubes to chemical processing: an electron microscopy investigation.* Carbon, 2001. **39**: p. 1251.

32.   Takagi H., Hatori H., Soneda Y., Yoshizawa N., and Yamadab Y., *Adsorptive hydrogen storage in carbon and porous materials.* Mater. Sci. Eng. B, 2004. **108**: p. 143.

33.   Nakamizo M., Honda H., and Inagaki M., *Raman spectra of ground natural graphite.* Carbon, 1978. **16**(4): p. 281.

34.   Orimo S., Majer G., Fukunaga T., Züttel A., Schlapbach L., and Fujii H., *Hydrogen in the mechanically prepared nanostructured graphite.* Appl. Phys. Lett., 1999. **75**: p. 3093.

35.   Orimo S., Matsushima T., Fujii H., Fukunaga T., and Majer G., *Hydrogen desorption property of mechanically prepared nanostructured graphite.* J. Appl. Phys., 2001. **90**: p. 1545.

36.   Yang R.T., *Hydrogen storage by alkali-doped carbon nanotubes - revisited.* Carbon, 2002. **38**: p. 623.

37.   Chen P., Wu X., Lin J., and Tan K.L., *High H_2 uptake by alkali-doped carbon nanotubes under ambient pressure and moderate temperatures.* Science, 1999. **285**: p. 91.

38.   Zhong Z.Y., Xiong Z.T., Sun L.F., Luo J.Z., Chen P., Wu X., Lin J., and Tan K.L., *Nanosized nickel (or cobalt)/graphite composites for hydrogen storage.* J. Phys. Chem. B, 2002. **106**: p. 9507.

39.   Boudart M., Vannice M.A., and Benson J.E., *Adlineation portholes spillover.* Z. Phys. Chem. Neue Fol., 1969. **64**(1-4): p. 171.

40.   Boudart M., Aldag A.W., and Vannice M.A., *On the slow uptake of hydrogen by platinized carbon.* J. Catal., 1970. **18**: p. 46.

41.   Robell A.J., Ballou E.V., and Boudart M., *Surface diffusion of hydrogen on carbon.* J. Phys. Chem., 1964. **68**: p. 2748.

42.   Sancier K.M. and Inami S.H., *ESR evidence of hydrogen migration on supported metal catalysts.* J. Catal., 1968. **11**: p. 135.

43.   Lueking A. and Yang R.T., *Hydrogen spillover from a metal oxide catalyst onto carbon nanotubes - implications for hydrogen storage.* J. Catal., 2002. **206**: p. 165.

44.   Leuking A. and Yang R.T., *Hydrogen storage in carbon nanotubes: residual metal content and pretreatment temperature.* AIChE J., 2003. **49**(6): p. 1556.

45.   Leuking A.D. and Yang R.T., *Hydrogen spillover to enhance hydrogen storage - study of the effect of carbon physicochemical properties.* Appl. Catal., 2004. **265**: p. 259.

46.   Rowsell J.L.C. and Yaghi O.M., *Metal-organic frameworks: a new class of porous materials.* Micro. Meso. Mat., 2004. **73**: p. 3.

47.   Yaghi O.M., O'Keeffe M., Ockwig N.W., Chae H.K., Eddaoudi M., and Kim J., *Reticular synthesis and the design of new materials.* Nature, 2003.

48.   Yaghi O.M. and Rowsell J.L.C., *Strategies for hydrogen storage in metal-organic frameworks.* Angew. Chem. Int. Ed., 2005. **44**: p. 4670.

49.   Rowsell J.L.C., Millward A.R., Sung Park K., and Yaghi O.M., *Hydrogen sorption in functionalized metal-organic frameworks.* J. Am. Chem. Soc., 2004. **126**: p. 5666.

50.   Rosi N.L., Eckert J., Eddaoudi M., Vodak T., Kim J., O'Keeffe M., and Yaghi O.M., *Hydrogen storage in microporous metal-organic frameworks.* Science, 2003. **300**: p. 1127.

51.   Batten S.R. and Robson R., *Interpenetrating nets: ordered, periodic entanglement.* Angew. Chem. Int. Ed., 1998. **37**: p. 1460.

52.   Chen B., Eddaoudi M., Hyde S.T., O'Keeffe M., and Yaghi O.M., *Interwoven metal-organic framework on a periodic minimal surface with extra-large pores.* Science, 2001. **291**: p. 1021.

53.   Grochala W. and Edwards P.P., *Thermal decomposition of the non-interstitial hydrides for the storage and production of hydrogen.* Chem. Rev., 2004. **104**: p. 1283.

54.   Li H., Eddaoudi M., Groy T.L., and Yaghi O.M., *Establishing microporosity in open metal-organic frameworks: Gas sorption isotherms for Zn(BDC) (BDC=1,4-Benzenedicarboxylate).* J. Am. Chem. Soc., 1998. **120**(73): p. 81.

55.   Budd P., Butler A., Selbie J., Mahmood K., McKeown N.B., Ghanem B., Msayib K., Book D., and Walton A., *The potential of organic polymer-based hydrogen storage materials.* CHECK! 2007. **15**: p. 1802.

56.   McKeown N.B. and Budd P., *Polymers of intrinsic microporosity (PIMs): organic materials for membrane separations, heterogeneous catalysis and hydrogen storage.* Chem. Soc. Rev., 2006. **35**: p. 675.

57.   McKeown N.B., Ghanem B., Msayib K.J., Budd P.M., Tattershall C.E., Mahmood K., Tan S., Book D., Langmi H.W., and Walton A., *Towards polymer-based hydrogen storage materials: Engineering ultramicroporous cavities within polymers of intrinsic microporosity.* Angew. Chem. Int. Ed., 2006. **45**: p. 1804.

58.   Germain J., Hradil J., Fréchet J.M.J., and Svec F., *High surface area nanoporous polymers for reversible hydrogen storage.* Chem. Mater., 2006. **18**(18): p. 4430.

59.   Lee J., Wood C.D., Bradshaw D., Rosseinsky M.J., and Cooper A.I., *Hydrogen adsorption in mircoporous hypercrosslinked polymers.* Chem. Commun., 2006(25): p. 2670.

60.   Cummings D.L. and Powers G.J., *The storage of hydrogen as metal hydrides.* Ind. Eng. Chem. Proc. DD, 1974. **13**(2): p. 182.

61.   Gilman P.S and Benjamin J.S., *Mechanical alloying.* Annu. Rev. Muter. Sci., 1983. **13**: p. 279.

62.   Ivanov E., Konstanchuk A., Stepanov A., and Boldyrev V., *Magnesium mechanical alloys for hydrogen storage.* J. Less Common Met., 1987. **131**: p. 25.

63.   Reilly J.J. and Wiswall R.H., *Reaction of hydrogen with alloys of magnesium and nickel and the formation of Mg_2NiH_4.* Inorg. Chem., 1968. **7**(11): p. 2254.

64.   Reilly J.J. and Wiswall R.H., *Formation and properties of iron titanium hydride.* Inorg. Chem., 1974. **13**(1): p. 218.

65.   Manchester F.D. and Khatamian D., *Mechanisms for activation of intermetallic hydrogen absorbers.* Mater. Sci. For., 1988. **31**: p. 261.

66.   Yürüm Y., *Hydrogen energy system: production and utilization of hydrogen and future aspects*. 1995, Dordrecht, Boston, London: Springer. 341.

67.   http://www.chemicool.com/elements/lanthanum.html.

68.   Aoyagi H., Aoki K., and Masumoto T., *Effect of ball milling on hydrogen absorption properties of FeTi, Mg_2Ni and $LaNi_5$.* J. Alloy. Compd., 1995. **231**(1-2): p. 804.

69.   Zaluski L., Zaluska A., and Strőm-Olsen J.O., *Hydrogen absorption in nanocrystalline Mg_2Ni formed by mechanical alloying.* J. Alloy. Compd., 1995. **217**: p. 245.

70.   Srivastava S., Raman S.S.S., Singh B.K., and Srivastava O.N., *On the synthesis and characterization of some new AB5 type $MmNi_{4.3}Al_{0.3}Mn_{0.4}$, $LaNi_{5-x}Si_x$ (x=0.1, 0.3, 0.5) and Mg-x wt% $CFMmNi_{5-y}$ wt% hydrogen storage materials.* Int. J. Hydrogen Energ., 2000. **25**: p. 431.

71.   Zaluski L., Zaluska A., Tessier P., Strőm-Olsen J.O., and Schulz M., *Catalytic effect of Pd on hydrogen absorption in mechanically alloyed Mg$_2$Ni, LaNi$_5$ and FeTi.* J. Alloy. Compd., 1995. **217**: p. 295.

72.   Sandrock G.D. and Goodell P.D., *Surface poisoning of LaNi$_5$, FeTi and (Fe,Mn)Ti by O$_2$, Co and H$_2$O.* J. Less Common Met., 1980. **73**(1): p. 161.

73.   Goodell P.D., *Cycling hydriding response of LaNi$_5$ in hydrogen containing oxygen as a minor impurity.* J. Less Common Met., 1983. **89**(1): p. 45.

74.   Imoto T., Satoh K., Nishimura K., Yonesaki T., Fujitani S., and Yonezu I., *Poisoning by air of AB$_5$ type rare-earth nickel hydrogenabsorbing alloys.* J. Alloy. Compd., 1995. **223**: p. 60.

75.   Block F.R. and Bahs H.J., *Investigation of selective absorption of hydrogen by LaNi$_5$ and FeTi.* J. Less Common Met., 1983. **89**(1): p. 77.

76.   Schűth F., Bogdanović B., and Felderhoff M., *Light metal hydrides and complex hydrides for hydrogen storage.* Chem. Commun., 2004: p. 2249.

77.   Chen P., Xiong Z., Luo J., Lin J., and Lee Tan K., *Interaction between lithium amide and lithium hydride.* J. Phys. Chem. B, 2003. **107**: p. 10967.

78.   Bogdanović B. and Schwickardi M., *Ti-doped alkali metal aluminium hydrides as potential novel reversible hydrogen storage materials.* J. Alloy. Compd., 1997. **253-254**: p. 1.

79.   Bogdanović B., Brand R.A., Marjanović A., Schwickardi M., and Tölle J., *Metal-doped sodium aluminium hydrides as potential new hydrogen storage materials.* J. Alloy. Compd., 2000. **302**: p. 36.

80.   Chen J., Kuriyama N., Xu Q., Takeshita H.T., and Sakai T., *Reversible hydrogen storage via titanium-catalyzed LiAlH₄ and Li₃AlH₆.* J. Phys. Chem. B, 2001. **105**: p. 11214.

81.   Løvvik O.M., *Adsorption of Ti on LiAlH₄ surfaces studied by band structure calculations.* J. Alloy. Compd., 2003. **373**(1-2): p. 28.

82.   Juza R. and Opp K., *Metallamide und metallnitride.24. die kristallstrucktur des lithiumamides.* Z. Anorg. Allg. Chem., 1951. **266**: p. 313.

83.   Chen P., Xiong Z.T., Luo J.Z., Lin J.Y., and Tan K.L., *Interaction of hydrogen with metal nitrides and imides.* Nature, 2002. **420**(6913): p. 302.

84.   Kojima Y. and Kawai Y., *IR characterizations of lithium imide and amide.* J. Alloy. Compd., 2005. **395**: p. 236.

85.   Hu Y.H. and Ruckenstein E., *Ultrafast reaction between LiH and NH₃ during H₂ storage in Li₃N.* J. Phys. Chem. A, 2003. **107**: p. 9737.

86.   Ichikawa T., Hanada N., Isobe S., Leng H., and Fujii H., *Mechanism of novel reaction from LiNH₂ and LiH to Li₂NH and H₂ as a promising hydrogen storage system.* J. Phys. Chem. B, 2004. **108**: p. 7887.

87.   Shaw L.L., Osborn W., Markmaitree T., and Wan X., *The reaction pathway and rate-limiting step of dehydrogenation of the LiHN₂ + LiH mixture.* J. Power Sources, 2008. **177**: p. 500.

88.   Orimo S., Nakamori Y., Kitahara G., Miwa K., Ohba N., Towata S., and Züttel A., *Dehydriding and rehydriding reactions of LiBH₄.* J. Alloy. Compd., 2005. **404-406**: p. 427.

89.   Soulié J., Renaudin G., Černý R., and Yvon K., *Lithium boro-hydride LiBH₄ I. Crystal structure.* J. Alloy. Compd., 2002. **346**: p. 200.

90.   Corey R.L., Shane D.T., Bowman R.C. Jr., and Conradi M.S., *Atomic motions in LiBH$_4$ by NMR.* J. Phys. Chem., 2008. **112**: p. 18706.

91.   Shane D.T., Bowman R.C. Jr., and Conradi M.S., *Exchange of hydrogen atoms between BH$_4$ in LiBH$_4$.* J. Phys. Chem. C Lett., 2009. **113**: p. 5039.

92.   Hao S. and Sholl D.S., *The role of interstitial H$_2$ in hydrogen diffusion in light metal borohydrides.* Phys. Chem. Chem. Phys., 2009. **11**: p. 11106.

93.   Kang J.K. and Kim S.Y., *A candidate LiBH$_4$ for hydrogen storage: Crystal structures and reaction mechanisms of intermediate phases.* Appl. Phys. Lett., 2005. **87**: p. 11904.

94.   Mosegaard L., Møller B., Jørgensen J., Bösenberg U., Dornheim M., Hanson J.C., Cerenius Y., Walker G.S., Jakobsen H.J., Besenbacher F., and Jensen T.R., *Intermediate phases observed during decomposition of LiBH$_4$.* J. Alloy. Compd., 2007. **446-447**: p. 301.

95.   Orimo S., Nakamori Y., Ohba N., Miwa K., Aoki M., and Towata S., *Experimental studies on intermediate compound of LiBH$_4$.* Appl. Phys. Lett., 2006. **89**: p. 021920.

96.   Friedrichs O., Remhof A., Hwang S.-J., and Züttel A., *Role of Li$_2$B$_{12}$H$_{12}$ for the formation and decomposition of LiBH$_4$.* Chem. Mater., 2010. **22**: p. 3265.

97.   Friedrichs O., Kim J.W., Remhof A., Wallacher D., Hoser A., Cho Y.W., Oh K.H., and Züttel A., *Core shell structure for solid gas synthesis of LiBD$_4$.* Phys. Chem. Chem. Phys., 2010. **12**: p. 4600.

98.   Remhof A., Friedrichs O., Buchter F., Mauron Ph., Züttel A., and Wallacher D., *Solid-state synthesis of LiBD$_4$ observed by in situ neutron diffraction.* Phys. Chem. Chem. Phys., 2008. **10**: p. 5859.

99. Muller A. and Mathey F., *Production of hydrogen*, USPTO, Editor. 1980: United States of America.

100. Zuttel A., Rentsch S., and Emmenegger Ch., *Hydrogen storage properties of LiBH$_4$.* J. Alloy. Compd., 2003. **356-357**: p. 515.

101. Au M., Spencer W., Jurgensen A., and Zeigler C., *Hydrogen storage properties of modified lithium borohydrides.* J. Alloy. Compd., 2008. **462**(1-2): p. 303.

102. Yu X.B., Grant D.M., and Walker G.S., *Dehydrogrenation of LiBH$_4$ destabilized with various oxides.* J. Phys. Chem. C, 2009. **113**(41): p. 17945.

103. Kang X.-D., Wang P., Ma L.-P., and Hui-Ming C., *Reversible hydrogen storage in LiBH$_4$ destabilized by milling with Al.* Appl. Phys. A, 2007. **89**: p. 963.

104. Zhang Y., Tian Q., Zhang J., Liu S.-S., and Sun L.-X., *The dehydrogenation reactions and kinetics of 2LiBH$_4$-Al composite.* J. Phys. Chem. C, 2009. **113**(42): p. 18424.

105. Friedrichs O., Kim J.W., Remhof A., Buchter F., Borgschulte A., Wallacher D., Cho Y.W., Fichtner M., Oh K.H., and Züttel A., *The effect of Al on the hydrogen sorption mechanism of LiBH$_4$.* Phys. Chem. Chem. Phys., 2009. **11**: p. 1515.

106. Kostka J., Lohstroh W., Fichtner M., and Hahn H., *Diborane release from LiBH$_4$/silica-gel mixtures and the effect of additives.* J. Phys. Chem., 2007. **111**: p. 14026.

107. Yu X.B., Wu Z., Chen Q.R., Li Z.L., Weng B.C., and Huang T.S., *Improved hydrogen storage properties of LiBH$_4$ destabilized by carbon.* Appl. Phys. Lett., 2007. **90**: p. 034106.

108. Fang Z.-Z., Kang X.-D., Wang P., and Cheng H.-M, *Improved reversible dehydrogenation of lithium borohydride by milling with as-prepared single-walled carbon nanotubes.* J. Phys. Chem., 2008. **112**: p. 17023.

109.   Xu J., Yu X., Ni J., Zou Z., Li Z., and Yang H., *Enhanced catalytic dehydrogenation of LiBH4 by carbon-supported Pd nanoparticles.* Dalton Trans., 2009: p. 8386.

110.   Vajo J. and Skeith S., *Reversible storage of hydrogen in destabilized LiBH$_4$.* J. Phys. Chem. B., 2005. **109**: p. 3719.

111.   Wan X., Markmaitree T., Osborn W., and Shaw L.L., *Nanoengineering-enabled solid-state hydrogen uptake and release in the LiBH$_4$ plus MgH$_2$ sytem.* J. phys. Chem. C, 2008. **112**(46): p. 18232.

112.   Crosby K. and Shaw L.L., *Dehydriding and re-hydriding properties of high-energy ball milled LiBH$_4$ + MgH$_2$ mixtures.* Int. J. Hydrogen Energ., 2010. **35**: p. 7519.

113.   Shaw L.L., Yang Z.G., and Ren R.M., *Synthesis of nanostructured Si$_3$N$_4$/SiC composite powders through high energy reaction milling.* Mater. Sci. Eng. A, 1998. **244**: p. 113.

114.   Price T.E.C, Grant D.M., Legrand V., and Walker G.S., *Enhanced kinetics for the LiBH$_4$:MgH$_2$ multi-component hydrogen storage system - The effects of stoichiometry and decomposition environment on cycling behaviour.* Int. J. Hydrogen Energ., 2010. **35**: p. 4154.

115.   Yu X.B., Grant D.M., and Walker G.S., *A new dehydrogenation mechanism for reversible multicomponent borohydride systems-The role of Li-Mg alloys.* Chem. Commun., 2006: p. 3906.

116.   Walker G.S., Grant D.M., Price T.E.C, Yu X., and Legrand V., *High capacity multicomponent hydrogen storage materials: Investigation of the effect of stoichiometry and decomposition conditions of the cycling behaviour of LiBH$_4$-MgH$_2$.* J. Power Sources, 2009. **194**: p. 1128.

117.   Crosby K., Wan X., and Shaw L.L., *Improving solid-state hydriding and dehydriding properties of the LiBH$_4$ plus MgH$_2$ system with the addition of Mn and V dopants.* J. Power Sources, 2010. **195**: p. 7380.

118. Wang P., Ma L., Fang Z., Kang X.-D., and Wang P., *Improved hydrogen storage property of Li-Mg-B-H system by milling with titanium trifluoride.* Energy Environ. Sci., 2009. **2**: p. 120.

119. Weng B.C., Yu X.B., Wu Z., Li Z.L., Huang T.S., Xu N.X., and Ni J., *Improved dehydrogenation performance of LiBH$_4$/MgH$_2$ composite with Pd nanoparticles addition.* J. Alloy. Compd., 2010. **503**: p. 345.

120. Aoki M., Miwa K., Noritake T., Kitahara G., Nakamori Y., Orimo S., and Towata S., *Destabilization of LiBH$_4$ by mixing with LiNH$_2$.* Appl. Phys. A, 2005. **80**: p. 1409.

121. Wentorf Jr. R.H., *Synthesis of cubic form boron nitride.* J. Chem. Phys., 1961. **34**: p. 809.

122. Pinkerton F.E., Meisner G.P., Meyer M.S., Balogh M.P., and Kundrat M.D., *Hydrogen desorption exceeding ten weight percent from the new quaternary hydride Li$_3$BN$_2$H$_8$.* J. Phys. Chem., 2005. **109**: p. 6.

123. Chater P.A., David W.I.F., Johnson S.R., Edwards P.P.E., and Anderson P.A., *Synthesis and crystal structure of Li$_4$BH$_4$(NH$_2$)$_3$.* Chem. Commun., 2006: p. 2439.

124. Wiberg E. and Bauer R., *Zur kenntnis eines magnesium-aluminium-wasserstoffs Mg(AlH$_4$)$_2$.* Z. Naturforsch B, 1950. **5**: p. 397.

125. Matsunaga T., Buchter F., Mauron P., Bielman M., Nakamori Y., Orimo S., Ohba N., Miwa K., Towata S., and Züttel A., *Hydrogen storage properties of Mg[BH$_4$]$_2$.* J. Alloy. Compd., 2008. **459**(1-2): p. 583.

126. Kima Y., Lee E., Shima J., Choa Y.W., and Yoon K.B., *Mechanochemical synthesis and thermal decomposition of Mg(AlH$_4$)$_2$.* J. Alloy. Compd., 2006. **28**(1-2): p. 283.

127. Gremaud R., Borgschulte A., Lohstroh W., Schreuders H., Züttel A., Dam A., and Griessen R., *Ti-catalyzed Mg(AlH₄)₂: A reversible hydrogen storage material.* J. Alloy. Compd., 2005. **404-406**: p. 775.

128. Leng H.Y., Ichikawa T., Hino S., Hanada N., Isobe S., and Fujii H., *New metal-N-H system composed of Mg(NH₂)₂ and LiH for hydrogen storage.* J. Phys. Chem. B, 2004. **108**: p. 8763.

129. Leng H.Y., Ichikawa T., Isobe S., Hino S., Hanada N., and Fujii H., *Desorption behaviours from metal-N-H systems synthesized by ball milling.* J. Alloy. Compd., 2005. **404-406**: p. 443.

130. Luo W., *(LiNH₂-MgH₂): a viable hydrogen storage system.* J. Alloy. Compd., 2004. **381**(1-2): p. 284.

131. Nakamori Y., Kitahara G., Miwa K., Ohba N., Noritake T., and Towata S., *Hydrogen storage properties of Li-Mg-N-H systems.* J. Alloy. Compd., 2005. **404-406**: p. 396.

132. Luo W. and Sickafoose S., *Thermodynamic and structural characterization of the Mg-Li-N-H hydrogen storage system.* J. Alloy. Compd., 2006. **407**(1-2): p. 274.

133. Chen Y., Wu C., Wang P., and Cheng H., *Structure and hydrogen storage property of ball-milled LiNH₂/MgH₂ mixture.* 2006. **31**(9): p. 1236.

134. Zaluska A., Zaluski L., and Strőm-Olsen J.O., *Nanocrystalline magnesium for hydrogen storage.* J. Alloy. Compd., 1999. **288**: p. 217.

135. Chen C.P., Liu B.H., L. Z.P., and Wang Q.D., *The activation mechanism of Mg-based hydrogen storage alloys.* Z. Phys. Chem., 1993. **181**(1-2): p. 259.

136. Hjort P., Krozer A., and Kasemo B., *Hydrogen sorption kinetics in partly oxidized Mg films.* J. Alloy. Compd., 1996. **237**(1-2): p. 74.

137. Vigeholm B., Jensen K., Larsen B., and Schroder-Pedersen A., *Elements of hydride formation mechanisms in nearly spherical magnesium powder particles.* J. Less Common Met., 1987. **131**: p. 133.

138. Noritake T., Aoki M., Towata S., Seno Y., and Hirose Y., *Charge Density Analysis in Magnesium Hydride.* R&D Rev. Toyota CRDL, 2003. **38**(2): p. 15.

139. George L. and Saxena S.K., *Structural stability of metal hydrides, alanates and borohydrides of alkali and alkali- earth elements: A review.* Int. J. Hydrogen Energ., 2010. **35**: p. 5454.

140. Bortz M., Bertheville B., Böttger G., and Yvon K., *Structure of the high pressure phase γ-MgH$_2$ by neutron powder diffraction.* J. Alloy. Compd., 1999. **287**(L4-L6).

141. Huot J., Liang G., Boily S., Van Nesteb A., and Schulz R., *Structural study and hydrogen sorption kinetics of ball-milled magnesium hydride.* J. Alloy. Compd., 1999. **293-295**: p. 495.

142. Varin R.A., Czujko T., Chiu Ch., and Wronski Z., *Particle size effects on the desorption properties of nanostructured magnesium dihydride (MgH$_2$) synthesized by controlled reactive mechanical milling (CRMM).* 2006. **424**(1-2): p. 356.

143. Varin R.A., Czujko T., and Wronski Z., *Particle size, grain size and γ-MgH$_2$ effects on the desorption properties of nanocrystalline commercial magnesium hydride processed by controlled mechanical milling.* Nanotechnology, 2006. **17**: p. 3856.

144. Barkhordarian G., Klassen T., and Bormann R., *Kinetic investigation of the effect of milling time on the hydrogen sorption reaction of magnesium catalysed with different Nb$_2$O$_5$ contents.* J. Alloy. Compd., 2006. **407**: p. 249.

145. Schimmel H.G., Johnson M.R., Kearley G.J., Ramirez-Cuesta A.J., Huot J., and Mulder F.M., *Structural information on ball milled magnesium hydride from vibrational spectroscopy and ab-initio calculations.* J. Alloy. Compd., 2005. **393**: p. 1.

146.   Varin R.A., Czujko T., Chiu Ch., and Wronski Z., *Particle size effects on the desorption properties of nanostructured magnesium dihydride (MgH_2) synthesized by controlled reactive mechanical milling (CRMM).* J. Alloy. Compd., 2006. **424**(1-2): p. 356.

147.   Hanada N., Ichikawa T., Orimo S., and Fujii H., *Correlation between hydrogen storage properties and structural characteristics in mechanically milled magnesium hydride MgH_2.* J. Alloy. Compd., 2004. **366**(1-2): p. 269.

148.   Gennari F.C., Castro F.J., and Urretavizcaya G., *Hydrogen desorption behaviour from magnesium hydrides synthesized by reactive mechanical alloying.* J. Alloy. Compd., 2001. **321**: p. 46.

149.   Varin R.A., Li S., Wronski Z., Morozova O., and Khomenko T., *The effect of sequential and continuous high-energy impact mode on the mechano-chemical synthesis of nanostructured complex hydride Mg_2FeH_6.* J. Alloy. Compd., 2005. **390**: p. 282.

150.   Ares J., Aguey-Zinsou K.-F., Klassen T., and Bormann R., *Influence of impurities on the milling process of MgH_2.* J. Alloy. Compd., 2007. **434-435**: p. 729.

151.   Liang G., Huot J., Boily S., Van Nesteb A., and Schulz R., *Hydrogen storage properties of the mechanically milled MgH_2 - V nanocomposite.* J. Alloy. Compd., 1999. **291**: p. 295.

152.   Hanada N., Ichikawa T., and Fujii H., *Catalytic effect of Ni nano-particle and Nb oxide on H-desorption properties in MgH_2 prepared by ball milling.* J. Alloy. Compd., 2005. **404-406**: p. 716.

153.   Barkhordarian G., Klassen T., and Bormann R., *Effect of Nb_2O_5 content on hydrogen reaction kinetics of Mg.* J. Alloy. Compd., 2004. **364**: p. 242.

154.   Bobet J.-L., Castro F.J., and Chevalier B., *Effects of reactive mechanical milling conditions on the physico-chemical properties of Mg + Cr_2O_3 mixtures.* J. Alloy. Compd., 2004. **376**: p. 205.

155. Huang Z.G., Guo Z.P., Calka A., Wexler D., Lukey C., and Liu H.K., *Effects of iron oxide (Fe$_2$O$_3$, Fe$_3$O$_4$) on hydrogen storage properties of Mg-based composites.* J. Alloy. Compd., 2006. **422**(1-2): p. 299.

156. Bystrzyckia J., Czujko T., and Varin R.A., *Processing by controlled mechanical milling of nanocomposite powders Mg + X (X = Co, Cr, Mo, V, Y, Zr) and their hydrogenation properties.* J. Alloy. Compd., 2005. **404-406**: p. 507.

157. Borgschulte A., Bösenberg U., Barkhordarian G., Dornheim M., and Bormann R., *Enhanced hydrogen sorption kinetics of magnesium by destabilized MgH$_{2-\delta}$.* Catal. Today, 2007. **120**: p. 262.

158. Zaluska A. and Zaluski L., *New catalytic complexes for metal hydride systems.* J. Alloy. Compd., 2005. **404-406**: p. 706.

159. Hanada N., Ichikawa T., Hino S., and Fujii H., *Remarkable improvement of hydrogen sorption kinetics in magnesium catalysed with Nb$_2$O$_5$.* J. Alloy. Compd., 2006. **420**: p. 46.

160. Hanada N., Ichikawa T., Isobe S., Nakagawa T., Tokoyoda K., Honma T., Fujii H., and Kojima Y., *X-ray absorption spectroscopic study on valence state and local atomic structure of transition metal oxides doped in MgH$_2$.* J. Phys. Chem., 2009. **113**: p. 13450.

161. Hanada N., Ichikawa T., and Fujii H., *Hydrogen absorption kinetics of the catalysed MgH$_2$ by niobium oxide.* J. Alloy. Compd., 2007. **446-447**: p. 67.

162. Aguey-Zinsou K.-F., Ares Fernandez J.R., Klassen T., and Bormann R., *Using MgO to improve the (de)hydriding properties of magnesium.* Mater. Res. Bull., 2006. **41**: p. 1118.

163. Vajo J., Mertens F., Ahn C.C., Bowman R.C., and Fultz B., *Altering hydrogen storage properties by hydride destabilization through alloy formation: LiH and MgH$_2$ destabilized with Si.* J. Phys. Chem. B, 2004. **108**: p. 13977.

164. Reilly J.J and Wiswall R.H., *The reaction of hydrogen with alloys of magnesium and copper.* Inorg. Chem., 1967. **6**: p. 2220.

165. Johnson S.R., Anderson P.A., Edwards P.P., Gameson I., Prendergast J.W., Al-Mamouri M., Book D., Harris I.R., Speight J.D., and Walton A., *Chemical activation of MgH$_2$; a new route to superior hydrogen storage materials.* Chem. Commun., 2005: p. 2823.

166. Mao J.F., Wu Z., Chen J., Weng B.C., Xu N.X, Huang T.S., Guo Z.P., Liu H.K., Grant D.M., Walker G.S., and Yu X.B., *Improved Hydrogen Storage of LiBH$_4$ Catalyzed Magnesium.* J. Phys. Chem. C, 2007. **111**: p. 12495.

3. Experimental

3.1 Sample preparation

3.1.1 Solid state reaction

All samples were prepared and handled in an argon-filled glove box with a typical oxygen content of less than 5-10 ppm; water content was also very low. Reagents were weighed out and mixed together in a mortar and pestle with thorough mixing for at least 5 minutes with the notable exception of Mg powder which was mixed lightly with any other pre-crushed reagent(s) due to its propensity to smear in the pestle reducing the accuracy of intended Mg content. The required reagent quantities were determined from molar ratios and then worked out from the compound's relative molecular mass.

Samples that were heated under static vacuum were carefully inserted into a quartz tube of approximately 10 mm internal diameter and typically 200 mm in length which had a piece of clean (and evacuated to remove physisorbed water and oxygen molecules) printer paper rolled around the length to avoid the sample sticking to the inside of tube and reacting when sealed, potentially breaking the tube. Once the paper was removed the tube was fitted to a Young's tap via a Swagelok Ultra-Torr fitting with rubber seals to stop mixing with atmosphere when removed from the glovebox (Figure 3.1.1). The assembly was then attached to vacuum equipment – usually an oil-based diffusion or turbo pump backed with a rotary pump – which allowed careful evacuation to pressures of approximately 1×10^{-6} bar near the sample. Once the required vacuum level was achieved the assembly was removed from the vacuum equipment and sealed off with a gas torch and this sealed tube placed in a furnace for heat treatment of the sample. If dynamic vacuum was required for the experiment then the assembly was left attached to the vacuum equipment and heated in situ.

For experiments where a flow of gas was required a specialist piece of glassware was used in conjunction with the Ultra-Torr fittings (Figure 3.1.1) which allowed connection to a gas line
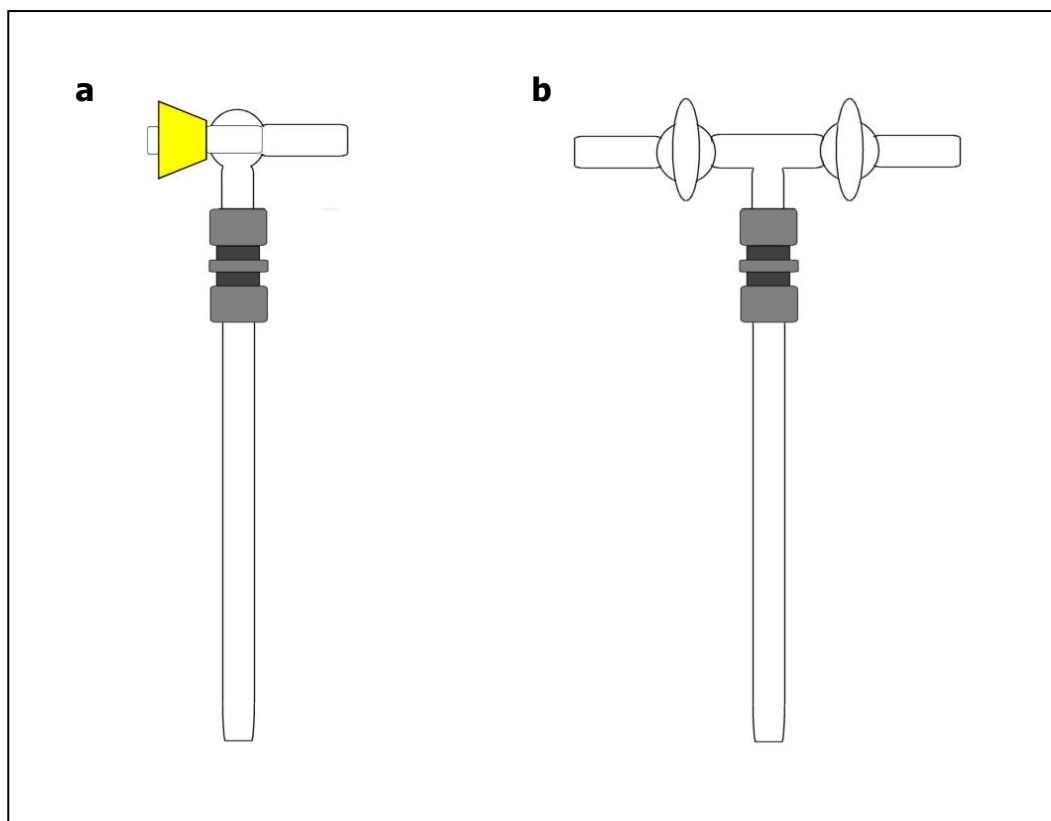
Figure 3.1.1 : Schematic of a) static vacuum and b) flowing gas sample assemblies

fitted with acid- or oil-based bubblers and which was flushed into a well-ventillated fume cupboard.

3.1.1 (a) Heat treatment of MgH_2 + 10% $LiBH_4$ under static vacuum

Aldrich magnesium hydride (90% MgH_2, 10% Mg) was mixed together by hand, via the process outlined in section 3.1.1, with an added 10mol% $LiBH_4$ (Acros Organics, 95%) for a total of 110mol% (overall percentage $LiBH_4$ in the mixture was 9.09%). Once the sample had been prepared through evacuation in a quartz tube and sealed, the tube containing the sample was placed in a programmable muffle furnace and heated up to 300°C at a ramp rate of 50°C/hour. The sample was then held at 300°C for 12 hours and then allowed to cool back down to room temperature. The quartz tube was then returned to the glove box where it was split open with glass cutting tools and the sample recovered into a storage vial.

The length of time, reagents and the ratio of reactants was altered as seen fit. A typical sample would weigh approximately 0.33 g.

3.1.1 (b) Heat treatment of MgH$_2$ + 10% LiBH$_4$ under flowing gas

Magnesium hydride (MgH$_2$) and lithium borohydride (LiBH$_4$) were measured out in the required amounts and mixed together and placed in a quartz tube as per section 3.1.1 (a). The quartz tube was then fitted with a Swagelok Ultra-Torr fitting to which was connected a specialised piece of glassware consisting of two rotating taps sealed with vacuum grease. This apparatus was closed off and then removed from the glove box and placed in a fume cupboard - held in a horizontal position via a clamp stand.

The valve on the cylinder containing the gas supply to be used was opened slightly and the system was purged for a minute to reduce the possibility of unwanted reactions of atmosphere with the sample. A plastic tube, connected to an acid bubbler (to scrub the gas of any unwanted impurities) which was in turn connected to the desired gas supply, was attached to one of the glass taps on the apparatus. A slight positive pressure of gas was allowed to build up in the tube as a second, exhaust tube that fed into a second acid bubbler which then vented into the fume cupboard system, was attached to the other tap. The exhaust tap was opened simultaneously with the admittance tap in order for the gas flow to begin immediately in order to limit the amount of oxygen and moisture entering the quartz tube. The gas flow was increased to a steady rate for 5 minutes to purge the apparatus of any except the desired gas(es). The flow rate was then reduced and the sample slotted into the hot zone of a tube furnace.

The tube furnace was programmed in the same manner as the muffle furnace and a heating rate of 50°C/hour was used to raise the temperature to the desired setting. Once the reaction was complete and the sample had cooled sufficiently, the quartz tube was removed from the tube furnace and the exhaust gas tap on the apparatus closed before stopping the flow of the gas from the cylinder. A slight positive pressure was allowed to build before the inlet tap was

also closed. The apparatus was removed from the clamp and plastic tubing and returned to the glove box for sample recovery.

3.1.2 Mechanical milling

The process of mechanical milling or high velocity ball milling (HVBM) is used to reduce the overall particle size of a powder, to reduce grain size and introduce defects into the surface structure of grains and particles. A Retsch PM400 planetary mill was used to synthesise the required powders for testing. The sample powder (20g, MgH_2 90%) and stainless steel milling balls (200g) were sealed inside a 250 ml stainless steel (89.5% Fe, 13% Cr) milling pot under argon atmosphere inside a glovebox. The pot was then removed and clamped inside the planetary mill and offset by a counterweight. The milling proceeded at 300 rpm for the required time with 15 minutes cooling for every 30 minutes of milling due to the build-up of
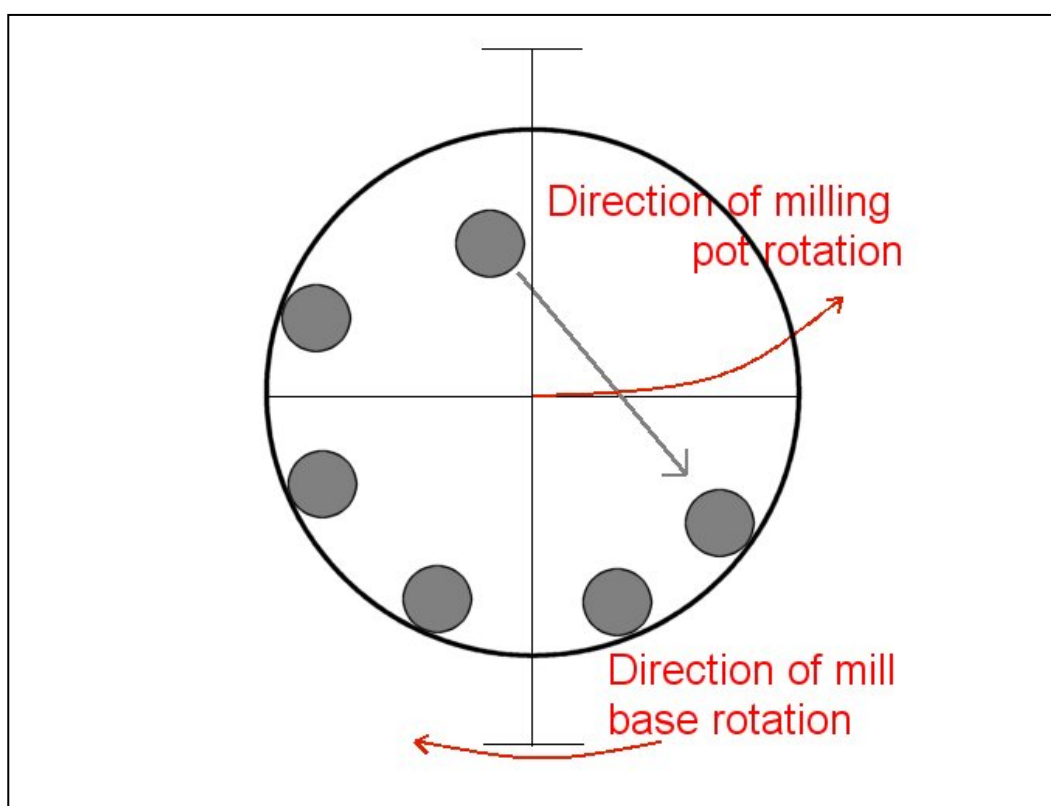
Figure 3.1.2 : Schematic showing a top-down view of the action of the ball mill

heat from the milling action of the stainless steel balls which can exceed temperatures of 300°C. The pots were removed to the glovebox for every three hours of milling time to avoid possible build-up of a large pressure of H_2 and to also allow for the re-mixing of the sample powder which can become attached to the pot and balls through the process of cold-welding. This reduces the impact of the balls on reducing the powder and also allows particle agglomeration to occur.

3.2 Intelligent gravimetric analyser (IGA)

The IGA is provided by Hiden Isochema and is a gravimetric system designed to accurately measure the mass change of a given sample over a range of temperatures and pressures: from -196 to 500°C and dynamic vacuum and 10 mbar to 20 bar. The IGA is a modular system allowing for inert loading of samples, varying gas mixtures via mass flow controllers as well as analysis of exhaust gases through a mass spectrometer and also a static pressure mode depending on the installed features of the system.

The IGA was used in two separate modes – isothermal and kinetic. Kinetic mode allows the user to monitor the change in mass for a temperature and/or pressure: the software will regulate both to a set value or will also run a programme that will allow changes in pressure and/or temperature. This mode was used to observe the reaction kinetics at a given temperature for samples of Mg/MgH_2 while pressure was changed to allow hydrogen absorption/desorption. Isothermal mode allows the user to determine thermodynamic information of the loaded sample through a succession of isotherms which can result in the heat of formation, ΔH_f.

The use of the IGA changed over the period of research as new features were installed. Importantly, the loading procedure was changed between early and more recent samples: earlier samples were loaded in atmosphere with effort made to minimise exposure of the

sample while later samples were loaded in an argon or nitrogen environment using a specially designed 'glovebox' that fit over the IGA reactor chamber.

Unless otherwise stated, hydrogen absorption was performed at 10 bar H_2, 300°C and desorption was performed at 10 mbar H_2, 300°C. A liquid nitrogen gas trap was also used on the H_2 inlet pipe during each experiment. This caught and liquefied O_2 and H_2O before they were admitted into the sample chamber. The quality of the H_2 gas was 99.999% so the level of contamination should have been very small, however, it has been shown that, below a certain cylinder pressure ~10-20 bar, liquefied water trapped in the cylinder over successive uses will begin to vaporise and enter the pipeline so there is a risk of sample contamination and reaction with undesired molecules.

3.3 HTP1-S Thermal desorption analyser

The HTP is a volumetric system provided by Hiden Isochema based around the Sieverts method[2] that is designed to accurately measure the change in pressure or the change in gas flow in a known volume for a given sample. The system is able to analyse very small sample amounts accurately and can operate from -196 to 500°C and from dynamic vacuum to 200 bar pressure. The system is very versatile, being able to perform kinetic, isothermal and temperature programmed desorption measurements (TPD) which can also be linked to a mass spectrometer for analysis of the products via a flow of helium.

Due to the HTP's sensitivity it is important to properly calibrate the equipment before each sample run to eliminate any experimental errors. This is a problem because the volume within the reactor is very small so even a slight miscalculation or blockage can result in wildly incorrect results.

3.4.1 Fourier transform infrared spectroscopy (FTIR)

Infrared absorption spectroscopy is a widely used technique that can help determine the types of chemical groups within a compound. It relies on the fact that molecules vibrate and rotate at specific frequencies corresponding to specific energy levels or vibrational modes. These energy levels are specific to each chemical group and depend heavily on the masses of the atoms involved. The technique passes infrared light (over a range of wavelengths) through the sample to excite the chemical groups within a molecule. The transmitted light is then analysed to determine how much was absorbed by the sample at a given wavelength which in turn indicates which type chemical group is likely to be present. A Fourier transform performs a mathematical function within the equipment's software that allows simultaneous analysis over all desired wavelengths instead of measuring the absorption of each wavelength individually.

During this investigation transmission FTIR was performed on a Thermo Nicolet Magna-IR on samples contained in a sealed diamond anvil cell which allows samples to be prepared under inert conditions and then transferred to the spectrometer. The cell lightly compresses the sample between two diamond surfaces which reflect the light transmitted through the sample onto a detector.

3.4.2 Raman spectroscopy

This is a technique that relies upon the inelastic scattering of monochromatic light from the interaction with phonons of a crystal lattice – giving information on vibrational and rotational modes in a sample. Raman scattering is weaker than Rayleigh scattering and this is removed or ignored from the obtained data when scanning the samples via a CCD.

Raman spectroscopy works by exciting an electron into a virtual energy state – at which point the electron relaxes back to an excited vibrational state which produces Stokes scattering.

Anti-stokes scattering is generated when an electron in an excited vibrational state is promoted to a virtual energy state and then relaxes back to a vibrational state (Figure 3.4.1).

Not all molecules exhibit Raman scattering as it is dependent on the variation in polarisability of a molecule during vibration. i.e. The electron cloud must exhibit deformation during the stretch or bend (Figure 3.4.2). The intensity of the Raman scattering depends on the amount of polarisability change while the Raman shift is equal to the vibrational level that is involved.

In this work, a Renishaw confocal dispersive Raman spectrometer with three lasers (488, 633 and 785 nm) available for use was utilised to track the change in $LiBH_4$ over the process of
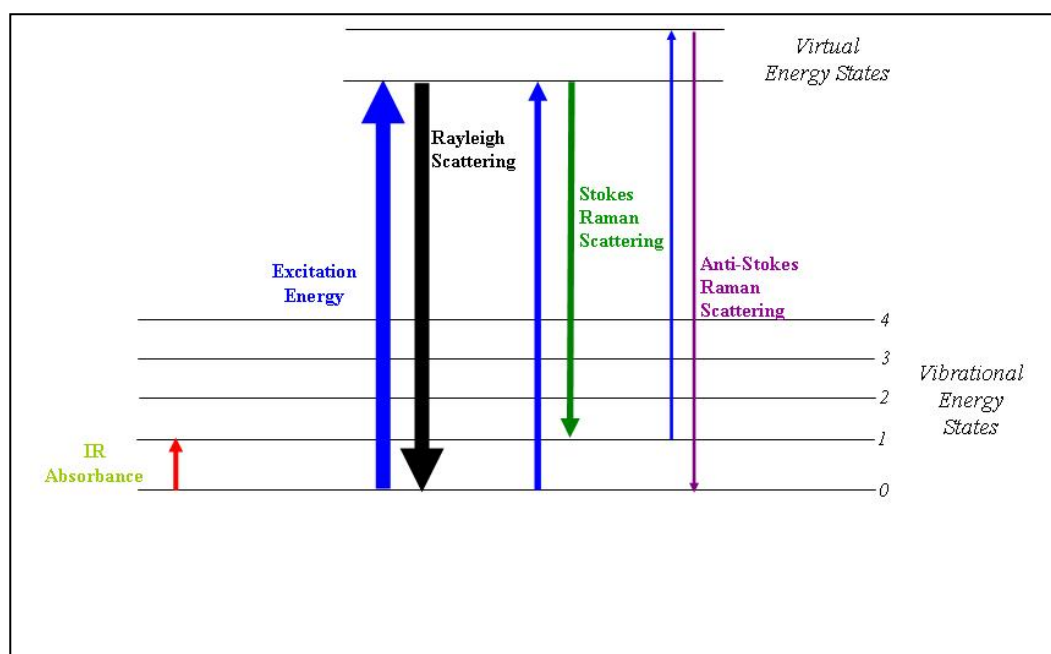
Figure 3.4.1 : Diagram showing the transitions between energy levels to produce Raman scattering compared with infra red spectroscopy and Rayleigh scattering

hydrogen cycling. The 488 nm laser was picked for the MgH_2 + $LiBH_4$ samples and a sealed, pressure cell was used to ensure that oxidation of the sample did not occur; samples were
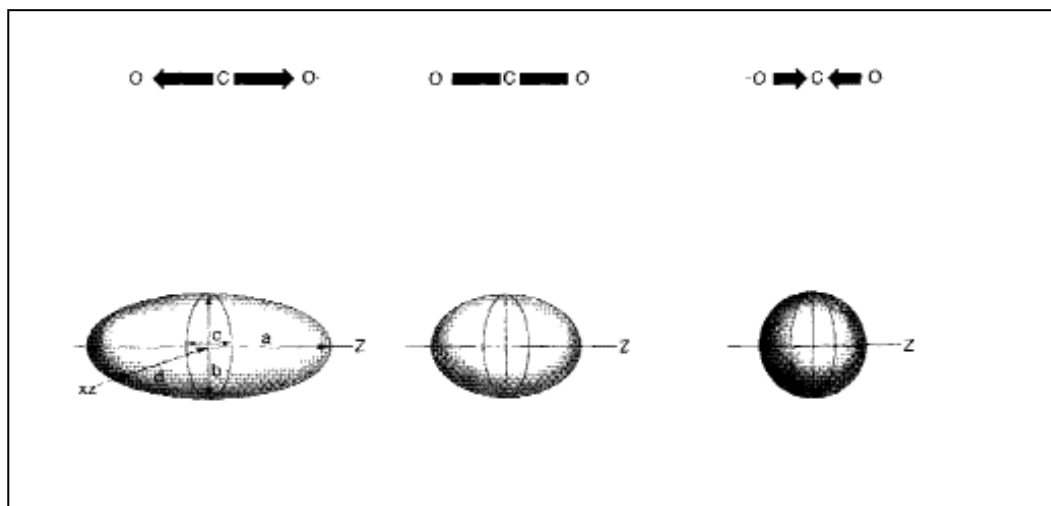
Figure 3.4.2 : Depiction of the change in electron cloud during the CO_2 symmetrical stretch

loaded in the pressure cell in an argon-filled glovebox.

3.5.1 X-ray Diffraction (XRD)

X-rays are generated by firing electrons at a metal target (usually Cu or Co) from a tungsten filament: these electrons provide enough energy to promote electrons from the 1s orbital. Electrons from the outer shells of the metal atom then fall back to the 1s orbital, producing radiation. For a copper anode the electrons that make the transition from the 2p to 1s orbitals produce a doublet of radiation named Kα 1 and Kα 2, electrons that make the transition from the 3p to 1s orbitals produce Kβ 1 radiation[3].

X-ray diffraction techniques utilise Bragg's law, stating that crystals consist of layers with an interplanar distance, d (Figure 3.5.1). X-rays will penetrate a crystal lattice until they encounter an atom on a lattice plane at which point they will be reflected at a certain angle, θ.
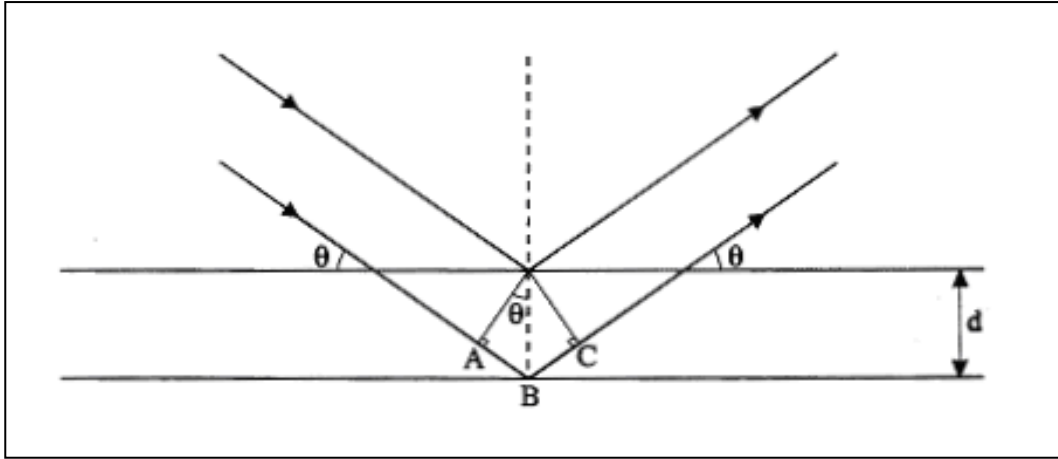
Figure 3.5.1 : Representation of the reflection of an incident X-ray with a crystal lattice plane

Therefore the d-spacing can be derived (using trigonometric principles) to be:

$$(AB + BC) = (d_{hkl}\sin\theta + d_{hkl}\sin\theta) = 2d_{hkl}\sin\theta$$

For constructive interference to occur A→B→C has to be an integer multiple of the wavelength of the incident light; therefore the equation can be written as:

$$n\lambda = 2d_{hkl}\sin\theta$$

This can be applied to any crystal lattice and once d is known can be used to determine the dimensions and geometry of the orthogonal unit cells by the following formula:

$$\frac{1}{d^2} = \frac{h^2}{a^2} + \frac{k^2}{b^2} + \frac{l^2}{c^2}$$

and which, for a cubic unit cell can be simplified to:

$$d_{hkl} = \frac{a}{\sqrt{h^2 + k^2 + l^2}}$$

Once the X-ray has been reflected, its angle is detected through the use of a position sensitive detector (PSD) which depends on the X-ray to ionise the gas within the detector and

give a signal. This method gives us information on θ and λ from which we can derive the unit cell parameters and assign observed peaks to their Miller indices using the above equations. This was accomplished by using the programme CELL which uses a non-linear least squares refinement:

$$F = \sum_{hkl} w(\sin^2 \theta_{obs} - \sin^2 \theta_{calc})^2$$

where w is a weighting factor were a unit weight is used for each reflection, θ_{obs} is the angle at which the experimental reflection occurs and θ_{calc} is initially the ideal or known position of that reflection according to the space group and associated unit cell parameters.

Five refinement cycles were performed for each analysis which also calculates standard errors and a mean square deviation according to:

$$R = \frac{\sqrt{(\theta_{obs} - \theta_{calc})^2}}{(N - M)}$$

where N is the number of unknown values and M is the number of observed values from the unit cell parameters, a, b, c, α, β, γ. CELL is no longer widely used or supported, however, new programmes such as Checkcell and Celref have been built on the foundations of this programme and despite a different graphical interface they produce the same results.

It is also possible to infer relative grain size from X-ray data according to the relation between the observed peak width at half the peak height (Full Width Half Maxima) with grain size:

$$L \propto \frac{1}{FWHM}$$

Numerical values for grain size can be determined by the Scherrer equation

$$B_{hkl} = \frac{K\lambda}{L_{hkl}\cos\theta_{hkl}}$$

Where B is the width at half the peak height (FWHM) in radians and is determined by subtracting the lower limit of the peak from the upper limit of the peak at half the peak height. K is a constant (where 0.89<K<1) dependent on the method of taking the FWHM and L is the crystallite length and is volume averaged. During this investigation, K was taken to be 0.9 as the observed particles were of undefined shapes whereas 0.89 corresponds to completely spherical particles and 0.94 for cubic particles.

A Siemens D5000 diffractometer was used to analyse samples in the lab. This model strips out the unwanted Kα 2 and Kβ 1 radiation through the use of a monochromator leaving only the Kα 1 radiation which has a wavelength of 1.5406 Å and is configured for transmission diffraction rather than reflective diffraction which results in an improved signal to noise ratio as well as a lack of signal from the sample holder. However this experimental set up requires the use of tape to keep the sample in the target zone. Scotch Magic™ tape produced by 3M allows minimal, amorphous signal at low angles and was used on both sides of the metal place sample holder to keep the sample in position.

Samples were prepared under an argon atmosphere inside a glovebox by first placing Magic tape across the underside of the metal sample plate's aperture. The sample was loaded uniformly across the tape and filled to the extent of the sample holder's thickness ~1.5 mm. A second strip of Magic tape was then adhered to the top of the plate to avoid any movement or spillage of the sample. The sample holder was then transferred from the glovebox to the diffractometer and immediately measured. The act of using the Magic tape to enclose the sample was proven to successfully protect the sample from oxidation or hydration. One test showed minimal difference in the presence of an oxide or hydroxide phase on a protected sample of MgH_2 over a 48 hour period from the point it was removed from the glovebox compared to an unprotected sample exposed to atmosphere.

3.5.2 Synchrotron sourced X-rays – ESRF, Grenoble

Synchrotron source X-rays are generated by accelerating electrons or positrons to near the speed of light around an evacuated, magnetised ring. These particles produce electromagnetic radiation when under the influence of an accelerating field – the wavelength and energy of which is proportional to the velocity of the particles.

Samples were measured in the ESRF beamline ID31. The beam is monochromated by a cryogenically cooled double-crystal monochromator containing Si 111 and Si 311 crystals - the former for normal operation and the latter for high energy resolution). The Si 111 crystal was used in the experiments in this study and is cooled by liquid nitrogen flowing through copper heat exchangers. Water-cooled slits control the size of the beam that is incident on the monochromator and from the monochromator to the sample. The measurement technique was powder diffraction which requires a relatively large beam to illuminate a large portion of sample to allow for the averaging of the diffraction from crystals in different orientations so no focusing was required.

The diffractometer itself is composed of a sample holder – capable of accepting capillaries or flat plate specimens – and a bank of nine detectors that scan vertically to measure the diffracted intensity as a function of 2θ (Figure 3.5.2)[4]. There is also a bank of Si 111 crystals in between the sample and the detectors which allow for the simultaneous scanning of multiple angles of 2θ. This means that, for dynamic measurements, the detector arm only need move no more than 2.3° to measure an angular range of 18° in 2θ. The crystals are mounted on a rotation stage that allows one calibration to be made for all the detectors when the wavelength is altered.
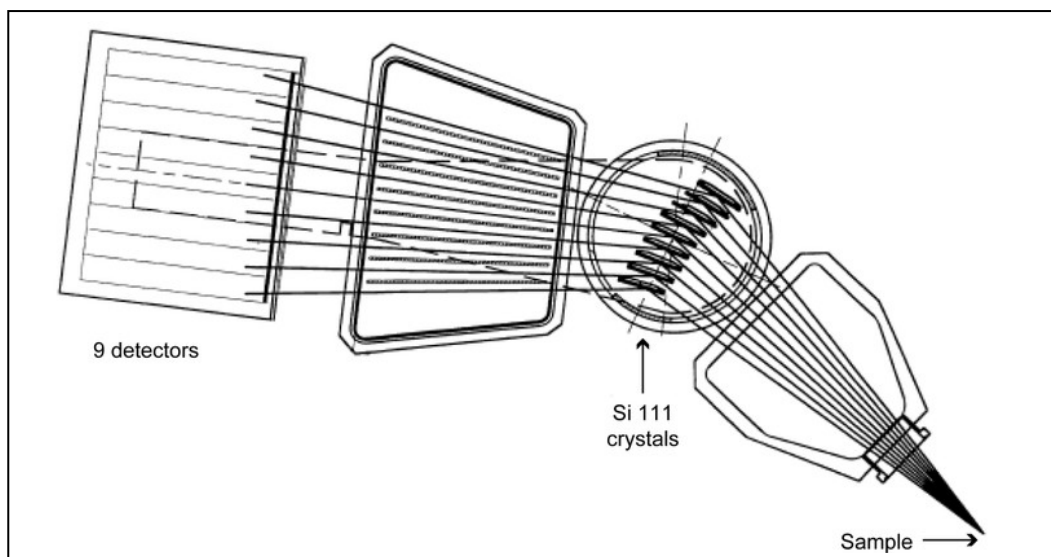
Figure 3.5.2 : Diagram of the diffracted X-ray detector for the ID31 beamline[1]

To be able to combine the data collected by the different detectors the offset between the detector channels (which is 2° at ID31) must be accurately calibrated to allow the differences in offsets and channel effiencies to be corrected and combined by computer so that the signals can be superimposed as closely as possible[5]. The set-up of the analyser results in precise, sharp reflections from the compounds in a given sample due to the mechanical accuracy of the diffractometer (± 1 arcsec, 0.003° 2θ instrumental linewidth broadening) and high collimation of the beam and is immune to problems such as specimen transparency and sample misalignment in the diffractometer as can be experienced for PSD arrangements (e.g. D5000). This allows observation of any minority phases that may have formed or unit cell distortions due to possible intercalation or doping of different elements and ionic units.

This study used spinning capillary measurements on the ID31 beamline to reduce preferred orientation effects on peak intensities for the compounds measured (needle-like samples can align with the axis of the capillary). The available energy range of the beam combined with the selection of capillary diameter means that absorption of the X-rays can be minimised – even for heavy elements. ID31 is also equipped with an automatic sample changer which can change up to 50 samples in capillaries in one measurement period.

The samples to be measured were ground and loaded into glass capillaries within a glove bag or glove box containing argon and then sealed with wax or vacuum grease. These capillaries were then mounted onto a multi-sample loading stage that was placed on the automatic robot sample changer. The samples were the measured across a range of 2θ – usually from 3-100° 2θ though some samples were measured from 3-60° 2θ due to limited equipment time. The wavelengths of the beamline changed over multiple visits, however all samples were wavelength corrected and have been displayed at a wavelength of 1.5406 Å for direct comparison with powder diffraction patterns obtained from the D5000. The step size used for the measurements was 0.00499° 2θ and the averaged step time was 3 seconds per step.

3.6 Differential scanning calorimetry (DSC)

Differential scanning calorimetry is an analytical technique used to determine the work done on a given sample to initiate phase changes and decompositions. The software monitors the sample pan as well as an empty pan for reference and compares the difference in energy required to raise the temperature of each. This method can be used to determine the enthalpy of transition for a given process (e.g. phase formation, decomposition) from the area under the curve from the following equation:

$$\Delta H = kA$$

where k is the calorimetric constant (which is different for each set of equipment) and A is the area under the curve.

A DSC 204 HP Phoenix was used inside an argon-filled glovebox so as to load samples without exposing them to atmosphere. Sample pans were aluminium and a heating rate of 2°C per minute was used for each experiment. The equipment was capable of measuring from atmospheric pressure to 150 bar in argon or hydrogen.

3.7.1 Scanning electron microscopy (SEM)

Scanning Electron Microscopy is an analytical method used to indirectly observe the surface of a material at the nano- to micrometer scale by interpreting the electrical signal generated from electrons emitted from the sample. The electrons are generated in a similar manner to those in X-ray diffraction: from a heated tungsten filament under vacuum. These are then accelerated through a magnetic field to the target sample where they interact to release X-rays and visible light with secondary (emitted) electrons being a by-product. However not all of the electrons interact in this fashion and the remaining electrons will be scattered or absorbed (Figure 3.7.1).

The emitted electrons are collected via a detector but each electron will only provide information on an individual point on the surface. To build up an image of an area the sample is scanned via the raster method which is achieved by accurately altering the pathway of the electrons via a scan coil without having to realign the beam for each point in the area. This information is then able to be displayed in real-time and recorded, allowing study of the surface to be undertaken and points of interest to be captured.

In this work a JOEL 7000 and a JOEL 6060 microscope were used. The samples were fixed to a sticky carbon disc and placed on a loading plate in an argon-filled glovebox then transported under an argon environment in a Kilner jar. The plate was then loaded under atmospheric conditions before being evacuated and placed under the electron beam because there were no inert loading facilities available for either microscope.
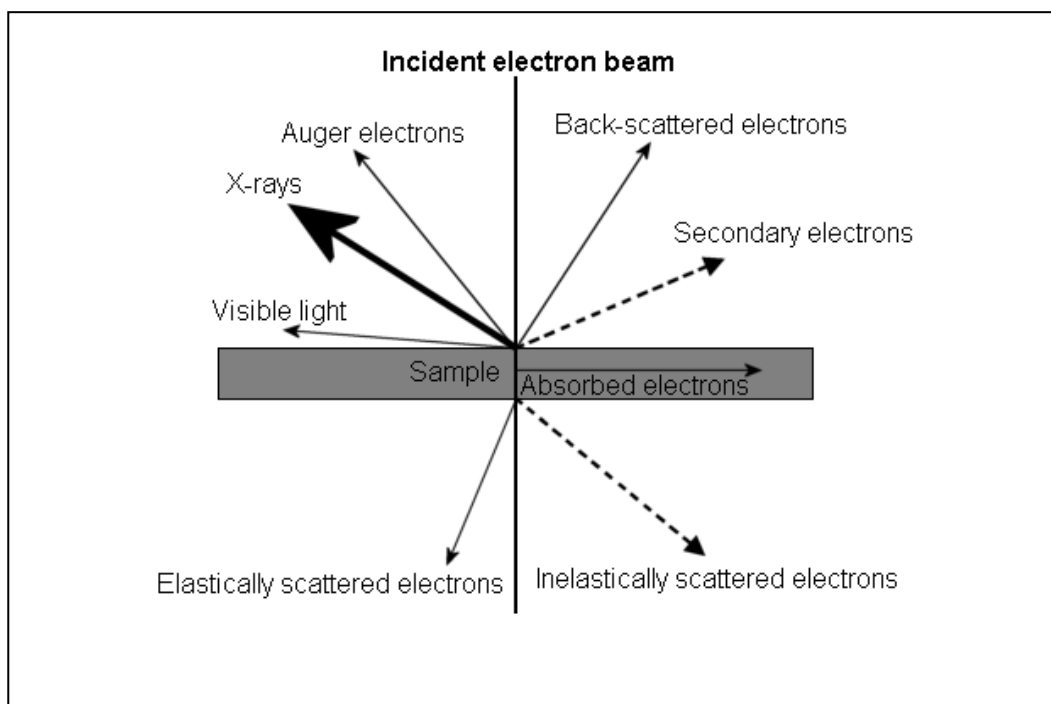
Figure 3.7.1 : Representation of the interaction between the incident electrons and the sample

3.7.2 Energy dispersive X-ray spectroscopy (EDX)

EDX is a method that allows the qualitative and quantitative determination of the composition of a point or area on a sample. This composition is determined via analysis of the observed X-rays derived from the interaction of an electron with an atom as described in section 3.5 (a) from the area being analysed. Each element has unique photon energies for the generated X-rays and can therefore be identified qualitatively from other elements present: the collected X-ray spectrum from the sample shows the relative amounts present by the height and breadth of the observed peaks. To determine the amounts of each element quantitatively a standard must first be analysed before the experimental session – usually a highly stable and crystalline material or the pure element.

Samples that were analysed via EDX were prepared in an argon-filled glovebox and suspended in a Cu-based polymer mixture (Technovik). These moulds were then ground on three grades of silicon carbide papers (400, 800 and 1200) to expose the sample before

further polishing on a cloth impregnated with diamond paste. The samples were lubricated and washed with cyclohexane during the grinding and polishing process. This procedure allowed a smooth sample surface to be analysed via EDX and for minimal reaction of the present, air sensitive chemicals to take place.

3.7.3 Wavelength dispersive X-ray spectroscopy (WDX)

WDX is used to count the number of emitted X-rays at a specific wavelength from a sample undergoing analysis from electron microscopy. This method relies on the fact that for a well-defined crystal lattice an incident X-ray of a specific single wavelength will produce constructive interference – effectively amplifying the 'signal' at the X-ray detector for this wavelength if present. Each element emits a unique X-ray spectrum when bombarded with electrons and so by selecting an appropriate crystal to diffract the emitted X-rays from a sample it is possible to determine if a specific element is present. This allows for detection of elements which have a low electron scattering potential and is often utilised in conjunction with EDX to more accurately determine the content of a given sample.

Samples analysed by wavelength dispersive X-ray spectroscopy were done so in the JOEL 7000 and prepared in the same manner as that used for EDX analysis (section 2.7 (b)). Due to the available diffracting crystals being limited, WDX was only carried out for the analysis of the presence of boron within a sample.

3.8 Flowing TPD system

To meet the requirement of being able to synthesise activated MgH_2 in larger quantities a flowing rig with temperature and pressure control was designed and built to allow both small and large sample synthesis. The system allowed isolation of the reaction chamber via two plug valves which sealed the sample environment from the two halves of the flowing

apparatus (Figure 3.9.1 a)). The Swagelok fittings on the outer side of the plug valves could be unscrewed, allowing the central reaction chamber to be removed and loaded into a glove box for removal or loading of the sample under an inert atmosphere.

Contamination via oxygen or moisture was avoided by evacuating and flushing the system with inert gas (argon or nitrogen) for the pipe work before the sample and by flushing out the exhaust with a positive pressure of inert gas once the sample chamber was reconnected to the middle part of the rig.
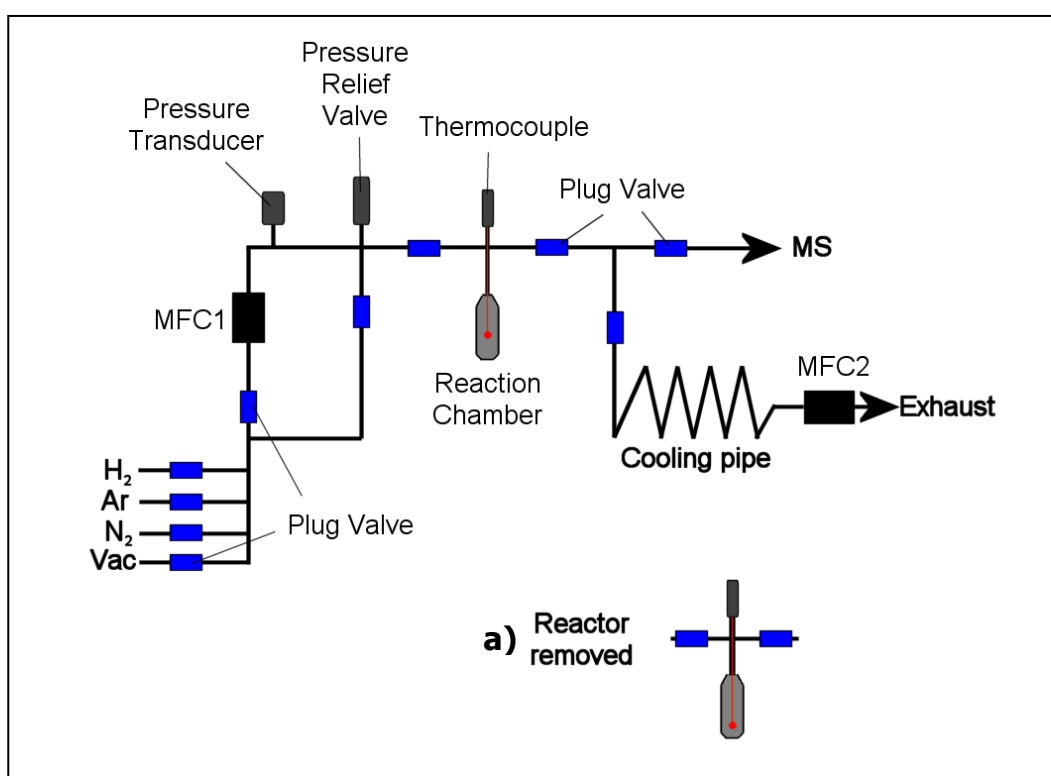
Figure 3.9.1 : Schematic of the flowing TPD system with, a), a representation of the sample chamber removed from the main rig

Temperatures of ~500°C are possible through use of a band heater that could be fitted to the outside of the reaction chamber and pressures of up to 10 bar can be monitored through the pressure transducer. The pressure release valve was configured to 12 bar so, in the case of an unwanted build-up of pressure, the system would safely dispose of the excess gas.

The mass flow controller that is before the sample (MFC1) controls the flow rate into the main part of the rig – where the sample chamber is located. It can be bypassed by opening the plug valve connected below the pressure transducer – this function is utilised to evacuate the pipeline to where the sample reactor unit is joined onto the rig, allowing for the removal of O_2 and moisture. The second mass flow controller controls the back pressure regulation when it is active and is linked in the software to the pressure transducer so that a change in pressure will either allow gas to flow out through the exhaust or into the system via MFC1 whilst keeping MFC2 closed. This functionality enables simple volumetric measurement of samples to be undertaken and thus allows a measure of how much a sample is absorbing and when it begins and stops absorbing. Both mass flow controllers are calibrated to work with the molecular size of hydrogen but the software has a gas conversion variable that can be changed so

The temperature at the sample is measured by a thermocouple that is placed through a compression fitting in the top of the reactor unit and can be replaced through removal of this

The software monitors the temperature, the pressure and the flow rate as well as controlling the heating rate and temperature of the band heater and can be made to record all inputs to a CSV file.

The system could be operated at a static pressure, flowing at atmospheric pressure or flowing at controlled pressure by changing which of the exhaust valves were open. The mass flow controllers were calibrated for hydrogen but the software allowed the input of a conversion factor to enable accurate controlling of pressure and flow rates of large gas molecules such as N_2 or Ar.

The TPD system also allowed gas to flow to a mass spectrometer so that evolved gases could be monitored.

1.   [http://www.esrf.eu/usersandscience/experiments/structmaterials/ID31techni caldescription](http://www.esrf.eu/usersandscience/experiments/structmaterials/ID31technicaldescription), *ESRF Beamline ID31 technical description*. 2010.

2.   Sieverts A., *Zeitschrift fur physikalische chemie - Stochiometrie und verwandtschaftslehere.* Z. Phys. Chem., 1914. **88**(4): p. 451.

3.   Giacovazzo C., Monaco H.L., Artioli G., Viterbo D., Ferraris G., Gilli G., Zanotti G., and Catti M., *Fundamentals of Crystallography*. Second ed. IUCr Texts on Crystallography - 7, ed. Giacovazzo C. 2002: Oxford University Press. 825.

4.   Hodeau J.L., Bordet P., Anne M., Prat A., Fitch A.n., Dooryheé E., Vaughan G.B.M., and Freund A., *Nine crystal multi-analyser stage for high-resolution powder diffraction between 6 and 40 keV.* Proc. SPIE, 1998. **3448**: p. 353.

5.   Wright J.P., Vaughan G.B.M., and Fitch A.N., *Merging data from a multi-detector continuous scanning powder diffraction system.* IUCr Comp. Comm. News., 2003(1): p. 92.

4.1   Sorption properties of magnesium hydride

Experimental technique 4.1

Sample handling

All samples were handled in an inert atmosphere as much as was possible. MgH_2 powder (Aldrich, 90% purity, 10% Mg) was stored in an argon-circulating positive pressure glove box fitted with oxygen and moisture scrubbers. When samples had to be removed from the glove box, e.g. for measurement they were done so in glass vials sealed with a plastic stopper and wrapped with cellulose tape to form an air tight seal around the joint. For trips that required longer times the vials were placed within kilner jars within the glove box, sealing a protective pocket of argon around the sample vial.

IGA – Intelligent Gravimetric Analyser

The IGA was set up in kinetic measurement mode. A quartz sample holder was calibrated against the counter weight on the microbalance and the initialisation of the experiment begun. The quartz sample holder bulb was loaded onto the platinum wire hook with a piece of glass wool inside it and the sample reaction chamber fitted to the IGA to reduce air flow around the sample holder as it would affect the accuracy of the reading of the balance. The weight of the bulb was 'zeroed' – i.e. the mass of the sample holder was taken into consideration for the measurement. The buoyancy correction factor, used to offset the effect of the density imbalance between the counterweight and the sample holder and sample and the resultant effect of the measurement gas on the recorded mass of the sample during measurement, was set at the density of magnesium, 1.74 g/cm^3. The reaction chamber was detached and the quartz sample holder removed from the hook. The sample was loaded into the sample holder from a sealed vial (as described above), the sample was kept inside the quartz bulb by placing the glass wool inside the opening. This also served to ensure that the sample powder would not exit the bulb during the measurement – giving a false reading. The bulb was replaced on the hook and the reaction chamber replaced to reduce air currents. If the sample was within the centre of the limits of measurement then the reaction chamber would be sealed with bolts and a copper flange. If the sample was not heavy enough, or was too heavy the bulb would be removed and sample added to or removed from the bulb. The typical sample size was ~100mg.

Once the chamber was sealed and the balance had settled to give an accurate weight for the sample the experiment was started in the IGAS software. The sample chamber would then be evacuated via the rotary or vane pump attached to the IGA system and once this reached a few millibar a valve to a wide bore (1/2 inch) evacuation pipe was slowly opened, allowing the turbomolecular pump to act on the sample chamber. The sample was monitored via a chart on the computer controlling the IGA, the chart could be set to monitor pressure, temperature, weight and the time of the experiment. Each chart could be saved to the experiment file or discarded – once an experiment was started the experiment file was saved automatically to the IGAS software log but charts in progress would not be saved in the event of a computer crash or power outage. The pressure would be monitored until it reached $\sim 1 \times 10^{-6}$ at which point the valve to the turbomolecular pump was closed.

Before the measurements took place a dewer of liquid nitrogen was placed over an oxygen and moisture trap in the H_2 pipeline connected to the IGA to ensure the least amount of sample contamination from the hydrogen source. The dewer was refilled during the experiment to maintain the trap's effectiveness. The hydrogen was supplied from a cylinder of high purity grade hydrogen (99.999% H_2) that was set at a pressure of 20 bar from the regulator to provide a pressure overhead during experiments.

For samples that were considered to be in a fully hydrided state, the pressure was set to 10 bar H_2 under pressure control (this setting was used to keep the pressure at a constant level as opposed to inputting a static volume of gas) at a ramp rate of 0.5 or 1 bar/min. Once this was reached, the sample was heated to the required temperature at a rate of 5°C/minute whilst monitoring the chart recording for any absorption. If no absorption occurred a new chart recording was started and the pressure was lowered to the required setting at a rate of 1 bar/min for large pressure changes and 200 mbar/min or lower for smaller changes. This was the start of the measurement.

For samples that were considered to be in a fully dehydrided state, the pressure was increased to 10mbar H_2 under pressure control. When the pressure had settled, a new chart was started and the temperature was set to the required value at a rate of 5°C/minute and this was denoted as the start of the measurement.

Completion of a H_2 absorption or desorption measurement was determined by monitoring the chart in the IGAS software and judging when a plateau in mass had been achieved. This was a visual judgement based on the provided on-screen graph as there was no way to export the information in a chart while

it was still in use for more detailed analysis. As such, the completion of hydrogenation or dehydrogenation can sometimes be difficult for experiments that proceed over a long period of time as a gradual slope will appear as a straight line. In later software versions the IGAS software a feature was implemented that allowed the user to zoom in on a portion of the graphics on screen, however, at the time of these measurements it was not implemented and in the period of research where it was implemented (Chapter 4.3 onwards) it would regularly crash the IGAS software, causing loss of any on-screen and current chart data and as such the feature was not utilised.

After the first H_2 absorption or desorption step was completed, the chart data was saved and a new chart was created. This was because the IGAS software culls data for longer periods of time, reducing the amount of fine-detailed information available during lengthy sorption measurements. The next step was then started with a change in pressure (10 bar H_2 for absorption and 10 mbar H_2 for desorption) with the temperature kept at a constant unless otherwise stated for the specific sample. This process was repeated for all subsequent hydrogenations and dehydrogenations.

Once the experiment was concluded, the reaction chamber was cooled to room temperature and then evacuated as per the previous evacuation technique listed above by first using the rotary pump and then switching to the turbomolecular pump. This was to ensure no hydrogen was released into the laboratory. The valve to the turbomolecular pump was closed and the evacuation process in the pressure control system in the IGAS software stopped and the experiment ended in the software. The air admittance valve was then carefully opened allowing a slow equalisation of pressure between the laboratory and the reaction chamber. Once the pressure was equilibrated, the sample was removed and placed in a new glass vial in a glove box for storage until subsequent analysis was performed.

Determination of the weight percent of H_2 absorbed

Using the data collected via the IGAS software the weight percent of hydrogen absorbed and desorbed was determined. To do this a simple equation was used:

$$wt\% = \left(\frac{\partial W}{W_{hyd}} \right) \times 100$$

Where W_{hyd} is the weight of the fully hydrided phase of the sample and δW is the change in weight of the sample from W_{hyd}. The start point of the measurement was used as the point at which the gas was admitted or removed from the reaction chamber. During the change in pressure (within the first ten

minutes of a measurement) the sample was greatly affected by currents and buoyancy effects due to the large pressure difference between 10 mbar and high pressure and as such many graphs begin with featureless undulations in weight and therefore weight percent that do not give any accurate or relevant information and may, at the very beginning of the data result in small negative values. Once the flow effects caused by such rapid (de)pressurisation have passed (within a few minutes) the 'true' result is once again observed.

The kinetic measurements often displayed variability in capacity and kinetics from sample to sample and from different absorption and desorption measurements for the same sample. There are several factors that can influence this behaviour:

- Incomplete H_2 desorption and absorption

- Sublimation of Mg at near vacuum pressures and temperatures around 300°C

- Reaction with contaminants in the system such as O_2 or H_2O

- Restricted hydrogen diffusion pathways in the sample particles during measurements

Typically, the variation in H_2 capacity within a sample across multiple measurements would be a maximum of 10% of the wt%. Variation in total H_2 capacity between samples could be as high as 20-30% of the wt% value.

Kinetic variation is more complex and is highly dependent on the diffusion of hydrogen which is linked to the evolution of microstructure upon sequential hydrogen cycling. There is a small amount of decrepitation (the process of a particle breaking apart) over the course of an absorption and desorption. For milled materials this is not a concern due to their altered microstructure and, while samples milled for shorter times will see a large increase in sorption kinetics over the course of the 6 H_2 cycles typically run for the samples measured, samples milled for longer periods of time (>10 hrs) saw very little kinetic improvement upon H_2 cycling. As-received Mg, MgH_2 and other variants on these two reagents saw a large variation in sorption kinetics as a function of increased hydrogen cycling and it is apparent from SEM images in sections 4.1 and 4.2 that there is an amount of refinement of microstructure which

definitely improves the sorption kinetics. However, this is not a guaranteed improvement and thus even the same sample measured twice will not necessarily display the exact same kinetic features upon successive H_2 cycles.

XRD – X-ray diffraction

X-ray diffraction was performed on a Brüker D5000 as described in section 3.5.1. Samples were prepared under an argon atmosphere inside a glovebox by thoroughly grinding in a mortar and pestle. Then Magic tape™ was placed across the underside of the metal sample plate's aperture. The sample was loaded uniformly across the tape and filled to the extent of the sample holder's thickness ~1.5 mm. A second strip of Magic tape™ was then adhered to the top of the plate to avoid any movement or spillage of the sample. The sample holder was then transferred from the glovebox to the diffractometer. It was clamped within a spring-loaded loading plate which was attached magnetically to the equipment that was aligned in the axis of the diffractometer and immediately measured. The act of using the Magic tape to enclose the sample was proven to successfully protect the sample from oxidation or hydration. The samples were measured over a range of 20 – 100° 2θ with a step size of 0.02027° and a step time of 0.35s and observed peaks were identified using the crystallographic database software EVA. The width of a peak at half the height (FWHM) was calculated after a background subtraction had been performed on the diffraction pattern.

SEM – Scanning Electron Microscopy

The samples were mounted onto an adhesive-lined carbon disc which was then loaded in air onto the mounting mechanism for the microscope before the chamber was evacuated and the sample inserted into the electron beam. A voltage of 20 kV was used so as not to decompose the sample when it was under the beam and a distance of 16mm was kept from the sample. Pictures were taken of various points on the surface of the sample at x200 and x400 magnification. Particle sizes were measured using the scale on the micrographs.

Mechanical Milling

A range of milling times was decided upon for this study based on literature showing the evolution of microstructure within samples. 5, 15 and 60 hours of milling time were used to process MgH_2 powder as described in section 3.1.2.

Grain size determination

The grain size (L) was determined using the Scherrer equation:

$$L_{hkl} = \frac{K\lambda}{B_{hkl}\cos\theta_{hkl}}$$

B, the FWHM (Full Width Half Maxima), was calculated through analysis of the powder XRD patterns in degrees 2θ and had to be converted to radians from degrees. K, the shape factor of the crystallite, was taken as 0.9 as this averages out the differences in grain shape. λ, the wavelength in angstroms, was 1.5406Å for the experiments performed on the D5000 diffractometer. θ, the peak position of the peak being used to generate the FWHM, was halfed and converted to radians from the observed 2θ value on the diffraction pattern.

Due to instrumental line broadening inherent in the X-ray equipment set up and the various sizes and orientation of crystallite in the sample, highly crystalline standards of SiO_2 and Al_2O_3 were measured on the X-ray diffractometer. The FWHM of these samples from reflections at or near the same 2θ values as the reflections being analysed to determine the grain size were measured and were subtracted from the measured FWHM of the MgH_2 reflections being used. This approximation was used to remove the instrumental line-broadening and is able to be used because of the high crystallinity of the SiO_2 and Al_2O_3 samples creates a reflection that is essentially as close to the reflectance line as possible and therefore all observed broadening is assumed to be caused by the instrumental set up.

4.1 (a) MgH$_2$

Magnesium hydride is a promising hydrogen storage medium due to its relatively high percentage H_2 content. In comparison with alternative hydrogen storage materials, magnesium is cheap to produce and is widely available in large quantities from various chemical suppliers. The compound is reversible according to equation 4.1.1 at temperatures around 300°C and the plateau pressure at this temperature is approximately 1 bar. Re-hydriding conditions are usually carried out under an excess of pressure at 300°C but hydrogen sorption kinetics tend to be slow even at this elevated temperature.
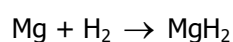
$$Mg + H_2 \rightarrow MgH_2 \qquad\qquad \textbf{Eq. 4.1.1}$$

Though some fuel cells operate at temperatures above 300°C[1] and various methods can be employed in the construction of the hydrogen store to reduce the energy required to sustain hydrogen evolution - such as re-routing waste heat from the fuel cell - these operating conditions are not favourable in many applications and much of any stored energy is lost due to this inefficiency.

Improving the hydrogen sorption kinetics or decreasing the onset temperature of both dehydrogenation and rehydrogenation are two ways in which MgH_2 can be made to be more desirable for use in commercial applications.

The hydrogen sorption kinetics of MgH_2, sourced from Aldrich (90% MgH_2, remainder Mg, <1% MgO), were measured at 300°C under a hydrogen atmosphere. Dehydrogenation was carried out under 10 mbar H_2 while hydrogenation steps were carried out at 10 bar H_2. To simulate the charging and discharging of a hydrogen store in a real world application, successive hydrogenation and dehydrogenation steps were performed on the sample (hydrogen cycling) to determine the effect that this process has on MgH_2. The samples were loaded under atmosphere and then degassed before being heated and exposed to hydrogen.

Figure 4.1.1 shows the effect of hydrogen cycling on the kinetics of absorption for the Aldrich MgH_2. After six cycles the formation of the MgH_2 phase occurred at a slightly slower rate with the first cycle completing in around 350 minutes whilst the sixth completed in around 450 minutes. The total hydrogen capacity was also slightly reduced indicating either partial oxidation of the sample from a contaminated gas supply – MgH_2 is quite sensitive to oxygen and water – or agglomeration of the particles resulting in a reduced surface area and thus reducing H_2 penetrat ion into the material which results in reduced uptake within a certain time period.
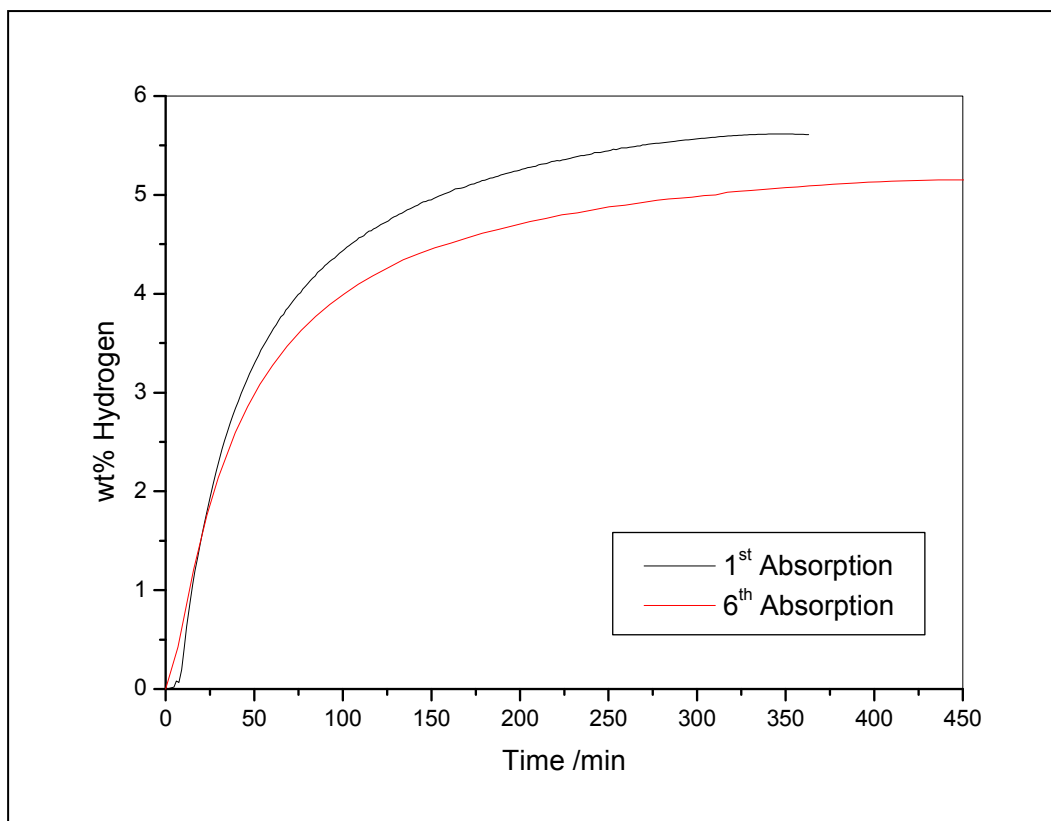
Figure 4.1.1 : Kinetic traces showing hydrogen absorption at 300°C for MgH$_2$ cycled 6 times on an IGA

Figure 4.1.2 shows that upon cycling, desorption kinetics improved. The first desorption had to be carried out at 350°C and so is not directly comparable to the subsequent desorptions. No loss of mass was observed at 300°C for this initial desorption which is attributed to formation of an oxide layer on the particles during sample loading which blocks hydrogen diffusion into the particles. Heating to 350°C allows the oxide layer to be broken down and hydrogen diffusion into the particles to take place.

The second desorption was performed at 300°C and so direct comparison can be performed on the time to complete desorption. This completed in 1200 minutes whereas the sixth desorption was complete in 900 minutes.
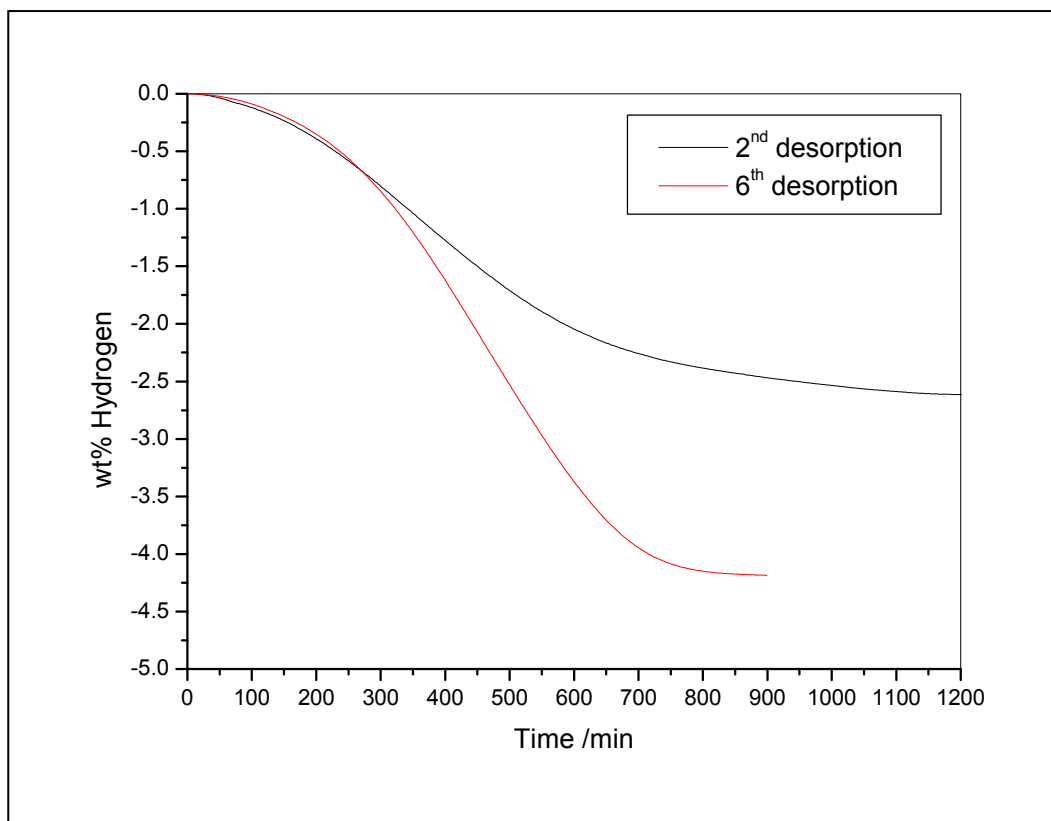
Figure 4.1.2 : Desorption kinetic traces for MgH$_2$ at 300°C cycled 6 times on an IGA

Figure 4.1.3 depicts SEM images obtained for Aldrich MgH$_2$ as-received and after six hydrogen cycles on an IGA. The particle size was observed to be 50 – 100 μm for the initial material while the cycled material was less well defined: decrepitation had occurred which resulted in 'furring' and agglomeration of the particles. The estimated particle size for the cycled material was 30 – 110 μm but since the particles are more porous in structure there is a higher surface area for the hydrogen to react with.
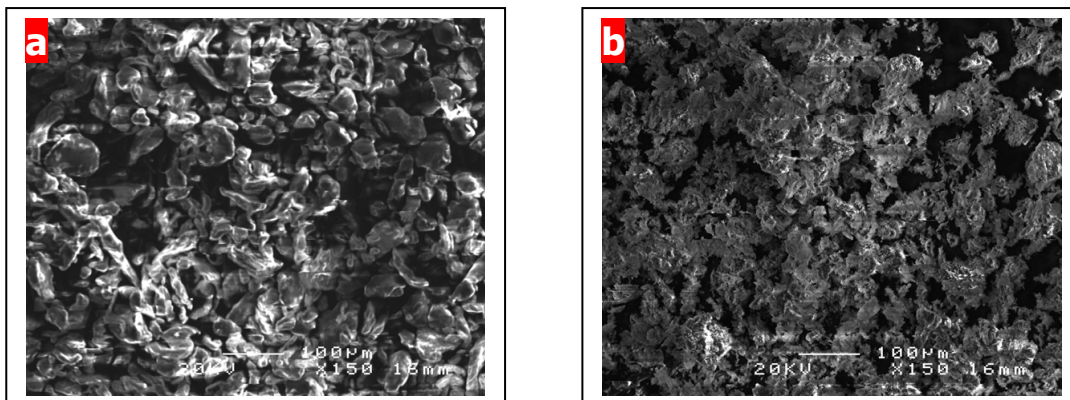
Figure 4.1.3 : SEM images of Aldrich MgH₂ (a) before and (b) after cycling on an IGA at 150 times magnification

Figure 4.1.4 depicts the diffraction patterns of MgH$_2$ before and after cycling on an IGA. The samples had a fine grain size both before and after the cycling process – with no change in lattice parameters – though there was a slightly larger magnesium oxide peak at 42.8° 2θ after cycling, which is due to exposure to air during the loading and unloading procedure on the IGA.
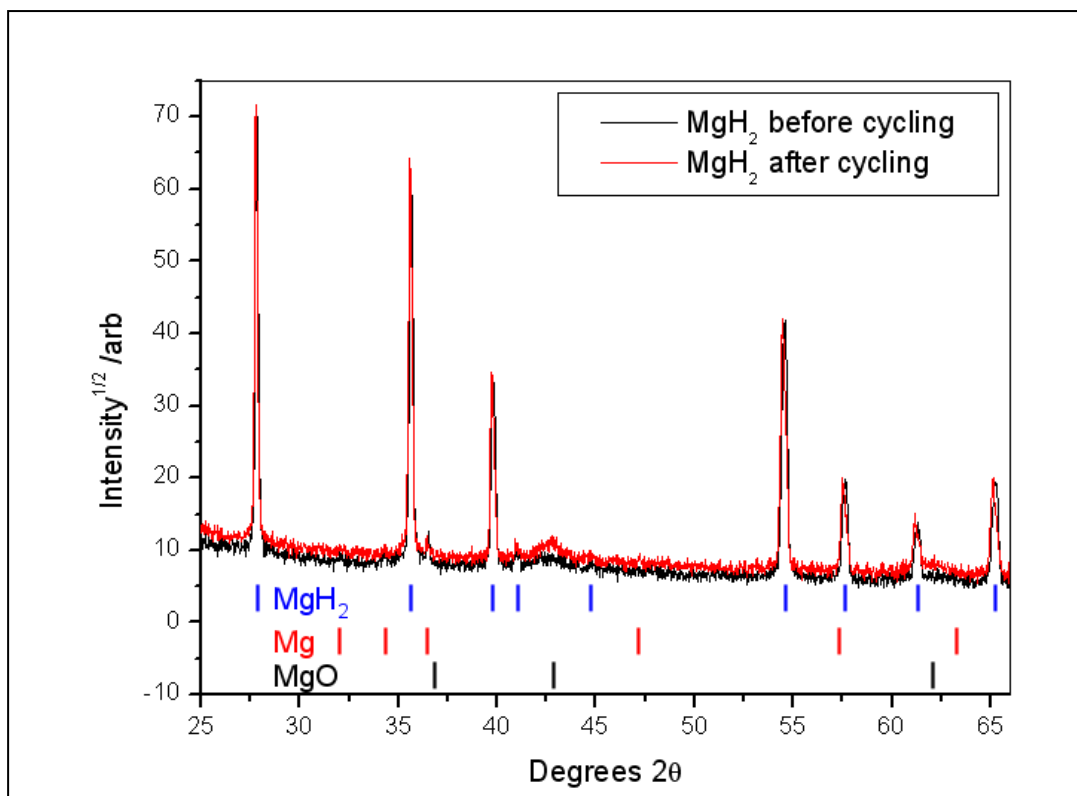
Figure 4.1.4 : X-ray diffraction patterns showing Aldrich MgH₂ before and after hydrogen cycling on an IGA

4.1 (b) Mechanical Milling

To improve the reaction kinetics of magnesium with hydrogen, samples of Aldrich MgH₂ were refined by high velocity ball milling. Milling has been shown to increase the reactive surface area of materials by introducing strain and defects into the crystal lattice. The process also reduces the average particle and grain size and this allows the hydrogen molecules to propagate deeper into the structure.

MgH₂ powder was milled for 5 hours in a planetary ball mill and the resulting sample was analysed via XRD and SEM. Figure 4.1.5 shows the diffraction patterns for Aldrich MgH₂ before and after milling. A substantial increase in peak width is observed for the milled sample, indicating a loss of long-range order of the crystal structure. The Scherrer equation (Eq. 4.1.2) describes the relationship between the peak width and grain size and shows that

they are inversely proportional. Using this method it is apparent that an increase in peak width corresponds to a decrease in grain size.

$$L_{hkl} = \frac{K\lambda}{\beta_{hkl}\cos\theta}$$ **Eq. 4.1.2**

Other groups have reported the appearance of the γ-phase of MgH₂ after milling however this phase was not observed in our study.
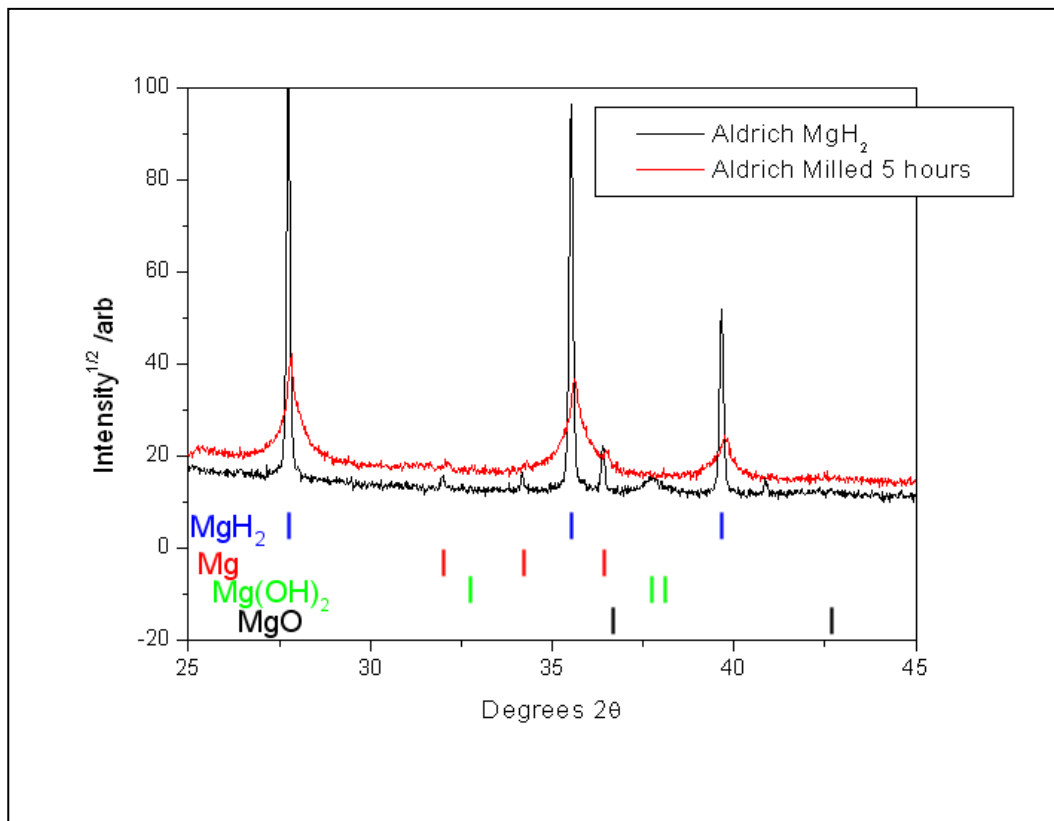
Figure 4.1.5 : X-ray diffraction patterns comparing Aldrich MgH₂ both before and after mechanical milling for 5 hours

Figure 4.1.6 shows an SEM image for MgH₂ milled for 5 hours. The image shows that although the minimum particle size had been reduced by the milling process, the sample was not homogenous – displaying a large range of particle sizes from 1 – 30 µm.
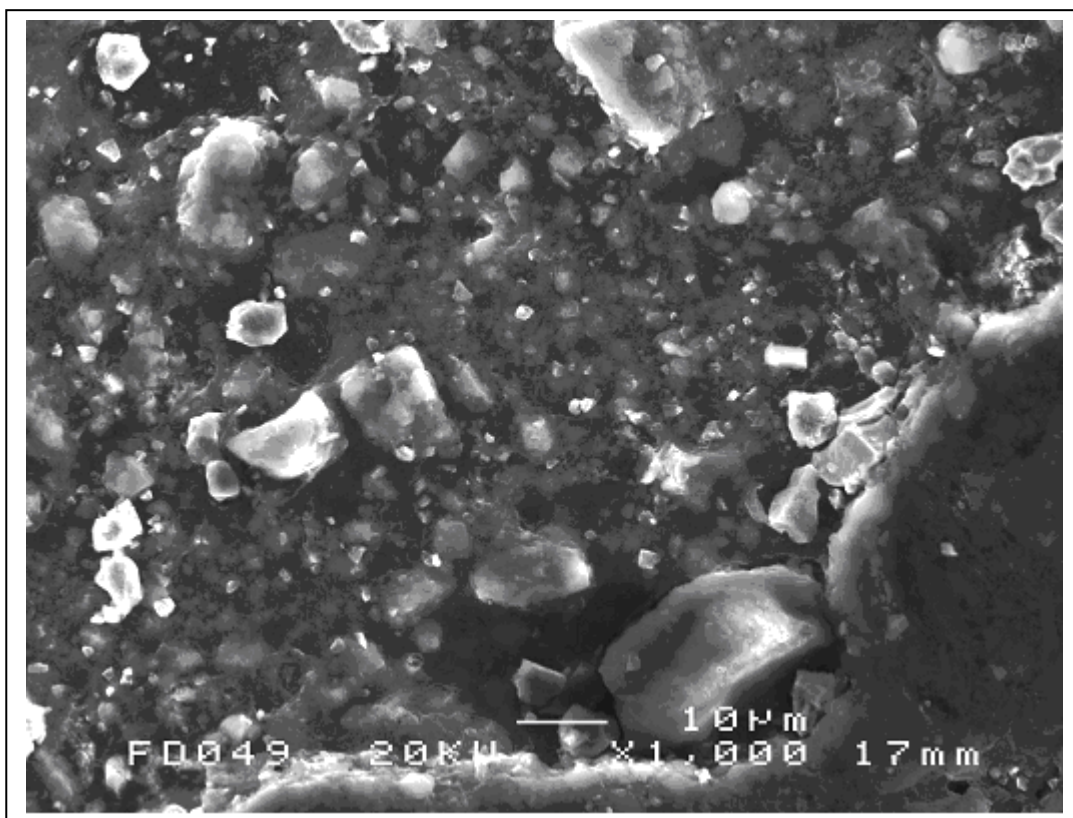
Figure 4.1.6 : SEM image showing MgH₂ milled for 5 hours in a planetary mill at 1000 times magnification

The hydrogen sorption properties of the milled MgH_2 sample were investigated using gravimetric analysis under the same conditions as the pre-milled Aldrich MgH_2 sample. Figure 4.1.7 shows the fourth, fifth and sixth desorption kinetics traces. The initial desorption was carried out at 350°C as per the original MgH_2 sample though this was completed in 72 minutes compared with 150 for the received reagent. Subsequent desorptions at 300°C were also quicker to complete when compared with the pre-milled MgH_2 sample - the sixth desorption completed in 790 minutes for the milled material, compared with 900 minutes for the pre-milled material. However, the majority of the hydrogen was desorbed much quicker when compared to the pre-milled material: the time to reach 90% completion was 190 and 740 minutes for the milled and pre-milled samples, respectively.
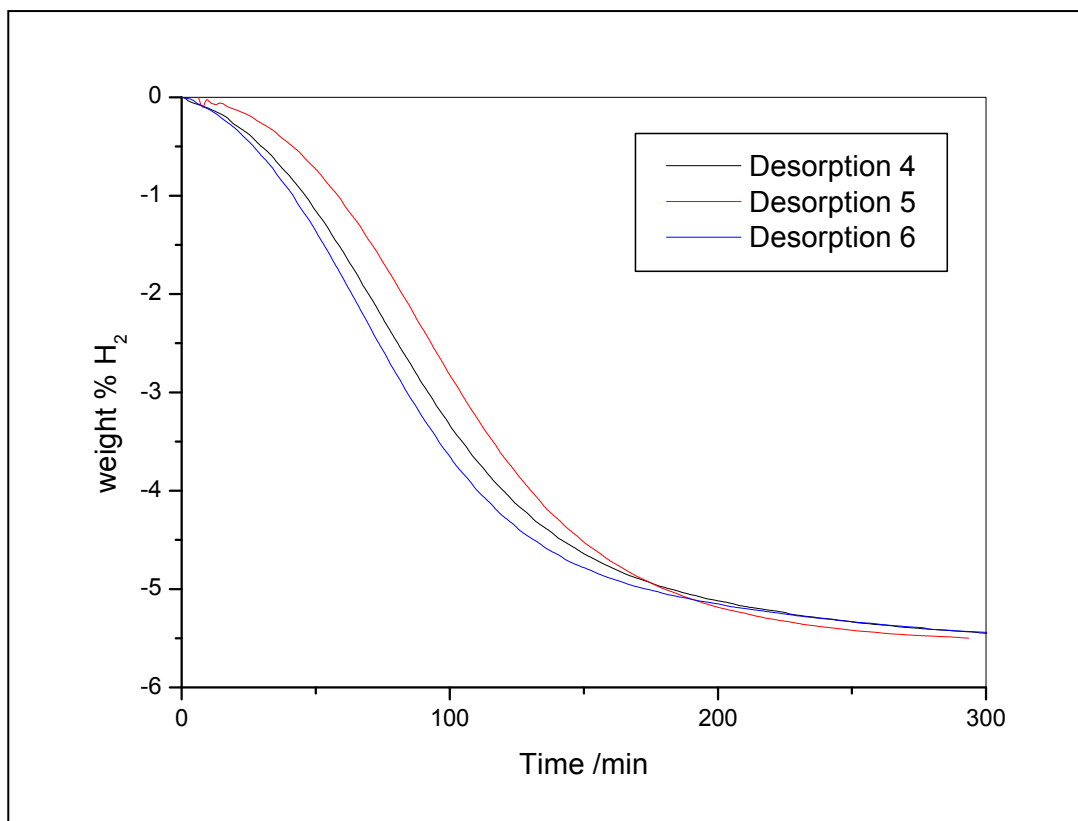
Figure 4.1.7 : Kinetic traces performed on an IGA showing desorption times at 300 °C for MgH$_2$ milled for 5 hours

Figure 4.1.8 shows absorption kinetics traces for the 5 hour milled sample. There is a vast improvement over pre-milled MgH$_2$ with the initial absorption completing in around 100 minutes and 90% of the hydrogen uptake achieved within 20 minutes. Subsequent absorptions were completed in similar times although there was a slight loss of capacity from 6.4 wt% for the 1st absorption to 5.8 wt% for the 6th absorption over the cycling process.
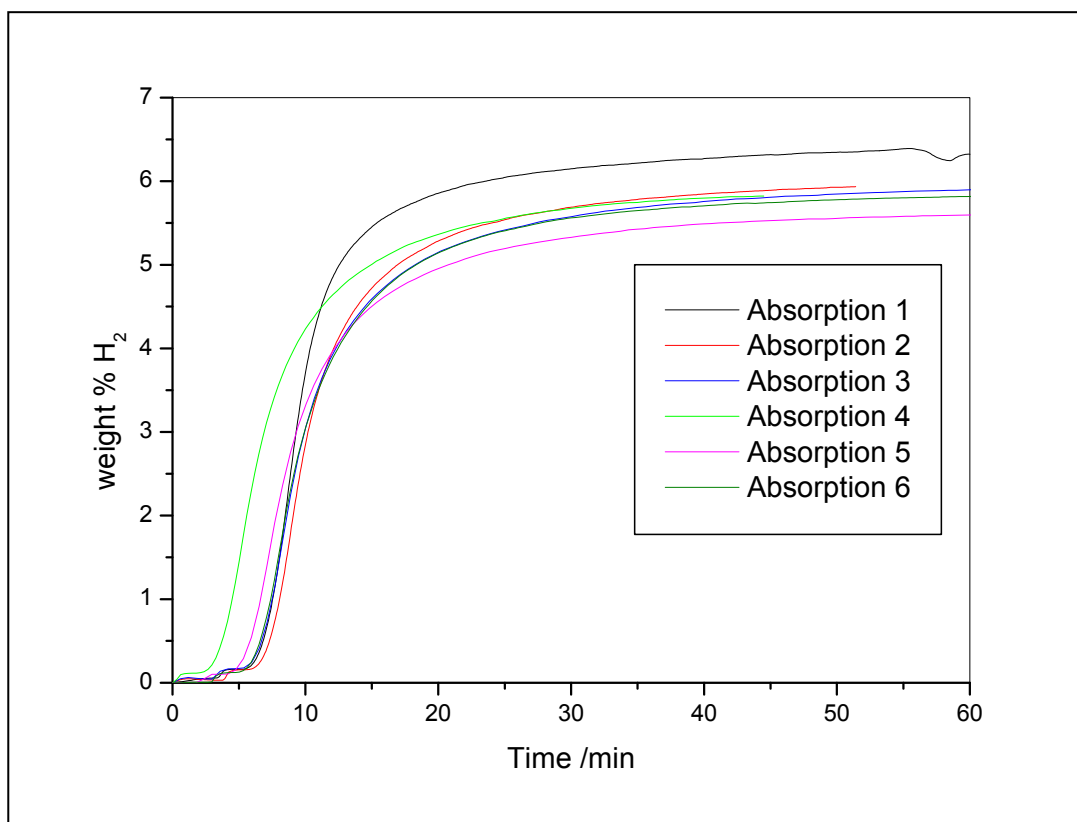
Figure 4.1.8 : Kinetic traces performed on an IGA showing absorption times at 300°C for MgH$_2$ milled for 5 hours

The effect of hydrogen cycling on the milled material was investigated via XRD and SEM. Figure 4.1.9 shows the diffraction patterns after the 1st desorption and the 1st and 6th absorptions. The peak widths of the reflections for MgH$_2$ and Mg were very small, even after the first desorption, which indicates that grain growth of the forming Mg and MgH$_2$ phases occurs. This is not unexpected behaviour due to the fact that each absorption and desorption results in the renucleation and growth of the hydrided and dehydrided phase and the consequent loss of grain size information.

Table 4.1.1 shows the full width half maximum (FWHM) values for MgH$_2$ milled for 5 hours, after the 1st desorption and absorption and the 6th absorption. This shows that, upon cycling, the FWHM of the first peak was reduced by more than half after the first cycle and remained

at around that value, indicating that some of the reduction in grain size after refinement of

the microstructure by milling, is lost during grain growth through hydrogen cycling.
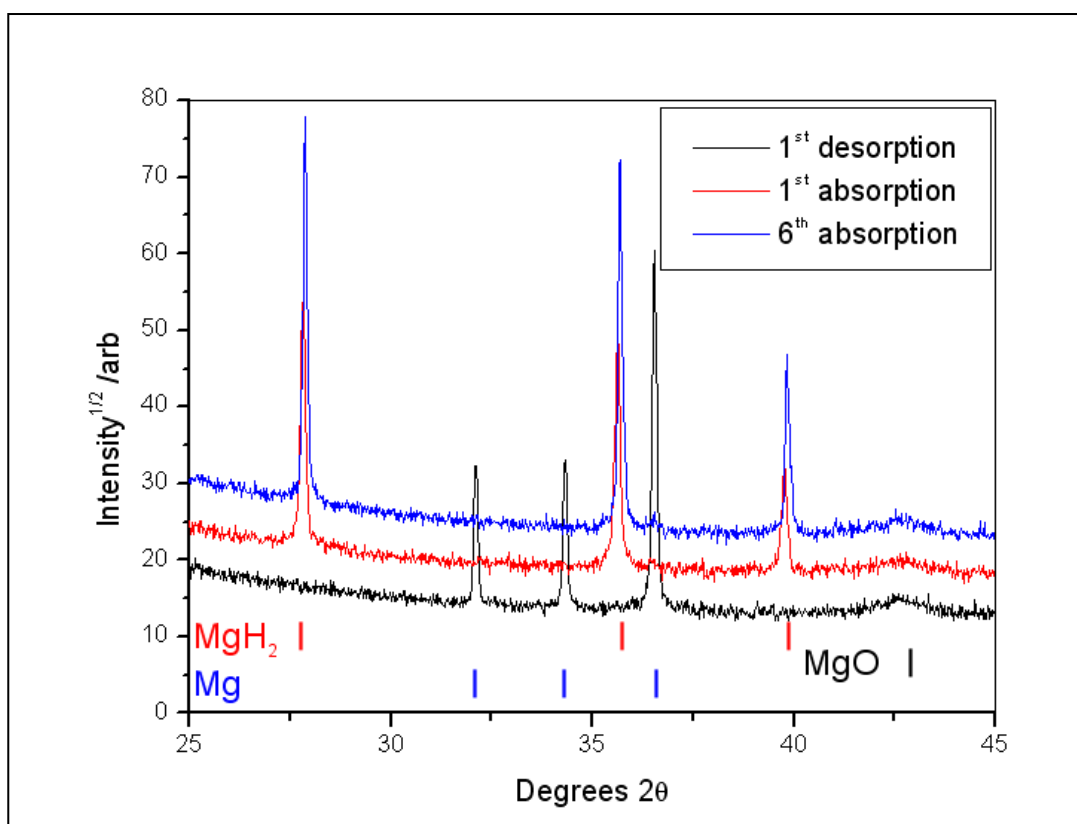
Figure 4.1.9 : Powder X-ray diffraction patterns showing the Mg and MgH₂ phases after desorption and absorption steps for MgH₂ milled for 5 hours

5 hr Milled MgH₂	FWHM (° 2θ)	Grain size (nm)
Un-cycled	0.252(±0.01)	60(±2)
1st absorption	0.106(±0.01)	77(±2)
2nd absorption	0.108(±0.01)	75(±2)
6th absorption	0.097(±0.01)	84(±2)

Table 4.1.1 : Full width at half the maximum peak height values for the first reflection of MgH₂ milled for 5 hours and cycled on the IGA with associate grain size as determined from the Scherrer equation

Figure 4.1.10 shows SEM images for MgH₂ milled for 5 hours before and after hydrogen

cycling. The average particle size after cycling the sample in a hydrogen environment had

decreased but the sample was still not homogenous, with a range of particle sizes (1 - 10 µm) present.
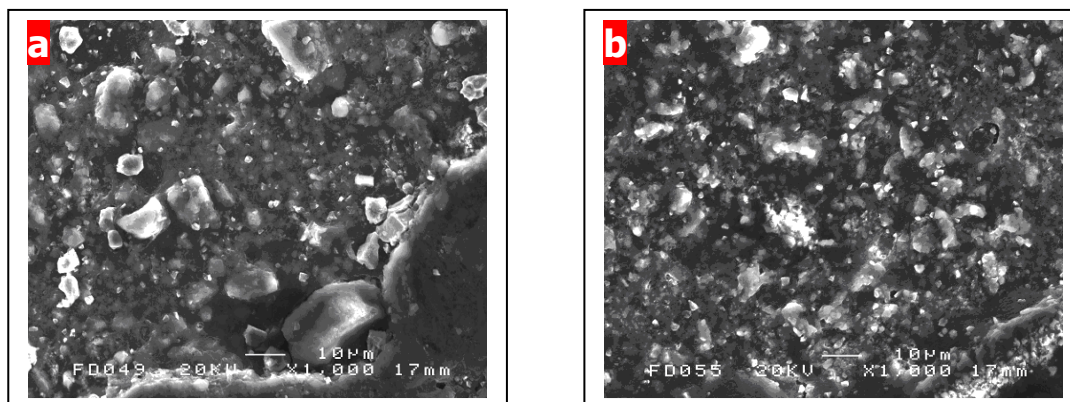
Figure 4.1.10 : SEM images showing the range of particle sizes in MgH$_2$ after (a) 5 hours milling and then (b) 6 cycles on the IGA at x1000 magnification

This agrees with the SEM images obtained for the unmilled material which show a slight decrease of particle size on cycling, though for the milled material the particles themselves remain fairly well defined in structure when compared to the large amount of 'furring' on the surface of each particle caused by decrepitation in the larger particles (30 – 110 µm) of unmilled MgH$_2$ observed in figure 4.1.3.

4.1 (c) Effect of milling time on hydrogen sorption kinetics

To determine the effect of increased milling time on the hydrogen sorption kinetics of magnesium hydride, samples of Aldrich MgH$_2$ were ball milled for 15 and 60 hours. Gravimetric measurements were performed to characterise the kinetic properties while SEM and XRD were used to analyse the particle and grain sizes.

Figure 4.1.11 shows the powder X-ray diffraction patterns for MgH$_2$ before milling and after the three different milling times. Increased milling time results in increased peak width for

each sample indicating a decrease in grain size, which is in agreement with observations from previous groups[2, 3].
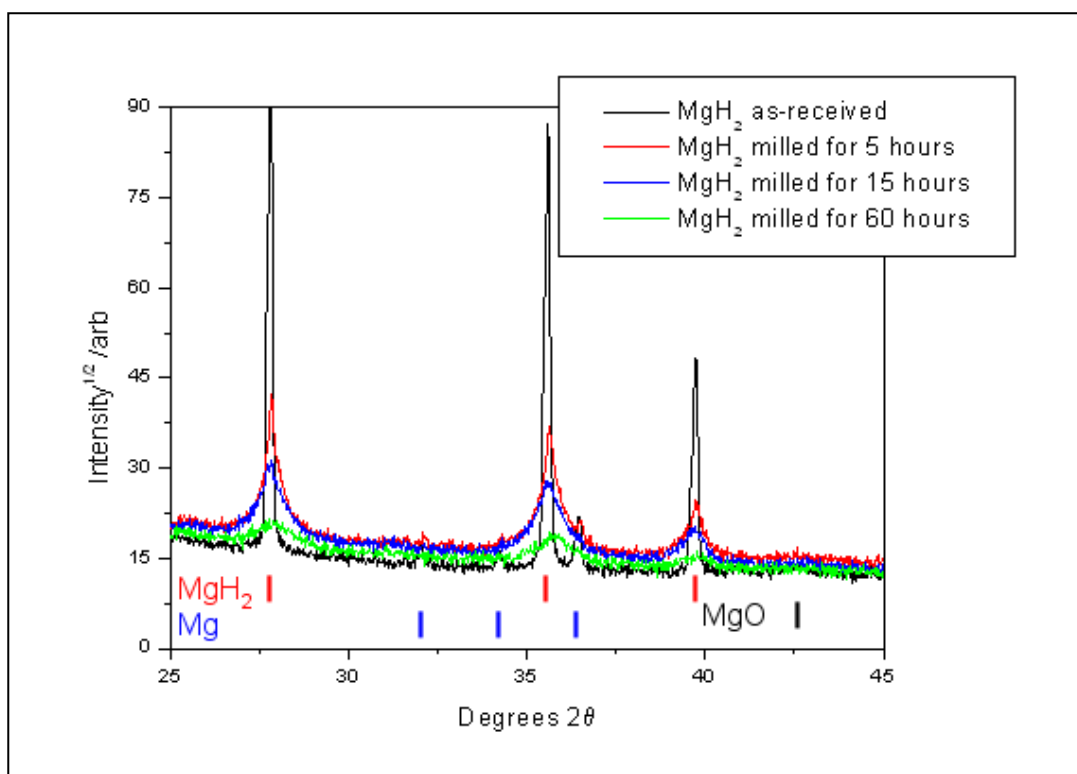
Figure 4.1.11 : Powder X-ray diffraction patterns comparing Aldrich MgH$_2$ milled for different lengths of time

Hours milled	Average grain size (nm)
0 (as-received)	125(±2)
5	41(±2)
15	13(±2)
60	10(±2)

Table 4.1.2 : MgH$_2$ grain size averaged over the peaks at 27.8, 35.6 and 39.72 and 54.59 2θ
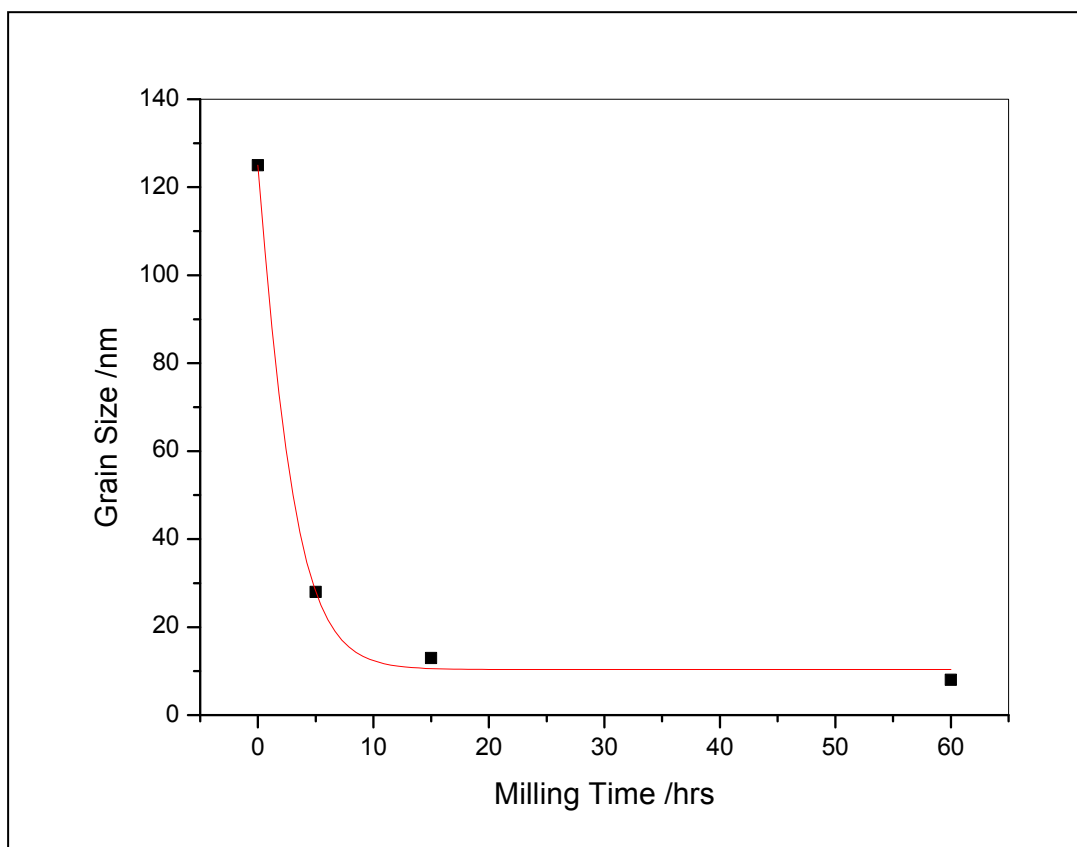
Figure 4.1.12 : Graph showing the relation between increased milling time and average grain size (data from Table 4.1.2)

Table 4.1.2 and Figure 4.1.12 show the effect of milling on the average grain size. While short periods of milling decrease the grain size considerably, with longer periods there is little further reduction in grain size. After 15 hours of milling the average grain size is similar to that found at 60 hours of milling and so would suggest that the optimum milling time is closer to 15 hours than 60.

Figure 4.1.13 displays SEM images for MgH_2 ball milled for 15 and 60 hours and the same samples after hydrogen cycling. The majority of particle sizes ranged from 0.5 – 7 μm for both the 15 and 60 hour milled samples however there are still particles up to 20 μm even after 60 hours though these larger particle sizes were more prevalent in the 15 hour milled sample.

After 6 dehydrogenations and hydrogenations the particle size for the 15 hour milled sample ranges from 0.5 - 6 μm. Particle formation is fairly discrete in comparison with the furred

surface of the cycled Aldrich sample with little growth on the surface of the particles. The 60 hour milled material displayed the same features but is more homogeneous in particle size with the majority of particles being less than 5 µm; the largest particles reached approximately 10 µm.
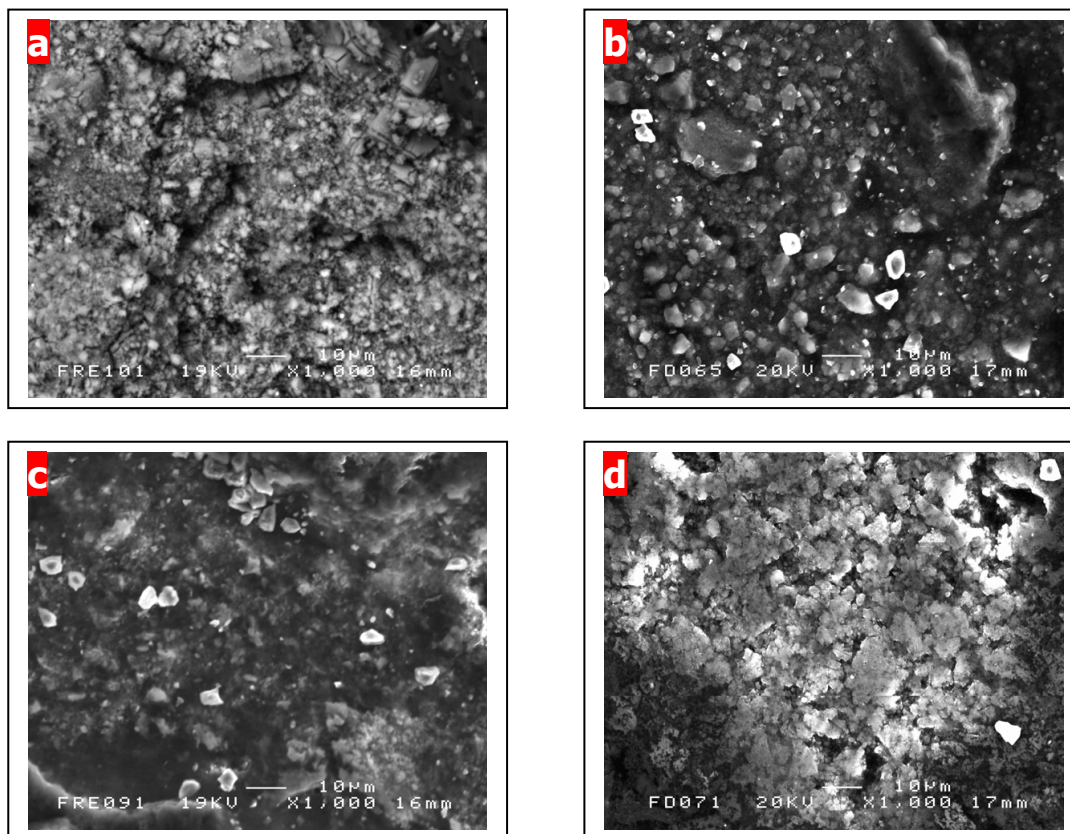
Figure 4.1.13 : SEM images showing the range of particle sizes in MgH$_2$: (a) after 15 hours milling, (b) after 60 hours milling (c) 15 hours milled after 6 cycles on the IGA and (d) 60 hours milled after 6 cycles on the IGA at 1000 times magnification

Gravimetric analysis was performed on the 15 and 60 hour milled samples. Similar results to the 5 hour milled material were obtained with quick uptake of hydrogen during absorption measurements but with little improvement with successive hydrogen cycling.

Figure 4.1.14 shows the absorption kinetics of the samples milled for 5, 15 and 60 hours on the 6th hydrogen absorption. Near the start of the traces the process of admitting gas at a high rate affected the buoyancy of the sample and therefore measurement of the true weight

of the sample, though, once enough gas had been admitted and convection was no longer a strong force acting on the sample holder, this effect was reduced at higher pressures. This resulted in slightly negative values for the weight at the very start of each absorption experiment. The data indicate that the kinetic barrier for reaction between magnesium and hydrogen is reduced upon increased milling time. The samples reached full absorption in 100, 40 and 30 minutes for 5, 15 and 60 hour milled samples respectively - 90% of each of those total absorptions was attained in 18, 15 and 10 minutes, respectively.
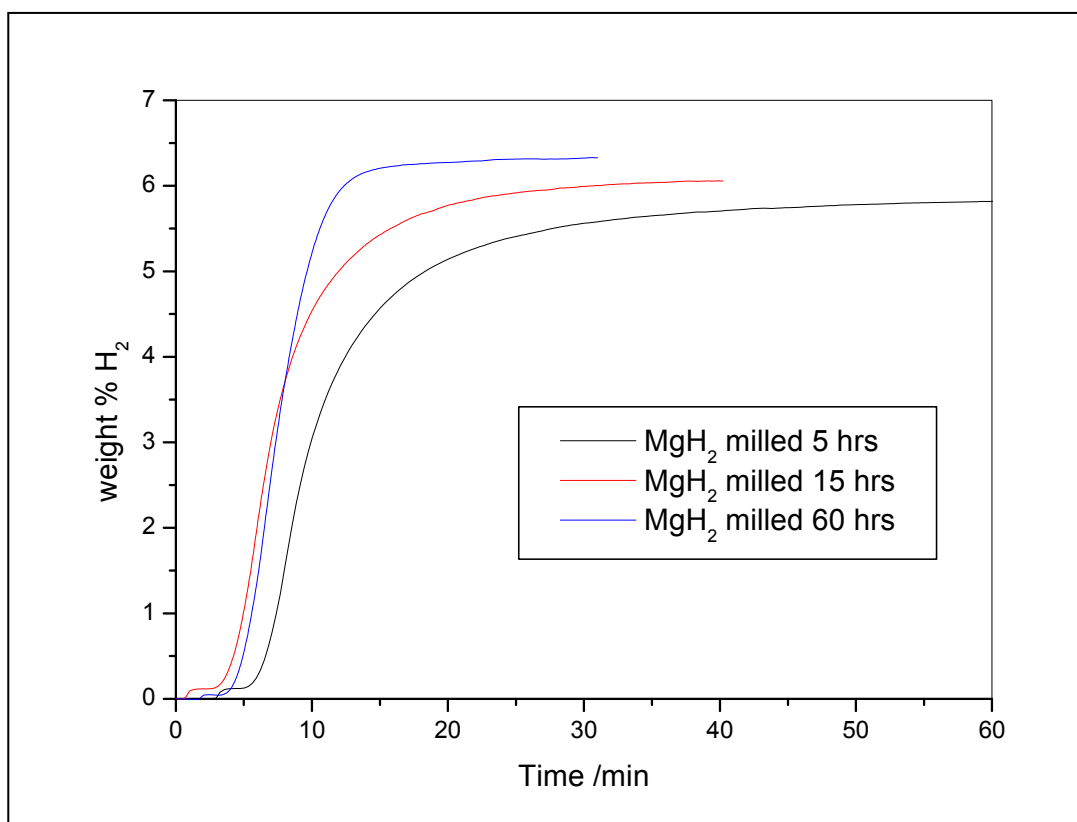
Figure 4.1.14 : Absorption kinetics for Aldrich MgH$_2$ samples after various milling times and after 6 hydrogen cycles on an IGA at 300°C

Figure 4.1.15 shows the desorption kinetics for the milled materials on the 6th hydrogen desorption measurement. Kinetics improved with increased milling time with full desorption reached in 790, 214 and 50 minutes for 5, 15 and 60 hour milled samples, respectively. The time to reach 90% of this desorption was 190, 143 and 37 minutes, respectively, for the three samples.

Interestingly, the desorption kinetics for the 60 hour milled sample were much improved when compared to the 5 and 15 hour milled samples and also in comparison to the relative improvement to absorption kinetics over six successive hydrogen cycles for these samples.
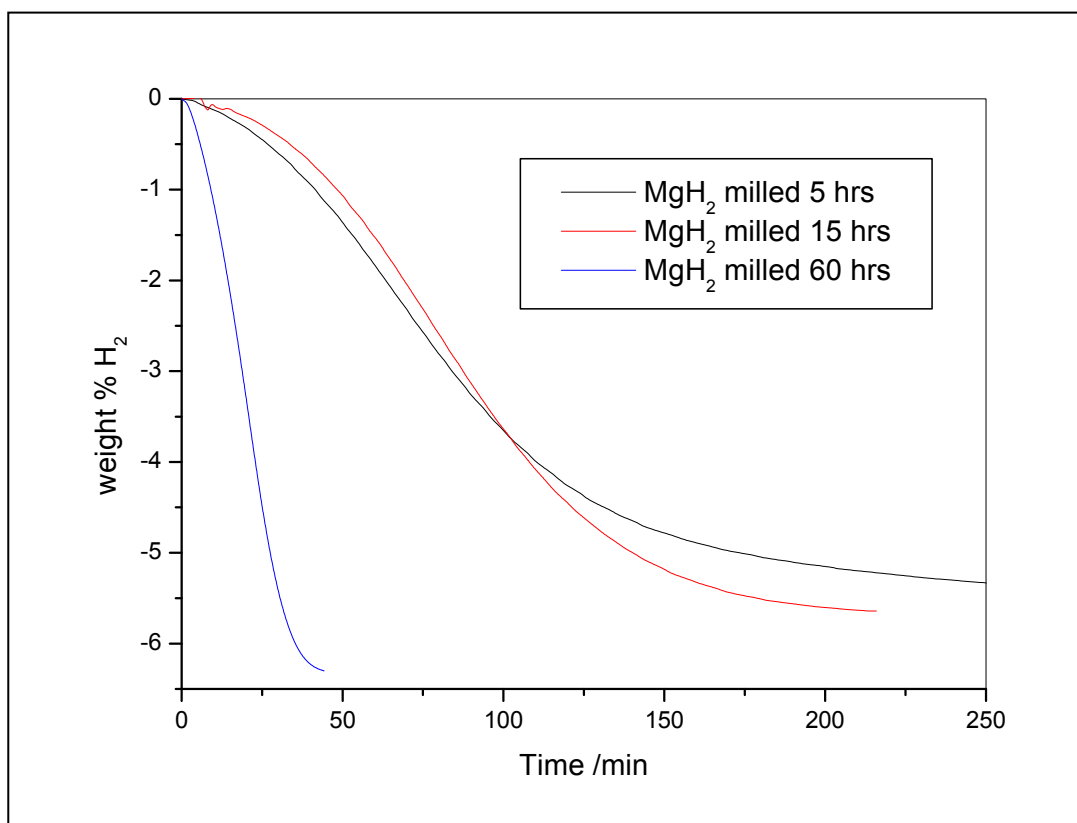
Figure 4.1.15 : Desorption kinetics for Aldrich MgH$_2$ samples after various milling times and after 6 hydrogen cycles on an IGA at 300°C

These results suggest that particle size has a large effect on hydrogen sorption kinetics. Although average grain sizes were similar for samples milled for 15 and 60 hours (Table 4.1.3), average particle size had been reduced for the 60 hours milled MgH$_2$ sample (Fig. 4.1.13). The observed improvement in desorption kinetics for the 60 hour milled material can be attributed to this change in morphology and as such it is possible to suggest that, with increased milling time and therefore grain and particle reduction, as the particle size approaches the grain size, diffusion of hydrogen occurs with comparative ease during the desorption process. The more comparable absorption times for all three milled samples could

be explained by seeding of crystal growth. If the magnesium grain boundaries that border the surface of a particle are hydrogenated first then diffusion of hydrogen through the MgH_2 phase into the core of a particle will be the limiting step.

It has previously been shown that the milling process itself introduces impurities from the milling tools. Ares et al. reported inclusion of Fe impurities in milled MgH_2 from steel milling tools during the milling process[4]. These impurities reached 1 wt% within 100 hours milling time and it was shown that the presence of these impurities facilitated particle agglomeration and cold-welding of the particles in the sample. These two processes hinder particle size reduction and the associated improvement in kinetics that comes with increased surface area. Fe impurities have been shown to reduce the total H_2 capacity of magnesium hydrides[5] and this could have an effect in the present study – though it is likely that any effect is very small as none of the observed capacities for samples that were milled longer were diminished in comparison with those samples milled for shorter times and the longest milling time was 60 hours at which point less than 1 wt% of Fe impurity would be predicted in the sample.

Table 4.1.3 shows the effect of hydrogen cycling on particle size in the as-received and milled samples of MgH_2. As observed in Table 4.1.1 there is grain growth occurring during hydriding and dehydriding process. Interestingly, there appears to be less grain growth in the milled samples than in as-received MgH_2 suggesting that the microstructure gained from the mechanical milling process is retained to a degree.

	Average grain size (nm) (±2)	
	Before H_2 cycling	After 6 H_2 cycles
MgH_2 as-received	125	357
MgH_2 milled 5 hrs	41	89
MgH_2 milled 15 hrs	13	83
MgH_2 milled 60 hrs	10	N/A

Table 4.1.3 : MgH_2 grain size averaged over the peaks at 27.8, 35.6 and 39.72 and 54.59 2θ for samples before and after H_2 cycling on an IGA (data for the 60 hr milled sample was not obtained)

	Range of particle size (µm)	
	Before H$_2$ cycling	After 6 H$_2$ cycles
MgH$_2$ as-received	50-100	30-110
MgH$_2$ milled 5 hrs	1-30	1-10
MgH$_2$ milled 15 hrs	0.5-7	0.5-6
MgH$_2$ milled 60 hrs	0.5-7	<5

Table 4.1.4 : Observed range of majority MgH$_2$ particle sizes for samples before and after H$_2$ cycling on an IGA as observed via SEM

Paik et al. studied the effects of milling on MgH$_2$ particle and grain size and reported that, while use of the Scherrer equation could yield approximations of the trends in grain size it is not accurate for larger grain sizes (>200nm), electron microscopy techniques are more accurate at determining grain size[6]. It was also shown that, because the Scherrer equation does not take into account the effect of strain within the material, the techniques utilising XRD to determine grain size will underestimate the actual size distribution of grains within the sample.

Paik et al.'s findings mirror the trends seen in the results reported in this study and others[7-9]; a sharp decrease in grain and particle size within a few hours of milling time followed by a levelling-off in the reduction of the two parameters towards 30 hours of milling. However, they report a further reduction towards 60 hours of milling time – roughly half that of the grain size at 30 hours and approximately 200nm reduction for particle size over the same period. The effect of hydrogen cycling on MgH$_2$ and its milled forms' particle and grain sizes was also reported, with grain growth on the first H$_2$ cycle resulting in similar grain size for MgH$_2$ for all milled powders that were analysed, which is in broad agreement with the results in table 4.1.3.

1.   Grochala W. and Edwards P.P., *Thermal Decomposition of the Non-Interstitial Hydrides for the Storage and Production of Hydrogen.* Chem. Rev., 2004. **104**: p. 1283.

2.   Huot J., Liang G., Boily S., Van Neste A., and Schulz R., *Structural study and hydrogen sorption kinetics of ball-milled magnesium hydride.* J. Alloy Compd., 1999. **293-205**: p. 495.

3.   Varin R.A., Czujko T., Chiu Ch., and Wronski Z., *Particle size effects on the desorption properties of nanostructured magnesium dihydride (MgH$_2$) synthesized by controlled reactive mechanical milling (CRMM).* J. Alloy Compd., 2006. **424**(1-2): p. 356.

4.   Ares J.R., Aguey-Zinsou K.-F., Klassen T., and Bormann R., *Influence of impurities on the milling process of MgH$_2$.* J. Alloy Compd., 2007. **434-435**: p. 729.

5.   Huang Z.G., Guo Z.P., Calka A., Wexler D., Lukey C., and Liu H.K., *Effects of iron oxide (Fe$_2$O$_3$, Fe$_3$O$_4$) on hydrogen storage properties of Mg-based composites.* J. Alloy. Compd., 2006. **422**(1-2): p. 299.

6.   Paik B., Jones I.P., Walton A., Mann V., Book D., and Harris I.R., *Evolution of microstructure in MgH$_2$ powder particles during high energy ball milling and hydrogen cycling.* Journal of Alloys and Compounds, 2010. **492**: p. 515.

7.   Varin R.A., Czujko T., and Wronski Z., *Particle size, grain size and γ-MgH$_2$ effects on the desorption properties of nanocrystalline commercial magnesium hydride processed by controlled mechanical milling.* Nanotechnology, 2006. **17**: p. 3856.

8.   Varin R.A., Czujko T., Chiu Ch., and Wronski Z., *Particle size effects on the desorption properties of nanostructured magnesium dihydride (MgH$_2$) synthesized by controlled reactive mechanical milling (CRMM).* J. Alloy. Compd., 2006. **424**(1-2): p. 356.

9.   Hanada N., Ichikawa T., Orimo S., and Fujii H., *Correlation between hydrogen storage properties and structural characteristics in mechanically milled magnesium hydride MgH$_2$.* J. Alloy. Compd., 2004. **366**(1-2): p. 269.

4.2 Sorption properties of MgH$_2$ + LiBH$_4$

Experimental technique 4.2

Sample preparation and heating under static vacuum

Magnesium hydride (Aldrich, 90% MgH$_2$, 10% Mg) was mixed together by hand with an agate mortar and pestle with LiBH$_4$ (Acros Organics, 95%) in an argon-circulating glove box for 5 minutes until a fine powder remained. The ground mixture was carefully inserted into a quartz tube of approximately 10 mm internal diameter and typically 200 mm in length which had a piece of clean (and evacuated to remove physisorbed water and oxygen molecules) printer paper rolled around the length to avoid the sample sticking to the inside of tube and reacting when sealed, potentially breaking the tube. Once the paper was removed the tube was fitted to a Young's tap via a Swagelok Ultra-Torr fitting with rubber seals to stop mixing with atmosphere when removed from the glove box (Figure 3.1.1). The assembly was then attached to vacuum equipment which allowed careful evacuation to pressures of approximately 1 x 10^{-6} bar near the sample.

Once the required vacuum level was achieved, the assembly was removed from the vacuum equipment and sealed off with a gas torch and this sealed tube containing the sample was placed in a programmable muffle furnace and heated up to 300°C at a ramp rate of 50°C/hour. The sample was then held at 300°C for 12 hours and then allowed to cool back down to room temperature. The quartz tube was then returned to the glove box where it was split open with glass cutting tools and the sample was ground again in a mortar and pestle and then placed in a storage vial.

The quartz tube was observed to be discoloured by reaction with the liquid LiBH$_4$ at temperatures above the melting point, Mg and MgH$_2$ had a minimal effect on the quartz tube after heating. The length of time, reagents and the ratio of reactants was altered as seen fit. A typical sample would weigh approximately 0.33 g. Due to the equilibrium pressure of MgH$_2$ being approximately 1 bar H$_2$ at 300°C the reaction between MgH$_2$ and LiBH$_4$ would have taken place under a hydrogen environment from H$_2$ desorbed from both compounds.

Heating in flowing gas environment

Magnesium hydride (MgH_2 - 90%, 10% Mg) and lithium borohydride ($LiBH_4$, Acros Organics, 95%) were measured out in the required amounts, mixed together and placed in a quartz tube, as above. The quartz tube was then fitted with a Swagelok Ultra-Torr fitting to which was connected a specialised piece of glassware consisting of two rotating taps sealed with vacuum grease (Figure 3.1.1). This apparatus was closed off and then removed from the glove box and placed into a fume cupboard - held in a horizontal position via a clamp stand.

The valve on the cylinder containing the gas supply to be used was opened slightly and the system was purged for a minute to reduce the possibility of unwanted reactions of atmosphere with the sample. A plastic tube, connected to an acid bubbler (to scrub the gas of any unwanted impurities) which was, in turn, connected to the desired gas supply, was attached to one of the glass taps on the apparatus. A slight positive pressure of gas was allowed to build up in the tube as a second, exhaust tube that fed into a second acid bubbler which then vented into the fume cupboard system, was attached to the other tap. The exhaust tap was opened simultaneously with the admittance tap in order for the gas flow to begin immediately in order to limit the amount of oxygen and moisture entering the quartz tube. The gas flow was increased to a steady rate for 5 minutes to purge the apparatus of any except the desired gas(es). The flow rate was then reduced and the sample slotted into the hot zone of a tube furnace.

The tube furnace was programmed in the same manner as the muffle furnace and a heating rate of 50°C/hour was used to raise the temperature to the desired setting. Once the reaction was complete and the sample had cooled sufficiently, the quartz tube was removed from the tube furnace and the exhaust gas tap on the apparatus closed before stopping the flow of the gas from the cylinder. A slight positive pressure was allowed to build before the inlet tap was also closed. The apparatus was removed from the clamp and plastic tubing and returned to the glove box for sample recovery. Gases of Argon (99%) and H_2/N_2 (10:90, 98%) from BOC were used.

Aluminium foil

The preparation of the sample was carried out as above however, once ground in a mortar and pestle the sample was then transferred onto a thin sheet of aluminium foil that was then folded into a packet around the sample to stop it reacting with the quartz tube. The sample was then sealed in an evacuated quartz tube as above and heated in a muffle furnace. Once the aluminium packet was recovered from the quartz tube after heating the sample was separated from it and stored in the glove box. The aluminium foil was observed to be blackened by reaction with the $LiBH_4$ during heat treatment.

Synchrotron X-ray experiments

The equipment used was at the European Synchrotron Radiation Facility in Grenoble, France. The beamline was ID31 and its operation is outlined more thoroughly in section 3.5.2.

The samples to be measured were ground and loaded into glass capillaries within a glove bag or glove box containing argon and then sealed with wax or vacuum grease. These capillaries were then mounted onto a multi-sample loading stage that was placed on the automatic robot sample changer. The samples were the measured across a range of 2θ – usually from $3\text{-}100°$ 2θ though some samples were measured from $3\text{-}60°$ 2θ due to limited equipment time. The wavelengths of the beamline changed over multiple visits, however all samples were wavelength corrected and have been displayed at a wavelength of 1.5406 Å for direct comparison with powder diffraction patterns obtained from the D5000. The step size used for the measurements was $0.00499°$ 2θ and the averaged step time was 3 seconds per step.

General experimental techniques

The milling procedure of MgH_2 + $LiBH_4$ was performed as described for MgH_2 in section 3.1.2. Milling times of 10 and 40 hours were performed. XRD on the D5000, IGA and SEM measurements and wt% calculations were performed as described in the Experimental Technique 4.1 section.

4.2 (a) Chemical Modification

It has been established that MgH_2 has slow kinetics unless mechanically modified and also suffers from a high heat of formation. However, there have been many attempts to reduce the heat of formation of the hydride through alloying[1, 2] or provide a catalytic pathway to reduce the onset temperature of formation of the hydrided and dehydrided phases[3-6] via introduction of chemical additives to improve the sorption kinetics by improving H_2 diffusion and splitting of molecular H_2. This area of research is dominated by studies that introduce new additives through mechanical milling – there are relatively few studies that chemically react two or more compounds. While the energies involved in mechanical milling can facilitate chemical reaction, the results are not always analogous to a thermal reaction between the same materials, therefore it is important that conventional chemical routes are explored as well.

The targets set by governments for a storage medium and discussed in section 1 (e.g. D.O.E. in the US) led us investigate the combination of light elements or their compounds with MgH_2. Hydrides, and specifically light element borohydrides, were attractive additives due to their relatively light weight and high percentage of hydrogen. Lithium was immediately selected as a potentially beneficial dopant due to its known alloying properties with magnesium[7, 8]. Out of the prospective Li and H containing compounds (covered in section 2.3.3) $LiBH_4$ was selected due to its high weight% H_2 content and similar dissociation temperature to MgH_2.

$LiBH_4$ (Acros Organics 95%) was heated with MgH_2 (Aldrich 90%) in the ratio of 1:10, as described in the experimental section, at 300°C in static vacuum (1×10^{-6} bar) for 12 hours; heated (MgH_2 + 10% $LiBH_4$). When mixing the reactants it was noted that the MgH_2 exhibited static-like properties and stuck to particles of $LiBH_4$ and formed small balls within the test tube. It was also noted that after reaction in the furnace, the quartz tube was stained an off-

orange colour which was attributed to reaction of LiBH$_4$ with the glass after studying the effect of both MgH$_2$ and LiBH$_4$ on quartz.

Powder XRD analysis of the reacted sample detected no LiBH$_4$ (Figure 4.2.1) in contrast to mixed/ground and unreacted samples in which LiBH$_4$ was clearly observed. This could point towards partial incorporation of the LiBH$_4$ into the Mg or MgH$_2$ lattice or possibly the phase becoming amorphous due to the heat treatment and subsequent melting at 300°C.
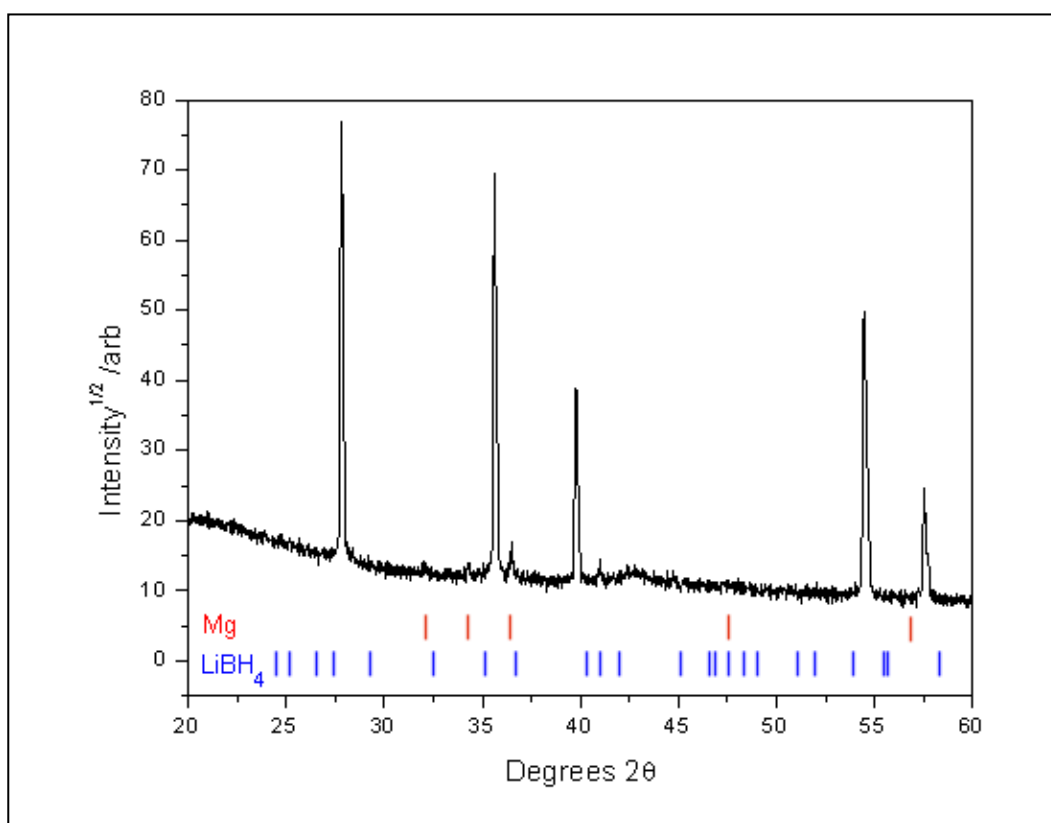

Figure 4.2.1 : Powder XRD trace showing Aldrich MgH$_2$ + 10% LiBH$_4$, after heat treatment at 300°C under static vacuum

The kinetics of hydriding and dehydriding were then measured on an IGA: desorption kinetics (Figure 4.2.2) were vastly improved over the original, as-received MgH$_2$ material shown in section 4.1. It was not possible to desorb the sample at 300°C initially and the first desorption was carried out at 350°C which resulted in complete desorption in under 150 minutes. The rest of the desorption steps were carried out at 300°C and, remarkably, shared similar times to desorb. As with the as-received material the kinetics were again improved

131

slightly through cycling, though some variation for the final total H_2 capacity and time to completion for this capacity was noted from cycle to cycle.
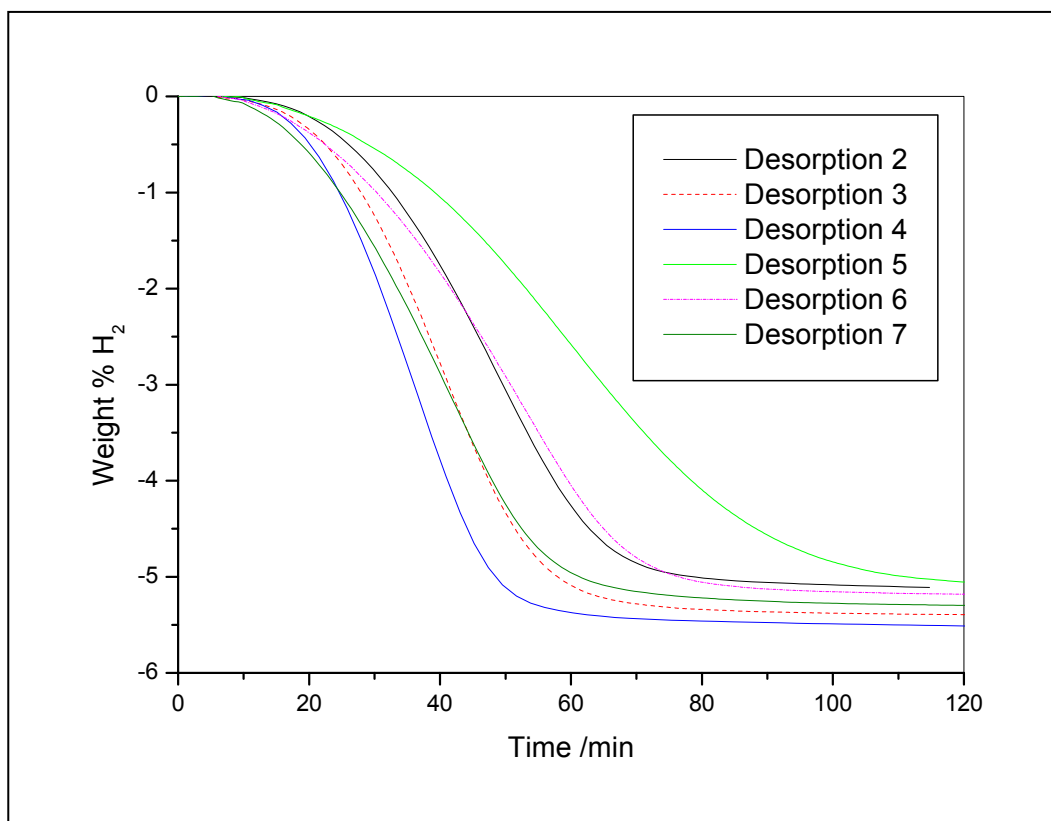
Figure 4.2.2 : Kinetic traces showing desorption characteristics of MgH$_2$ + 10% LiBH$_4$, at 300°C, 10 mbar performed on an IGA

Absorption kinetics for the heated (MgH$_2$ + 10% LiBH$_4$) sample were slow to begin with (Figure 4.2.3) as the initial hydrogenation took 1300 minutes to near completion but had not reached a steady state. The improvement over subsequent absorption cycles was substantial, with the sample reaching saturation in 225 minutes in the second and around 80 minutes in the final absorption. This was in stark contrast to results from the as-received MgH$_2$ material where absorption kinetics became slower on cycling though a more consistent hydrogenation time between 600 and 1000 minutes was observed for all cycles.

The total weight % absorbed for each cycle of heated (MgH$_2$ + 10% LiBH$_4$)varied slightly depending on the previous desorption step, the first gaining 5.2 wt% and the 6th about 5.6 wt% H$_2$, which is comparable with the end points for the as-received MgH$_2$ sample.
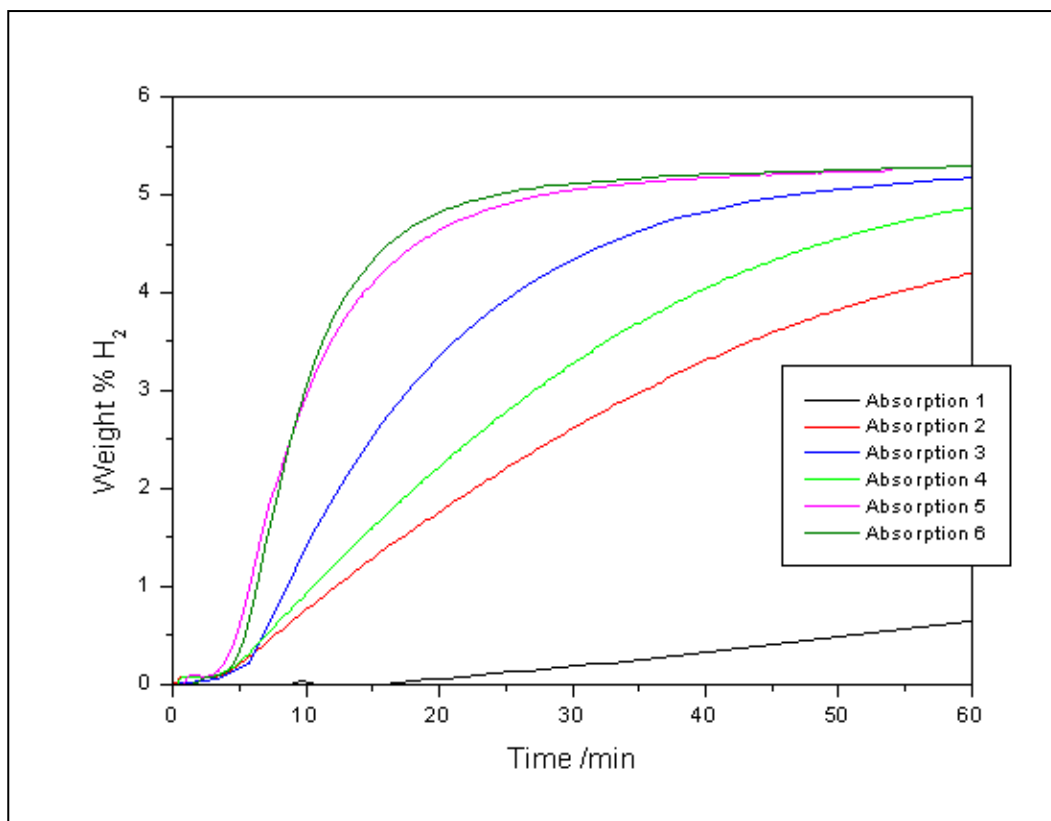
Figure 4.2.3 : Kinetic traces showing absorption characteristics of MgH$_2$ + 10% LiBH$_4$, at 300°C, 10 bar performed on an IGA

Figures 4.2.4 and 4.2.5 compare the absorption kinetics for MgH$_2$, heated (MgH$_2$ + 10% LiBH$_4$) and milled material. These show that although the initial absorption step is much slower than MgH$_2$ material, by the sixth cycle the MgH$_2$ + LiBH$_4$ sample was comparable with the material that had been milled for 5 hours and much quicker than the MgH$_2$ sample, albeit with a slightly lower weight percent capacity for hydrogen. The graph is not corrected for LiBH$_4$ content since the remaining amount and form of this compound is unknown. Possible reasons for the slow kinetics on the first absorption will be discussed in chapter 5.

Desorption kinetics are also interesting: all samples were initially desorbed at 350°C, though as certain samples were desorbed at 10 mbar and others at 1 bar, these are not directly comparable. The second desorption sample conditions were much more consistent and thus these have been used for comparison with the sixth desorption (Figures 4.2.6 and 4.2.7).
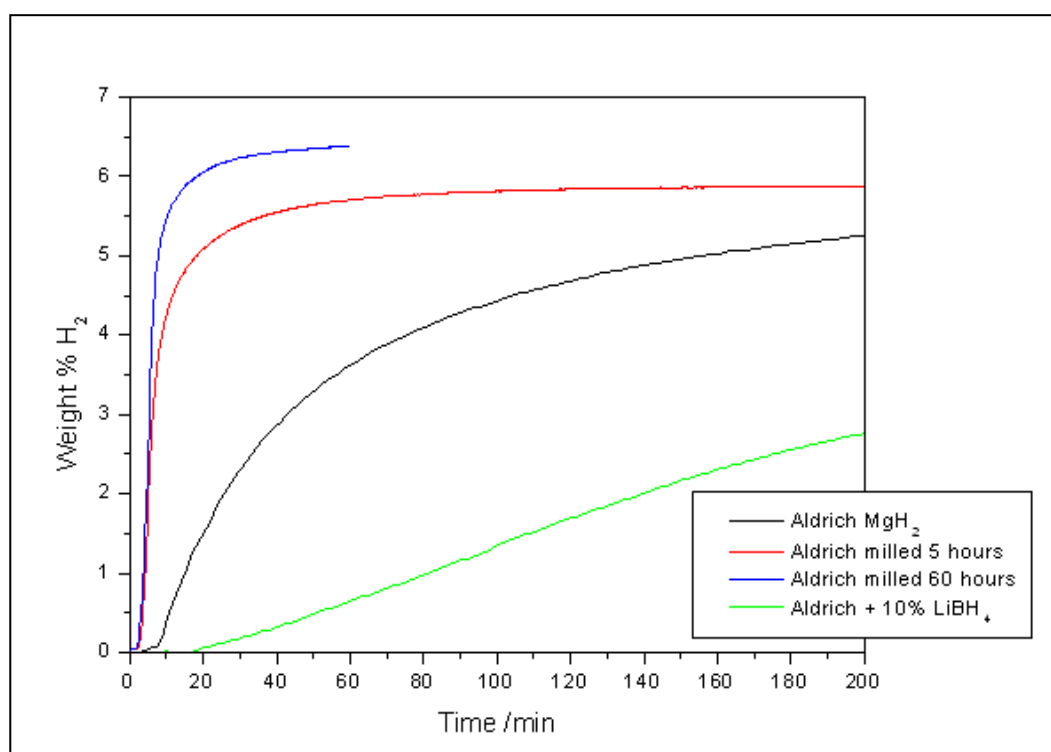
Figure 4.2.4 : Kinetic traces comparing the 1st absorptions at 300°C of samples after three different types of treatment
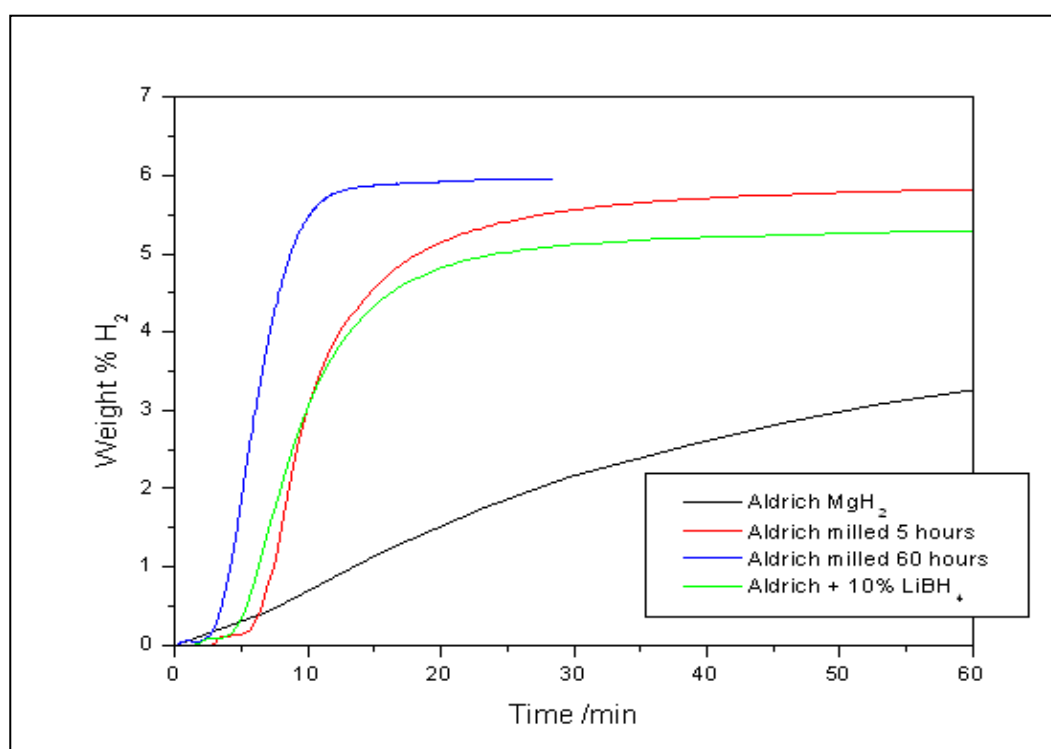
Figure 4.2.5 : Kinetic traces comparing the 6th absorptions at 300°C of samples after three different types of treatment
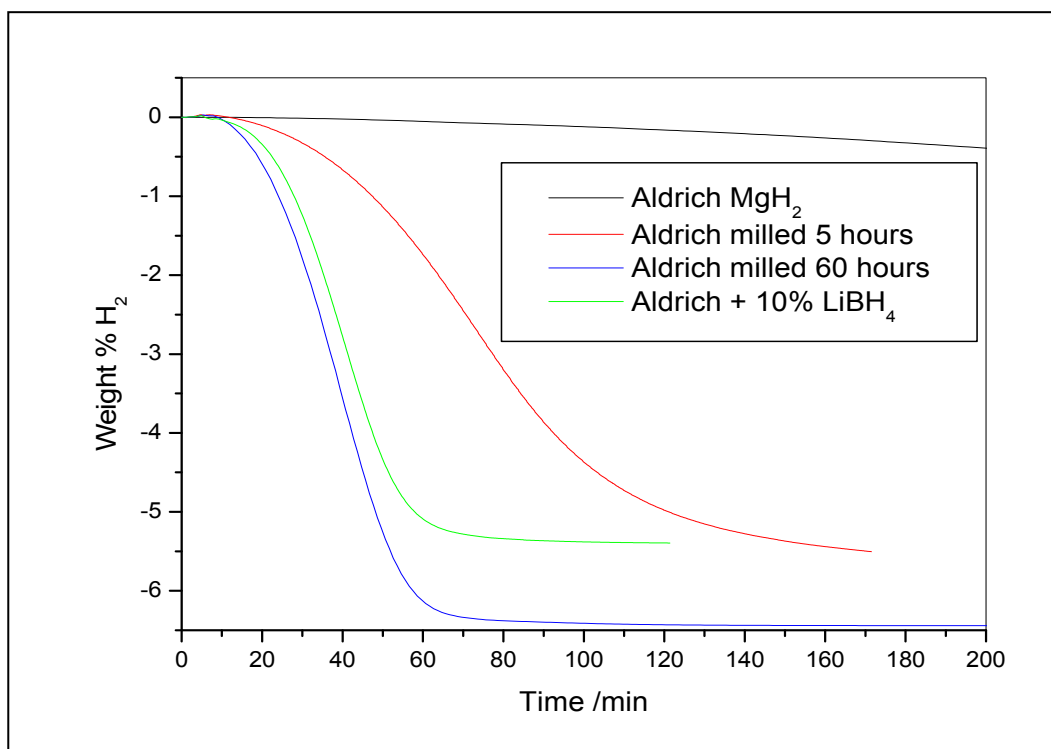
Figure 4.2.6 : Kinetic traces comparing the 2nd desorptions at 300°C of samples after three different types of treatment
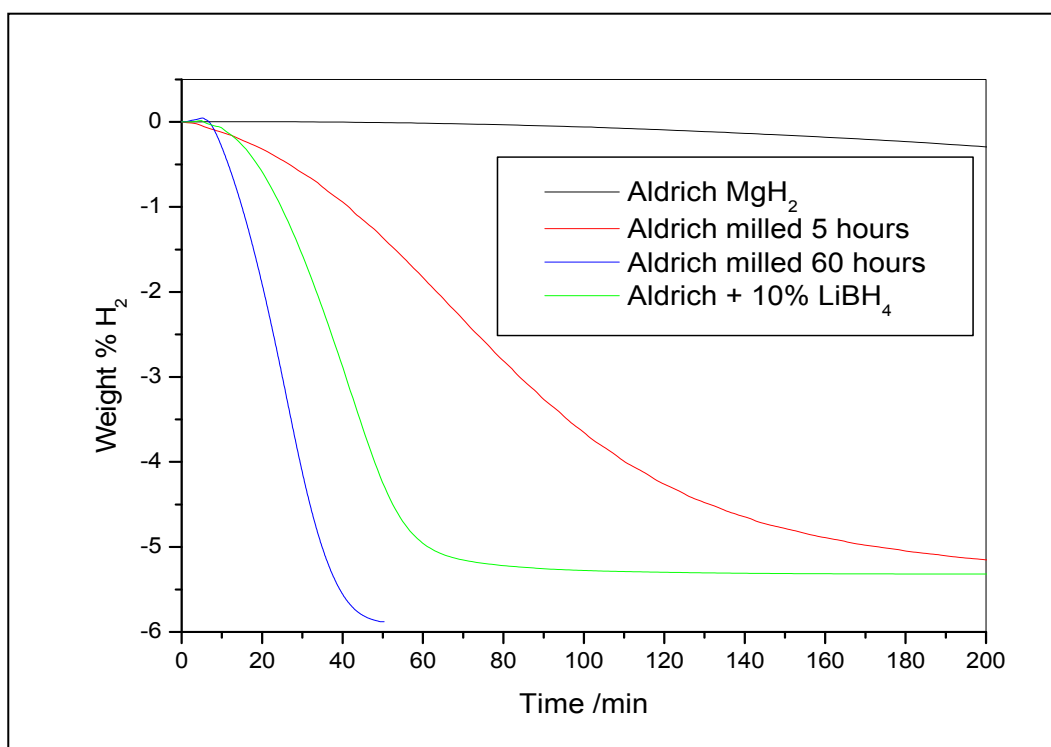
Figure 4.2.7 : Kinetic traces comparing the 6th desorptions at 300°C of samples after three different types of treatment

Although Aldrich MgH_2 desorption kinetics improve significantly with cycling, the milled MgH_2 and $LiBH_4$ doped materials do not show the same trend. Instead, a slight variation was observed for the total desorption time over each cycle. While the completion of the last 10% of H_2 capacity varies widely for each cycle of a sample the main change per desorption (i.e. 90% of H_2 capacity) lies within a much narrower range and is perhaps a better indicator of the actual improvements in kinetics of a sample as this would ignore much of the effect of poor H_2 diffusion through hydride layers of >50 nm[9] (Table 4.2.1).

	Time to 90% completion /mins	
2nd cycle	Desorption	Absorption
Aldrich	847	n/a
MgH_2 + 10% $LiBH_4$	54	84
MgH_2 milled 5 hours	195	23
MgH_2 milled 60 hours	57	12
6th cycle		
Aldrich	738	170
MgH_2 + 10% $LiBH_4$	56	24
MgH_2 milled 5 hours	189	23
MgH_2 milled 60 hours	32	11

Table 4.2.1 : 90% completion times for absorption and desorption kinetics in the 2nd and 6th cycles at 300°C

It is possible that the observed variation for a particular sample could be partially attributed to particle or grain agglomeration, which would change over the course of cycling, with some cycles being slightly slower due to hydrogen diffusion becoming more difficult and others slightly faster, resulting in absorption and desorption of the majority of the hydrogen more quickly. Vigeholm et al. reported seeing increased particle agglomeration through sintering upon repeated H_2 cycles that resulted in increased porosity for a sample of MgH_2[10].

It could also result from poor hydrogen diffusion to the centre of larger particles due to the nucleation of the hydrided phase around the circumference of the particles (Figure 4.2.8). This behaviour featuring nucleation and growth of the MgH_2 phase and the resultant hinderance in hydrogenation is well understood in literature[9, 11]. It was observed that (at

constant temperature) upon increasing the hydrogen pressure above the equilibrium point for MgH$_2$ formation the total H$_2$ capacity was reduced and the kinetics of absorption varied greatly but in no general trend[10]. This might correlate with the observed variations in kinetics and H$_2$ uptake of each hydrogen cycle for individual samples measured on the IGA (Figure 4.1.8).

The effect of this mechanism on hydrogen absorption kinetics and capacity could easily be tested for a sample by repeating the experiments of Vigeholm et al.; selecting a temperature and then performing numerous hydrogenation measurements at increasing pressures from the equilibrium pressure. It was also reported by Vigeholm et al. that, at 300°C, pressures below 20 bar H$_2$ were required to reach complete hydrogenation for particles between 5–75 μm – above 20 bar incomplete hydrogenation was observed – and as such, measurements around and above this pressure would help elucidate any effect of this mechanism in the sample.
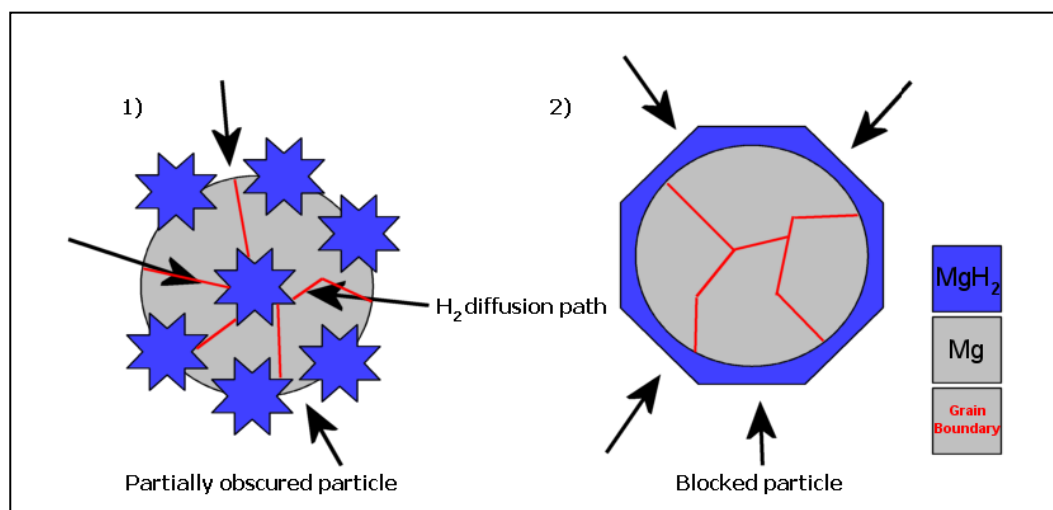
Figure 4.2.8 : Diagram depicting H$_2$ diffusion pathways into an magnesium particle: 1) Obscured diffusion, 2) Blocked diffusion

X-ray diffraction of heated (MgH$_2$ + 10% LiBH$_4$) after cycling on the IGA showed no evidence of LiBH$_4$, only MgH$_2$, Mg and MgO (Figure 4.2.9). The increased presence of magnesium oxide
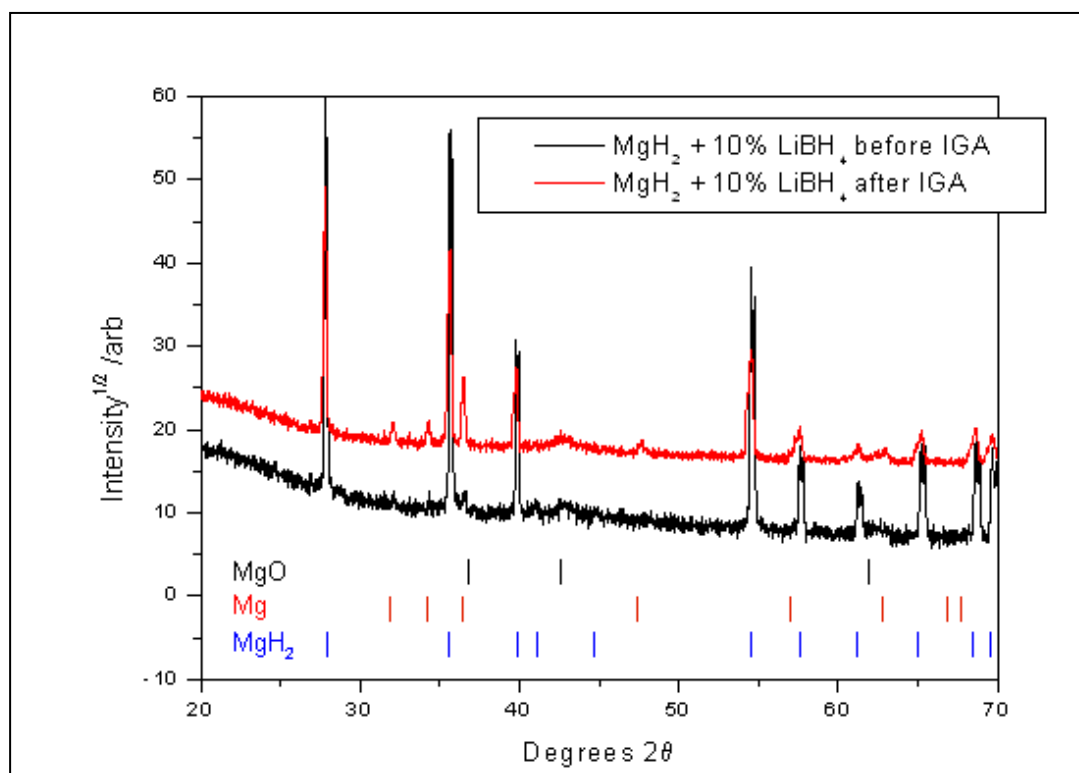
Figure 4.2.9 : Powder XRD traces comparing heated (MgH$_2$ + 10% LiBH$_4$) samples before and after 6 H$_2$ cycles on an IGA at 300°C, 10 mbar on desorption and 10 bar on absorption

was due in part to the loading and unloading procedure when using the IGA, both of which exposed the sample to air for short durations of time. Further contamination from any impurities in the hydrogen source during the experiments at 300°C could also have occurred.

SEM images taken before and after hydrogen treatment on an IGA showed interesting morphological changes (Figure 4.2.10). It can be seen that the particle shape and size after sample reaction but before hydrogen cycling was coarse and large. In comparison, after 6 cycles on the IGA (and in a hydrided state) the particle size and shape is much smaller: the structure has become finer and looks 'coral-like' in form. Undoubtedly, this morphological change has a strong effect on the sorption kinetics, facilitating hydrogen diffusion and crystal growth during hydrogenation. Vigeholm et al. observed similar structural evolution in unmilled MgH$_2$ over the course of 31 H$_2$ cycles and described it as a porous agglomerate[10]. It is

interesting that this structural refinement is more enhanced after 6 H_2 cycles for MgH_2 + 10% $LiBH_4$ than that of pure MgH_2 after 31 H_2 cycles and suggests that the interaction of $LiBH_4$ with MgH_2 promotes decrepitation on release of H_2 of each particle to form agglomerations of smaller particles with a higher surface area. This process is seen to occur for pure MgH_2 but over longer H_2 cycling periods[9] and is reported to have a greater effect on the H_2 absorption kinetics due to the diffusion of hydrogen being the rate-limiting step.
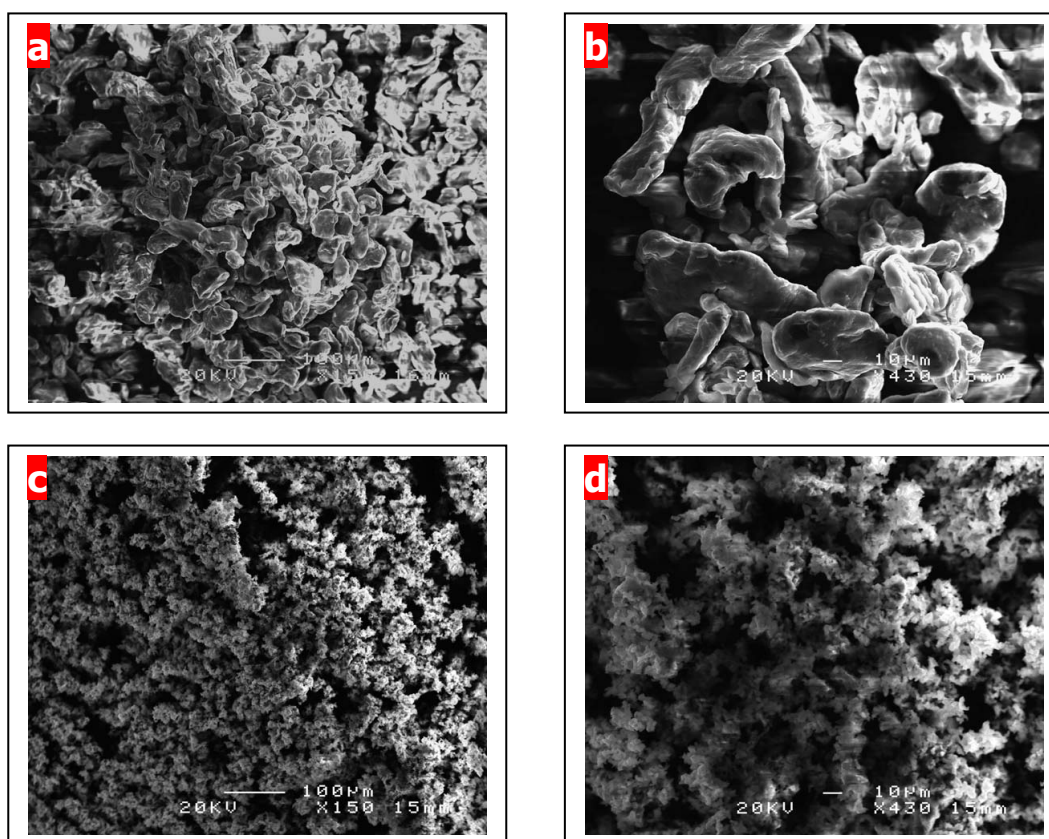
Figure 4.2.10 : SEM images of heated (MgH_2 + 10% $LiBH_4$) at 300°C, under static vacuum ($1x10^{-6}$ bar) at a) x150 and b) x430 magnification and heated (MgH_2 + 10% $LiBH_4$) after after 6 H_2 cycles on the IGA at c) x150 and d) x430 magnification

After observing the improvement when MgH_2 was heated with $LiBH_4$, it was decided to combine this method with milling to determine whether further improvements could be applied to milled MgH_2. Two different ways of combining the methods were tried: firstly, milled MgH_2 was heated with $LiBH_4$ at 300°C under static vacuum; secondly, a mixture of MgH_2 and $LiBH_4$ was milled for 10 and then 40 hours.

The 6th absorptions of these materials were compared with 60 hr milled MgH_2 (Figure 4.2.11) and showed that the addition of $LiBH_4$ to milled material did not appreciably improve the kinetics of the system as the results are comparable to milled samples. The sample of MgH_2 and $LiBH_4$ milled for 40 hours was slightly faster than the rest though it is difficult to determine whether this small improvement is due to a refinement of the microstructure as discussed in section 2.3.4. as $LiBH_4$ is a relatively soft compound[3].
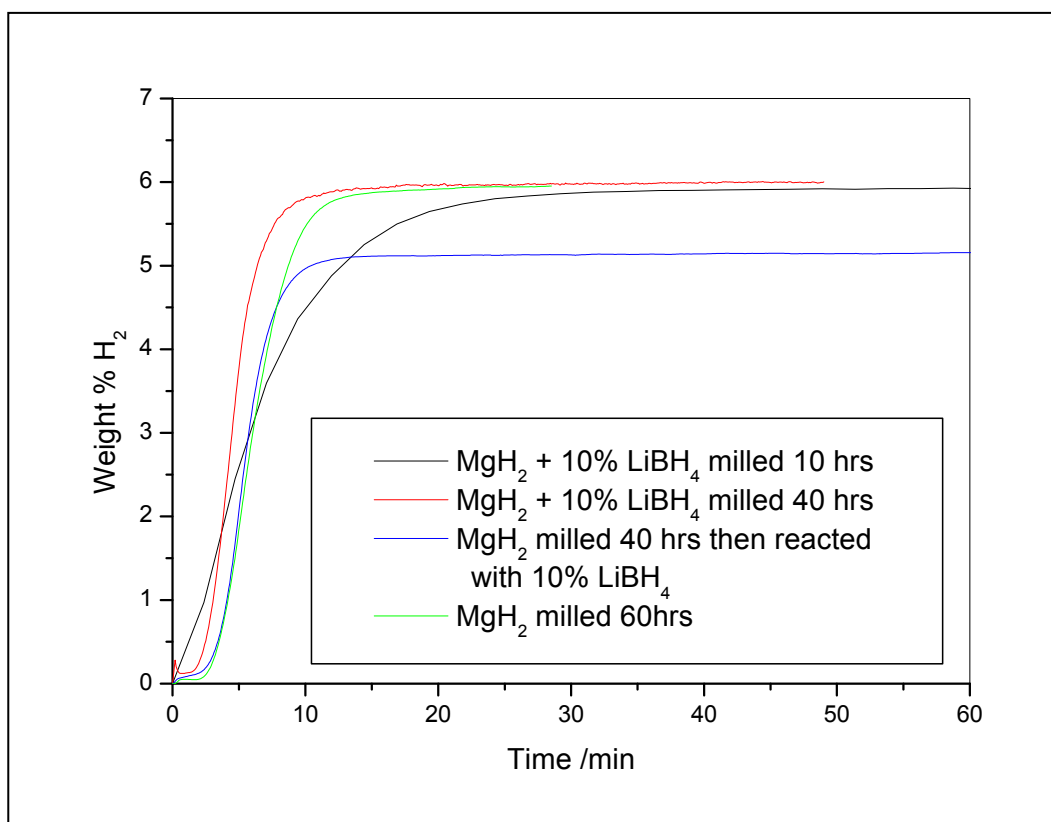
Figure 4.2.11 : Kinetic traces comparing the 6th absorption of various milled samples

4.2 (b) Reaction conditions

Reacting MgH_2 and $LiBH_4$ for 12 hours was shown to be beneficial to the kinetics of hydrogenation/dehydrogenation of the system. Therefore, it was decided to explore both

shorter and longer reaction times. Samples were heated for 6 and 60 hrs and then measured on an IGA.

After cycling 6 times, desorption kinetics showed a similar improvement (Figure 4.2.12), however, times to completion varied significantly. The 6 hour sample finished desorbing in around 500 minutes with the 12 and 60 hour samples completing in around 250 and 100 minutes, respectively. The 12 hour heated sample has a lower total weight percent due to being only partially hydrided on the previous absorption. Also, due to effects similar to those postulated in figure 4.2.8 the final 10% of H_2 capacity can vary between hydrogen cycles for
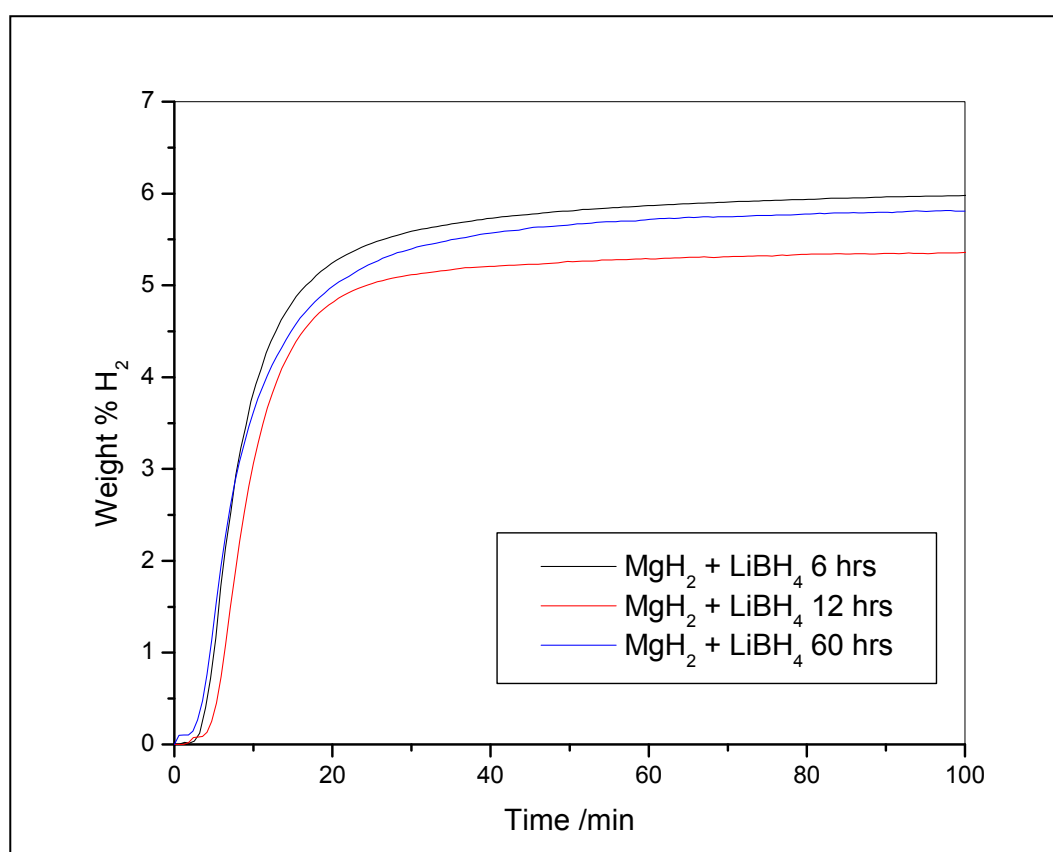

Figure 4.2.12 : Kinetic traces showing the 6th desorption performed on an IGA for heated (MgH$_2$ + 10% LiBH$_4$), heated for 6, 12 and 60 hours, respectively
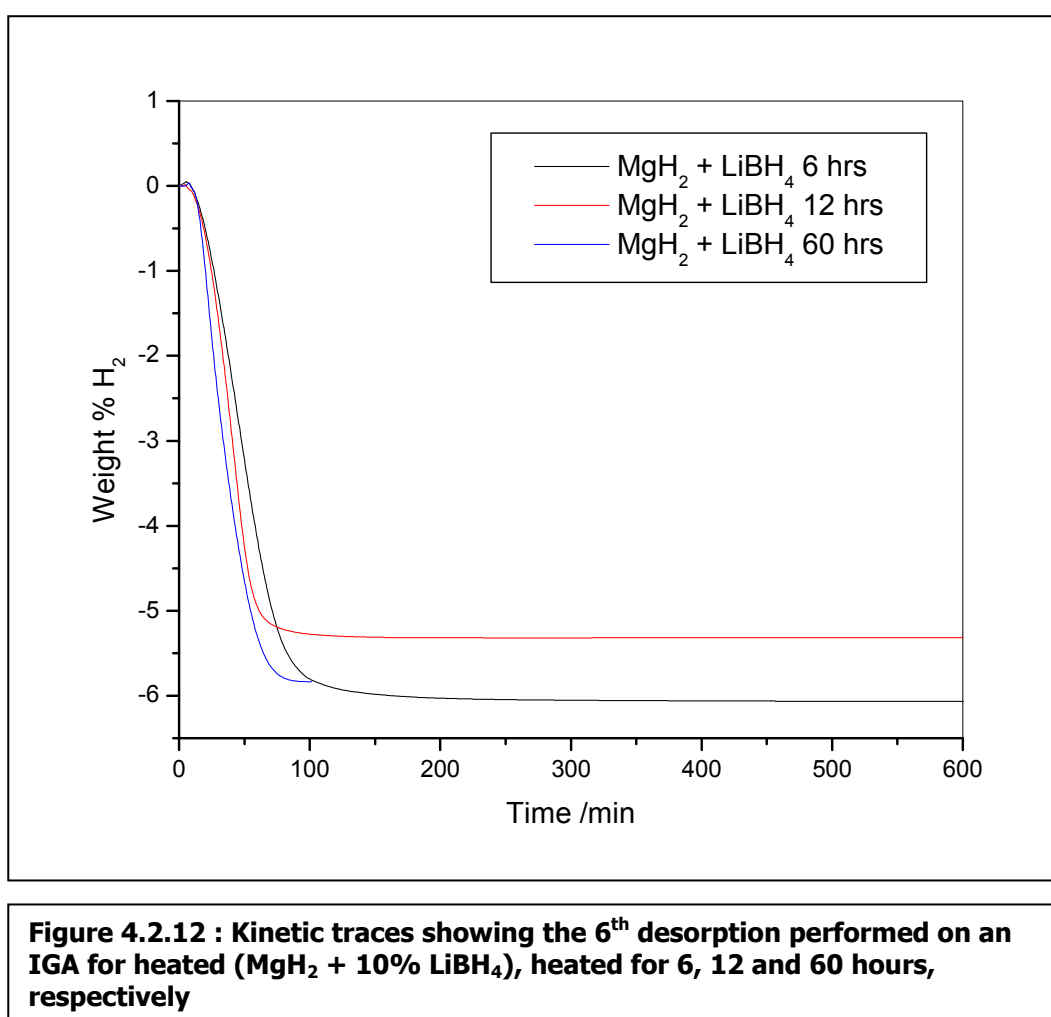
the same sample and between similar samples. To reduce this inaccuracy, times to reach 90% of estimated H_2 saturation are compared. Though these results would suggest that the effect occurring between MgH$_2$ and LiBH$_4$ is slow and happens over a long period of time, the times taken to desorb 90% of the total weight% loss were much closer: 81, 56 and 59

141

minutes for 6, 12 and 60 hrs, respectively. This potentially shows that the refinement of the microstructure caused by the interaction of MgH_2 and $LiBH_4$ is almost complete after 12 hours with further improvement of the remaining material bringing a diminishing increase in desorption kinetics.

Absorption kinetics were more similar for the three samples (Figure 4.2.13) though the end point of each absorption trace was more difficult to ascertain since the relative change in mass was very small over a long period of time after about 98% completion. The experimenter must ultimately decide at which point to stop the experiment.

Figure 4.2.13 : Kinetic traces showing the 6th absorption performed on an IGA for heated (MgH_2 + 10% $LiBH_4$) heated for 6, 12 and 60 hours respectively

All three had an end point of between 821 and 850 minutes which, considering the above observation on the difficulty of determining when the compound is saturated at a given pressure, are indistinguishable within the limits of error.

The point of 90% of total absorption was calculated and the 6, 12 and 60 hr samples all achieved 90% saturation at around 30 minutes: 31, 23 and 30 minutes, respectively. Although these results are not conclusive, it appears that reaction time may have a small effect on the performance of the sample. The 6 hour sample has slightly slower desorption kinetics, though this could be due to sample inconsistencies and variations in crystal growth during the Mg/MgH_2 phase transitions upon cycling in a hydrogen atmosphere.

Synchrotron powder XRD performed on the samples heated for different times showed no difference. However, synchrotron powder XRD showed evidence of an unknown phase in the sample heated for 6 hours, with four peaks at 21.3, 30.2, 31.6 and 33.91° 2θ that were not observed for the 12 and 60 hour heat-treated samples (Figure 4.2.14). One other aspect of XRD for the 6 hour heat-treated sample is that there is a decrease in intensity for all
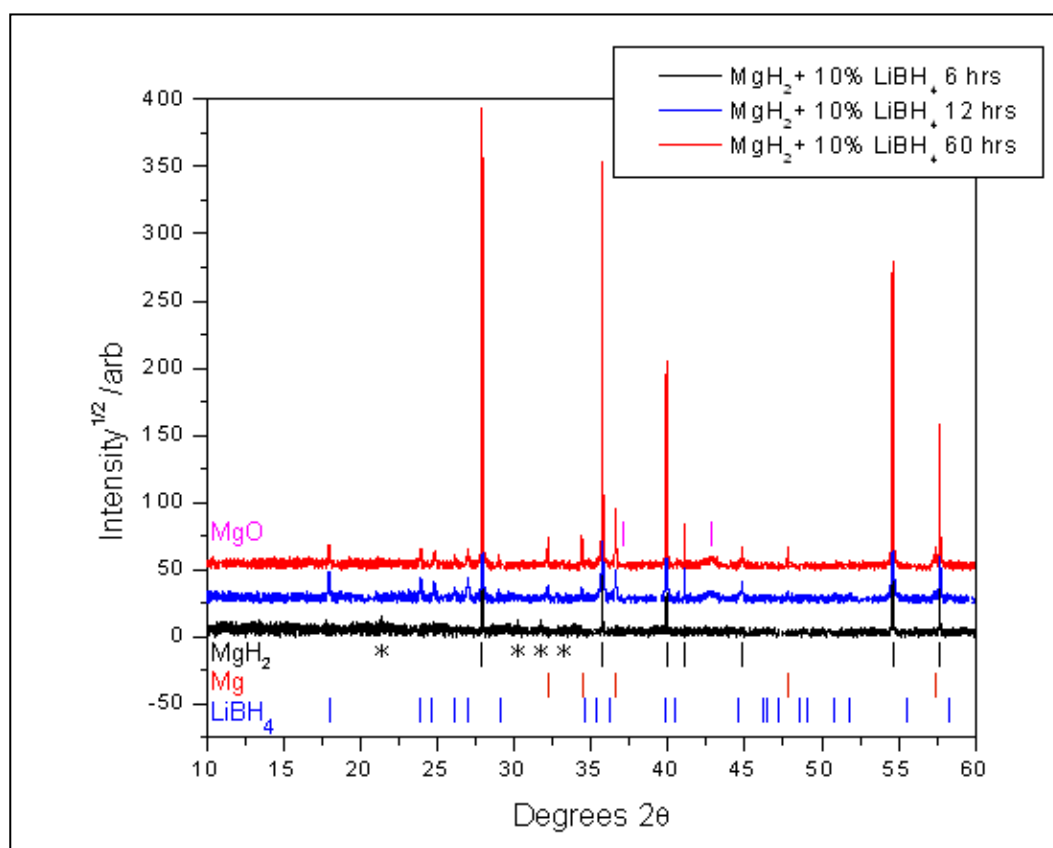
Figure 4.2.14 : Synchrotron powder XRD patterns for heated (MgH_2 + 10% $LiBH_4$) heated for 6, 12 and 60 hours. *Unknown phase marked with asterisks

observed peaks, including MgH$_2$ and Mg. These features might suggest that there is less long-range crystallinity within the sample. Other groups have observed intermediate phases during the decomposition of LiBH$_4$ above 150°C – Li$_2$B$_{12}$H$_{12}$ and Li$_2$B$_{10}$H$_{10}$[12, 13] – and thus it is possible that being held at 300°C for a number of hours results in the evolution of these or similar intermediate phases. Interestingly, the samples held at 300°C for 12 and 60 hours show no signs of new phases or impurities. Indeed, they show fully crystalline MgH$_2$, Mg and LiBH$_4$. The observed peaks were not able to be matched to any known lithium oxides or hydroxides though these compounds would not account for the reduction in reflection intensities for the sample. The synchrotron experimental data was performed very late in the study and therefore there was no further experimental time available to perform follow-up studies on short heat-treatment times for MgH$_2$ + LiBH$_4$ mixtures.
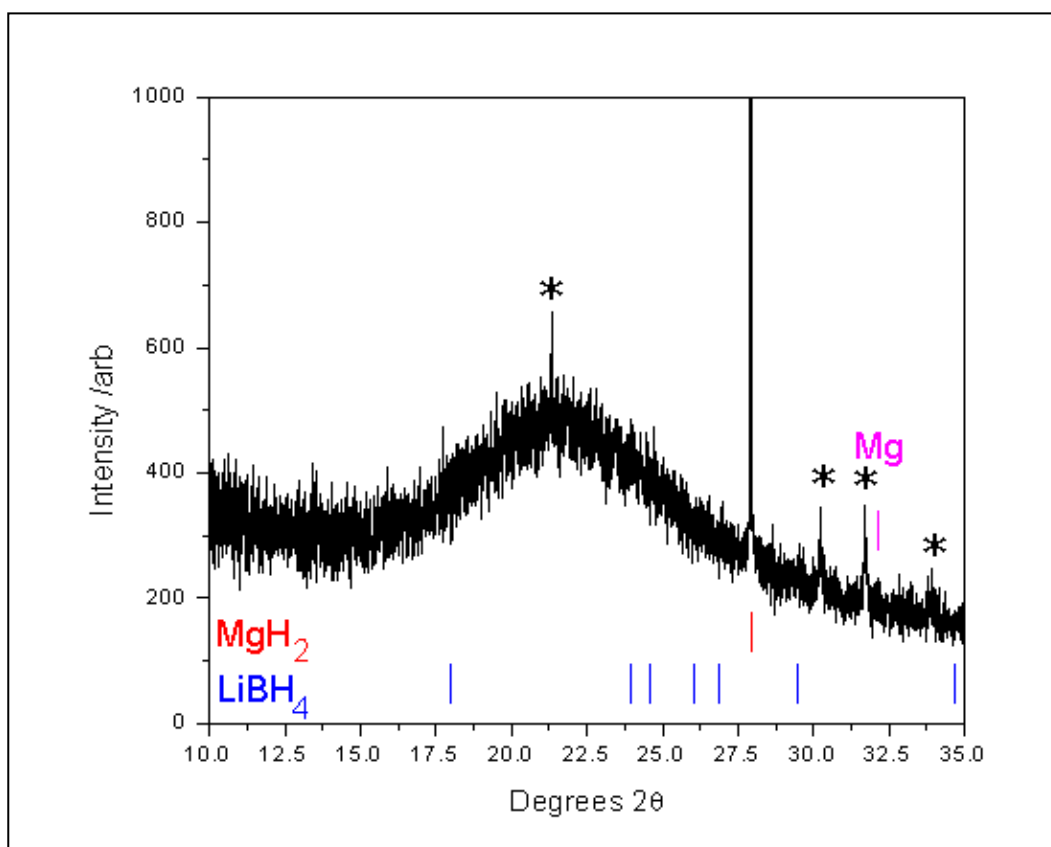
Figure 4.2.15 : Synchrotron powder XRD pattern for heated (MgH$_2$ + 10% LiBH$_4$) heated for 6 hours not corrected for background. *Unknown phase marked with asterisks

To determine whether reaction environment had an effect on the performance of hydrogenation/dehydrogenation kinetics, some samples were prepared under different gas atmospheres. Argon and a H_2/N_2 (10:90) mixed gas were chosen and experiments were performed under flowing conditions as described in the experimental section.

Absorption traces show that the sample kinetics are similar in performance to the vacuum-treated sample (Figures 4.2.16 and 4.2.17). The time to reach 90% completion of hydrogen uptake is 23 and 26 minutes for the H_2/N_2 and Ar gas atmospheres respectively, which is in line with the results observed above, though there is one notable difference in the progression of the kinetics of these samples. The first absorptions of the samples took similar times to reach completion as the previous samples, however the subsequent absorption cycles were much quicker and uniform in their times to completion in comparison with figure 4.2.3 – a behaviour which was previously only seen with milled samples of MgH_2. It is possible that this trend was caused by desorbing the materials under dynamic vacuum at 300°C or that treatment under a gas atmosphere provided superior protection from oxygen
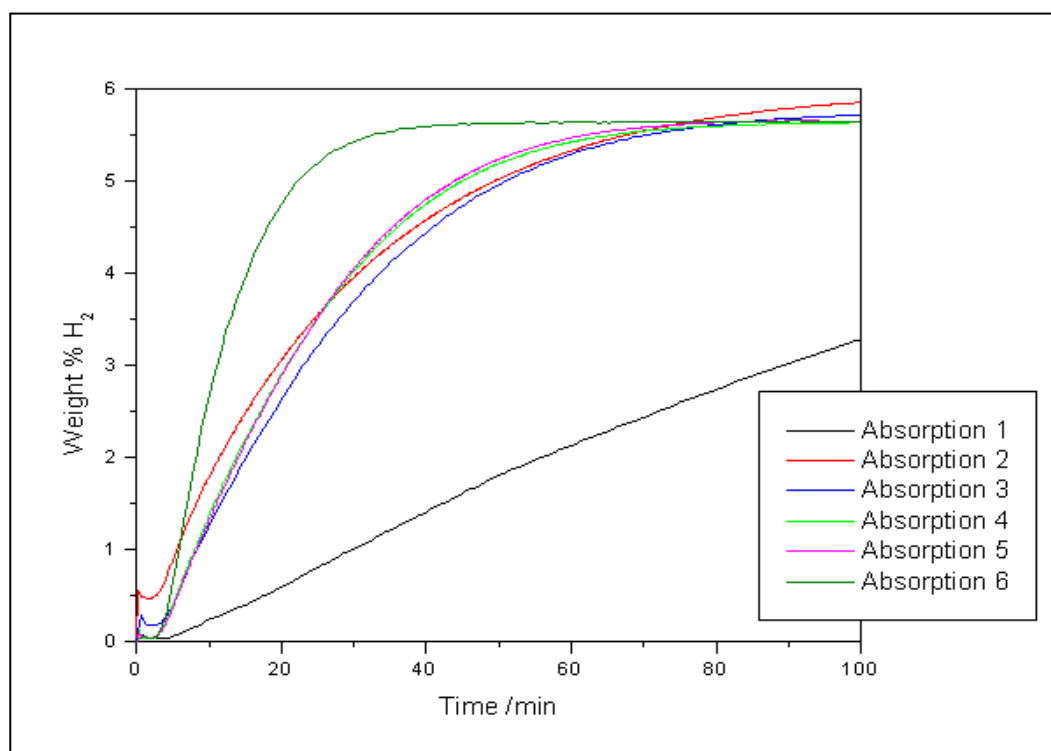
Figure 4.2.16 : Kinetic traces showing the 6 absorption cycles of (MgH_2 + 10% $LiBH_4$) (heated under a flowing H_2/N_2 gas mixture) on an IGA
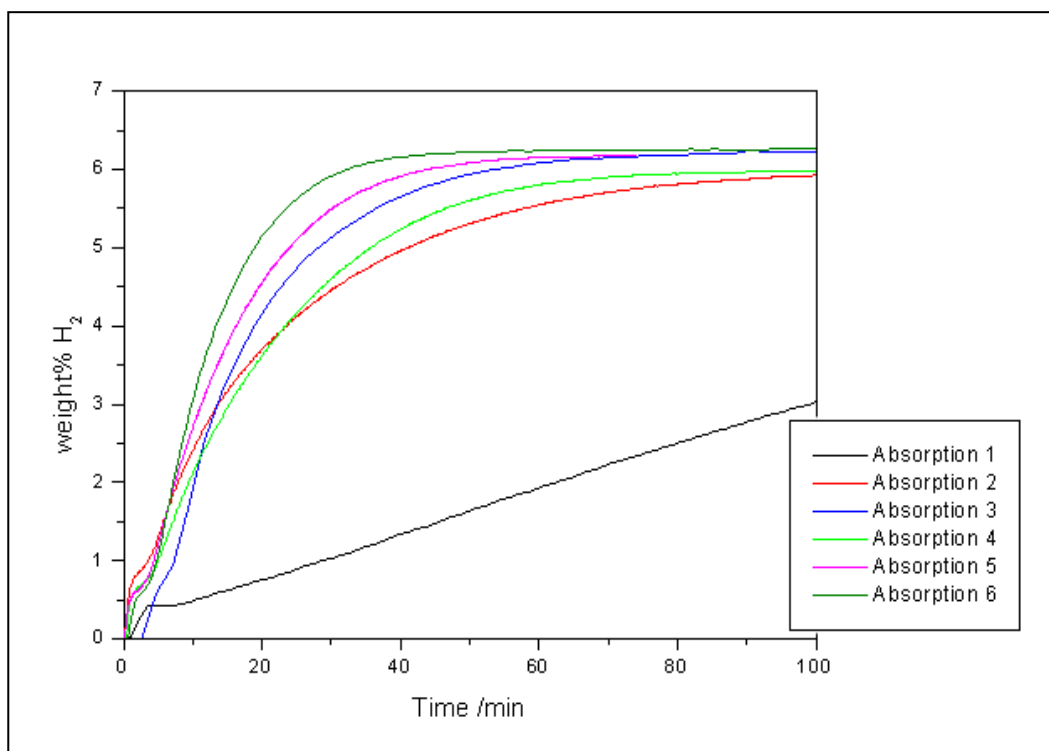
145

Figure 4.2.17 : Kinetic traces showing the 6 absorption cycles of heated (MgH$_2$ + 10% LiBH$_4$) (heated under flowing argon) on an IGA

and water that a relatively short evacuation did not.

During the gravimetric testing of these materials, desorption traces were carried out under dynamic vacuum as per previous research[14] due to equipment time constraints. The result was significantly faster desorption times but these results cannot be directly compared with the previously presented information within this thesis and thus will be left out of the discussion.

Further experiments were carried out to determine if the observed results were due purely to the inclusion and reaction of LiBH$_4$ with MgH$_2$, and how much of an effect the amount has on the kinetics or if there were other factors during the reaction that were affecting the kinetics.

The effect of pre-reaction (i.e. the method of reacting the MgH$_2$ and LiBH$_4$ together before kinetic analysis) was studied by only mixing the sample and not heating it before performing pressure controlled gravimetric analysis (IGA). Absorption kinetics showed that although the

initial uptake was completed in 500 minutes, the kinetic improvement levelled off after the third absorption cycle (Figure 4.2.18).
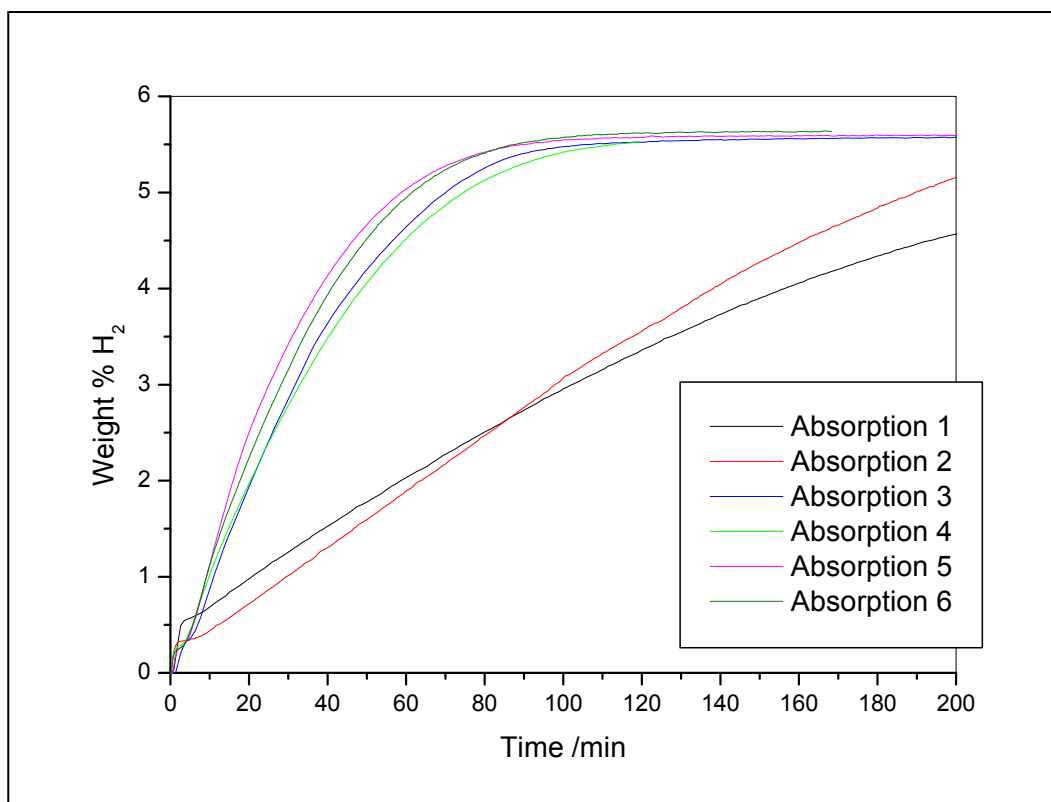

Figure 4.2.18 : Kinetic traces showing the 6 absorption cycles of (MgH$_2$ + 10% LiBH$_4$) (not pre-heated before kinetic analysis) on an IGA

The sixth absorption completed in around 120 minutes with the 90% completion point at 64 minutes, three times that of the pre-heated materials. This indicates that pre-heating is an important step in the process which will be discussed in chapter 5.

The next experiment was carried out to determine the effect that contact with the quartz tube had on the reaction: SiO$_2$ has been shown to reduce the decomposition temperature of LiBH$_4$[15]. During reaction at temperatures up to 300°C LiBH$_4$ melts and stains the quartz tube an orange colour probably from Li reaction with the SiO$_2$. It has also been shown that Mg will alloy with Si to form Mg$_2$Si during the decomposition of MgH$_2$ at 300°C[16]. It should be noted that samples measured on an IGA are also contained within a quartz holder and as such could provide the same effect. To remove any contact with the quartz, the sample was

wrapped in aluminium foil for 12 hours and then measured on an IGA (though still in contact with the quartz holder).

Absorption kinetics showed an improvement over all previously reported samples (Figure 4.2.19). The 1st absorption was effectively completed within 500 minutes whilst the 6th absorption was completed within 20 minutes and the 90% completion point was reached around 10 minutes – twice as fast as the analogous sample reacted when in contact with the quartz. Desorption kinetics were also much improved (Figure 4.2.20) in comparison with the (MgH_2 + 10% $LiBH_4$) mixtures reacted for 6, 12 and 60 hours. The 90% completion point was reached in around 30 minutes which is approximately half the time of previous samples.

These results show that reaction with the quartz tube might actually be detrimental to the reaction between magnesium hydride and lithium borohydride or conversely, a beneficial interaction with aluminium. However, reacting samples in this way is quite cumbersome and it is impossible to clean the aluminium foil, which is not reusable. Further experiments were not carried out in this manner.
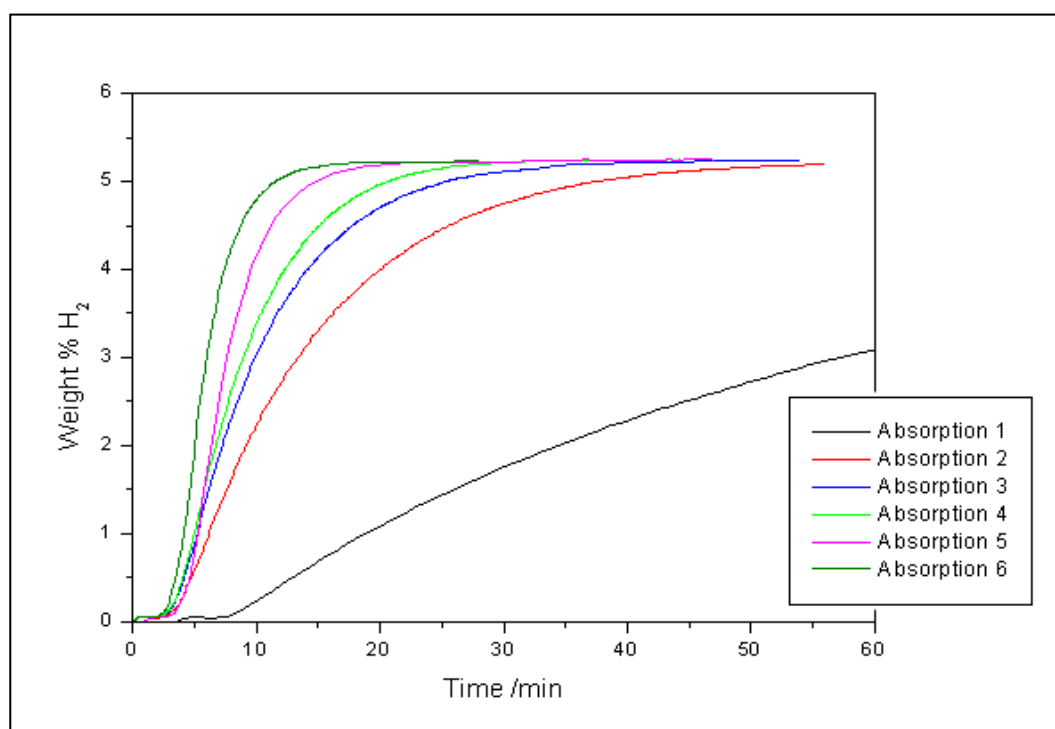

Figure 4.2.19 : Kinetic traces showing the 6 absorption cycles of (MgH_2 + 10% $LiBH_4$) (wrapped in aluminium foil during reaction) on an IGA
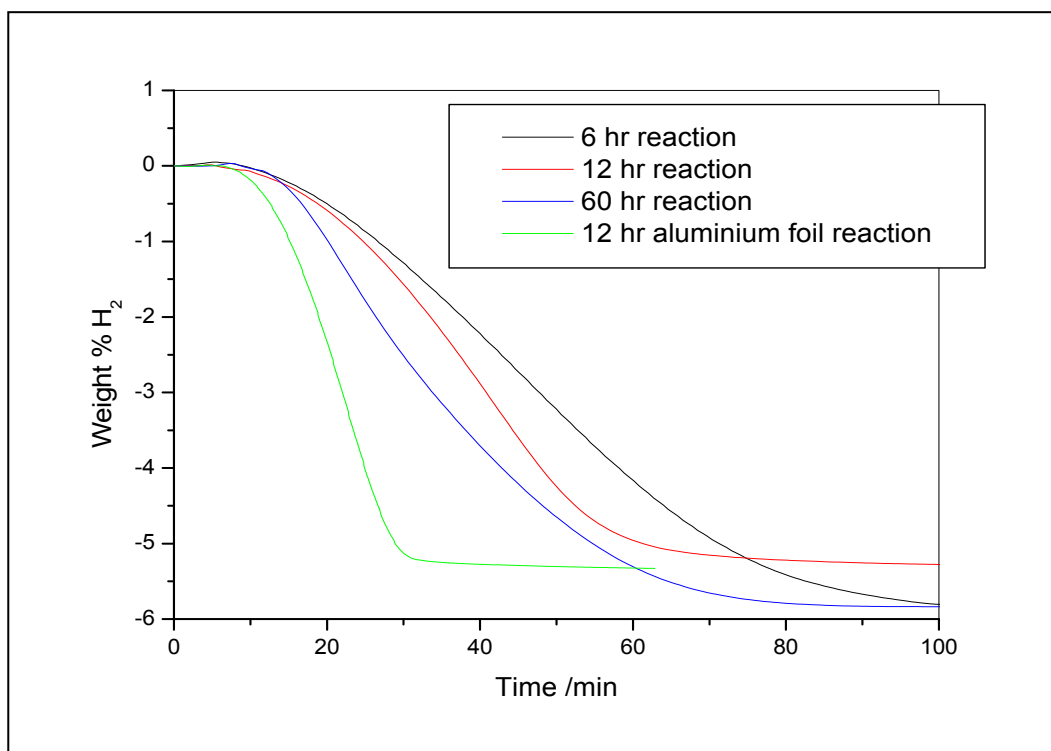
Figure 4.2.20 : Kinetic traces comparing the 6th desorptions of (MgH$_2$ + 10% LiBH$_4$) heated for different times under different conditions

At this point our supply of magnesium hydride (from Aldrich) had been depleted and unfortunately the line had been discontinued, forcing us to source our MgH$_2$ from elsewhere.

1. Reilly J.J. and Wiswall R.H., *Reaction of hydrogen with alloys of magnesium and nickel and the formation of Mg_2NiH_4.* Inorg. Chem., 1968. **7**(11): p. 2254.

2. Zaluski L., Zaluska A., and Ström-Olsen J.O., *Hydrogen absorption in nanocrystalline Mg_2Ni formed by mechanical alloying.* J. Alloy. Compd., 1995. **217**: p. 245.

3. Aguey-Zinsou K.F., Nicolaisen T., Fernandez J.R.A., Klassen T., and Bormann R., *Effect of nanosized oxides on MgH_2 (de)hydriding kinetics.* J. Alloys and Comp., 2007. **434**: p. 738.

4. Hjort P., Krozer A., and Kasemo B., *Hydrogen sorption kinetics in partly oxidized Mg films.* J. Alloy. Compd., 1996. **237**(1-2): p. 74.

5. Barkhordarian G., Klassen T., and Bormann R., *Effect of Nb_2O_5 content on hydrogen reaction kinetics of Mg.* J. Alloy. Compd., 2004. **364**: p. 242.

6. Bobet J.-L., Castro F.J., and Chevalier B., *Effects of reactive mechanical milling conditions on the physico-chemical properties of $Mg + Cr_2O_3$ mixtures.* J. Alloy. Compd., 2004. **376**: p. 205.

7. Nikulin L.V., Lykasova G.L., and Shklyaeva N.M, *Structure and properties of binary magnesium-lithium alloys subjected to pressure casting.* Met. Sci. Heat Treat+, 1986. **28**(10): p. 777.

8. Yang L., Li J., Yu Xiang., Zhang M., and Huang X., *Lanthanum-based conversion coating on Mg-8Li alloy.* Appl. Surf. Sci., 2008(5, Part 1): p. 2338.

9. Vigeholm B., Jensen K., Larsen B., and Schroder-Pedersen A., *Elements of hydride formation mechanisms in nearly spherical magnesium powder particles.* J. Less Common Met., 1987. **131**: p. 133.

10. Vigeholm B., Køller J., Larsen B., and Pedersen A.S., *Formation and decomposition of magnesium hydride.* J. Less Common Met., 1983. **89**: p. 135.

11. Friedlmeier G. and Groll M., *Experimental analysis and modelling of the hydriding kinetics of Ni-doped and pure Mg.* J. Alloy. Compd., 1997. **253-254**: p. 550.

12. Orimo S., Nakamori Y., Ohba N., Miwa K., Aoki M., and Towata S., *Experimental studies on intermediate compound of $LiBH_4$.* Appl. Phys. Lett., 2006. **89**: p. 021920.

13. Friedrichs O., Remhof A., Hwang S.-J., and Züttel A., *Role of $Li_2B_{12}H_{12}$ for the formation and decomposition of $LiBH_4$.* Chem. Mater., 2010. **22**: p. 3265.

14. Oelerich W., Klassen T., and Bormann R., *Hydrogen sorption of nanocrystalline Mg at reduced temperatures by metal-oxide catalysts.* Adv. Eng. Mater., 2001. **3**(7): p. 487.

15. Zuttel A., Wenger P., Rentsch S., Sudan P., Mauron Ph., and Emmenegger Ch., *$LiBH_4$ a new hydrogen storage material.* Journal of Power Sources, 2003. **118**: p. 1.

16. Vajo J.J., *Altering hydrogen storage properties by hydride destabilization through alloy formation: LiH and MgH_2 destabilized with Si.* J. Phys. Chem. B, 2004. **108**: p. 13977.

4.3   Study of alternative sources of MgH$_2$

Experimental technique 4.3

Infrared Spectroscopy

The infra-red spectra of samples was collected via a diamond anvil reflectance cell on a Nicolet Magna-IR infrared spectrometer. The diamond anvil cell consisted of a compression clamp that could be tightened with a torque wrench-type screw head. This compressed the sample between the diamond and an IR transparent surface was. There was a rubber O-ring around the sample window that prevented gas from entering the sample compartment and so limited the exposure to air of the samples. The samples were loaded in the cell within an argon circulating glove box then taken to the spectrometer. The cell was loaded and affixed to the spectrometer and nitrogen gas was flushed through the equipment for 5 minutes to purge it of CO_2 which has a strong absorption at ~ 2349 cm^{-1}. The sample was then measured between 400 and 4000 cm^{-1} and the sample disposed of.

Heat treatment of MgH$_2$ + 5 mol% MgB$_2$

A mixture of MgH$_2$ (Aldrich, 90% MgH$_2$, 10% Mg) and MgB$_2$ (Aldrich, $\geq$96% 4% Mg) was prepared for heat treatment under a static vacuum as described in Experimental Technique 4.2. The sealed quartz sample tube was heated to 300°C at a rate of 50°C/hour and held at this temperature for 12 hours and then allowed to cool. Very little discolouration of the quartz tube was observed after heat treatment and the sample was recovered within an argon circulating glove box.

IGA measurements carried out on this sample were performed as described in Experimental technique 4.1 with the exception of the absorption and desorption steps performed at 350°C. The desorption steps were performed at 1 bar H$_2$ pressure, 350°C. For 350°C desorption steps preceeded by a 300°C absorption step the temperature was raised before the pressure was reduced. The 350°C absorption steps preceeded by a desorption at 300°C had their pressure raised to 1 bar before the temperature was increased and only once the sample was at 350°C was the pressure increased to 10 bar.

Study of the change in unit cell parameters of MgH$_2$ and Mg

The effect of increasing LiBH$_4$ content during heating on the unit cell parameters of MgH$_2$ and Mg was studied: a range of ratios of MgH$_2$ + LiBH$_4$ samples were prepared via heat treatment under static vacuum at 300°C for 12 hours as described in Experimental Technique 4.2. Two types of MgH$_2$ were used – Avocado (98%, 2% Mg) and Goldschmidt (95% MgH$_2$, 5% Mg) with LiBH$_4$ (Acros Organics, 95%). The ratios of MgH$_2$:LiBH$_4$ for Avocado MgH$_2$ were 19:1, 9:1, 8:2, 7:3, 6:4, 5:5, 4:6, 3:7, 2:8 and 1:9 while the ratios for the Goldschmidt MgH$_2$ samples were 11:1, 10:2, 9:3, 8:4, 7:5, 6:6, 5:7, 4:8, 3:9, 2:10 and 1:11. The samples were then ground in a mortar and pestle and measured on beam line ID31 at the ESRF in Grenoble as described in Experimental Technique 4.2.

The reflections associated with MgH$_2$ and Mg in the powder XRD patterns were then indexed using the program CELL mentioned in section 3.5.1. This was achieved by inputting the unit cell parameters (a, b, c, α, β, γ, and the symmetry) from literature and crystal structure databases and then fitting them with a non-linear least squares refinement of the observed reflections in the diffraction patterns from the synchrotron source. This calculation gave the determined unit cell parameters of the indexed reflections and the estimated standard deviations of the unit cell and the reflections.

General experimental techniques

XRD performed on the D5000, IGA and SEM measurements and wt% calculations were performed as described in the Experimental Technique 4.1 section. Synchrotron source XRD were performed as described in Experimental Technique 4.2.

Evidence of contamination during IGA measurements

During this study, the laboratory where measurements were performed was refurbished this coincided with the move to find an alternative source of MgH$_2$ as per section 4.3 (a). Once everything was back in place and measurements were being performed again, there was a discrepancy between the hydrogen absorption and desorption kinetics of Aldrich MgH$_2$ + 10% LiBH$_4$ and those for the same ratio of Avocado and Goldschmidt MgH$_2$: mainly that they were slower than those samples reported in section 4.1 (also Table 4.3.2). The IGA was tested with standard samples of Pd/Pt and did not seem to evidence any problems during these measurements, so the problem was considered to be with the MgH$_2$ source. The possible contamination of the sample during IGA measurement affected all the IGA

kinetic measurements in the thesis from this point forward (the thermodynamic experiments were performed early in the study) and the problem was not fully appreciated until after the allotted experimental period for the research had expired. Towards the end of the thesis the IGA was no longer giving accurate results for sensitive samples though samples that were not reactive suffered no loss of H_2 capacity or kinetics. The problem was eventually discovered to be the seal around the bearing on the turbomolecular pump used for evacuating the IGA to pressures of 1×10^{-6} bar. During a period of maintenance where the vane pumps backing the turbomolecular pump were being replaced, the turbo pump was taken apart and carbon deposits were discovered inside it and in the stainless steel pipes that connected it to the reactor chamber of the IGA. This was corrected by purchasing a new turbo pump though there was no time to repeat the lengthy experiments that MgH_2 required for H_2 cycling.

While the exact cause of the problems with the samples is unclear – there was no conclusive evidence from infrared spectroscopy as might be expected: no sharp peaks between 1000-1500 cm^{-1} or 3000-4000 cm^{-1} that would suggest C–O, O–H or other types of stretches common in organic compounds (Figure 4.3.15). Due to the poor starting material from Avocado with a relatively large amount of $Mg(OH)_2$ and MgO present the problem was presumed to be with the starting reagent rather than the equipment.

The experiment in section 4.4 (c) that performed the H_2 cycling on a specially constructed flowing TPD system showed better reaction kinetics when measured on the IGA after first being H_2 cycled 5 times than the samples performed on the IGA from the first H_2 cycle (Figures 4.4.8 and 4.4.9). Strangely, this sample absorbed 6.9 wt% on its first H_2 absorption on the IGA, though very slowly in around 200 minutes and then became much quicker ~60 minutes to reach completion, however, the sample's H_2 capacity was now at ~62% of its H_2 capacity the previous absorption (4.3 wt%). Desorption capacity was identical though it reached completion within 80 minutes though 90% of this was achieved within 39 minutes which was equal to Aldrich MgH_2 + $LiBH_4$ samples that had been measured before the lab was refurbished. X-ray diffraction of samples that were measured in the IGA saw no evidence of carbon species or other compounds that might cause degradation in kinetic performance and a loss in H_2 capacity. Comparing the sample for Strem Mg + $LiBH_4$ (90:10, table 4.4.1) to the results obtained for the same ratio but cycled on the flowing TPD system in section 4.4 (c) there is a large difference in performance: the IGA cycled sample reached 90% absorption in 50 minutes and 90% desorption in 96 minutes compared to 36 minutes for the absorption and 49 minutes for desorption for the TPD sample. All captions that are possibly affected by this have been labelled with a double asterisk. (**)

4.3 (a) Reaction of Avocado MgH₂ with LiBH₄:

During the course of our investigations it became impossible to acquire further magnesium hydride from Aldrich and, as our supply was running low, we decided to investigate alternative, more reliable MgH_2 sources. Two powdered samples of MgH_2 were sourced from Avocado and Goldschmidt. At around the same time our lab was extensively refurbished: new features were added to the IGAs including the ability to load samples inertly via a bolt-on glovebox. It was decided to use this new facility to reduce oxidation that might occur during sample loading and as a result, initially samples were loaded in an argon atmosphere.

Figure 4.3.1 shows X-ray diffraction performed on the MgH_2 samples from different sources for comparison.
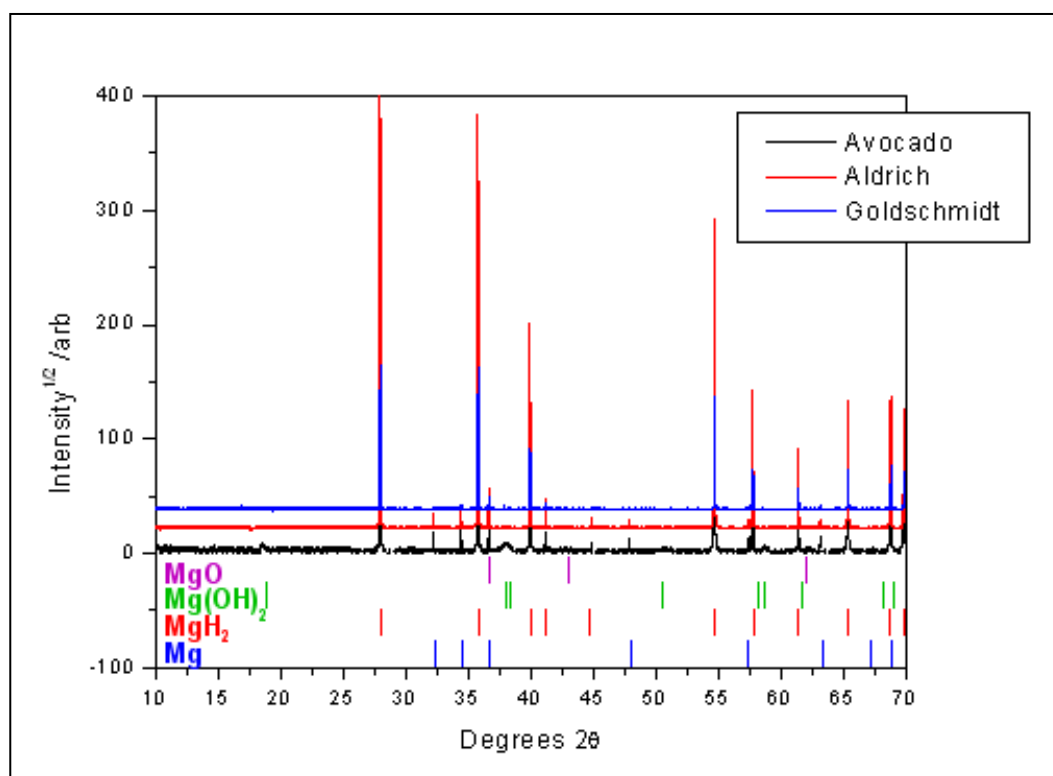
Figure 4.3.1 : Powder synchrotron X-ray diffraction patterns for MgH₂ from three sources showing relative amounts of MgO, Mg(OH)₂, Mg and MgH₂

The diffraction patterns show that both Aldrich and Avocado MgH_2 contain larger amounts of crystalline magnesium oxide, MgO than Goldschmidt. Avocado also has a large presence of

magnesium hydroxide, $Mg(OH)_2$. The product data sheets available with the MgH_2 sources outline the general wt% of constituents in each reagent: Avocado MgH_2 listed 98% MgH_2 with remainder Mg and <1% impurities while Goldschmidt MgH_2 listed 95% MgH_2 with remainder Mg <1% impurities and Aldrich listed (90% MgH_2, remainder Mg, <1% MgO). The diffraction patters show that Avocado MgH_2 is the least pure reagent and that it is has likely been contaminated in some way either during transit or via the production method. Alfa Aesar, Degussa-Goldschmidt and Aldrich were contacted for more information on their production method though only Degussa-Goldschmidt revealed that their reagent was ball-milled and no further information was gained. Following the halt in production of MgH_2 by Aldrich and after the completion of this study a new 'high purity' MgH_2 product was released by Aldrich. Compositional data was available for this product where it had not been for the previous three and was obtained. The results show minor impurities in the reagent primarily consisting of Al, Ca, Fe, K and Mn – all of which had a concentration of between 100-200ppm. It is reasonable to presume that, since this reagent is listed as being purer that there is at least this level of impurity and probably higher in the Aldrich reagent previously used in this study. While such minor impurities might serve to catalyse the hydrogenation and dehydrogenation of MgH_2 most reported improvements from transition metal oxide catalysts are reported in fractions of greater than 1wt% and it is unlikely that these would greatly affect the sorption kinetics observed in this study.

While MgH_2 is sensitive to the atmosphere, including water and oxygen, it was not known how the presence of these compounds would affect the hydrogen sorption kinetics, though one might predict that they would result in slower overall kinetics and certainly a lower weight percent in H_2 storage capacity. Avocado MgH_2 was selected as the first newly sourced material to be tested. A sample of MgH_2 + $LiBH_4$ (90:10) was heated under the same conditions used for the Aldrich material in a static vacuum at 300°C, then inertly loaded in an Ar atmosphere onto the IGA.

Figure 4.3.2 shows desorption kinetic traces for six dehydrogenation/hydrogenation cycles. As with the previous Aldrich samples the kinetics improved upon cycling, however, the first desorption showed an interesting attribute: while previous samples had required 350°C to
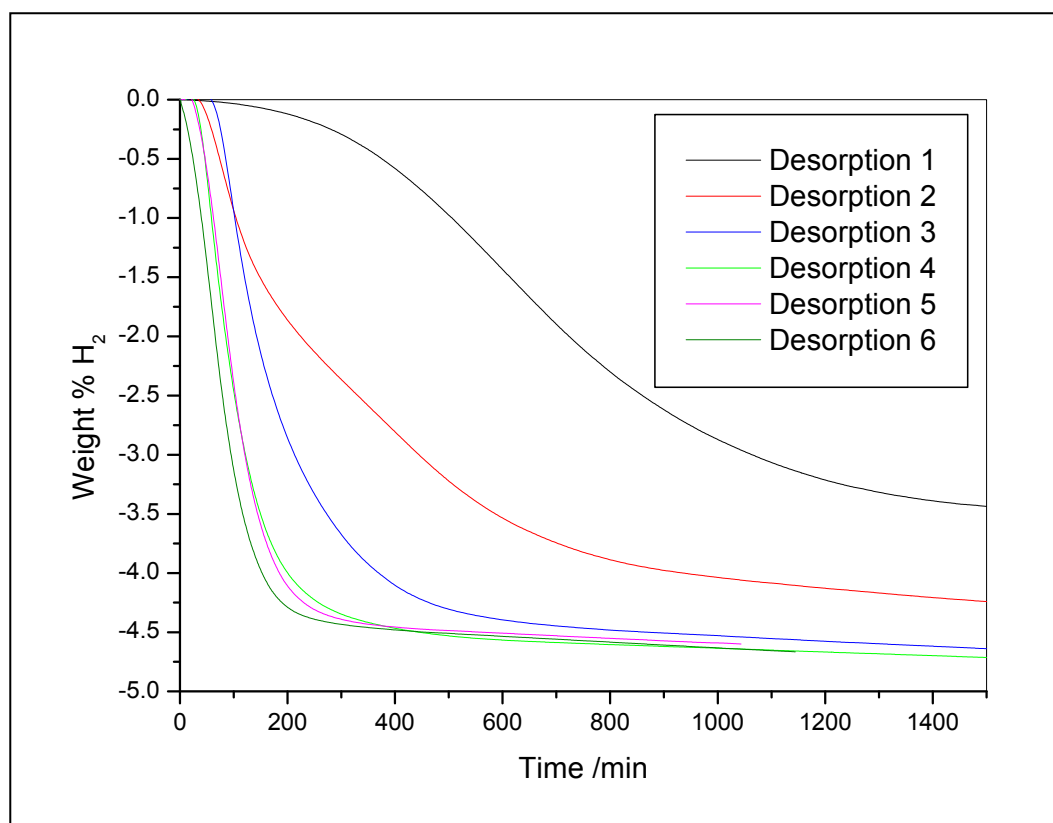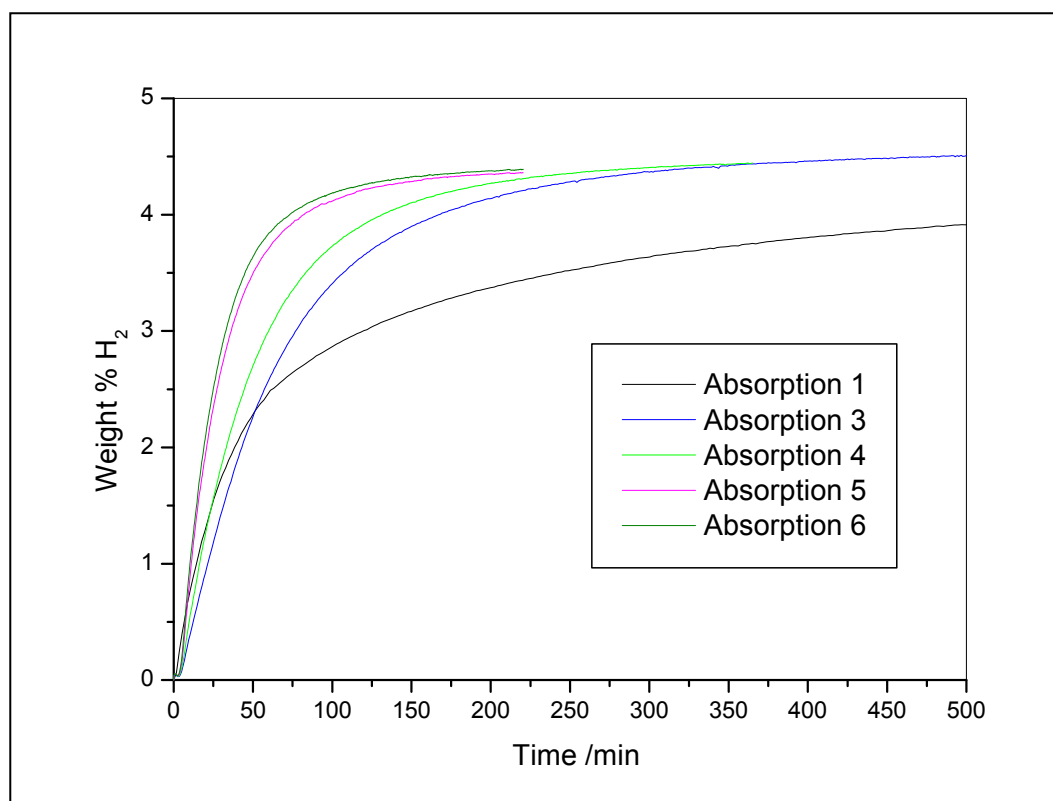

Figure 4.3.2 : Kinetic traces showing absorption characteristics for Avocado MgH$_2$ + LiBH$_4$ (90:10) at 10 mbar H$_2$, 300°C **

enable desorption to occur, at 300°C this sample readily desorbed in 2000 minutes. While this is much slower than the desorptions previously obtained at 350°C, the equivalent desorption for Aldrich samples would not have been complete in this time.

It is difficult to determine the end-point of the subsequent desorptions due to all of them resulting in a constant, linear decrease in mass which may indicate sublimation of magnesium metal – as observed in certain previous experiments. The result was that the end point of each run had to be manually estimated and the time to completion could not be compared directly to other samples. However, it is possible to approximate the time to desorb 90% of the total weight% lost per desorption by looking at the curve shapes previously seen. The

156

point at which 90% of the total weight% loss for the sixth desorption had occurred was approximately 180 minutes, which is around three times longer than equivalent Aldrich samples. Total H_2 capacity was much lower than for previous samples at around 4.5 wt% which was possibly due to the presence of a relatively large quantity of MgO and Mg(OH)$_2$ within the starting reagent.

Figure 4.3.3 shows the absorption kinetic traces for the same sample at 10 bar H_2, 300°C. Along with the reduced H_2 capacity, the hydrogenation kinetics are similarly slower than for the equivalent Aldrich samples with the first and sixth absorptions reaching completion in 2500 and 220 minutes, respectively. The 90% completion point occurred within 70 minutes – again, three times that of the equivalent Aldrich sample.

Figure 4.3.4 shows the comparison of diffraction patterns for Avocado MgH$_2$, Avocado MgH$_2$ + LiBH$_4$ (90:10) after reaction at 300 °C under static vacuum and the same sample after six successive hydrogenation/dehydrogenation cycles on an IGA. Both oxide and hydroxide peaks

Figure 4.3.3 : Kinetic traces showing absorption characteristics for Avocado MgH$_2$ + LiBH$_4$ (90:10) at 10 bar H$_2$, 300°C *

157

are observed before reaction with LiBH$_4$; the relative intensity of the hydroxide peaks is significantly reduced after the initial reaction and completely absent in the cycled pattern while the oxide content has increased. At the same time, there was an apparent decrease in LiBH$_4$ content where the strong reflections can still be observed at angles below 27 °2θ in the reacted sample but none are observed in the cycled sample pattern.
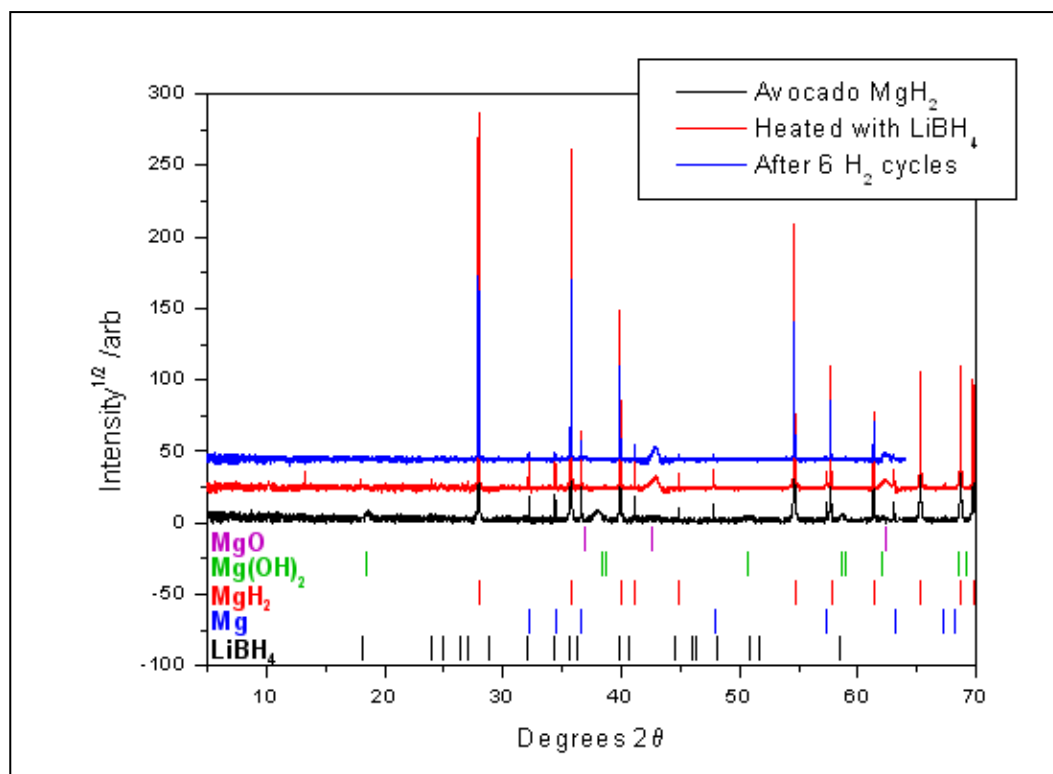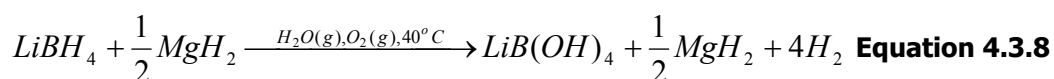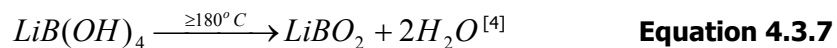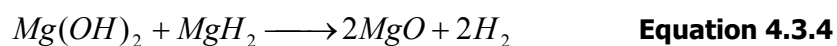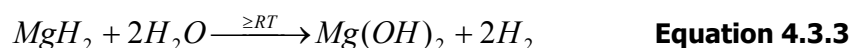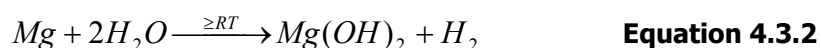

Figure 4.3.4 : Powder synchrotron X-ray diffraction patterns comparing Avocado MgH$_2$, Avocado heated with LiBH$_4$ (90:10) and the same sample after H$_2$ cycling **

One likely explanation for these observed trends in MgO, Mg(OH)$_2$ and LiBH$_4$ content could be the decomposition of magnesium hydroxide to water and magnesium oxide. This process occurs readily past 250 °C according to Equation 3.3.1 and complete decomposition of a sample that is 50-150 mg in size can be completed in under 50 minutes at 300 °C[1] – a much shorter time than is experienced by the samples in each step from initial reaction to successive hydrogenation/dehydrogenation cycles.

$$Mg(OH)_2 \xrightarrow{\geq 250^o C} MgO + H_2O \qquad \textbf{Equation 4.3.1}$$
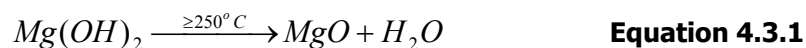
The evolution of water in the sample from this decomposition could also react with MgH_2, Mg and $LiBH_4$ (Equations 4.3.2-6). It has been shown that $LiBH_4$ will preferentially react with H_2O and O_2 when in a mixture with MgH_2 producing lithium tetrahydroxoborate ($LiB(OH)_4$) (Equation 4.3.8) whilst leaving the MgH_2 phase relatively untouched[2, 3]. While $LiB(OH)_4$ could be formed temporarily, this dehydrogenates at temperatures above 180°C to $LiBO_2$ (Equation 4.3.7) which is an incredibly stable compound with a melting point at 849°C. This lithium borate can also form directly from reaction with water (Equation 4.3.5).

$$Mg + 2H_2O \xrightarrow{\geq RT} Mg(OH)_2 + H_2 \qquad \textbf{Equation 4.3.2}$$

$$MgH_2 + 2H_2O \xrightarrow{\geq RT} Mg(OH)_2 + 2H_2 \qquad \textbf{Equation 4.3.3}$$

$$Mg(OH)_2 + MgH_2 \longrightarrow 2MgO + 2H_2 \qquad \textbf{Equation 4.3.4}$$

$$LiBH_4 + 2H_2O \xrightarrow{\geq RT} LiBO_2 + 4H_2 \qquad \textbf{Equation 4.3.5}$$

$$LiBH_4 + 4H_2O \xrightarrow{\geq RT} LiB(OH)_4 + 4H_2 \qquad \textbf{Equation 4.3.6}$$

$$LiB(OH)_4 \xrightarrow{\geq 180^o C} LiBO_2 + 2H_2O \, [4] \qquad \textbf{Equation 4.3.7}$$

$$LiBH_4 + \frac{1}{2}MgH_2 \xrightarrow{H_2O(g),O_2(g),40^o C} LiB(OH)_4 + \frac{1}{2}MgH_2 + 4H_2 \quad \textbf{Equation 4.3.8}$$
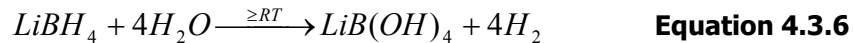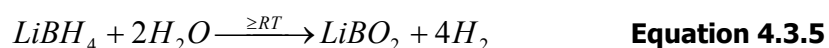
Thus the reaction and decomposition of $Mg(OH)_2$ could result in a cascade of fast reactions – most probably with $LiBH_4$ resulting in the loss of observed reflections in the XRD patterns – and is likely to reduce any positive effect $LiBH_4$ has on MgH_2 hydrogen sorption kinetics.

4.3 (b) Reaction of Goldschmidt MgH₂ with LiBH₄

It was decided that due to its slow kinetics and relatively high content of oxide and hydroxide that further progress using Avocado MgH₂ would not yield the best possible results. Figure 4.3.1 showed that Goldschmidt contained little or no MgO or Mg(OH)₂ and therefore it was logical to use this material preferentially.

Goldschmidt MgH₂ was therefore heated with LiBH₄ in the ratio 90:10 at 300°C under static vacuum as in previous syntheses. Figure 4.3.5 shows an X-ray diffraction pattern comparison between all three sources of MgH₂ reacted with LiBH₄ (90:10 ratio). Although the Goldschmidt sample contains some oxide, it is of the same relative magnitude as the Aldrich MgO phase. It is also worth noting that both the Aldrich and Goldschmidt diffraction patterns show peaks at higher angles for LiBH₄ whereas Avocado only exhibits the strongest reflections below 30° 2θ. Since Avocado has a higher probability of the LiBH₄ phase reacting with water due to the
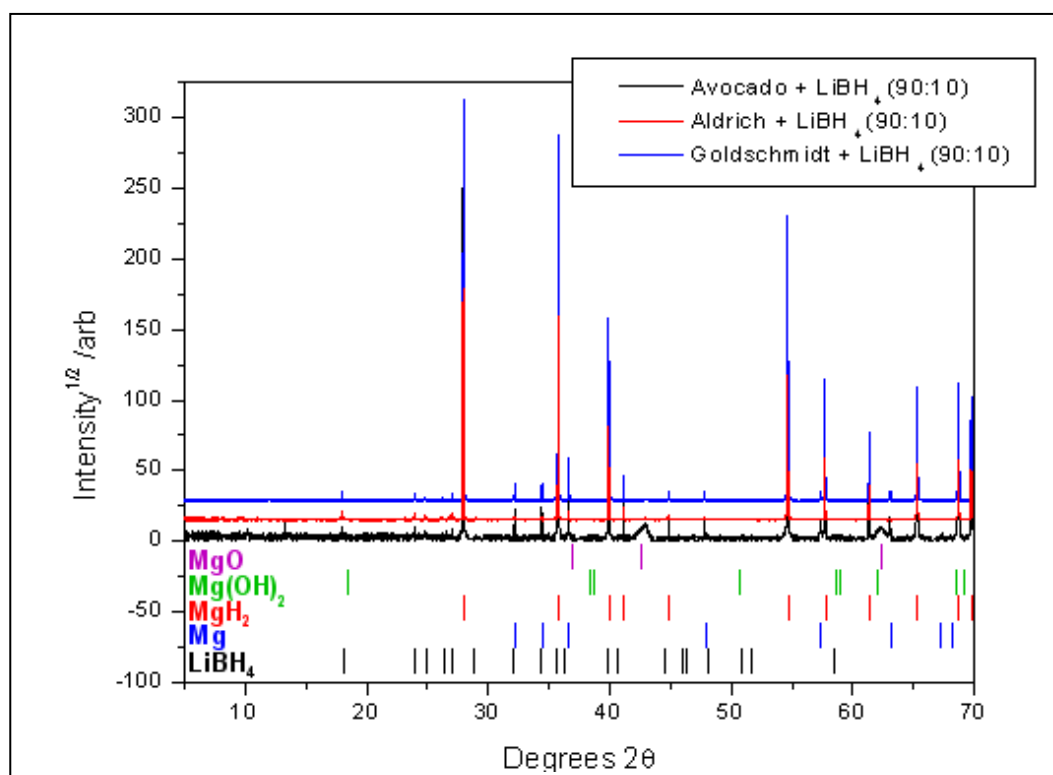

Figure 4.3.5 : Powder synchrotron X-ray diffraction patterns showing the three different MgH₂ materials heated with LiBH₄ (90:10 ratio) under static vacuum at 300°C

160

decomposition of the magnesium hydroxide during the initial static vacuum treatment it is possible that this is the reason the reflections are weaker.

Figure 4.3.6 shows hydrogen desorption kinetic traces for Goldschmidt MgH_2+ $LiBH_4$ (90:10). The sample was loaded in an Ar atmosphere and the first desorption was carried out at 350°C to speed up the initial cycle due to machine time restrictions. Interestingly there was no improvement upon cycling at 300°C with the sorption kinetics displaying stable times to total desorption of around 300 minutes from the second desorption onwards. The time to reach 90% of the total weight% loss was approximately 130 minutes for the sixth cycle – more than double the 56 minutes for an equivalent Aldrich sample.

A similar situation is seen for the absorption kinetics traces in figure 4.3.7. The times to completely absorb were approximately 1300 and 250 minutes for the first and sixth absorptions respectively. By comparison, the sixth cycle on an Aldrich sample was around 80 minutes. The time to reach 90% of the total weight% gain was 70 minutes – three times that of the ~20 minutes for the equivalent Aldrich sample.
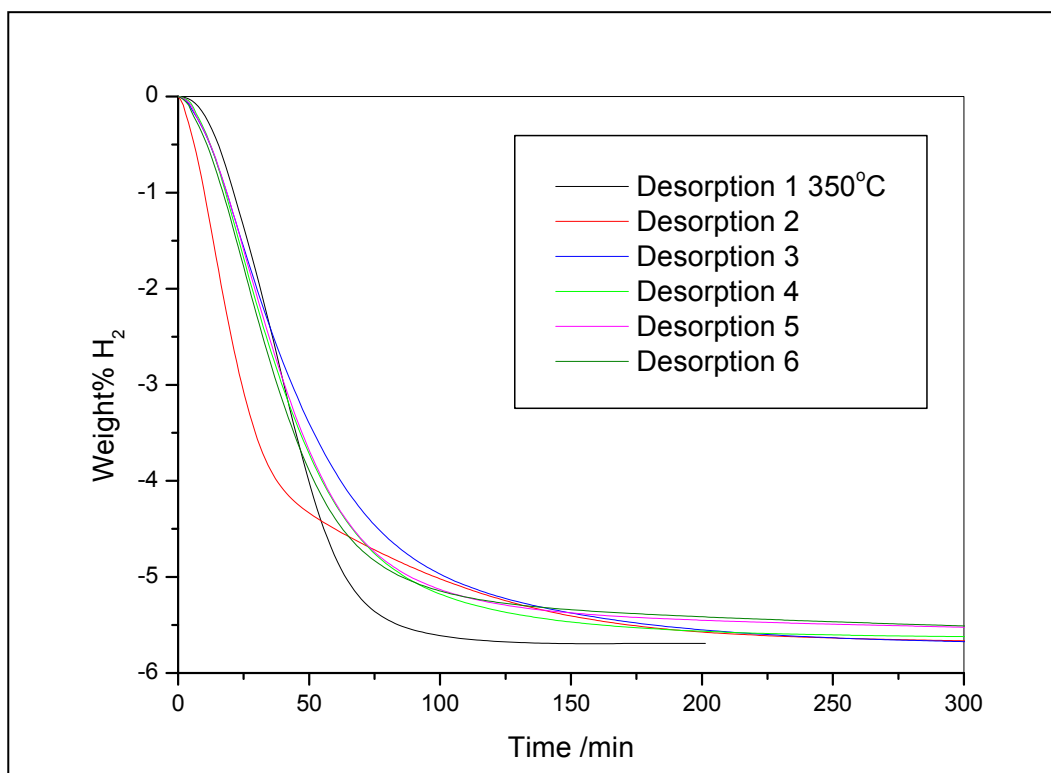
Figure 4.3.6 : Desorption kinetic traces for Goldschmidt MgH$_2$ + LiBH$_4$ (90:10) performed at 10 mbar H$_2$, 300°C (except first desorption) **
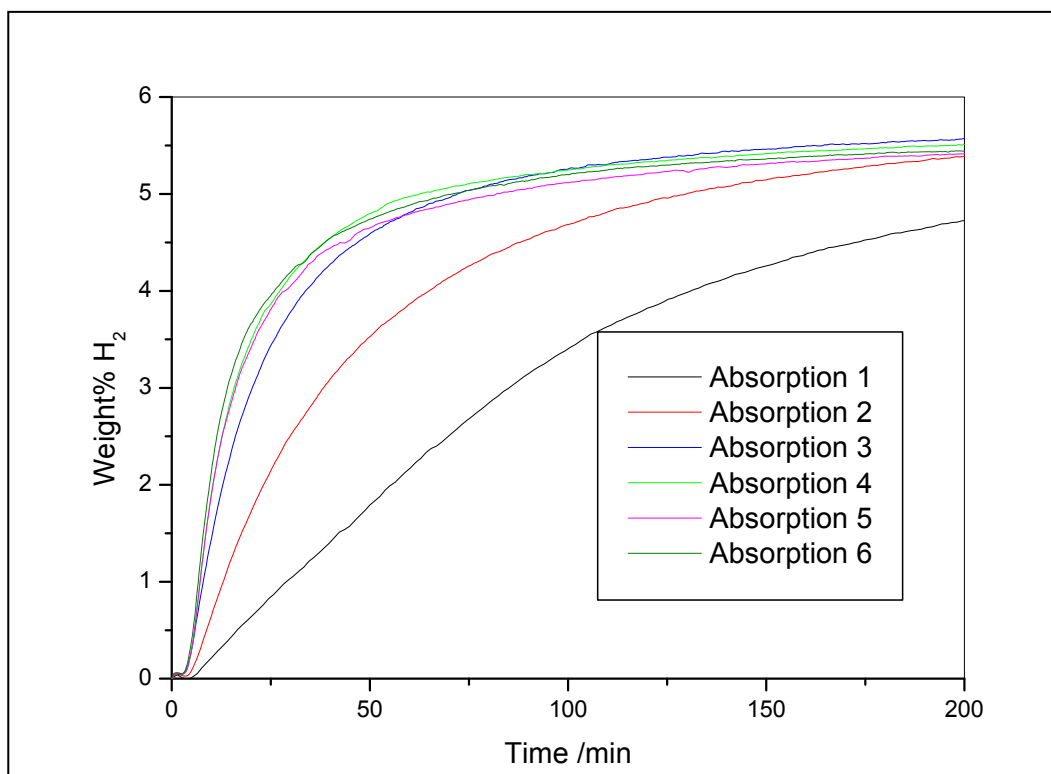

Figure 4.3.7 : Absorption kinetic traces for Goldschmidt MgH$_2$ + LiBH$_4$ (90:10) performed at 10 bar H$_2$, 300°C **

Though this sample of the Goldschmidt material had a more consistent performance than the Avocado sample, both had relatively similar sorption kinetics on the sixth hydrogenation/dehydrogenation cycle.

4.3 (c) Comparison of the effect of oxygen on hydriding kinetics

The main difference between the current experiments and the previous Aldrich experiments was the additional protective step of inertly loading the samples onto the IGA. To investigate whether this might have a detrimental effect on the samples, it was decided to compare the two loading methods on Goldschmidt samples. Figure 4.3.8 shows the initial desorption kinetics for three different samples of Goldschmidt MgH_2 + $LiBH_4$ (90:10). The sample measured at 350°C was taken from the above data while a second sample was measured at 300°C to correspond to the Avocado result shown in figures 4.3.2 and 4.3.3. Both of these were inertly loaded. A third sample, prepared in exactly the same way was loaded in air.
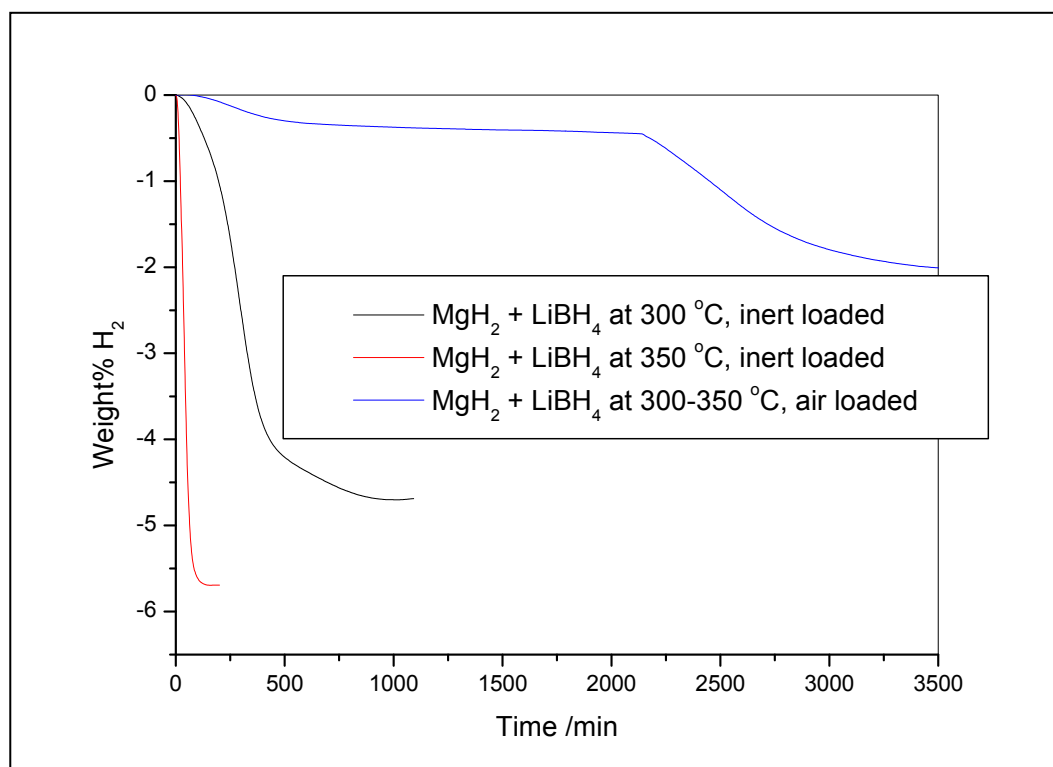

Figure 4.3.8 : 1st desorption kinetic traces comparing different loading environments for Goldschmidt MgH_2 + $LiBH_4$ (90:10) to determine the effect of atmosphere on the sorption properties **

The air-loaded sample was heated to 300°C and then, once it was observed that desorption kinetics were very poor, increased to 350°C in the same way as the original Aldrich samples.

The traces show that the ability of MgH_2 to desorb is severely inhibited by reaction with atmosphere. Other research groups have shown that oxide layers forming on the surface of the sample particles will inhibit hydrogen diffusion throughout the particle and grains[5].

The inertly loaded sample measured at 300°C showed some variability in the time to complete each desorption during cycling in a similar manner to previous Aldrich samples. However, its hydrogen sorption kinetics were relatively similar to current Goldschmidt samples. The time to reach saturation was approximately 300 minutes for the sixth absorption, with 90% of this reached in 64 minutes. Unfortunately, due to instrumental problems, data from the sixth desorption was lost. The fifth desorption took 300 minutes to reach completion at 4.3 wt% H_2, with 90% of the total mass loss reached in 96 minutes.

The inertly loaded sample measured at 350°C on the first desorption lost 5.56 wt% H_2 in the fifth cycle in 500 minutes with 90% of this being reached in 142 minutes and 4.3 wt% reached in 111 minutes. The air-loaded sample data was incomplete due to technical failures and as such only the first hydrogenation/dehydrogenation cycle was recorded. Due to limited equipment time the experiment could not be repeated. Data from the first absorption was very poor and showed much slower sorption kinetics in comparison with previous samples.

In an attempt to gauge the effect that the atmosphere had on MgH_2, a sample of MgH_2 + $LiBH_4$ (90:10) was exposed to atmosphere for an extended amount of time. Figure 4.3.9 shows the X-ray diffraction patterns for the sample after reaction, after 30 minutes and 28 hours.

Interestingly, the MgO phase did not increase over the period of exposure and no $Mg(OH)_2$ phase appeared with time. Though the environment of this sample was relatively water free, this result might suggest that a protective layer of oxide prevented complete oxidation of the Mg and MgH_2 particles.
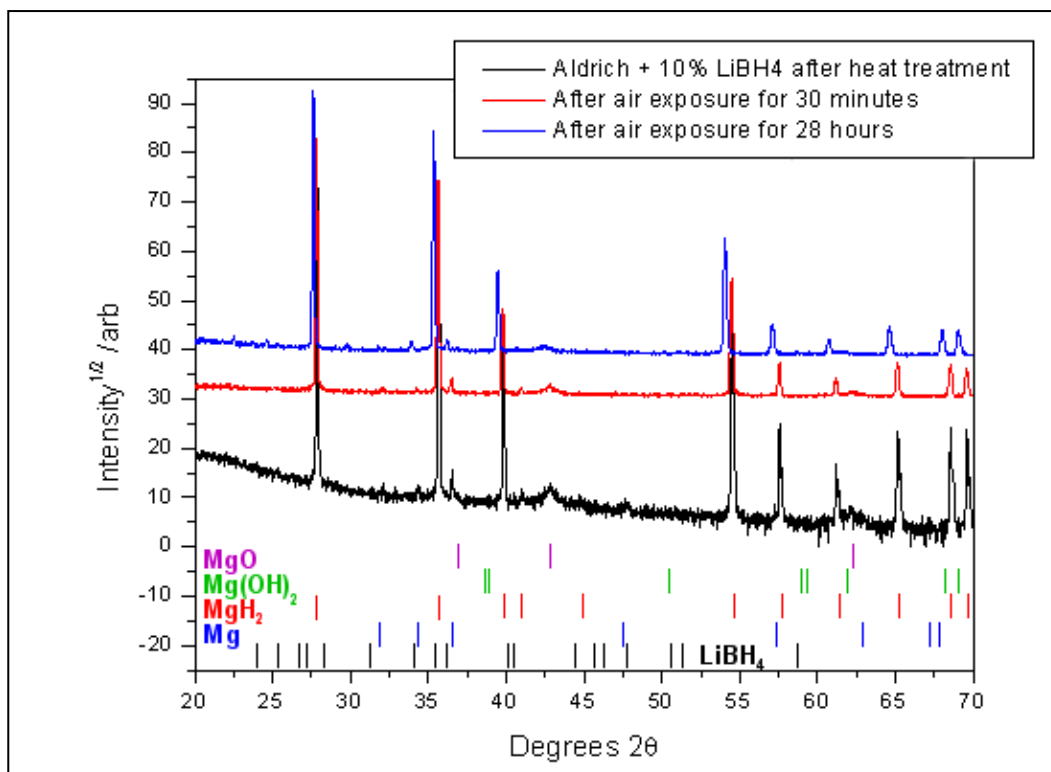
Figure 4.3.9 : X-ray diffraction patterns from a Brüker D5000 showing exposure to air of MgH$_2$ over an extended period. The XRD pattern for 28 hours exposure was slightly mis-aligned in the sample holder, therefore any shift to lower 2θ is an artefact of this experimental error

4.3 (d) Comparison of the microstructure of the MgH$_2$ reagents

Figure 4.3.10 shows SEM images that illustrate the relative particle size of MgH$_2$ from the three sources. Aldrich MgH$_2$ had the smallest observed particle size but the largest distribution of particle sizes, ranging from diameters of ~5 - 100 µm. However, even in these larger particles the centre is typically no more than 50 µm (which is equivalent to the radius of a larger particle) from the nearest edge which is the cut-off point at which H$_2$ can no longer easily diffuse through the MgH$_2$ phase[6]. Goldschmidt material was coarser, with particle sizes ranging from diameters of ~30 – 150 µm though, once again, the majority of the material in a particle is no further than 50 µm from the nearest surface. Avocado had the coarsest material with particle sizes ranging from ~10 – 110 µm with the majority of particles above 60 µm in diameter and fewer at the lower end of the range compared with Goldschmidt. Avocado also had more spherical particles, some of which had centres around

165

or further than 50 µm from the nearest edge which might result in difficulty in reaching full H2 capacity.

These features would affect the H_2 diffusion rate into the microstructure which in turn limit the kinetics of the samples. This could explain the relative speed of sorption that Aldrich had over Avocado and Goldschmidt samples and shows that preparation and selection of reagents
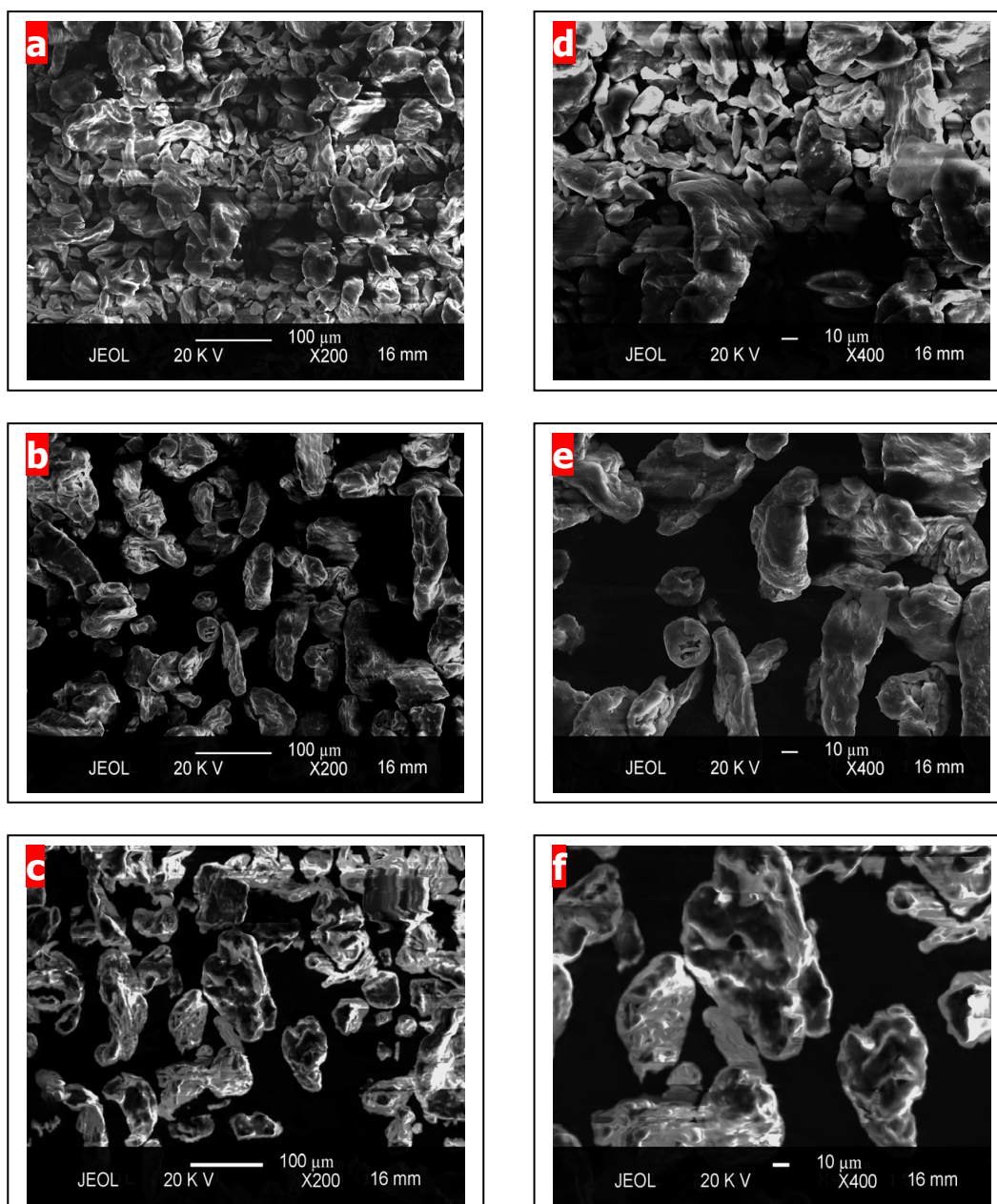

Figure 4.3.10 : SEM images comparing a) Aldrich, b) Goldschmidt, c) Avocado MgH$_2$ as received from the suppliers (magnification x200) and d) Aldrich, e) Goldschmidt, f) Avocado MgH$_2$ (magnification x400)

can have an important effect on experiments. The average MgH_2 crystallite size was determined using the Scherrer equation for the first three reflections from synchrotron data: Aldrich had the largest at 393 nm, while Avocado and Goldschmidt were approximately equal with 319 and 325 nm, respectively. These are larger values than those determined using lab-based X-ray sources in chapter 4.1 though neither sets have had the instrumental line widths subtracted from the value and thus it is likely that the true grain size lies in the 400 and 500 nm. This shows that Aldrich has the largest grain size whilst having the smallest particle size and this possibly explains the kinetic advantage this material has over Avocado and Goldschmidt MgH_2.

Enquiries were directed to Aldrich about the production of their reagent, however they refused to divulge any information on the process. Goldschmidt also would not divulge how the MgH_2 was manufactured but did specify that the material was subjected to mechanical milling as part of post production. Avocado also did not divulge the process for obtaining their reagent so no conclusions can be made regarding the best processing method for obtaining MgH_2 for hydrogen storage applications. One method of manufacturing MgH_2 is via reaction of magnesium with organic compounds before being subjected to a pressure of hydrogen in the presence of a catalyst[7]. However, these synthetic routes usually result in bound solvent complexes which would have been observed. Therefore it is plausible to rule out this type of production method.

4.3 (e) Determination of the fate of LiBH₄

Figure 4.3.11 shows the effect of hydrogen cycling on each of the MgH_2 reagents sourced. One consistent feature of the three is that $LiBH_4$ is present in the diffraction patterns before hydrogen cycling, however, after treatment there is no evidence of crystalline $LiBH_4$ remaining in the samples after being hydrided at 10 bar H_2, 300°C. There are four possible explanations as to the state of the borohydride. One is that it has been oxidised by contact with the various oxygen sources during treatment and no longer remains. The second explanation is that the borohydride has reacted with the magnesium hydride or magnesium in

some way and the third possibility is that the LiBH4 has melted during reaction (the melting point of LiBH$_4$ is around 275°C) and become very finely dispersed. It is also possible that the LiBH$_4$ has been partially dehydrided during the cycling process and is unable to be rehydrided under these relatively low temperature and pressure conditions.

If the lithium borohydride had been oxidised then there would likely be evidence of this within the diffraction patterns, however, a thorough check revealed no presence of Li$_2$O which has its first three reflections at 20.4°, 32.547° and 35.685° 2θ or LiOH which has reflections at 33.642°, 38.995° and 56.455° 2θ. Despite the lack of evidence for the oxidation of lithium, it is interesting to note that MgH$_2$ + LiBH$_4$ samples are more sensitive to oxidation than pure MgH$_2$, with large increases in the reflections pertaining to MgO at 42.8° 2θ for both Aldrich and Goldschmidt samples.
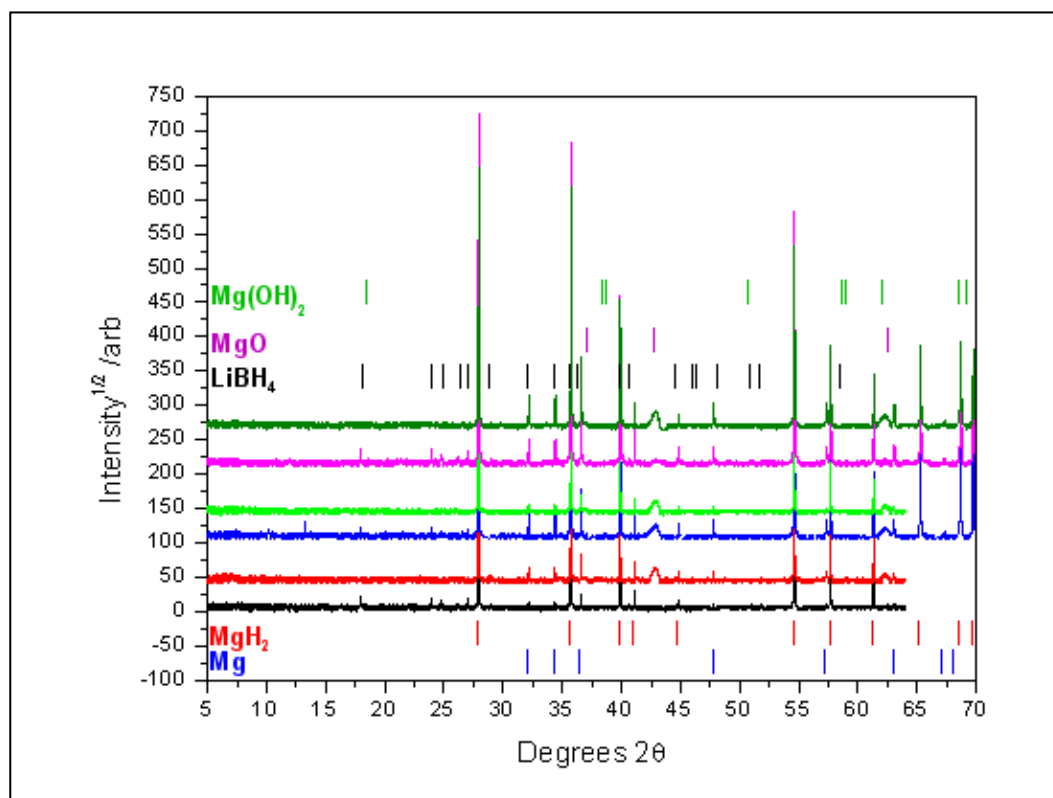

Figure 4.3.11 : Powder X-ray diffraction patterns showing a) Aldrich + LiBH$_4$ before hydrogen cycling on an IGA, b) after cyling, c) Avocado + LiBH$_4$ (90:10) before cycling, d) after cycling, e) Goldschmidt + LiBH$_4$ before cycling, f) after cycling **

Reaction with the magnesium or its hydride could take place through direct chemical reaction to form an alloy[8] or a Li-Mg borohydride complex in an analogous reaction pathway to those reported for MgH_2 and $LiNH_2$[9] and these compounds could result in extra reflections on their respective diffractograms.

Figure 4.3.12 shows two samples of MgH_2 + $LiBH_4$ (90:10) for Aldrich and Avocado with a comparison diffraction pattern of $LiBH_4$. Additional peaks due to minority phases were observed in the synchrotron data. These phases were present in a number of Aldrich and Avocado samples but were not consistently observed and none were found in Goldschmidt samples. Two of the reflections observed have been reported in the literature by Mao et al.[10] at 24.7° and 26.1° 2θ and are unidentified, though it was speculated that they might arise from oxidation of $LiBH_4$ as previously noted in 4.3 (a).
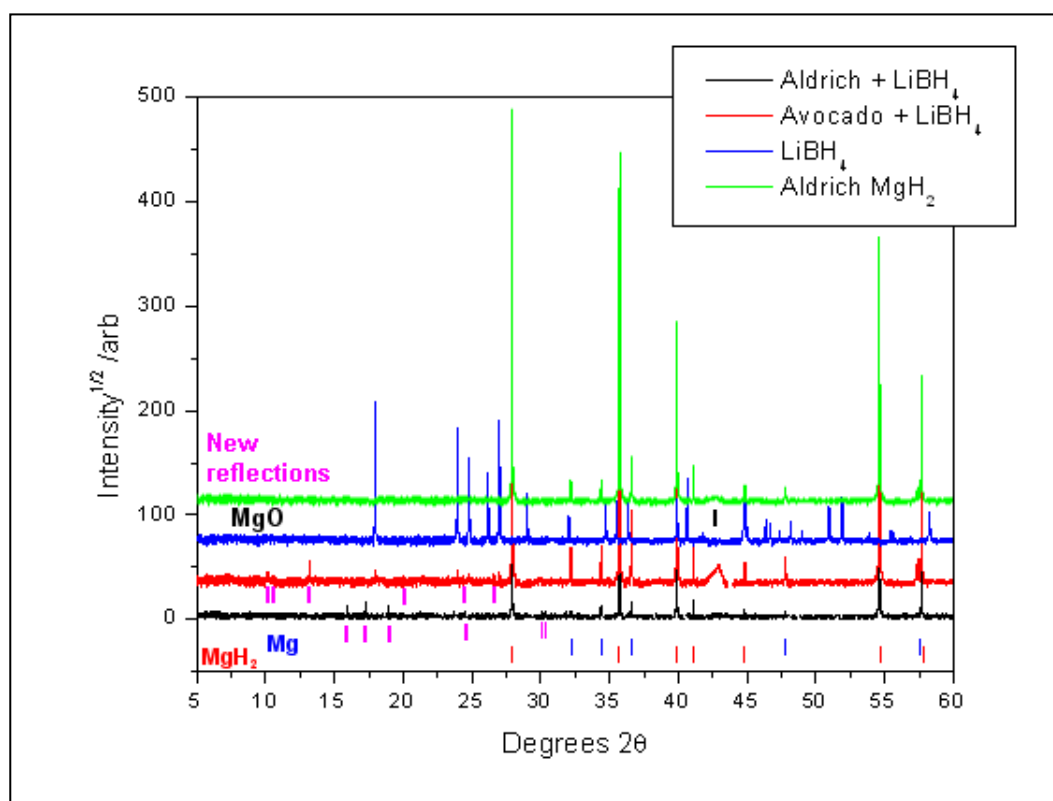

Figure 4.3.12 : Powder X-ray diffraction patterns depicting the newly observed reflections in two for heat-treated (300°C, svac, 12hrs) MgH_2 + 10% $LiBH_4$ samples from Aldrich and Avocado. Comparison diffraction patterns of as-received $LiBH_4$ and Aldrich MgH_2 are also included

However, none of the peaks observed could be indexed to any of the lithium borates or hydroxides identified as the decomposition products in the literature[2, 3].

It is also possible that $LiBH_4$ could partially decompose in such a way that Li^+ is formed substitutes within the MgH_2 or Mg lattice – the process of which would not necessarily produce new reflections. However, substitution could, in principle, be detected through changes in relative peak intensities and analysis of the size of the unit cell.

Figure 4.3.13 shows the result of a study of the change in unit cell volumes over a change in composition from pure MgH_2 to heated samples where the majority component was $LiBH_4$. The samples were heat-treated at 300°C for 12 hours under static vacuum in a sealed quartz tube. They were then removed from the quartz tube in a glove box with <10ppm O_2 and H_2O, ground in a motar and pestle and loaded into quartz capillaries sealed with wax. The capillaries were then scanned via synchrotron source radiation under the conditions outlined in the experimental section.

As-received reagents for Avocado and Goldschmidt (MgH_2) though not heat-treated were also included for comparison. Some samples such as Avocado MgH_2 + $LiBH_4$ in the ratios of 95:5, 20:80 and 10:90 did not sit fully within the beam line and so had low intensities for the observed reflections which increased the error margins on the calculations.

If Lithium or boron substituted into the MgH_2 lattice, a trend in expansion or contraction would be expected, however, analysis of the unit cell volumes shows no trend. The Avocado MgH_2 samples have slightly larger error margins which place all of the samples' unit cell volumes within 3 standard deviations of each other. Heated Goldschmidt MgH_2 + $LiBH_4$ samples also display a rough agreement within the confines of accepted error margins, though the pure MgH_2 appears to have a slightly larger unit cell.
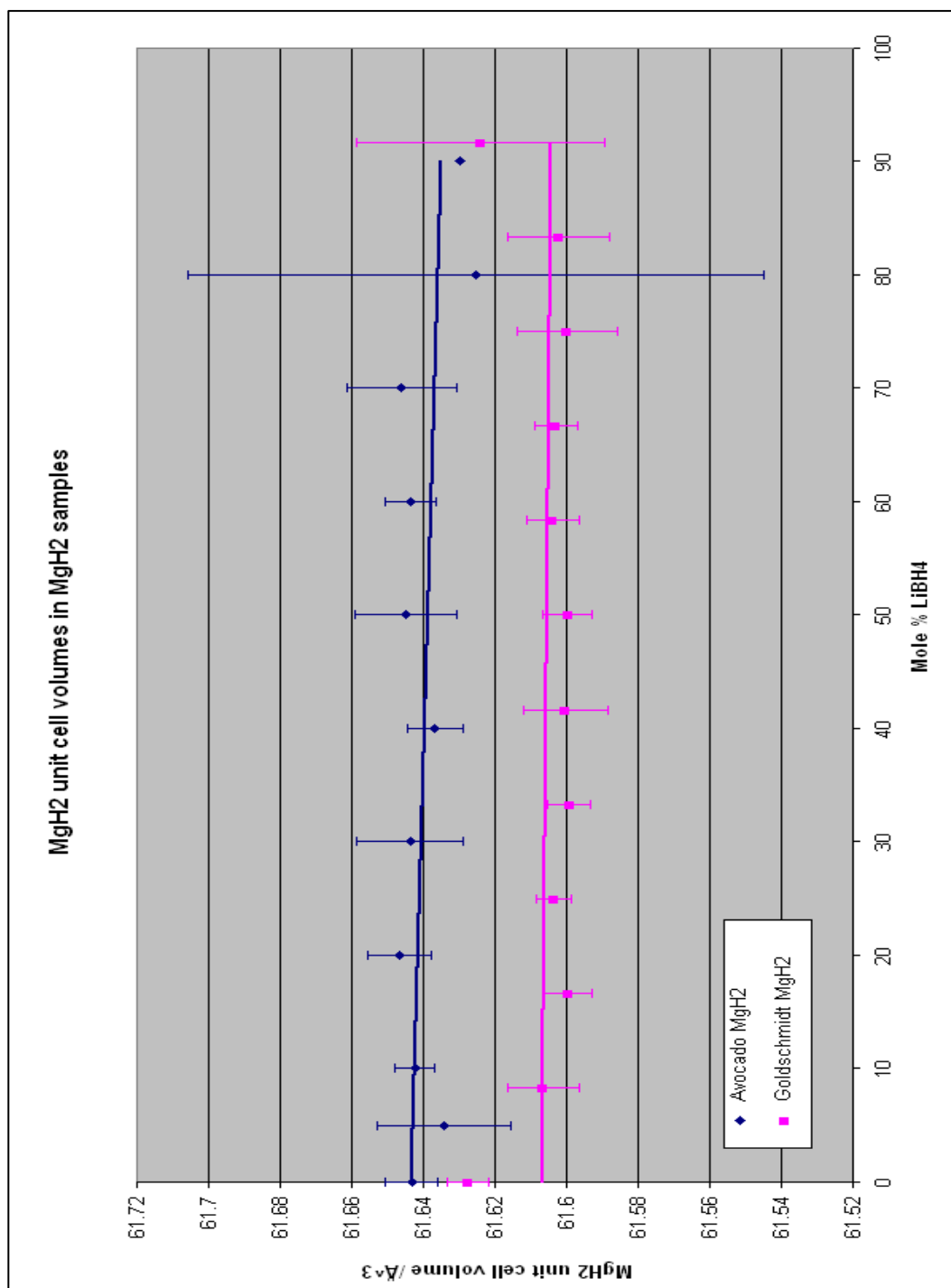
Figure 4.3.13 : Point plots comparing MgH₂ unit cell volumes of Avocado MgH₂ and Goldschmidt MgH₂ as-received and after heating at 300°C under static vacuum for 12 hours with LiBH₄ in the stated ratios. Error bars show the range of 3 standard deviations from each data point. All XRD data was obtained from the ESRF synchrotron source at Grenoble.

One interesting aspect of these results is that Avocado MgH₂ appears to have a slightly larger

unit cell throughout the measured samples (mean unit cell volume = 61.64 Å³ ±0.028)

compared to Goldschmidt MgH_2 heated with $LiBH_4$ samples which had a mean unit cell volume of 61.60 Å^3 ±0.011. Pure Goldschmidt MgH_2 itself had unit cell that was more similar to Avocado MgH_2 samples at 61.627 Å^3. This result might suggest that $LiBH_4$ has affected the MgH_2 crystal lattice for Goldschmidt but not for Avocado and it's possible that the presence of MgO and $Mg(OH)_2$ hinders any interaction between the two phases. However, this discrepancy might also be explained through instrumental error.

Analysis of the magnesium phase present in the starting material from Avocado and Goldschmidt showed that this difference might not be due to instrumental error. Figure 4.3.14 depicts unit cell calculations for Mg from the same samples of Avocado and Goldschmidt seen in figure 4.3.13. Once again, with the same exceptions regarding large errors for samples that have a low intensity due to poor alignment, most of the samples remain within 3 standard deviations of each other – though Goldschmidt MgH_2 + $LiBH_4$ 9:3 (75:25) might have a larger unit cell volume than the other samples – and all samples across both sources of MgH_2 display a mean unit cell volume of $\sim$ 53.7 Å^3 ($ESD_{Avocado}$= ±0.16, $ESD_{Goldschmidt}$= ±0.08). This result would suggest that the unit cell contraction observed for Goldschmit MgH_2 is not due to instrumental error or differences as a similar reduction would expect to be observed for the Mg unit cell parameters.
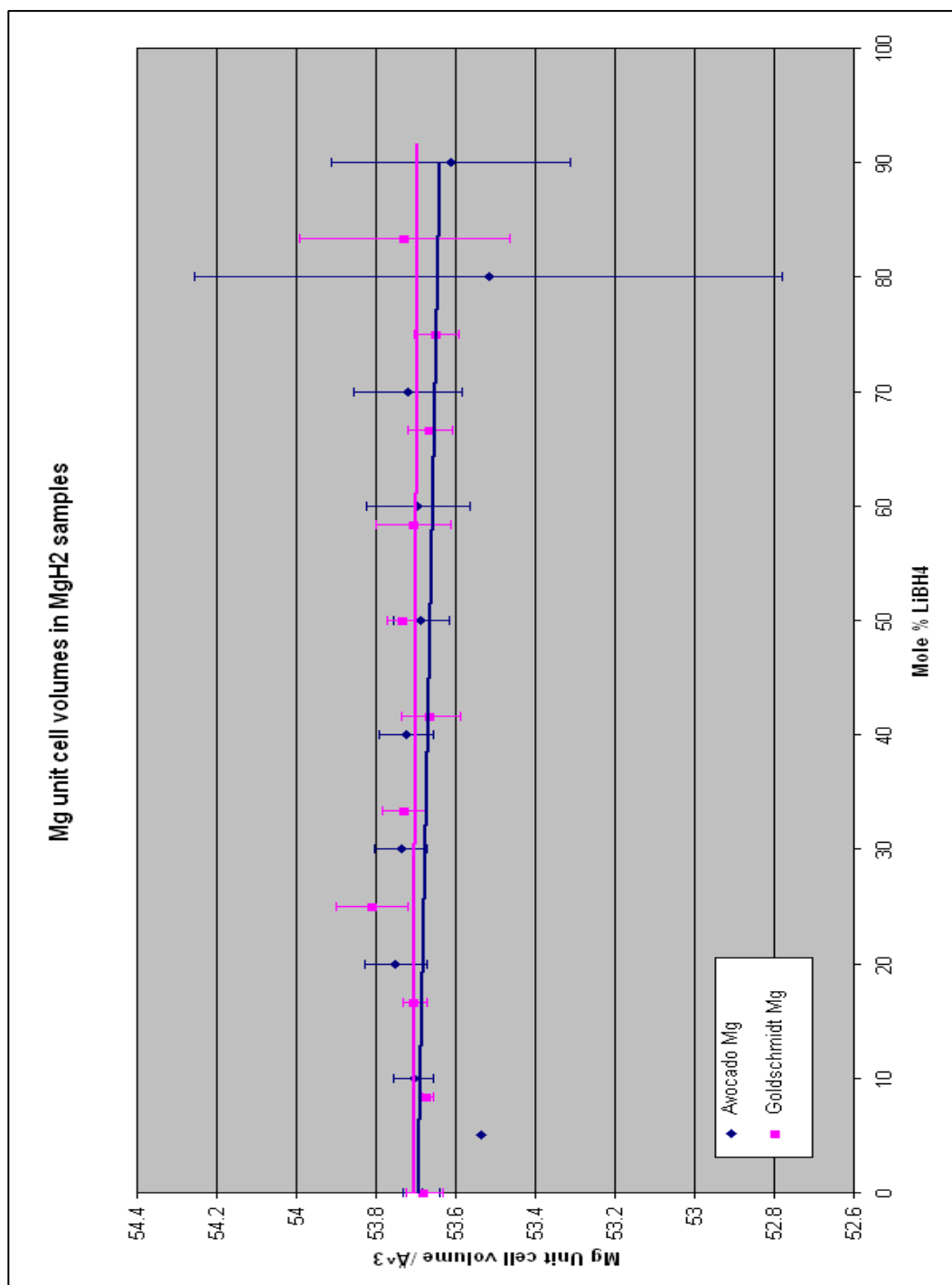
Figure 4.3.14 : Point plots comparing Mg unit cell volumes of Avocado MgH$_2$ and Goldschmidt MgH$_2$ as-received and after heating with LiBH$_4$ in the stated ratios. Error bars show the range of 3 standard deviations from each data point. All XRD data was obtained from the ESRF synchrotron source at Grenoble.

Comparisons with hydrogen cycled MgH$_2$ + LiBH$_4$ (90:10) showed that there was no variation outside of 1 standard deviation in unit cell volume after hydrogen treatment at 300°C with
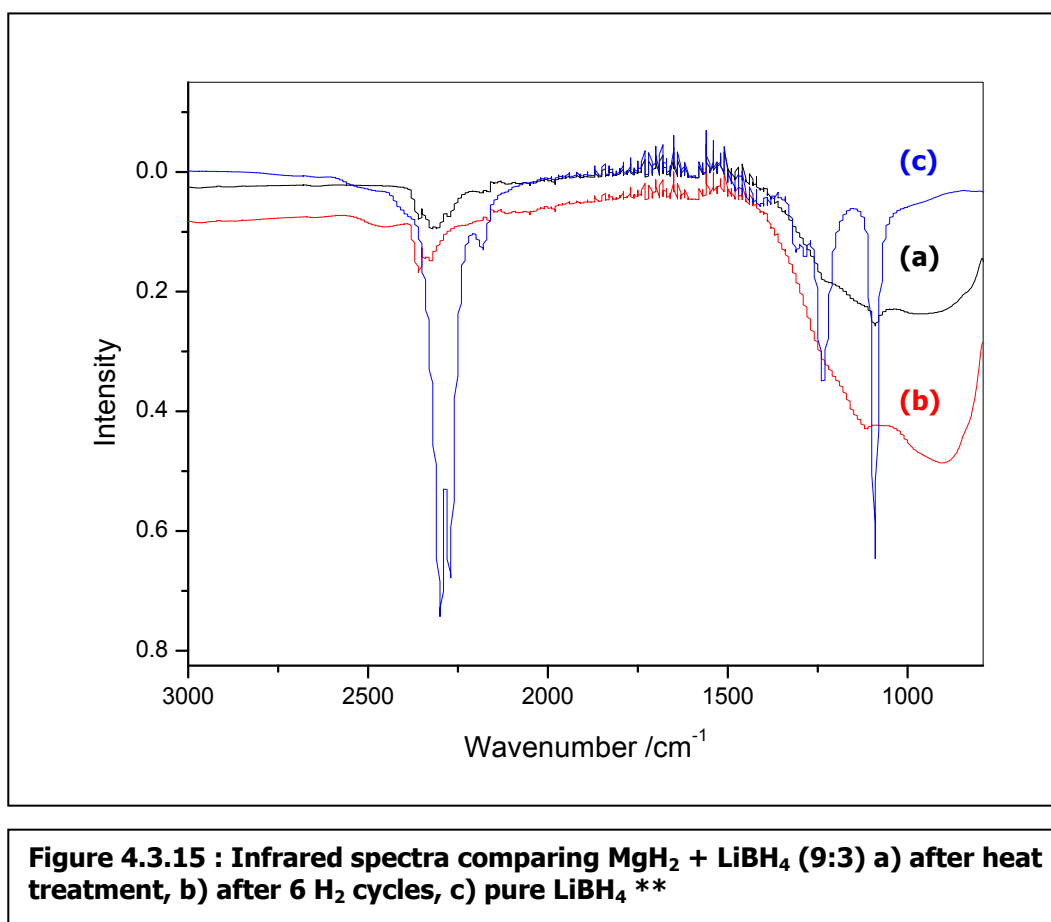
173

Avocado MgH_2 and Goldschmidt MgH_2 which would suggest that there is no increased interaction over successive cycles. The similar reduction in unit cell size over the whole range of MgH_2:$LiBH_4$ ratios could indicate that any Li or B substitution into the Mg lattice that does occur can only do so in very low concentrations.

The hydriding kinetics of Goldschmidt MgH_2 + $LiBH_4$ in the ratio 9:3 were investigated after the apparent discrepancy in unit cell volume was discovered. It was found that MgH_2 + $LiBH_4$ 9:3 completed desorption on the 6th cycle within 145 minutes, with 90% of the total weight loss reached within ~ 65 minutes compared to 130 minutes for the sample with a ratio of 9:1. The 6th cycle absorption completed within 245 minutes, reaching 90% of the total weight gain within 45 minutes compared with 70 minutes for the 9:1 ratio sample.

Infrared spectroscopy was performed on the sample and a comparison of two specimens in their hydrided state is shown in figure 4.3.15. It is immediately clear that $LiBH_4$ is present in some form after heat treatment and before hydrogen cycling as evidenced by the absorptions at 1090 and 1238 cm^{-1} corresponding to BH_2 deformation (and also previous X-ray data). However the absorptions at 2181, 2274, 2302 and 2379 cm^{-1}, corresponding to B-H terminal stretches, are not clearly visible due to both the low $LiBH_4$ content and also the occluding CO_2 asymmetric stretch occurring at ~ 2349 cm^{-1} that is a result of atmospheric CO_2 in the path of the IR beam.

After hydrogen cycling the $LiBH_4$ absorptions have disappeared or shifted which is in agreement with the lack of observed $LiBH_4$ X-ray reflections. There are new absorptions at 1112, 2318 and 2357 cm^{-1} though these are very close to $LiBH_4$ absorptions which may result from the presence of a modified B-H bonding environment which might suggest that the [BH_4^-] anion still exists though not in its usual conformation. Due to the relationship between wavenumber, bond strength and mass of the atoms involved in the bond, this shift to higher wavenumber might correspond to an increase in bond strength which might occur if magnesium had a partial bond with the hydrogen. However, this would be offset by increase

174

in the overall mass of atoms involved in bonding with the hydrogen which would result in a decrease in wavenumber. The increase in wavenumber might also be observed if the $LiBH_4$ structure was hydrogen deficient as this would cause the overall mass of atoms in the bonding environment to decrease whilst simultaneously strengthening the remaining B-H bonds due to the charge imbalance at the boron centre of a $[BH_3]$ complex compared to the Li^+.

Figure 4.3.15 : Infrared spectra comparing MgH$_2$ + LiBH$_4$ (9:3) a) after heat treatment, b) after 6 H$_2$ cycles, c) pure LiBH$_4$ **

While this result points to a unique interaction between MgH_2 and $LiBH_4$ it does not clarify what form this interaction takes.

4.3 (f) Investigation into the interaction between MgB$_2$ and MgH$_2$

Due to the increase in the hydrogen sorption kinetics of MgH$_2$ when heated with LiBH$_4$ and the lack of LiBH$_4$ reflections observed during XRD after hydrogen cycling in early experimentation, it was thought that MgB$_2$ might be formed in small amounts – perhaps microcrystalline and thus difficult to detect through powder XRD – and that the presence of this compound might have an important effect on magnesium H$_2$ sorption kinetics.

MgB$_2$ has recently been discovered to be a superconducting material[11] and it has also been shown that hydrogen will react with the compound at high temperatures and moderate pressures (600°C, ≤10bar) to form the stable phase MgB$_2$H$_{0.034}$[12]. While MgB$_2$ normally is not formed below temperatures of 530°C, it has been shown that reduction in Mg particle size or reaction with Mg vapour will reduce the temperature requirement for the formation of MgB$_2$[13]. The presence of excess magnesium also seems to encourage the formation of the MgB$_2$ phase.

To test this theory a sample of MgH$_2$ + MgB$_2$ (95:5) (to keep the molar ratio of boron the same) was heated at 300°C for 12 hours under static vacuum, as per previous MgH$_2$ + LiBH$_4$ (90:10) samples, and the hydrogen sorption kinetics were measured.

Figure 4.3.16 shows the comparison between powder X-ray diffraction patterns performed on a Siemens D5000 of the MgH$_2$ + MgB$_2$ (95:5) sample before and after hydrogen cycling. MgB$_2$ is clearly observed before and after cycling. The large proportion of MgO observed is due to its presence in the MgH$_2$ sourced from Avocado.

Table 4.3.1 shows the unit cell values for MgH$_2$, Mg and MgB$_2$ crystal structures both before and after hydrogen cycling. There was no significant change in the unit cell values after hydrogen cycling, therefore making it unlikely that MgB$_2$ interacted with either MgH$_2$ or Mg.
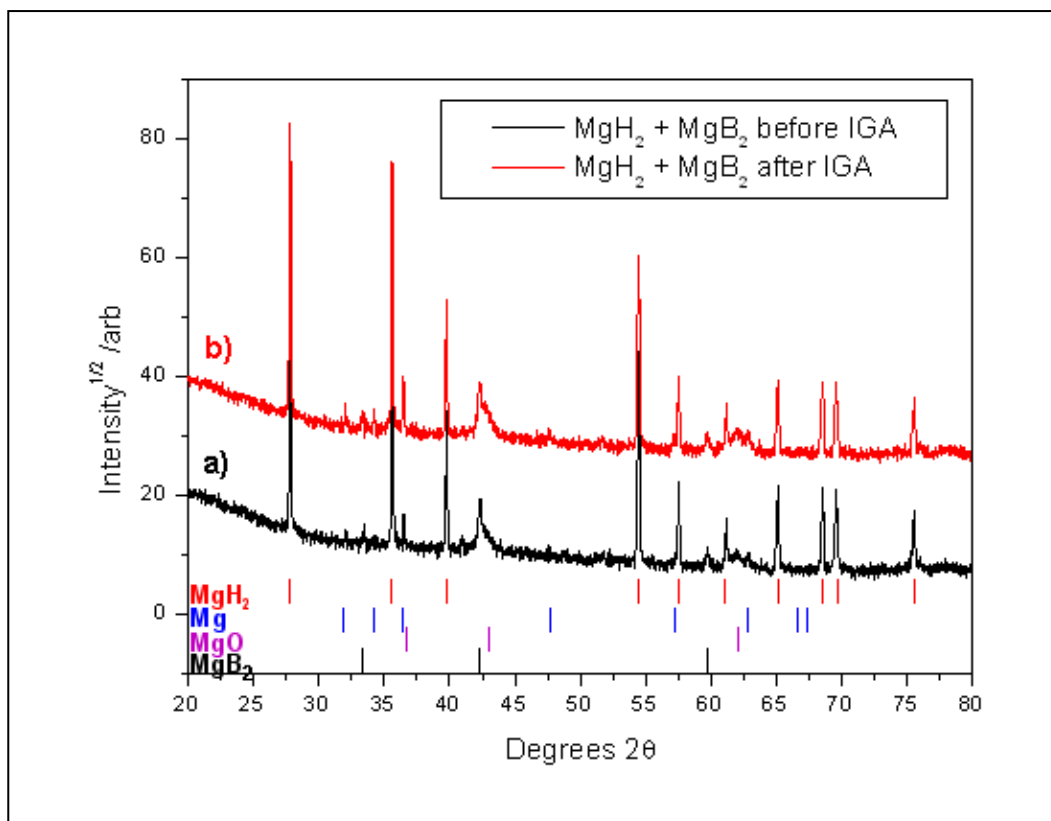
Figure 4.3.16 : Powder X-ray diffraction patterns for MgH₂ + MgB₂ (95:5) a) before and b) after hydrogen cycling **

Before H₂ cycling	a /Å	b /Å	c /Å
MgH₂	4.522(9)	4.522(9)	3.024(9)
Mg	3.21(5)	3.21(5)	5.21(5)
MgB₂	3.094(5)	3.094(5)	3.534(5)
After H₂ cycling			
MgH₂	4.521(8)	4.521(8)	3.024(8)
Mg	3.218(3)	3.218(3)	5.223(8)
MgB₂	3.094(5)	3.094(5)	3.528(6)

Table 4.3.1 : Calculated unit cell values from X-ray diffraction data

4.3 (g) Investigation into the effect of MgB$_2$ on the H$_2$ kinetics of MgH$_2$

Figure 4.3.17 shows the absorption kinetics for MgH$_2$ + MgB$_2$ (95:5). The sixth absorption achieved 4.9 wt% H$_2$ in 332 minutes with 90% of this reached within 121 minutes. This is in comparison with pure MgH$_2$ which achieved 5.0 wt% H$_2$ in 323 minutes, reaching 90% of this within 170 minutes – a slight improvement for the majority of the uptake.
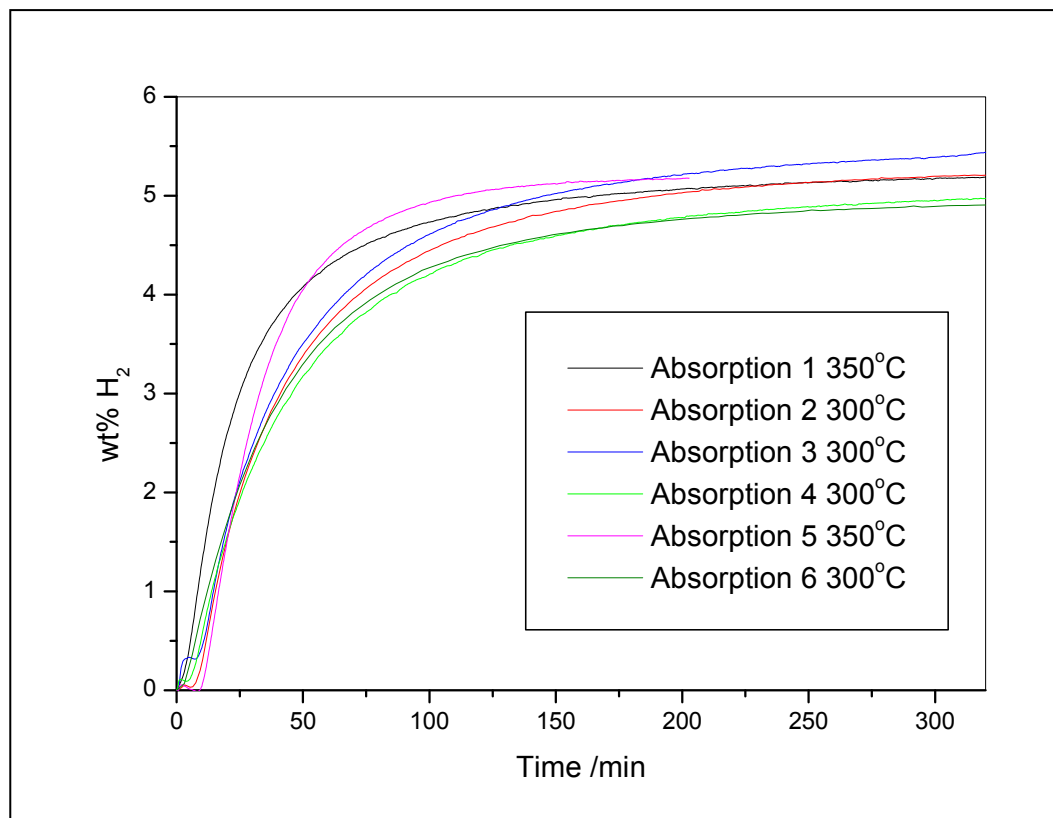

Figure 4.3.17 : Kinetic traces for MgH$_2$ + MgB$_2$ (95:5) for absorption steps under 10 bar H$_2$ at the indicated temperatures **

Figure 4.3.18 shows desorption kinetics for MgH$_2$ + MgB$_2$ (95:5), with most traces performed at 350°C due to time considerations. The sixth desorption achieved 5.2 wt% in 83 minutes with 90% of this loss occurring within 53 minutes. Further mass loss was observed for all desorption steps due to sublimation of the magnesium; this occured at a constant rate and can be disregarded, though it does account for differences in total wt% on each cycle.
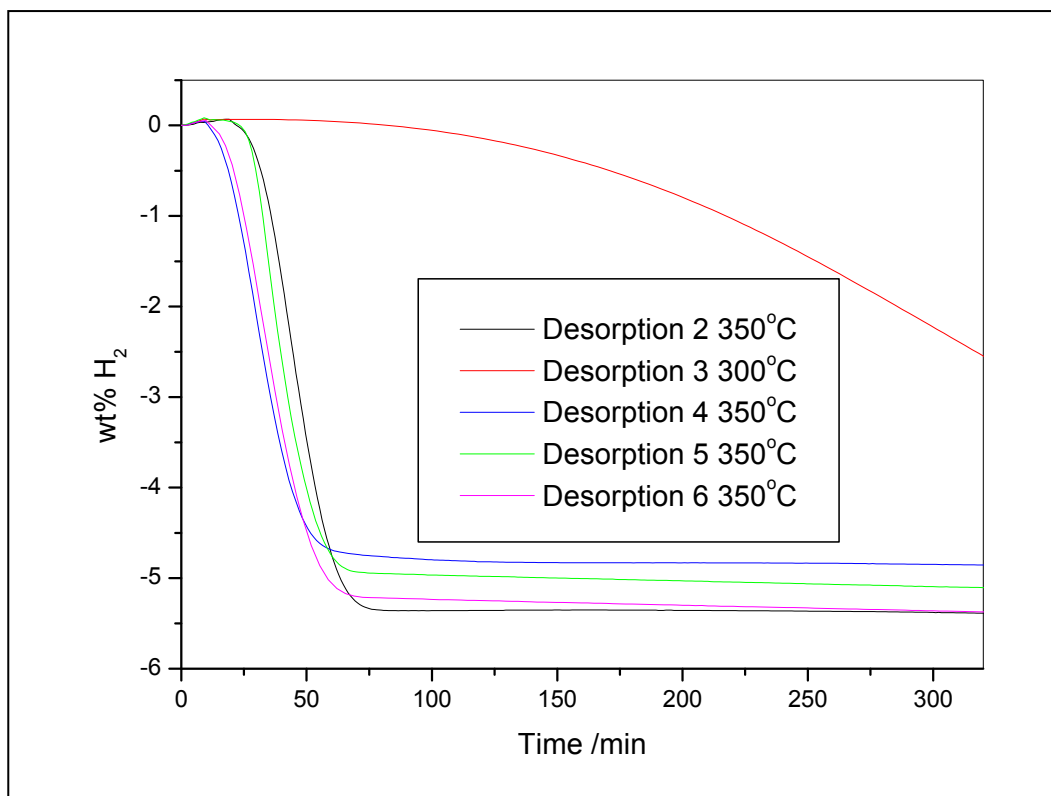
Figure 4.3.18 : Kinetic traces for MgH_2 + MgB_2 (95:5) for desorption steps under 10 mbar H_2 at the indicated temperature **

These results are interesting: while the kinetics of absorption and desorption are not as fast as for $LiBH_4$ containing samples, heating with MgB_2 still resulted in an improvement. Table 4.3.2 lists a comparison of the 90% completion times for absorption and desorption on the 2nd and 6th cycles. While the second absorption was comparable with a sample of Mg + $LiBH_4$ (90:10), the sixth absorption is slower than samples containing $LiBH_4$ but faster than pure MgH_2. Surprisingly, the desorption kinetics did not improve by the same amount.

Clearly, MgB_2 had a slightly beneficial effect on absorption kinetics but this also indicates that the kinetic improvements observed for MgH_2 + $LiBH_4$ could not only be caused by the possible presence of MgB_2 in the sample: Li must have an effect on the absorption kinetics and the evidence from IR spectroscopy for the samples heated with $LiBH_4$ suggests that there are still B-H bonding units present in the hydrided sample. It is also unlikely that, if formed at these low temperatures, MgB_2 would contribute towards hydrogen absorption or desorption by

179

facilitating the propagation of hydrogen by becoming partially hydrided as this process usually

takes place at temperatures above 600°C

2nd cycle	Time to 90% completion /mins	
	Desorption	Absorption
Aldrich MgH$_2$	847	n/a
Aldrich + LiBH$_4$ (90:10)	54	84
Mg + LiBH$_4$ (90:10)	103**	147**
MgH$_2$ + MgB$_2$ (95:5)	535 (3rd used)**	149**
6th cycle		
Aldrich MgH$_2$	38	170
Aldrich + LiBH$_4$ (90:10)	30	24
Mg + LiBH$_4$ (90:10)	n/a	49**
MgH$_2$ + MgB$_2$ (95:5)	53**	121**

Table 4.3.2 : 90% completion times for absorption and desorption kinetics in the 2nd and 6th cycles (6th cycle desorption kinetics are performed at 350°C) **

1. Anderson P.J. and Horlock R.F., *Thermal decomposition of magnesium hydroxide.* T. Faraday. Soc., 1962. 58(478): p. 1993.

2. James Jr. C.W., Tamburello D.A., Brinkman K.S., Gray J.R., Hardy B.J., and Anton D.L., *Environmental exposure of 2LiBH$_4$+MgH$_2$ using empirical and theoretical thermodynamics.* Int. J. Hydrogen Energ., 2010. Article in Press.

3. Brinkman K.S., Gray J.R., Hardy B., and Anton D.L., *The hydrolysis and oxidation behaviour of lithium borohydride and magnesium hydride (LiBH$_4$ MgH$_2$) determined by calorimetry*. 2008, Savannah River National Laboratory: URL:**http://sti.srs.gov/fulltext/WSRC-STI-2008-00155.pdf**.

4. Touboul M. and Bétourné E., *Dehydration process of lithium borates.* Solid State Ionics, 1996. 84: p. 189.

5. Varin R.A., Czujko T., Chiu Ch., and Wronski Z., *Particle size effects on the desorption properties of nanostructured magnesium dihydride (MgH$_2$) synthesized by controlled reactive mechanical milling (CRMM).* 2006. 424(1-2): p. 356.

6. Vigeholm B., Jensen K., Larsen B., and Schroder-Pedersen A., *Elements of hydride formation mechanisms in nearly spherical magnesium powder particles.* J. Less Common Met., 1987. 131: p. 133.

7. Bogdanovic B., Liao S., Schwicardi M., Sikorsky P., and Spliethoff B., *Catalytic synthesis of magnesium hydride under mild conditions.* Angew. Chem. Int. Ed. Engl., 1980. 19(10): p. 818.

8. Nikulin L.V., Lykasova G.L., and Shklyaeva N.M, *Structure and properties of binary magnesium-lithium alloys subjected to pressure casting.* Met. Sci. Heat Treat+, 1986. 28(10): p. 777.

9. Chen Y., Wu C., Wang P., and Cheng H., *Structure and hydrogen storage property of ball-milled LiNH$_2$/MgH$_2$ mixture.* 2006. 31(9): p. 1236.

10. Mao J.F., Wu Z., Chen T.J., Weng B.C., Xu N. X., Huang S., Guo Z.P., Liu H.K., Grant G.S., and Yu X.B., *Improved hydrogen storage of LiBH$_4$ catalyzed magnesium.* J. Phys. Chem. C, 2007. 111(33): p. 12496.

11. Nagamatsu J., Nakagawa N., Zenitani Y., and Akimitsu J., *Superconductivity at 39 K in magnesium diboride.* Nature, 2001. 410(6824): p. 63.

12. Flambaum V.V., Stewart G.A., Russell G.J., Horvat J., and Dou S.X., *The effect of hydrogenation on the superconducting transition temperature of MgB$_2$.* Physica C, 2002. 382: p. 213.

13. Yan S., Lu Y., Liu G., Yan G., and Zhou L., *The kinetic analysis of formation behavior for the MgB$_2$ phase.* J. Alloys Compd., 2007. 443: p. 161.

4.4   Sorption properties of magnesium

Experimental technique 4.4

Heat treatment of Mg + LiBH$_4$

A mixture of Mg (Strem, 99%) and LiBH$_4$ (Acros Organics, 95%) was prepared for heat treatment under a static vacuum as described in Experimental Technique 4.2. The sealed quartz sample tube was heated to 300°C at a rate of 50°C/hour and held at this temperature for 12 hours and then allowed to cool. Very little discolouration of the quartz tube was observed after heat treatment and the sample was recovered within an argon circulating glove box.

A range of mixture ratios were also prepared to study the change in unit cell parameters with increased LiBH$_4$ content during heat treatment as described in Experimental Technique 4.3. The ratios of Mg:LiBH$_4$ prepared were 11:1, 10:2, 9:3, 8:4, 7:5, 6:6, 5:7, 4:8, 3:9, 2:10 and 1:11.

Large sample preparation and processing

The TPD flowing rig was used to synthesise a larger sample of Mg + LiBH$_4$ (90:10) to assess the ease of scaling up the production of the mixture to form the kinetically faster H$_2$ storage material. Section 3.9 covers the layout and capabilities of the TPD flowing rig.

4.5 g of Mg (Strem, 99%) and 0.448 g LiBH$_4$ (Acros Organics, 95%) were mixed together (not ground in a mortar and pestle) in an argon circulating glove box. The mixture was then transferred to the stainless steel reaction chamber which was sealed by connecting the stainless steel T-piece that is affixed to the gas inlet and exhaust valves on the TPD rig via a Swagelok compression fitting that is sealed with an aluminium or copper gasket. The T-piece's plug valves were closed off and the whole apparatus was removed from the glove box and attached to the inlet and exhaust pipes on the flowing TPD system.

The pipeline leading to the gas inlet of the T-piece and reaction chamber was then evacuated to 1x10^{-3} by a rotary pump then filled with 1 bar argon and evacuated again – this process was repeated 3 times to remove any O$_2$ or H$_2$O. The inlet pipeline was then filled with a slightly positive pressure of argon and

a flow rate of 50 ml/min was programmed into the computer control system for the mass flow controllers on the rig. The inlet plug valve to the T-piece was then slowly opened at the same time as the exhaust plug valve to prevent back flow or mixing of atmospheric gases into the reaction chamber and was left to purge the system for 5 minutes. The thermocouple that sits in the reaction chamber through the T-piece was connected up to the monitoring system and the exhaust plug valve to the mass spectrometer was closed and the exhaust plug valve to the second mass flow controller was opened. This set up allows for pressure control with flow control. The band heater was also slotted over the reaction chamber in order to allow for increase in temperature.

For the absorption steps, the plug valve to the argon gas cylinder was closed off and the plug valve to the hydrogen cylinder was opened. A flow rate of 50ml/min was set: this was allowed to purge the system of argon for 5 minutes before flow control was turned off and instead pressure control was set to 10 bar with the regulator on the H_2 cylinder set to 12 bar (the mass flow controllers would vent excess pressure but input hydrogen gas if the pressure fell below 10 bar). Once at 10 bar pressure, the temperature control was set to ramp up to 300°C at a rate of 10°C/minute. The software on the computer was set to record the temperature and pressure changes and the sample was left to heat at 300°C until gas was no longer being admitted – denoting the point at which hydrogen was no longer being absorbed by the sample. The sample was then cooled to room temperature. Then the pipes were purged with argon for five minutes before closing all the plug valves, disconnecting the thermocouple and removing the band heater. The T-piece was then removed from the TPD rig and replaced in the glove box where a spatula was used to mix the sample within the sample chamber and some sample was removed and place in a vial for analysis. The T-piece was then refitted with a new gasket and removed from the glove box and replaced on the TPD rig which was flushed with argon as above.

For the desorption steps, the system was purged with argon as noted above and then a flow rate of argon was set at 50ml/min (pressure control was set to off). The band heater was fitted over the reaction chamber and the thermocouple was connected to the monitoring system. The temperature was then set to 300°C at a ramp rate of 10°C/minute. This was then left to desorb over a period of 12 hours at which point the sample was cooled, the thermocouple disconnected and band heater removed. The T-piece was removed after closing all the plug valves and replaced in the glove box for mixing with a spatula and removing some of the sample for further analysis.

Raman measurements

A Renishaw confocal dispersive Raman spectrometer was used to study the Raman shifts in samples from the large sample preparation between Mg + LiBH$_4$ in the ratio 90:10. In an argon circulating glove box the samples were loaded into a pressure cell that had an Raman inactive window in the lid, which was sealed with a rubber O-ring and bolts. The cell also had valves to admit gases though these were not used so they were closed off. The pressure cell was then removed from the glove box and placed within the Raman spectrometer.

The 488 nm laser was used to probe the samples for Raman shifts and they were recorded as spectra ranging from 80 – 4500 cm^{-1}.

General experimental techniques

XRD performed on the D5000, IGA and SEM measurements, grain size determination and wt% calculations were performed as described in the Experimental Technique 4.1 section. Synchrotron source XRD were performed as described in Experimental Technique 4.2.
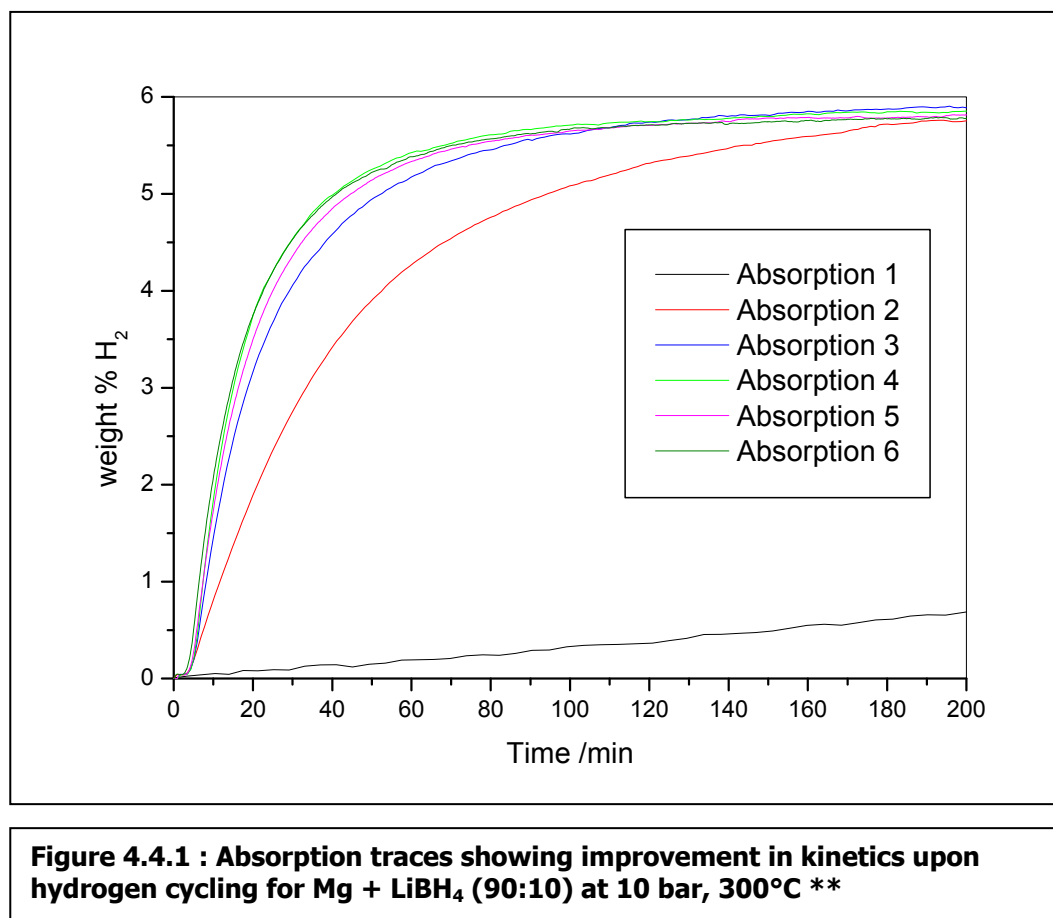
4.4 (a) Reaction of Mg with LiBH$_4$:

With the various inconsistencies inherent in having to rely on the quality of the sourced magnesium hydride and the discontinuation of the preferred source, the decision was made to study the amount of hydrogen cycling required and the effect of LiBH$_4$ on hydrogenation kinetics when starting from magnesium metal. There are commercial factors that favour magnesium as the starting reagent when compared with MgH$_2$: price and production. Magnesium is easier and cheaper to produce with fewer processing steps than magnesium hydride. There are also a number of different ways to produce a variety of particle sizes from gas-phase deposition to nano-cluster formation in organic reactions[1, 2]. Magnesium from the supplier Strem was obtained (-325 mesh, 99% Mg, 1% impurity). The mesh size puts a maximum value on particle size in the reagent and a -325 mesh corresponds to particles 44μm and below. The grain size was also determined via the scherrer equation to be 540nm ±2 which is larger than the previous MgH$_2$ grain sizes in as-received reagent.

Magnesium (Strem -325 mesh) was heated with LiBH$_4$ in a molar ratio of 90:10 under the same conditions as previous MgH$_2$ samples and the hydrogenation kinetics were measured gravimetrically. The sample was loaded onto the equipment under an argon atmosphere.

Figure 4.4.1 shows the absorption kinetic traces over six successive dehydrogenation /hydrogenation cycles. On the first hydrogenation 6.1 wt% H$_2$ uptake was observed over 4000 minutes (66 hours). Though subsequent absorptions did not reach this level of uptake, the sixth absorption achieved 5.7 wt% in 170 minutes with the 90% of this hydrogen absorption occurring within 50 minutes.

While the initial hydriding step took far longer than previous MgH$_2$ samples, a true comparison cannot be drawn due to the differences in starting composition of the Mg (hydrided vs unhydrided) and any beneficial processing effects that LiBH$_4$ has on the Mg/MgH$_2$ system during the initial desorption may not occur. What is interesting to note is that after the second desorption there is little kinetic improvement and this feature was

previously only seen for samples heated under flowing Ar and H_2/N_2 (10:90) and also the sample that was not pre-heated before cycling.

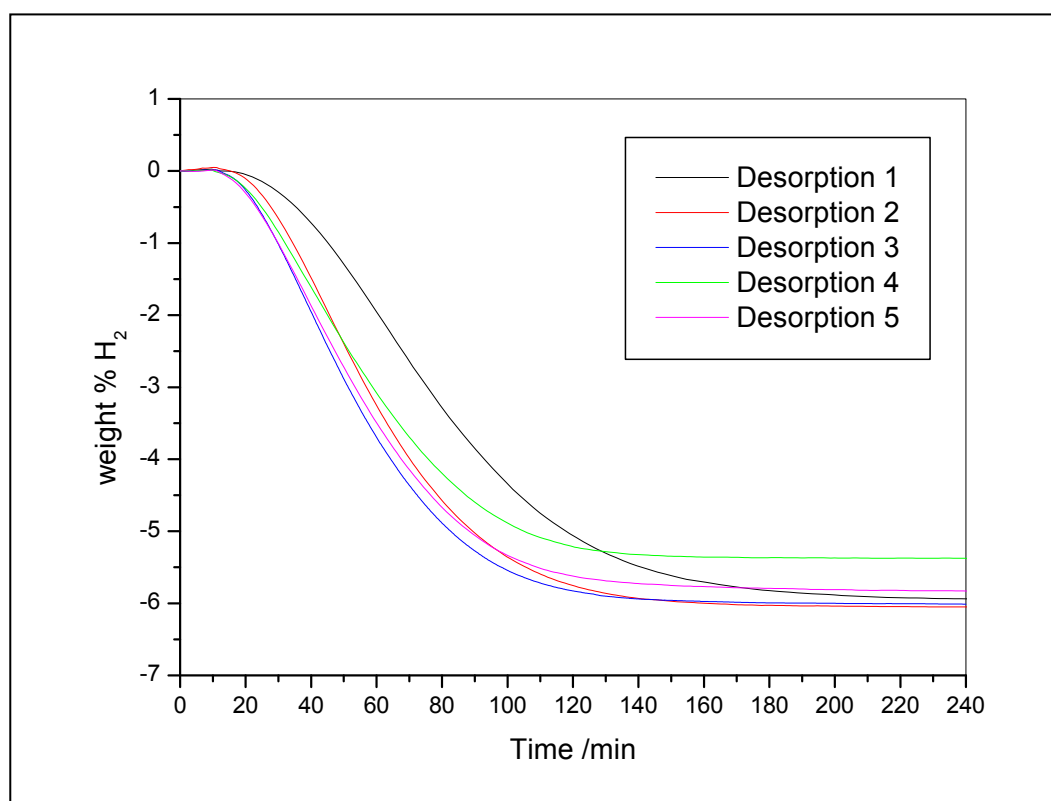**Figure 4.4.1 : Absorption traces showing improvement in kinetics upon hydrogen cycling for Mg + LiBH$_4$ (90:10) at 10 bar, 300°C ****

Desorption traces in figure 4.4.2 show that there was little or no improvement in kinetics upon cycling. The first desorption reached completion within 270 minutes, achieving a loss of 5.9 wt% H_2, while the fifth desorption reached completion within 190 minutes with a loss of 5.8 wt% H_2: 90% of the mass loss occurred before 96 minutes.

In comparison with the Aldrich MgH_2 + $LiBH_4$ (90:10) samples both absorption and desorption kinetics are slower, however, kinetic performance for absorption and desorption of the majority of the hydrogen capacity lies between that of Goldschmidt samples in the ratio 90:10 and 9:3 (Table 4.4.1). This would suggest that the $LiBH_4$ content is not the only variable affecting the kinetics. A number 325 mesh allows particles of 44 µm or less to pass through and it could be this aspect of the microstructure that enables easier H_2 diffusion.

2nd cycle	Time to 90% completion /mins	
	Desorption	Absorption
Strem + LiBH$_4$ 90:10	103**	147**
Aldrich + LiBH$_4$ 90:10	55	85
Avocado + LiBH$_4$ 90:10	705**	380**
Goldschmidt + LiBH$_4$ 90:10	163**	161**
Goldschmidt + LiBH$_4$ 9:3	50**	118**
6th cycle		
Strem + LiBH$_4$ 90:10	96**	50**
Aldrich + LiBH$_4$ 90:10	56	24
Avocado + LiBH$_4$ 90:10	180**	70**
Goldschmidt + LiBH$_4$ 90:10	130**	70**
Goldschmidt + LiBH$_4$ 9:3	65**	45**

**Table 4.4.1 : Comparison of desorption and absorption kinetics for the 2nd and 6th H$_2$ cycle (times to reach 90% completion) **

**Figure 4.4.2 : Desorption traces showing improvement in kinetics upon hydrogen cycling for Mg + LiBH$_4$ (90:10) at 10 mbar, 300°C **

Figure 4.4.3 displays the SEM images for the magnesium powder (-325 mesh) sourced from Strem. Particle sizes range from lengths of 10 – 90 µm with the majority of the particle material lying no more than 30 µm from the nearest edge. These values are lower than for the three MgH_2 reagents and the improved kinetics over the equivalent 90:10 ratio samples may result from this difference.
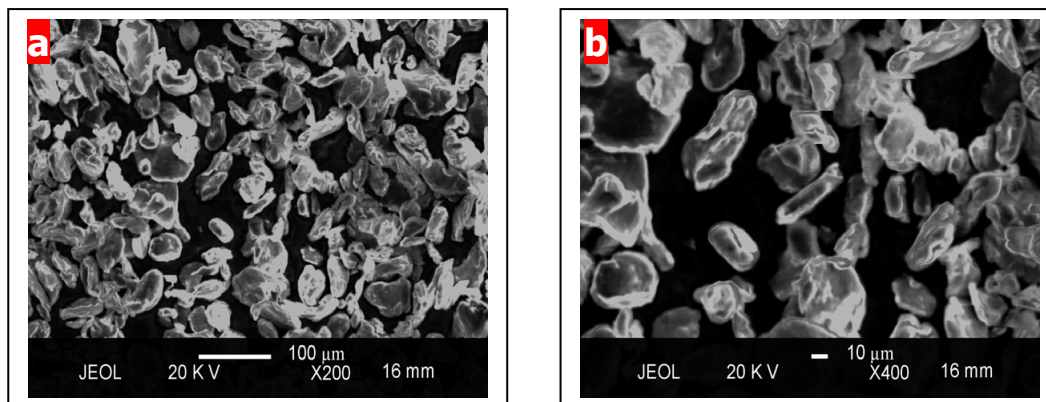
Figure 4.4.3 : SEM images showing Strem magnesium as received from the suppliers at a) x200 magnification and b) x400 magnification

4.4 (b) X-ray diffraction phase analysis

As with the MgH_2 + $LiBH_4$ samples, a range of Mg + $LiBH_4$ compositions were heated at 300°C for 12 hours under static vacuum in a sealed quartz tube and then studied via synchrotron X-ray diffraction. Figures 4.4.4 (a) and 4.4.4 (b) depict the synchrotron powder X-ray diffraction patterns for this series. Unfortunately, some ratios are missing from the series due to equipment error at the synchrotron facility. However, the most striking aspect of this series of experiments is that $LiBH_4$ hydrides the magnesium phase during heating under static vacuum. Ratios of 11:1, 10:2, 8:4 and 7:5 showed small amounts of MgH_2, ratios of 9:3, 5:7 and 2:10 showed a higher MgH_2 content but the ratio of 6:6 showed a large amount of MgH_2 present – though it is unknown why this is the case as there is no indication

in any of the unit cell information (Figures 4.4.5 (a) and (b)) that this may be a particularly reactive ratio.

This result might support the observed partial decomposition of $LiBH_4$ to $Li_2B_{12}H_{12}$ and $Li_2B_{10}H_{10}$ at temperatures above 150°C over a number of hours[3-5] and might suggest, with the evidence of new phases being formed from SPXRD in section 4.3 (e), the formation of an intermediate compound being formed and also being instrumental in the kinetic improvement observed for mixture of $Mg(H_2)$ + 10% $LiBH_4$.
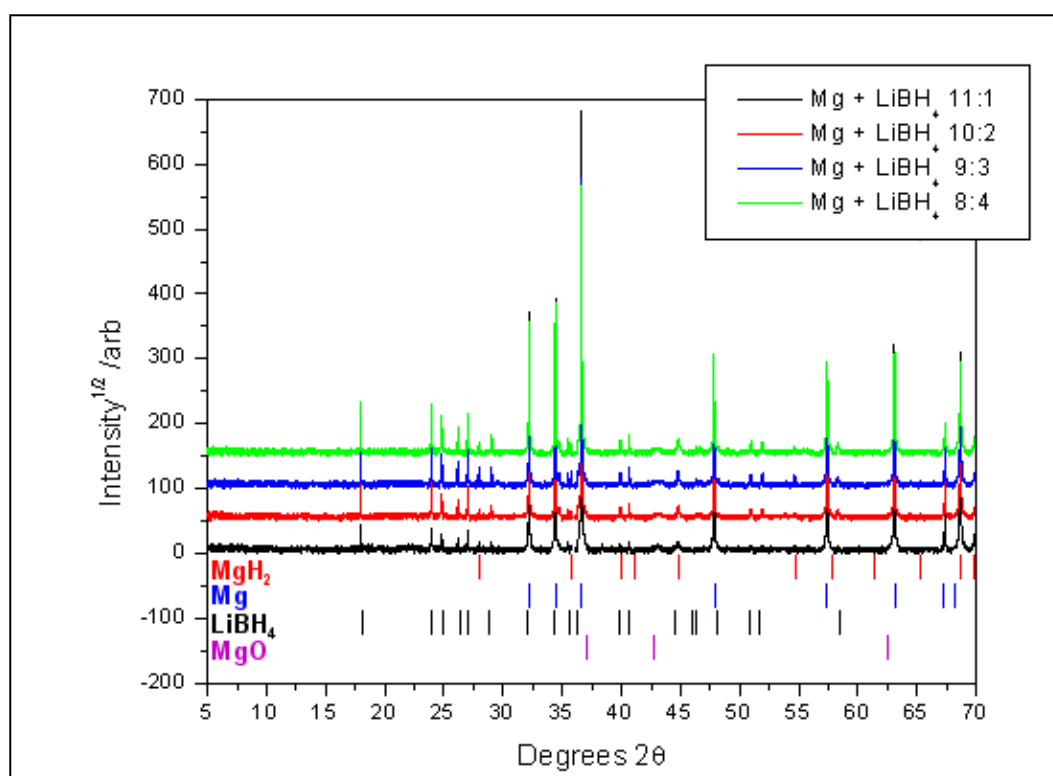
Figure 4.4.4 (a) : Synchrotron PXRD diffraction patterns for various ratios of Mg + LiBH$_4$ heat-treated at 300°C for 12 hours under static vacuum
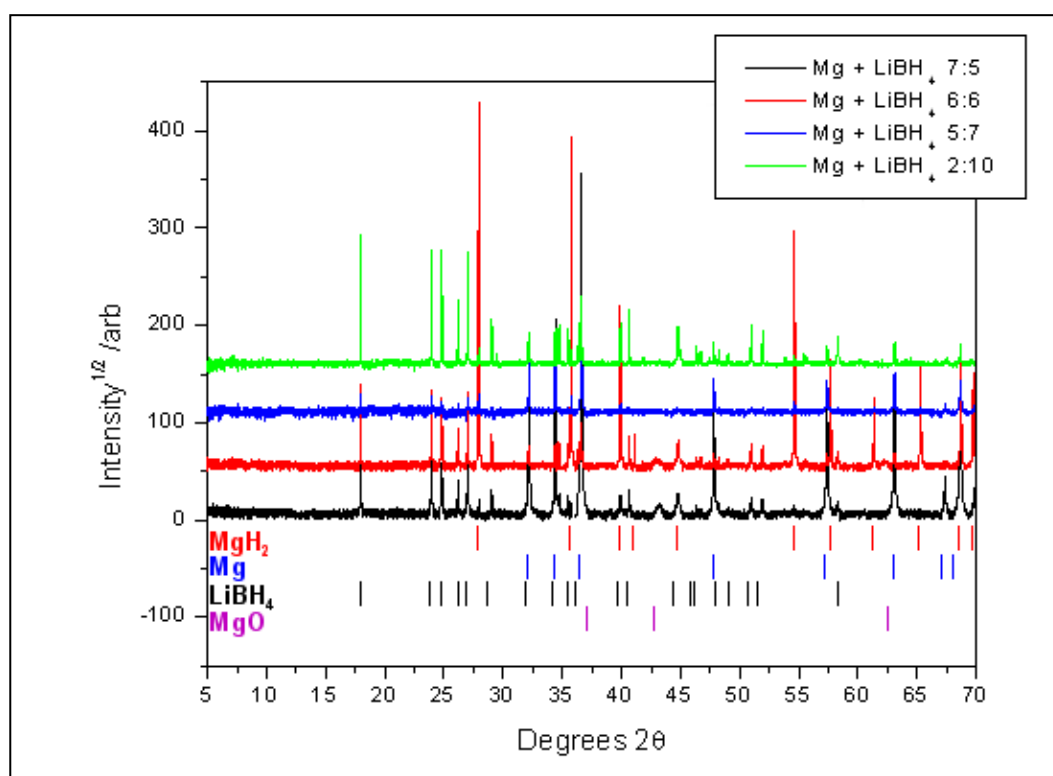
Figure 4.4.4 (b) : Synchrotron PXRD diffraction patterns for various ratios of Mg + LiBH₄ heat-treated at 300°C for 12 hours under static vacuum

Figures 4.4.5 (a) and (b) show a comparison between the calculated unit cell volumes for the MgH$_2$ and Mg phases observed for heated combinations of Goldschmidt MgH$_2$ + LiBH$_4$ and Strem Mg + LiBH$_4$. There was no MgH$_2$ phase present in the as-received Strem Mg reagent and the missing information at ratios 4:8, 3:9 and 1:11 is due to data loss during the experiment at the ESRF. Lack of error bars at some ratios – specifically for the hydride phase in Strem Mg + LiBH$_4$ series (Figure 4.4.5 (b)) - is due to the limited number of reflections available to index and low concentration of MgH$_2$ in the sample – estimated error and thus standard deviation could not be calculated by the CELL programme for these ratios, though points without error bars would have larger errors than the ones that have been presented.

While there is a slight downward trend for both Goldschmidt and Strem Mg unit cell values with increased LiBH$_4$ concentration, the Mg unit cell volumes are all within three standard deviations of as-received Strem and each other. The mean unit cell volume is 53.66 Å^3

±0.022 which is slightly lower than that observed for Goldschmidt (53.7 $Å^3$ ±0.08). This might suggest that lithium is being doped into the Mg crystal structure which might cause an overall reduction in unit cell size and therefore volume. However, the process of forming MgH_2 would remove magnesium from the Mg lattice which might also cause a slight contraction of unit cell values and thus volume.

Due to the poor quality of the calculated MgH_2 unit cell data in figure 4.4.5 (b), no conclusion can be drawn other than the observed values appear to be similar to those found in the Goldschmidt MgH_2 samples. The mean MgH_2 unit cell volume is 61.59 $Å^3$ ±0.26 which is within three standard deviations of the values for Goldschmidt and avocado MgH_2 samples.
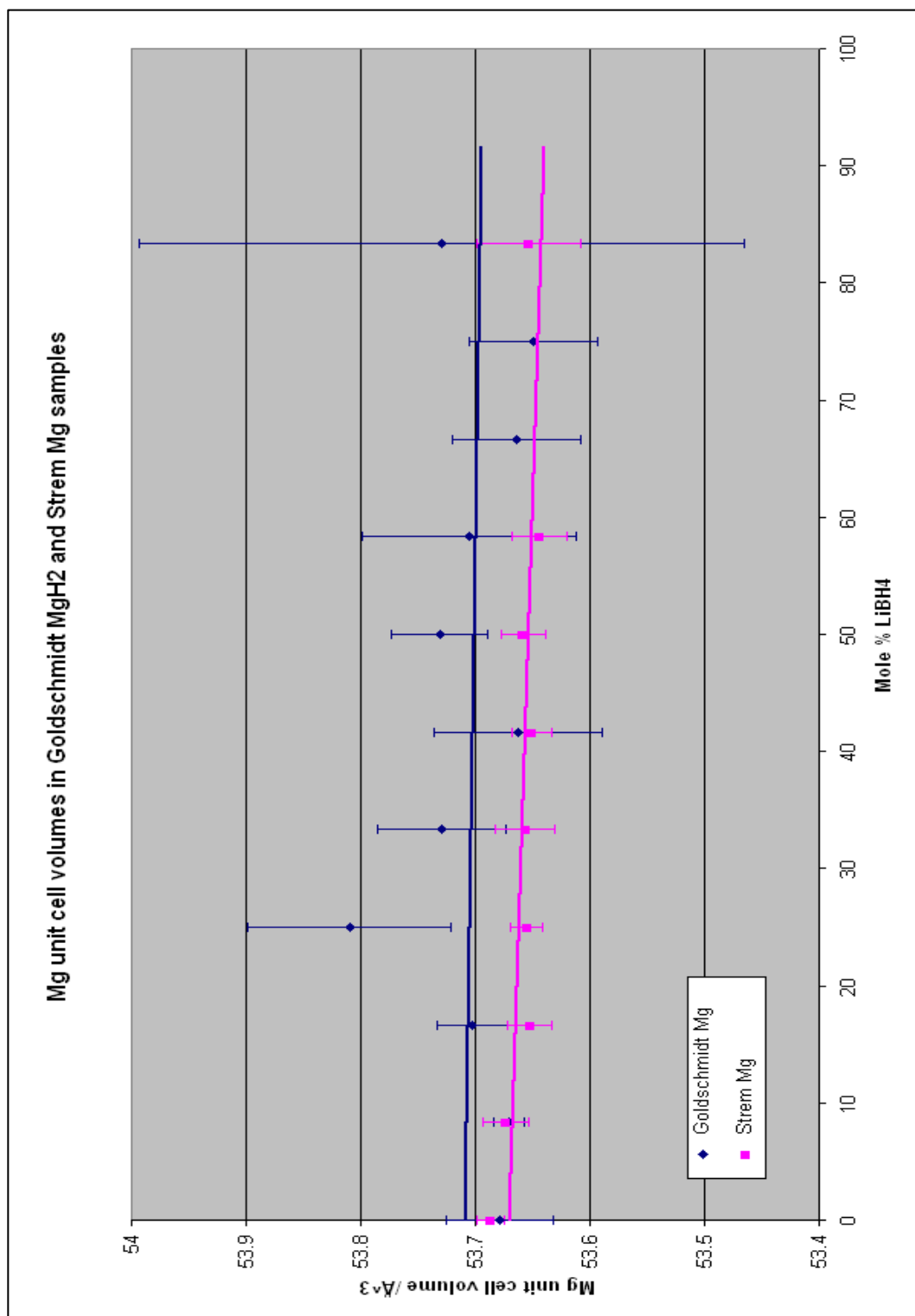
Figure 4.4.5 (a) : Point plots comparing unit cell volumes for the Mg phase for various Strem Mg + LiBH$_4$ and Goldschmidt MgH$_2$ + LiBH$_4$ compositions after heating with LiBH$_4$ in the stated ratios. Error bars show the range of 3 standard deviations from each data point. All data was obtained from the ESRF synchrotron source at Grenoble
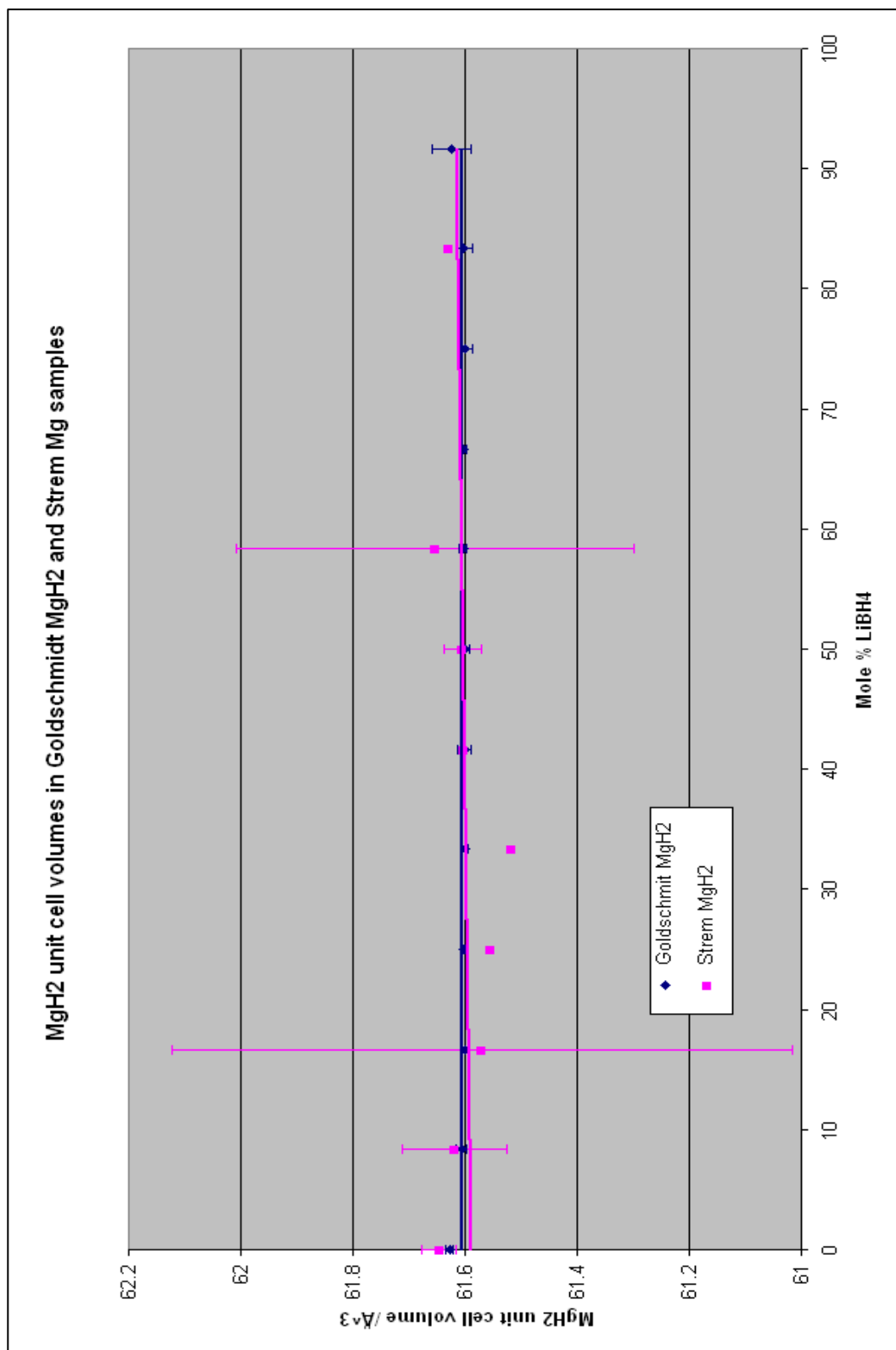
Figure 4.4.5 (b) : Point plots comparing unit cell volumes for the MgH$_2$ phase for various Strem Mg + LiBH$_4$ and Goldschmidt MgH$_2$ + LiBH$_4$ compositions after heating with LiBH$_4$ in the stated ratios. Error bars show the range of 3 standard deviations from each data point. All data was obtained from the ESRF synchrotron source at Grenoble

Figure 4.4.6 shows the calculated unit cell volumes for $LiBH_4$. Interestingly, these also seem to decrease with increased $LiBH_4$ content as compared with pure $LiBH_4$.

New phases were observed for Mg + $LIBH_4$ ratios of 11:1, 6:6 and 2:10 – each one with unique reflections and all of them at higher angles than those observed for samples of MgH_2 heated with $LiBH_4$ (Figure 4.4.7). It has been reported that doping of Li into the Mg lattice will convert the hexagonal structure to a cubic structure with partial conversion at 5.7 at% and complete at 10.7 at%[6] so it is possible that a small amount of Li is being inserted into the Mg structure to form a cubic Mg-Li alloy, however, preliminary cell refinements have not found an exact fit for the observed phases.
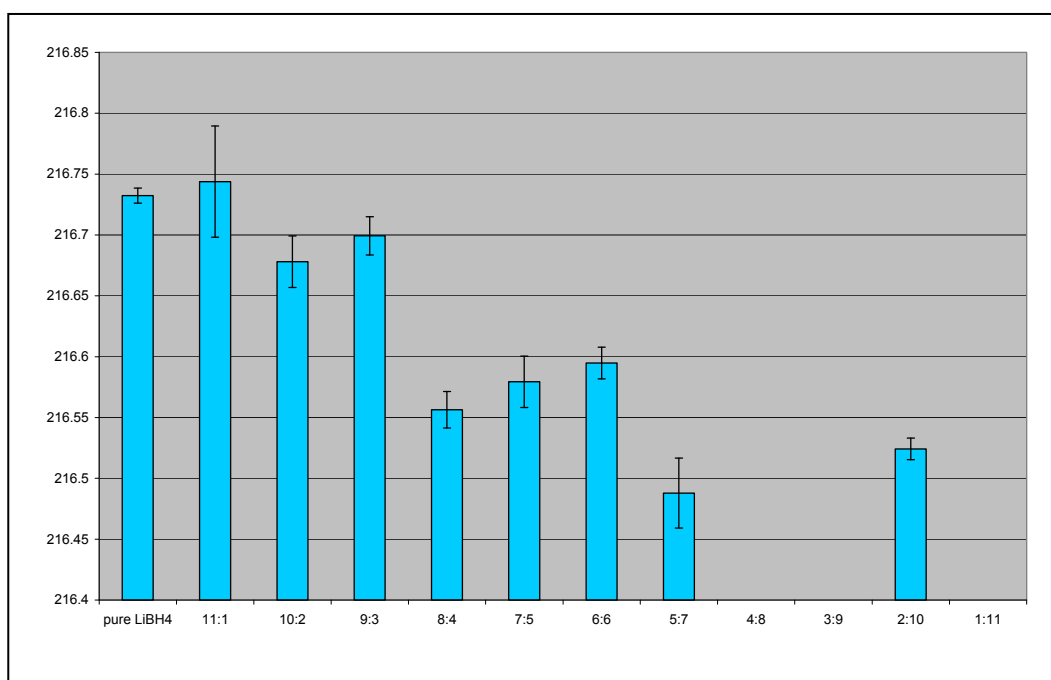

Figure 4.4.6 : Column plots depicting unit cell volumes for $LiBH_4$ over various Strem Mg + $LiBH_4$ compositions from pure $LiBH_4$ to Mg + $LiBH_4$ (2:10) after heating in the stated ratios. Error bars show the range of 2 standard deviations from each data point. All XRD data was obtained from the ESRF synchrotron source at Grenoble
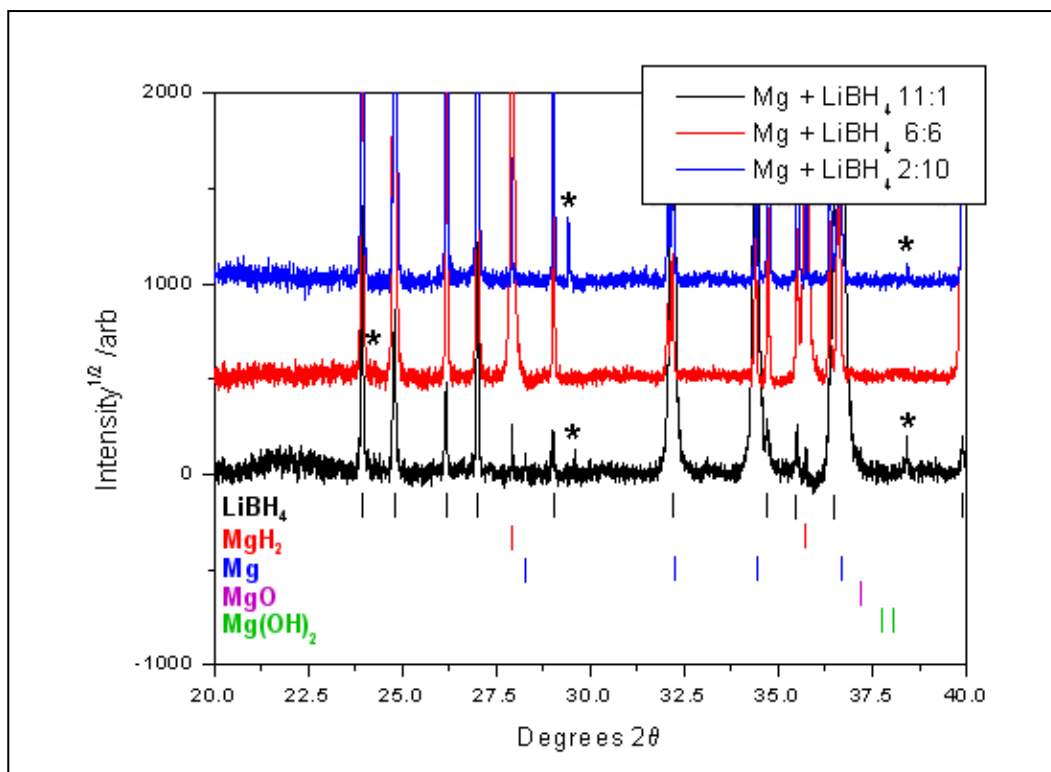
Figure 4.4.7 : Synchrotron PXRD diffraction patterns for heat-treated Mg + LiBH₄ samples in the shown ratios highlighting the new reflections that were observed. Complete spectra are shown in Figures 4.4.4 (a) and (b)

4.4 (c) Large sample preparation and processing:

A flowing TPD system was designed and built (a description of which can be found in the experimental section) to allow synthesis of larger sample amounts as well as direct hydriding and dehydriding the sample after synthesis. The system setup also allows the samples to be inertly loaded and unloaded to facilitate collection of material at intermediate steps of the process. The system is unable to measure absorption or desorption kinetics with accuracy and is therefore better suited for production of 'chemically activated' (i.e. heated combinations of Mg/MgH_2 + $LiBH_4$) material rather than analysis of its properties.

A sample of Mg + $LiBH_4$ (90:10 ratio) was processed using the TPD system: a 'synthesis' step (heating the sample under a static pressure of argon) was performed before subsequent absorption and desorption steps at 300°C under a static pressure of 10 bar H_2 and flowing

argon respectively. Samples were collected after each step for later analysis. After successively hydriding and dehydriding the sample five times the sample was removed and a small portion placed on the IGA under an argon atmosphere.

Figure 4.4.8 shows the absorption traces obtained from the IGA under the same conditions as previous samples. The sixth absorption (first of the IGA experiment) completed in 200 minutes with 6.9 wt% H_2 uptake achieved with 90% of this total being reached in 110 minutes – the strange curve of the trace is due to ramping temperature from 25 – 300°C. The subsequent absorptions were more uniform in their kinetic performance, completing within 60 minutes and achieving 90% of the total uptake within 36 minutes, though they all had a reduced maximum H_2 capacity. They also showed signs of reduced kinetics: each subsequent absorption reached completion over a longer period.

The desorption traces shown in figure 4.4.9 exhibit fast kinetics which agree with the improvement seen for the absorption traces. The sixth desorption reached its maximum point at 59 minutes (4.3 wt% H_2) though there a slight increase in mass after this point possibly due to absorption of a contaminant to end at 125 minutes with 4.2 wt%. The point at which 90% of the total desorption was reached was at 49 minutes.

There was a large amount of variation for the subsequent desorptions in time to completion and behaviour with regard to amount of mass increase. However, the total mass loss at the end of each desorption step was consistent with the total mass uptake on the corresponding absorption steps.
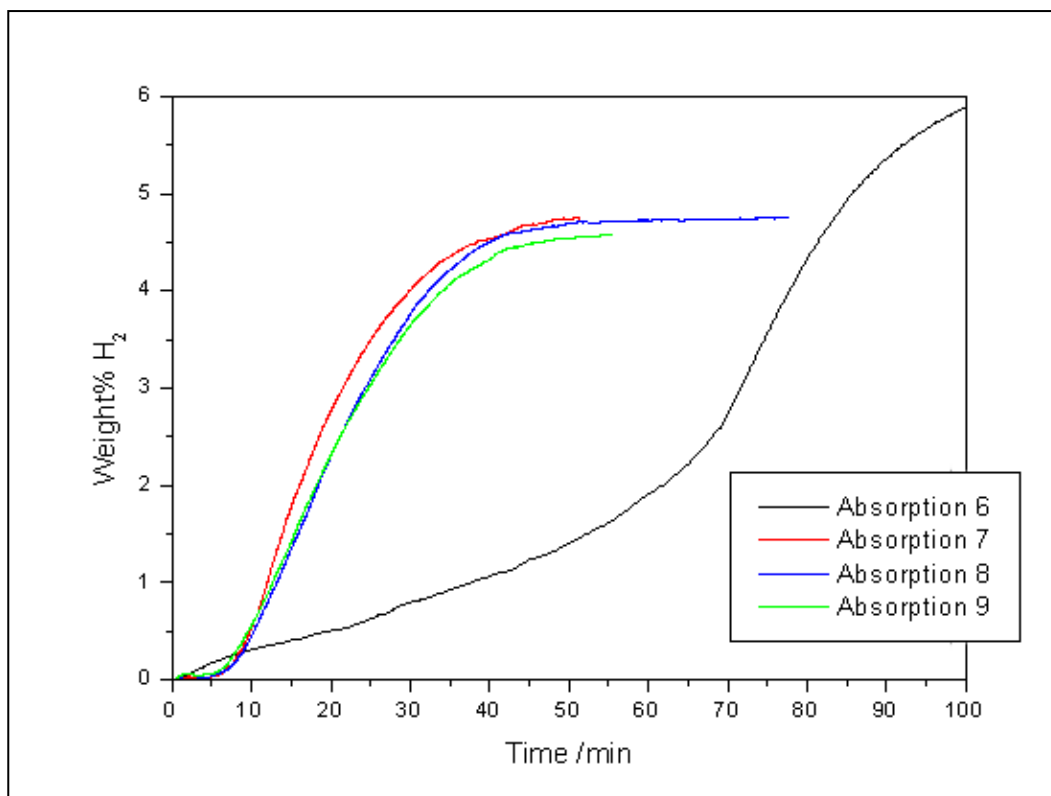
Figure 4.4.8 : Absorption traces for scaled-up Mg + LiBH$_4$ (90:10 ratio) synthesis at 10 bar H$_2$, 300 °C after being processed on a flowing rig

The seventh desorption reached its maximum in approximately 49 minutes with 4.5 wt% H$_2$ desorbed with 90% of this loss occurring in 39 minutes. The eighth cycle was chosen for comparison with earlier MgH$_2$ + LiBH$_4$ samples due to the consistency of the data in curve shape and total weight% of H$_2$. The 8th absorption completed in 77 minutes with an uptake of 4.7 wt% H$_2$ with 90% of this uptake being achieved in 36 minutes. The 8th desorption completed in 89 minutes at 4.4 wt% with 90% of this desorption achieved in 59 minutes.

All of the times for the 7th and 8th cycles are comparable with samples made from Aldrich MgH$_2$ though there is a large difference in total wt% of Hydrogen capacity which could have been affected by contamination which, from the performance seen in the desorption traces, appears to be introduced from the experimental setup. This is further examined in chapter 5.
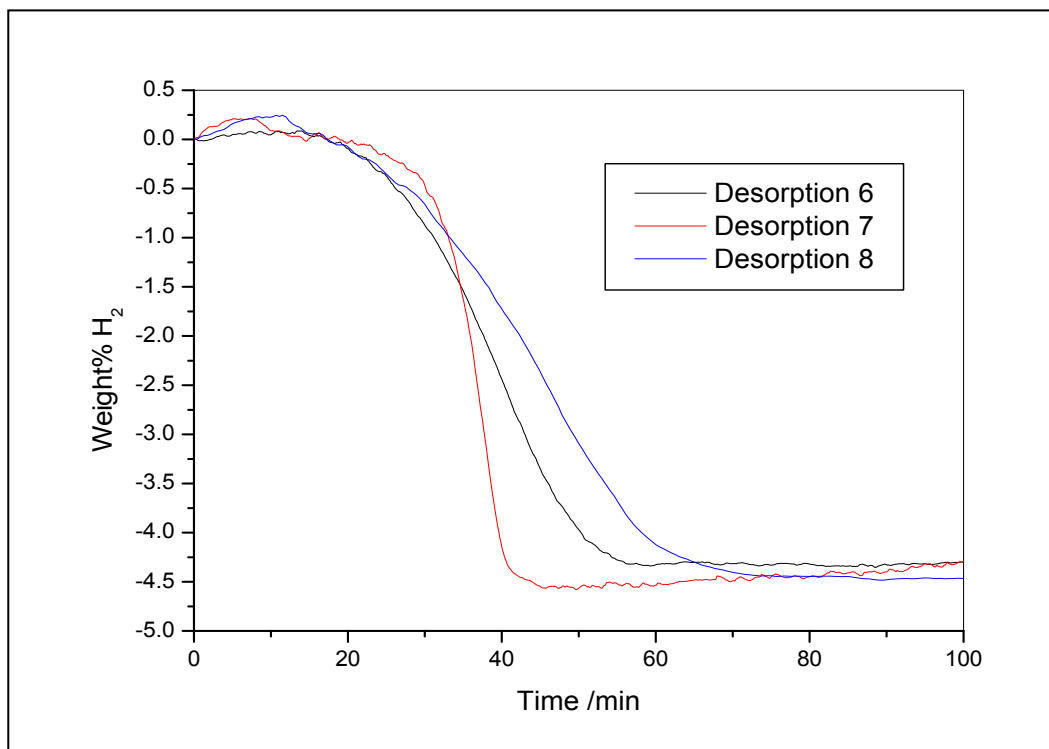
197

Figure 4.4.9 : Desorption traces for scaled-up Mg + LiBH$_4$ (90:10 ratio) synthesis at 10 mbar H$_2$, 300 °C after being processed on a flowing rig

Figure 4.4.10 shows SEM images for the hydrogen cycled Mg + LiBH$_4$ (90:10). The sample shows the same 'coral-like' structure observed in previous MgH$_2$ + LiBH$_4$ (90:10) samples and, as before, is not comprised of discrete particles that are easily identified. Instead, the material's 'growths' form agglomerations which are highly porous and not representative of the size of the particles in the agglomeration with respect to hydrogen diffusion distances - as in a particle of the same size. From the SEM images it is seen that the agglomerations range from ~ 5 μm to ~ 200 μm, with large agglomerations fairly common.
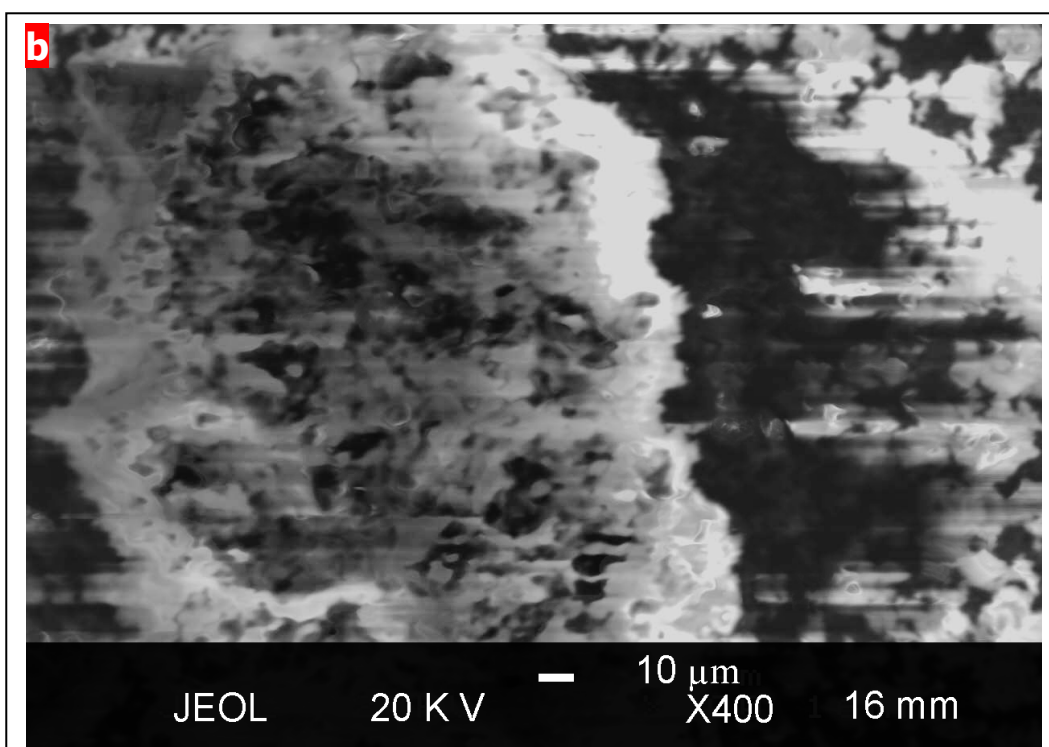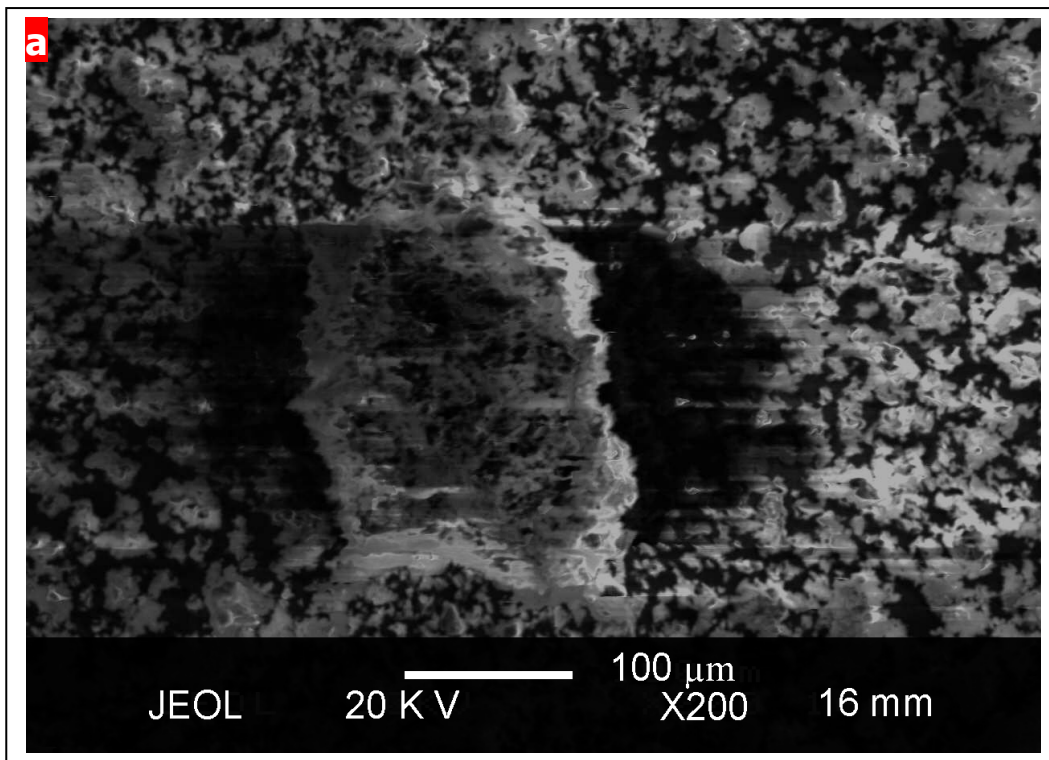
Figure 4.4.10 : SEM images of hydrided Mg + LiBH$_4$ (90:10) after hydrogen cycling at a) x200 and b) x400 magnification

4.4 (d) : Raman Spectroscopy Study

Samples taken from each step of the large sample experiment (both absorption and desorption) were analysed using Raman spectroscopy and compared to $LiBH_4$ and MgH_2 spectra obtained on the same apparatus. Figures 4.4.11 to 4.4.13 show selected room temperature Raman spectra after hydrogen absorption cycles 1, 3 and 5, respectively. Each spectrum of the sample is obtained from a different point on the sample surface. $LiBH_4$ has three types of Raman active modes: internal $[BH_4]^-$ stretching between 2000 and 2500 cm^{-1} (corresponding to peaks at 2157, 2176, 2271, 2299, 2316 and 2476 cm^{-1}), internal $[BH_4]^-$ bending between 1000 and 1350 cm^{-1} (corresponding to peaks at 1097, 1286 and 1316 cm^{-1}) and external modes of vibration between 100 and 350 cm^{-1} (corresponding to a peak at 190 cm^{-1})[7].

MgH_2 Stokes scattering is observed throughout the cycling progression at the reported Raman shifts of 298, 943 and 1274 cm^{-1} that correspond to the B_{1g}, E_g and A_{1g} symmetry vibrations[8]. In this experiment, however, the first two peaks are observed at 311 and 949 cm^{-1}. There are other peaks observed in the spectrum for as-received MgH_2 that are not reported in the literature and that are not observed in either the hydrided or dehydrided samples (2749, 3858 and 4032 cm^{-1}) suggesting that they are not due to elemental Mg which can give a large background. The peaks are also not due to the presence of MgO which has reported Raman shifts at 355 and 617 cm^{-1} and 595, 719 and 1060 cm^{-1} though these are liable to shift to slightly higher wavenumber as the particles trend towards the bulk material[9, 10]. Unfortunately, the MgH_2 vibrational shift at 1277 cm^{-1} obscures the shifts corresponding with internal bending region for the $[BH_4]^-$ anion, making it harder to identify any changes in the $LiBH_4$ environment.

The $LiBH_4$ peaks at 2157, at 2271 and 2299 cm^{-1} are not observed in every spectrum and this is perhaps indicative of the sample being inhomogeneous – it's possible that, due to the conditions during reaction on the flowing TPD system and the fact that $LiBH_4$ is melted at the

reaction temperature (300°C), the melted LiBH$_4$ moves to the bottom of the sample reactor. However, it is apparent that there is a mechanism for LiBH$_4$ to become mobile in the sample
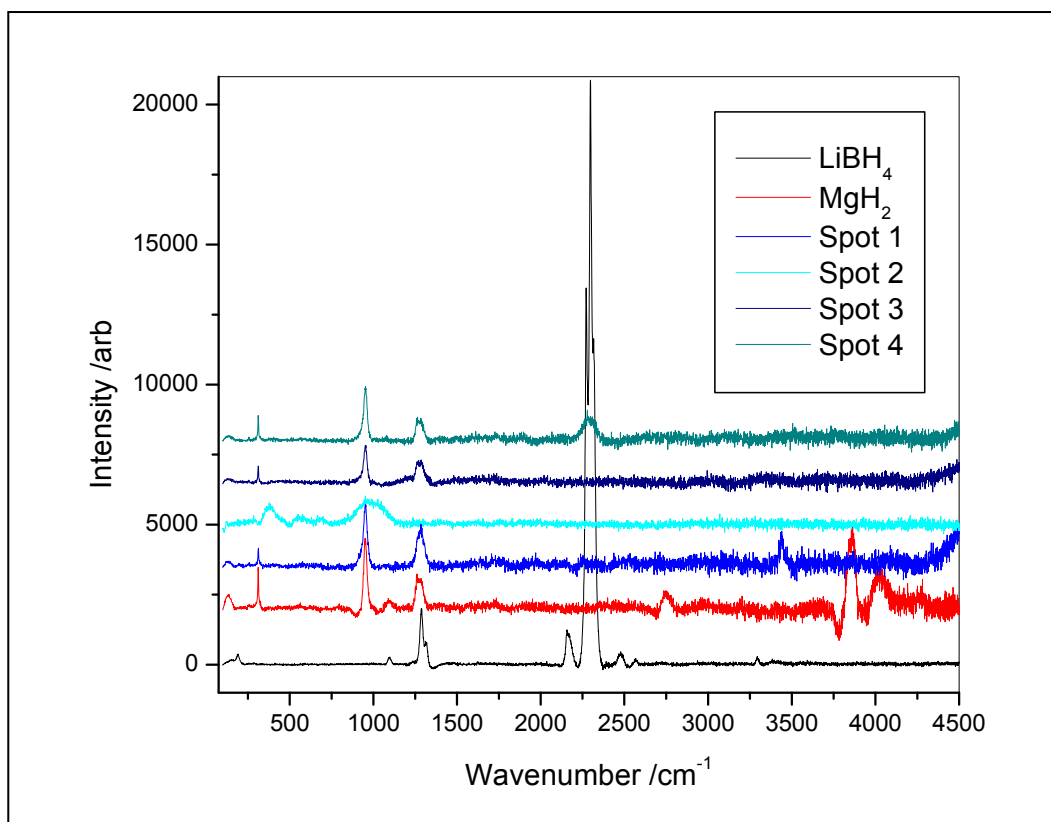

Figure 4.4.11 : Raman spectra obtained from Mg + LiBH$_4$ (90:10) after absorption cycle 1. Different spots of sample were chosen and scanned with the raman laser (blue spectra) and are compared against as-received LiBH$_4$ and MgH$_2$ (black and red spectra respectively)

as observed the fifth cycle, every spot of the Mg + LiBH$_4$ (9:1) that was measured had an amorphous peak that corresponded to the region that the B-H stretching bands exist.

The actual observed [BH$_4$]$^-$ stretching shift at ~2300 cm^{-1} lost its definition after heating and its appearance is similar to that of LiBH$_4$ once it has melted and transformed to the high-temperature hexagonal phase[7, 11]. This is interesting because these peaks are reduced in sharpness due to the increased symmetry in the [BH$_4$]$^-$ anion within the hexagonal unit cell and they reappear once the sample is cooled and the LiBH$_4$ returns to its low temperature orthorhombic structure. This feature signifies the reduction in B–H bond strength, allowing freer movement than at lower temperatures. Therefore it is possible that the observed

disappearance of the vibrational peaks could correspond to either partial or full desorption of hydrogen from the boron or be indicative of a boron environment which has lowered B–H bond energies through a structural alteration.

There are also a number of unassigned peaks observed: spot 2, after the first absorption, displayed a number of broad peaks below 1150 cm^{-1}, whilst spot 1 had a unique peak at 3434 cm^{-1}. The samples measured after the third absorption displayed new peaks; spot one had peaks at 1608 and 3564 cm^{-1}, with the former also observed at spot 3.

After five absorptions, all measured spots displayed the broad peak at ~2300 cm^{-1} as well as two new peaks at 1630 and 1754 cm^{-1} though it is not known what the cause of these Raman shifts is.

Figure 4.4.12 : Raman spectra obtained from Mg + LiBH$_4$ (90:10) after absorption cycle 3. Different spots of sample were chosen and scanned with the raman laser (blue spectra) and are compared against as-received LiBH$_4$ and MgH$_2$ (black and red spectra respectively)
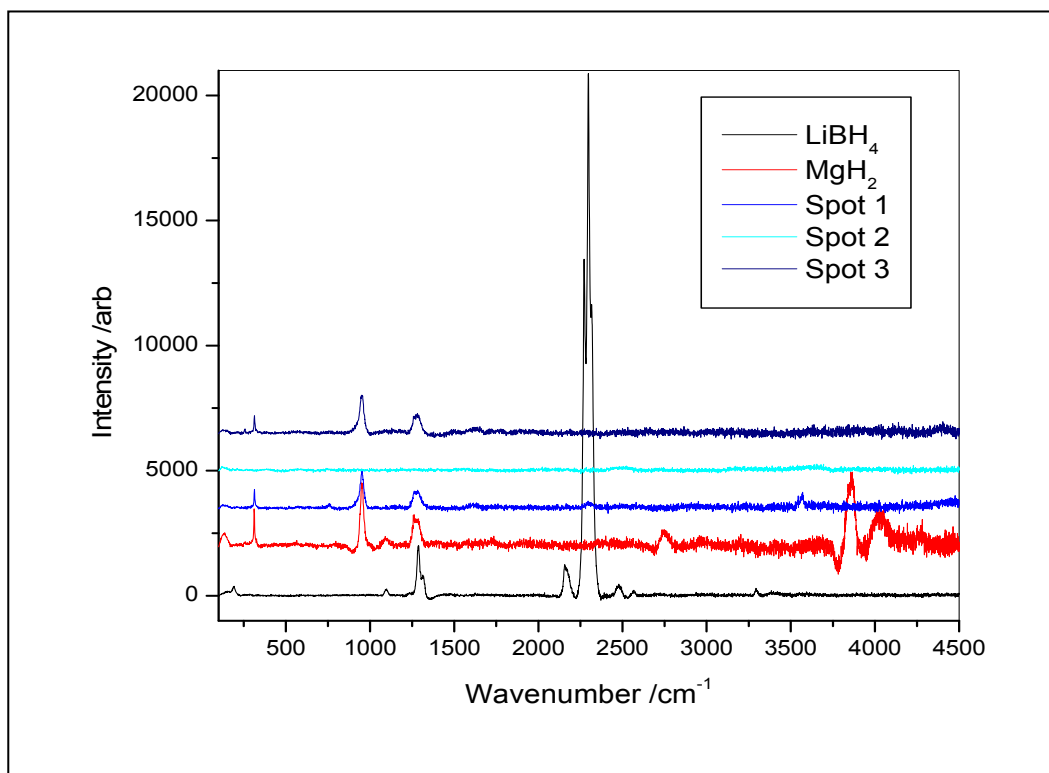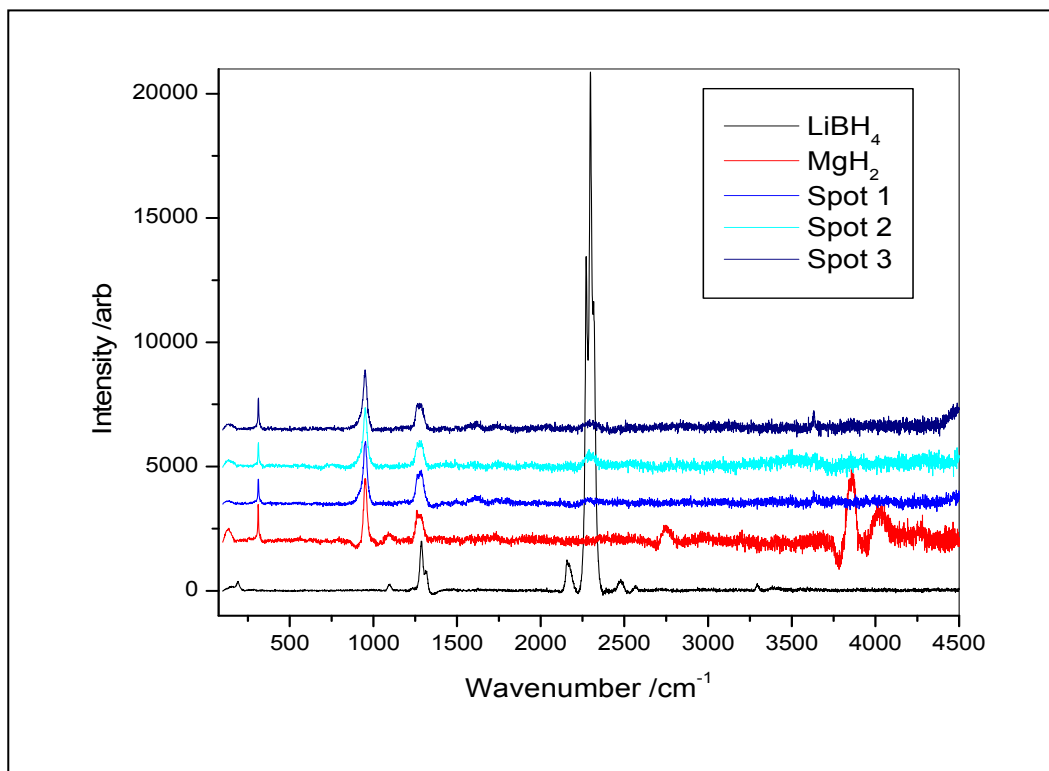
Figure 4.4.13 : Raman spectra obtained from Mg + LiBH₄ (90:10) after absorption cycle 5. Different spots of sample were chosen and scanned with the raman laser (blue spectra) and are compared against as-received LiBH₄ and MgH₂ (black and red spectra respectively)

Figures 4.4.14 to 4.4.16 show selected Raman spectra after desorption cycles 1, 3 and 5. The measurement after the first desorption displays no evidence of MgH_2 being present – none of the peaks at 311, 949 or 1274 cm^{-1} are observed. However, the poorly defined peak at ~2300 cm^{-1} that was observed after five hydrogenations and is thought to be associated with the B-H internal stretching is present in all spots on the sample. Spots 2 and 3 also exhibit small, broad peaks at low wavenumber, below 1000 cm^{-1} at 199, 384, 579, 759 and 920 cm^{-1}. These peaks do not appear to be associated with $LiBH_4$, MgH_2 or MgO. However, the intermediate phase, $Li_2B_{12}H_{12}$ is known to form from the partial decomposition of $LiBH_4$ above temperatures of 150°C[3-5]. The Raman shifts of this compound have also been reported in

the literature to be 580, 760, 920 and 2500 cm^{-1}[3, 12]. While the first three bands agree with

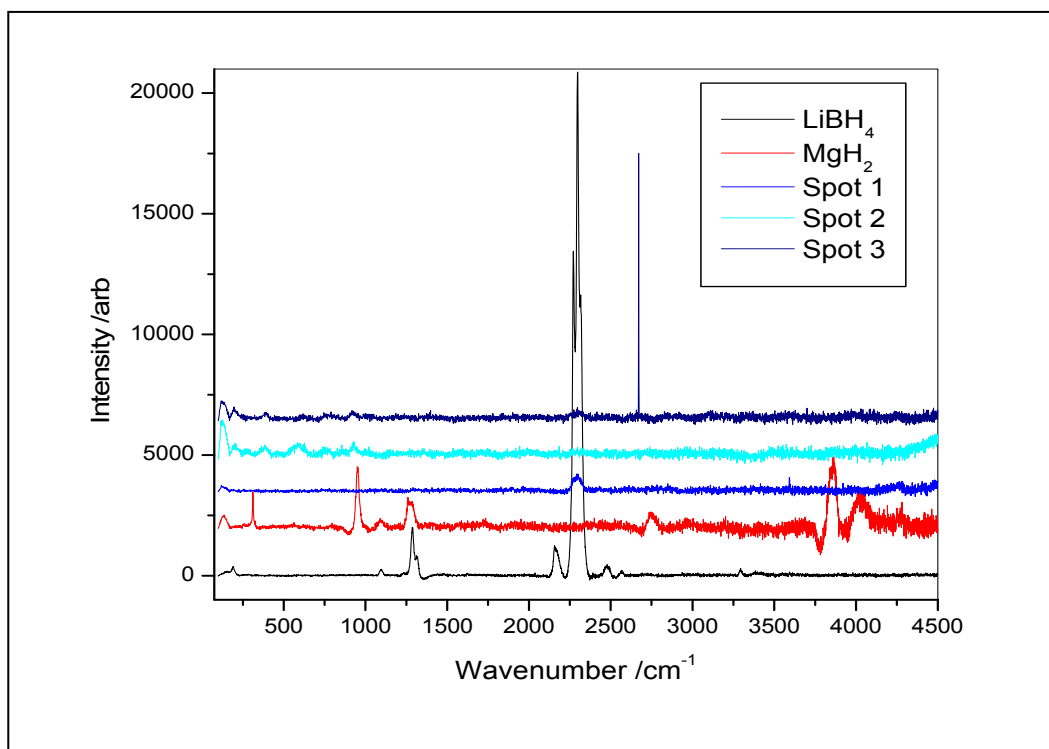the results observed for spot 2, the strongest Raman band at 2500 cm^{-1} is not observed.

Figure 4.4.14 : Raman spectra depicting Mg + LiBH$_4$ (90:10) after desorption cycle 1. Different spots of sample were chosen and scanned with the Raman laser (blue spectra) and are compared against as-received LiBH$_4$ and MgH$_2$ (black and red spectra respectively)

There is a further intermediate phase that is suggested to be formed through the partial

decomposition of LiBH$_4$ and Li$_2$B$_{12}$H$_{12}$ and that is Li$_2$B$_{10}$H$_{10}$[4]. However, this phase has only

been identified by proxy (using K$_2$B$_{10}$H$_{10}$ as a reference) in ^{11}B NMR and has yet to be

characterised by Raman or any other spectroscopic technique. Though the possibility of an

intermediate phase being present in the Mg + LiBH$_4$ system is intriguing, the observed

Raman bands after three and five desorptions become more complicated.

In the Raman spectra performed after the third desorption there are numerous, mostly broad

and ill-defined peaks observed in the sample; Spot 1 displays Raman bands at 256 (sharp),

345, 951, 1280, 1646 and 2247 (sharp) cm^{-1}. Spot 2 displays Raman bands at 317, 566, 745,

939, 1076, 1259, 1389, 1478, 1583, 1747, 2307 and 2504 cm^{-1}. Spot 3 displays Raman bands at 199, 392, 751, 930, 1046, 1198, 1343, 2443 and 2792 cm^{-1} (sharp).
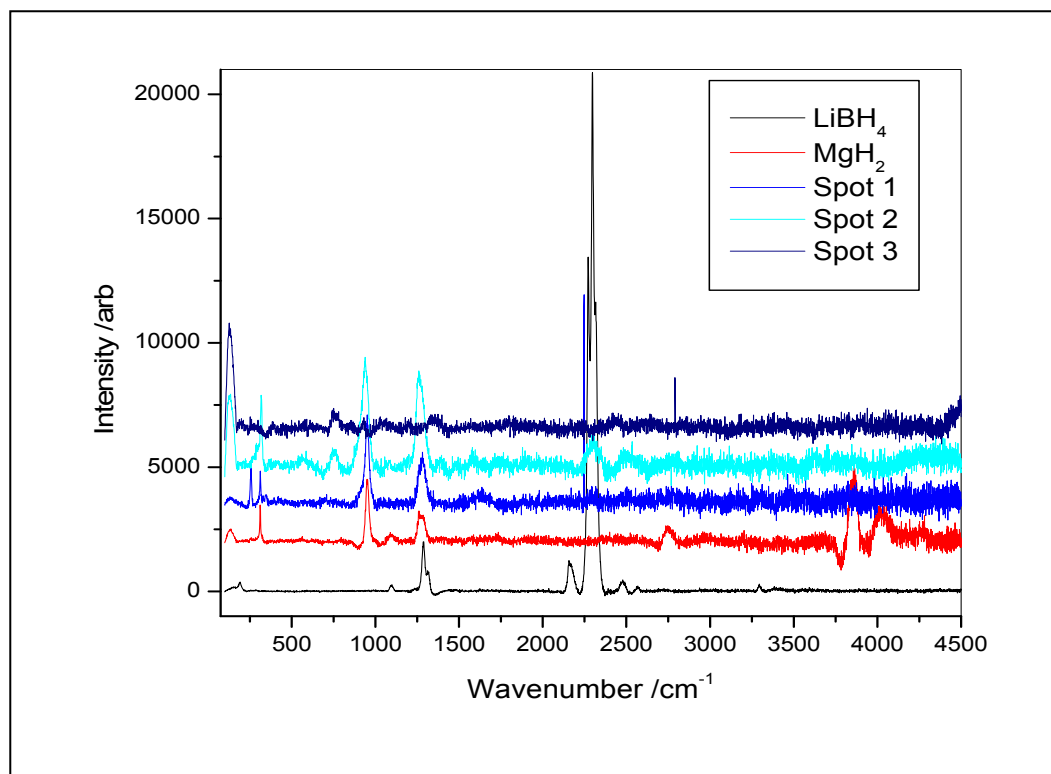

Figure 4.4.15 : Raman spectra depicting Mg + LiBH$_4$ (90:10) after desorption cycle 3. Different spots of sample were chosen and scanned with the raman laser (blue spectra) and are compared against as-received LiBH$_4$ and MgH$_2$ (black and red spectra respectively)

The peaks appearing at around 949, 1093 and 1274 cm^{-1} are possibly related to formation of MgH$_2$, however the peaks observed in the spectra of spots 1 and 2 have slightly shifted wavenumber that could correspond to strained Mg–H bonds. This might possibly be due to incomplete dehydriding, however, given the fact that Mg was hydrided by LiBH$_4$ during static vacuum synthesis at 300°C in a quartz tube, and that LiBH$_4$ does not fully decompose at that temperature, this might be suggestive of a transfer mechanism between Mg and LiBH$_4$ through the partial decomposition of LiBH$_4$ to an intermediate phase. The Raman bands observed at spot 2 after the third desorption would appear to suggest a compound with a

similar symmetry and vibrational movement to $Li_2B_{12}H_{12}$ (580, 760, 920 and 2500 cm^{-1}) with peaks appearing at 566, 745, 939 and 2504 cm^{-1}.

The Raman spectra performed after the fifth desorption show further change in vibrational modes. Spot 1 displayed weak, ill-defined peaks at 204, 280, 386, 753, 933, 2202 and 2508 cm^{-1}. Spot 2 displayed well-defined peaks at 222, 314, 755, 932, 1108 and 1243 cm^{-1}. Spot 3 displayed few peaks: 312, 561, 745 and 929 cm^{-1}. Spot 4 similarly displayed some well-defined peaks at 234, 390, 747, 924, 1076 and 1213 cm^{-1} and a sharp doublet at 1279 and 1289 cm^{-1}.

Interestingly, desorption cycle 5 had no evidence of a peak at ~2300 cm^{-1} and even the peaks that previously overlapped with those of MgH_2 at 949 and 1274 cm^{-1} have shifted to
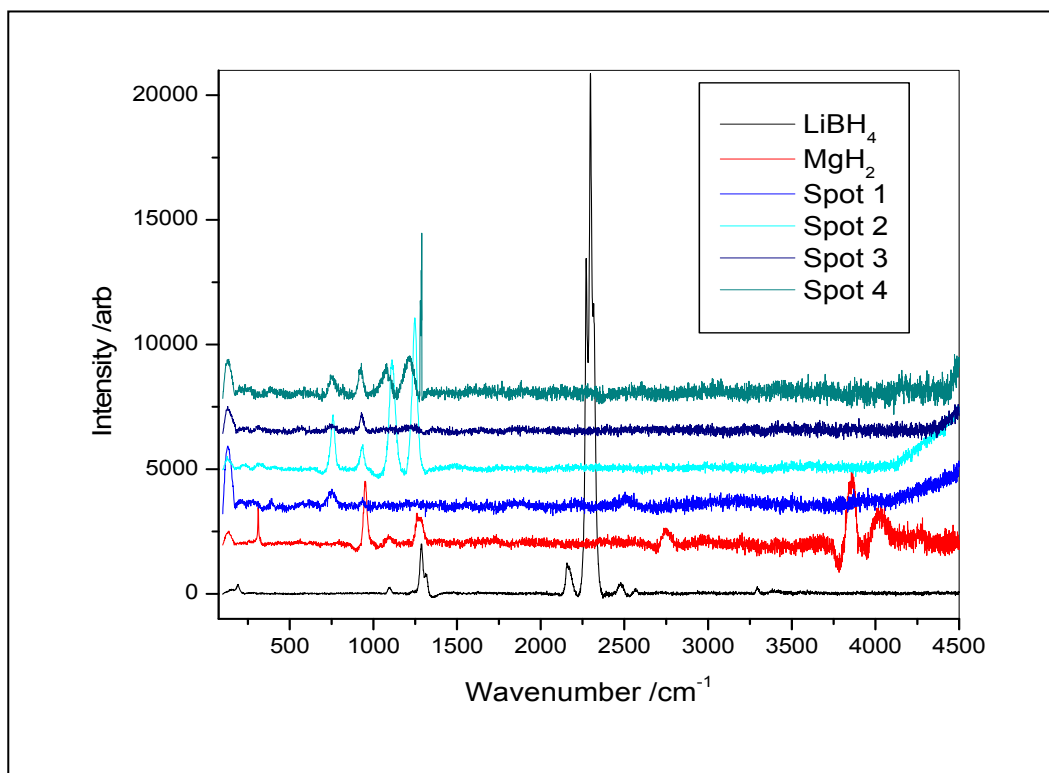

Figure 4.4.16 : Raman spectra depicting Mg + LiBH$_4$ (90:10) after desorption cycle 5. Different spots of sample were chosen and scanned with the raman laser (blue spectra) and are compared against as-received LiBH$_4$ and MgH$_2$ (black and red spectra respectively)

932 and 1243 cm^{-1} at spot 2 and 924 and 1213 cm^{-1} at spot 4. Indeed, there is now no evidence of a compound similar to $Li_2B_{12}H_{12}$ either, with very few peaks matching the observed Raman shifts for that compound or one like it. There is a possibility that these new Raman shifts are indicative of the decomposition of one or more phases within the sample. If the sample had been oxidised or formed the decomposition products of Mg + LiBH$_4$ then the observed peaks would be quite different.

Various research groups have reported that 2 LiBH$_4$ + MgH$_2$ would decompose to form 2 LiH +MgB$_2$ and 4 H$_2$[13]. If this pathway were occurring in this instance then the Raman shift of MgB$_2$ would be visible at ~600 cm^{-1}[14]. While there are peaks observed between 500 and 800 cm^{-1} it is unlikely that MgB$_2$ has formed at 300°C and none of the peaks correspond quite closely enough to the required wavenumber. Alternatively if water or oxygen were contaminating the system Mg(OH)$_2$ could be formed though at elevated temperatures during cycling it is more likely that MgO might be formed. MgO would be observed via Raman shifts at 355 and 617 cm^{-1} and 595, 719 and 1060 cm^{-1} for small particle sizes[9, 10] and Mg(OH)$_2$ has peaks at 280, 443, 725 and 810 cm^{-1}. Similarly, LiBH$_4$ could be oxidised to form a lithium oxide or hydroxide. LiOH has Raman peaks at 300, 320 and 620 cm^{-1}[15] and both it and Mg(OH)$_2$ would display O-H stretching modes at around 3600 cm^{-1}[16]. While there are some broad and ill-defined low wavenumber peaks observed in the Raman spectra it does not appear that they exist in large quantities in the measured samples.

The sudden evolution of the sharp, well-defined peaks between 690 and 1350 cm^{-1} seen at spots 2 and 4 would suggest the formation of a new bonding structure – possibly an intermediate compound that facilitates hydrogen desorption and absorption in the mixture of Mg/MgH$_2$ and LiBH$_4$ as there is no evidence of these Raman shifts after hydrogen absorption. If these were decomposition products or products formed via oxidation or hydrolysis then different and clearer Raman shifts would be observed. The Raman spectra point to the evolution of a new bonding arrangement and symmetry within the sample upon cycling. Interestingly, these are primarily observed upon desorption and might indicate that there is

greater chemical reaction between the two components in the dehydrided than the hydrided state.

4.4 (e) Reaction of LiBH$_4$ with an Mg surface:

To complement the information gained from X-ray diffraction and raman spectroscopy on the interaction between Mg and LiBH$_4$, a reaction between bulk magnesium and LiBH$_4$ was performed.

A cylindrical portion of magnesium (5mm x 5mm cylinder) was cut from an Mg rod and placed within a quartz tube and surrounded with LiBH$_4$ powder. This tube was evacuated and sealed before being heated at 300°C for 12 hours to replicate the reaction conditions used for previous samples. The resulting product was mounted then ground and polished before being analysed via SEM.

Figure 4.4.17 shows the edge of the Mg cube and the layer of LiBH$_4$ that forms a shell around it. While it was impossible to search for Li content, it was possible to monitor the Mg, O and B content of the sample. Figure 4.4.18 shows a zoomed area from figure 4.4.17 where light element analysis has been performed in a line of 16 μm across the border from the LiBH$_4$ shell to the bulk Mg of the cube.

The composition analysis of the three elements is seen in table 4.4.2. Somewhat surprisingly, we see large overlap and penetration of magnesium and boron within the bulk Mg cube and the LiBH$_4$ shell. Boron is present up to 10 μm into the bulk Mg from the clear distinction of the end of the LiBH$_4$ shell at linescan 4 and, for linescans 6 to 8, appears to have reached a distinct content ratio with magnesium (Mg:B of 82:17). Magnesium also reaches a similar though inverse ratio in linescans 1 to 3 (Mg:B of 18:81). These results help reinforce the fact that diffusion of LiBH$_4$ into Mg is favourable and that a ratio of around 1:5 for either compound might result in a stable compositional phase.
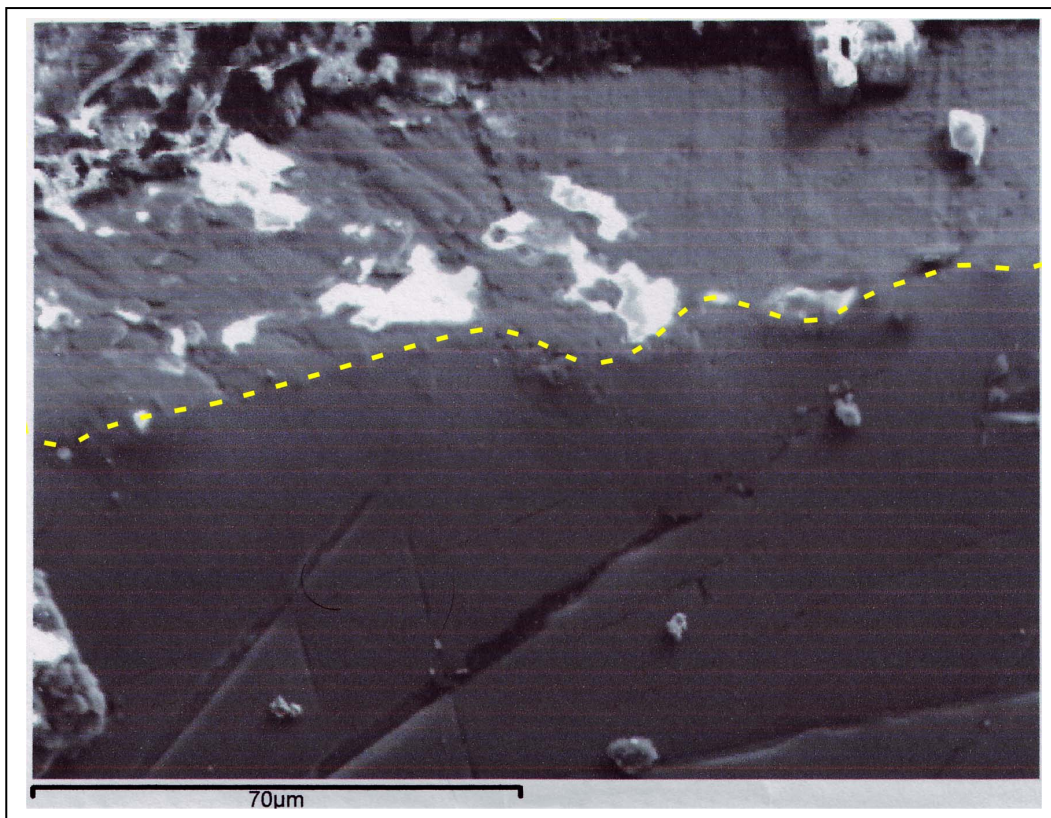
Figure 4.4.17 : An SEM image of the Mg cube – a layer of LiBH$_4$ can be seen as the lighter band across the top of the image with the cube occupying the lower portion of the image – taken on a JOEL 7000 instrument. The dashed yellow line indicates the interface between the Mg metal and the LiBH$_4$ coating

Of further interest is the oxygen content. The sample had minimal exposure to oxygen during loading onto the SEM apparatus and Mg itself is not strongly reactive towards oxygen though LiBH$_4$ is known to be easily oxidised. However, while there is a larger relative amount of oxygen in the LiBH$_4$ shell (linescan 1) when compared with that on the bulk Mg (linescan 8), it appears that increased Mg content in a boron-rich region (linescans 3 and 4) results in drastically increased sensitivity to oxygen. Linescan 3 has a Mg:B ratio of 27:73 whereas linescan 4 has a ratio of 42:58 and they have 8.5 and 10.2 times the amount of oxygen compared to linescan 1 respectively. This could suggest that the combination of Mg and LiBH$_4$ results in a more reactive material but may also be indicative of an oxide film being present on the surface of the bulk magnesium.
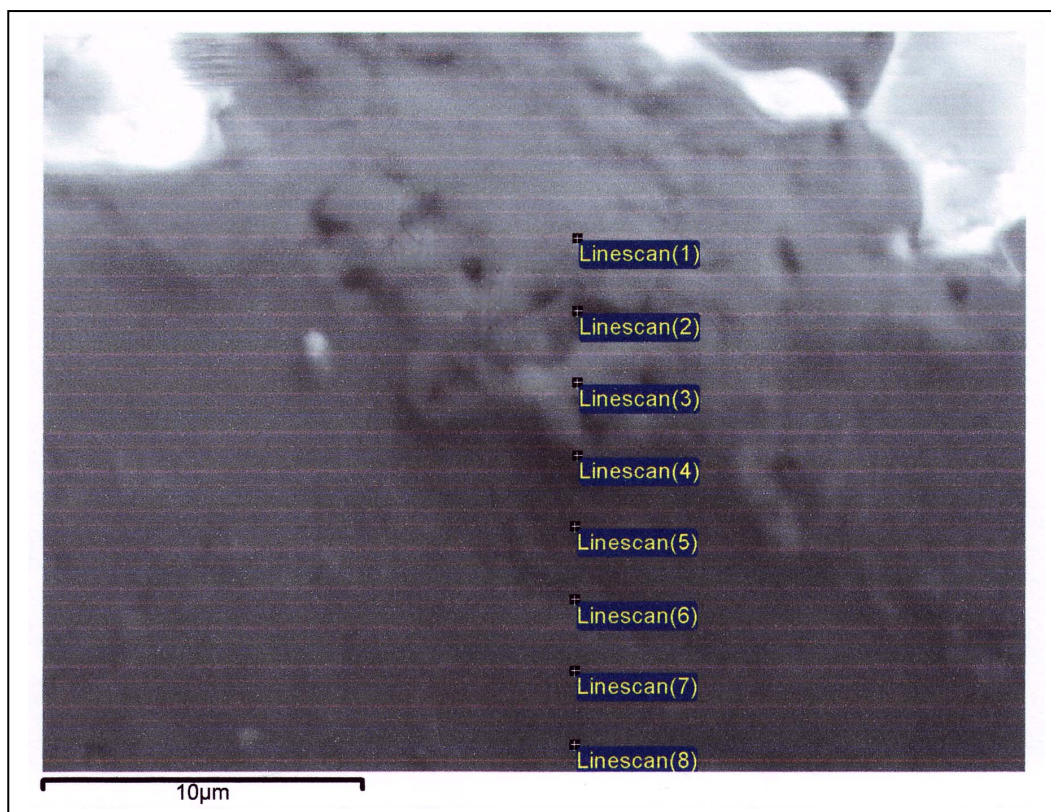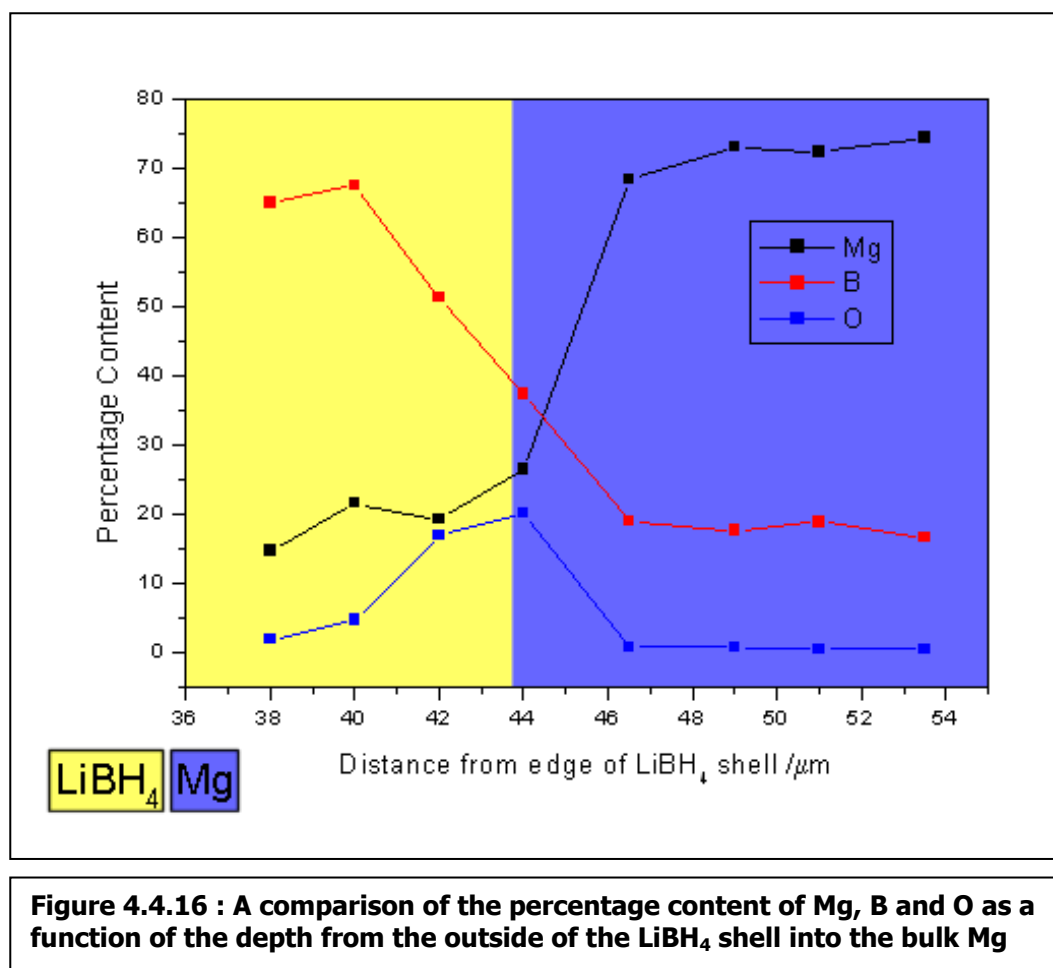
Figure 4.4.18 : SEM image showing a zoomed view of a location where the Mg cube intersects with the LiBH₄ shell

Position	Mg content (wt%) ±0.02	B content (wt%) ±6.77	O content (wt%) ±0.84
Linescan 1	14.84	65.1	1.98
Linescan 2	21.66	67.57	4.80
Linescan 3	19.41	51.46	16.96
Linescan 4	26.62	37.48	20.19
Linescan 5	68.48	19.08	0.96
Linescan 6	73.06	17.74	0.89
Linescan 7	72.46	18.98	0.65
Linescan 8	74.43	16.67	0.66

Table 4.4.2 : Composition report for each linescan point in figure 4.4.18 for the relative amount of magnesium, boron and oxygen

Figure 4.4.19 shows the information in table 4.4.2 as a function of distance from the outer edge of the LiBH$_4$ shell. It illustrates the sudden jump in oxygen content and also the plateau in Mg and B content in the bulk LiBH$_4$ and Mg respectively and it would also suggest that a region which is Mg-rich is less susceptible to oxidation than one between ratios of 1:1 and 1:3 (Mg:B). The boundary between LiBH$_4$ and Mg is taken as the point where the dashed yellow line lies in figure 4.4.17 and the edge of the LiBH$_4$ coating/shell is measured from the point at which the carbon mounting is encountered on the micrograph in a straight line extrapolated from the position that the compositional linescan had taken.

Figure 4.4.16 : A comparison of the percentage content of Mg, B and O as a function of the depth from the outside of the LiBH$_4$ shell into the bulk Mg

1. Suzuki M., Kagawa M., Syono Y., and Hirai T., *Synthesis of ultrafine single-component oxide particles by the spray-ICP technique.* J. Mater. Sci., 1992. **27**(3): p. 679.

2. Zhu Y.M., YEX H., Wang X.Y., and Wang L.X., *Preparation of nano-MgO and investigation of its infrared absorption properties.* Powder Technology and application, 2009. **58**: p. 115.

3. Orimo S., Nakamori Y., Ohba N., Miwa K., Aoki M., and Towata S., *Experimental studies on intermediate compound of LiBH$_4$.* Appl. Phys. Lett., 2006. **89**: p. 021920.

4. Friedrichs O., Remhof A., Hwang S.-J., and Züttel A., *Role of Li$_2$B$_{12}$H$_{12}$ for the formation and decomposition of LiBH$_4$.* Chem. Mater., 2010. **22**: p. 3265.

5. Mosegaard L., Møller B., Jørgensen J., Bösenberg U., Dornheim M., Hanson J.C., Cerenius Y., Walker G.S., Jakobsen H.J., Besenbacher F., and Jensen T.R., *Intermediate phases observed during decomposition of LiBH$_4$.* J. Alloy. Compd., 2007. **446-447**: p. 301.

6. Frost P.D., *Technical and economic status of magnesium-lithium alloys*, in *Technology Utilisation Report*. 1965, NASA: Washington D.C.

7. Gomes S., Hagemann H., and Yvon K., *Lithium boro-hydride LiBH$_4$ II. Raman spectroscopy.* J. Alloy Compd., 2002. **346**: p. 206.

8. Santisteban J.R., Cuello G.J., Dawidowski J., Fainstein A., Peretti H.A., Ivanov A., and Bermejo F.J., *Vibration spectrum of magnesium hydride.* Phys. Rev. B, 2000. **62**(1): p. 37.

9. Khambátá S.J., *Raman Spectrum of Magnesium Oxide.* Proc. Phys. Soc. A, 1956. **69**: p. 426.

10. Schlecht R.G. and Böckelmann H.K., *Raman scattering from microcrystals of MgO.* Phys. Rev. Lett., 1973. **31**(15): p. 930.

11. Orimo S., Nakamori Y., and Züttel A., *Material properties of MBH$_4$ (M = Li, Na, and K).* Mater. Sci. Eng. B, 2004. **108**: p. 51.

12. Reed D. and Book D., *In-situ raman study of the thermal decomposition of LiBH$_4$.* Mater. Res. Soc. Symp. Proc., 2010. **1216**(1216-W06-05).

13. Vajo J. and Skeith S., *Reversible storage of hydrogen in destabilized LiBH$_4$.* J. Phys. Chem. B., 2005. **109**: p. 3719.

14. Shui L., Zhang H., Chen L., and Feng Y., *The raman spectrum and lattice parameteres of MgB$_2$ as a function of temperature.* J. Phys.:Condens. Mat., 2004. **16**: p. 6541.

15. Charton S., Maupoix C., Delaunay F., Saviot L., and Bernard F. *Experimental investigation on lithium hydride hydrolysis.* in *WHEC 16*. 2006. Lyon, France.

16. Dawson P., Hadfield C.D., and Wilkinson G.R., *The polarized infra-red and raman spectra of Mg(OH)$_2$ and Ca(OH)$_2$.* J. Phys. Chem. Solids, 1973. **34**: p. 1217.

4.5 Investigation into the thermodynamic properties of the MgH$_2$–LiBH$_4$ System

Experimental technique 4.5

Isothermal IGA measurements

Isothermal IGA measurements were carried out in a similar manner to the kinetic measurements as described in Experimental technique 4.1. The sample (typical mass was the same as for kinetic measurements ~100 mg) was loaded in an identical way however the system was set to perform isothermal measurements. This setting changes the way the IGA processes an experiment: A temperature is chosen and then the user sets up a range of pressure steps for the gas to be admitted in. The user also defines the type of material and what sort of gas uptake it is thought or known to possess and at what point the programme should move onto the next pressure point. For these experiments pressure steps of 200 mbar where used from 10mbar to 8 bar. The type of absorption profile was set to metal hydride settings and the programme was set to move on to the next pressure point at 98% absorption completion. The programme was also set to time-out if no absorption (or increase in absorption) was observed after 1 hour.

The sample was first desorbed at 300°C, 10 mbar and then the isothermal experiment was begun. At each pressure step, the IGAS programme calculates a fit to the weight curve based on the amount of weight gained and in the time period it was gained in – this would determine the saturation of H$_2$ absorption for that pressure at the isothermal temperature. From this it calculates the point at which the sample is predicted to reach 98% completion for absorption for that temperature and pressure. If the analysis of the real time data did not match the calculated fit then a new fit would be calculated from the experiment data. If the analysis did not alter the calculated fit within a certain time frame then the programme would assume that the fit was correct and assign the predicted weight and then move on to the next pressure point. If there was no absorption within the 1 hour time frame then it would move on to the next pressure point.

From this series of equilibrium points for the sample the H$_2$ plateau pressure for the measured temperature can be determined – from which the enthalpy of formation of the hydride phase can be

calculated. Once the experiment was ended, the sample was removed from the IGA as described in Experimental technique 4.1.

Isothermal HTP measurements

The HTP uses the same software that the IGA but is a volumetric system and uses the sieverts method instead of gravimetric analysis. The sample was first weighed and then loaded in the sample chamber within an argon circulating glove box. The typical sample mass was ~100 mg. This was then sealed in a transfer vessel and removed from the glove box and placed in a small bolt-on glove box that fitted onto the top of the HTP system. This was purged with argon for an hour, at which point the flow rate was reduced and the sample was loaded into the reactor. The reactor was sealed via a compression joint and a copper gasket and the small flowing glove box was removed. The thermocouples were attached and the HTP lid was closed over, allowing the experiment to be started.

The HTP software requires the density and weight of the sample to be inputted and requires the same range of pressure steps to be chosen for a given temperature. 200 mbar pressure steps from 10 mbar to 8 bar were set and a cut off of point of 1 hour in the case of no absorption or desorption taking place and an absorption or desorption 98% completion cut off was also selected. The HTP software has to perform both an absorption and desorption isotherm in the same experiment – compared to the IGA which can perform either one independently. Before the isotherm was started the sample was desorbed at 10 mbar and 300°C. The HTP controls pressure by filling a known volume with a known pressure of gas. This chamber is sealed and the gas is released into the sample chamber and the pressure equalises between the two volumes. The change in pressure is then recorded and this is what is used to perform the calculation of the equilibrium point for that pressure and temperature.

During the isotherm, the HTP software calculates at what point the absorption or desorption will reach completion based on the current gain or loss of pressure in the sample chamber. Similar to the method used by the IGAS software it will move onto the next pressure point if no change is detected after 1 hour and will re-calculate the completion point if the absorption or desorption proceeds at a slower or faster rate than it has predicted. The HTP software will also move onto the nest pressure point if the prediction is being met for a certain time frame.

Once the sample has had an isotherm performed for both absorption and desorption it can be removed or left to perform another isotherm at a different temperature.

The sample can be removed with the use of the glove box, however this was not the case for this experiment – the sample was removed in air and disposed of.

DSC measurements

The DSC measurements were performed using a DSC 204 HP Phoenix inside an argon-filled glovebox. This allowed the loading of samples without exposing them to atmosphere. The sample pans were made of aluminium. DSC was connected to a low pressure and high pressure H_2 pipeline (20 bar max and 150 bar max respectively) as well as an argon pipeline of 10 bar. The conditions of experiment were chosen – the temperature ramp rate, maximum temperature, how long to hold the temperature and also the pressure setting. Using this information blank calibration measurements were performed so that the heat change of the equipment would be taken into account during the actual experiments.

Pressures of 5, 10, 15, 20 and 25 bar H_2 were chosen and a heating rate of 2°C from 25°C to 500°C and from 500°C to 25°C also at a cooling rate of 2°C: there was no temperature plateau at 500°C. Once the relevant calibration measurements had been completed a sample was weighed and loaded into the DSC in an aluminium pan. The weight of the sample was typically ~5 mg. The reactor chamber was sealed and then purged with a flow of hydrogen gas for 30 minutes. At this point the pressure control was set and the pressure increase to the desired level and a flow rate of 100 ml was set. The calibration file was loaded to act as a background against the experimental measurement.

Once the measurement was finished the next pressure measurement was performed until all five had been completed. The sample chamber was then purged with argon and the pressure reduced to 1 bar, at which point the sample was removed and disposed of.

4.5 (a) IGA Study

The thermodynamic properties of magnesium hydride have been extensively studied by many groups. The heat of formation of MgH_2 is reported to be around -75 kJmol^{-1}[2], however, there are a relatively broad range of values reported in the literature for $\Delta H_f[MgH_2]$[1, 3-5]. This means that, for the sake of reliable comparison, any observed value for the enthalpy of hydriding (ΔH_{hyd}) after alloying or chemical reaction should be compared to the base value for MgH_2 measured under similar conditions on the same piece of equipment.

The Van't Hoff equation (Eq. 4.5.3) is derived from combining the equations 4.5.1 and 4.51 – for the Gibbs free energy. From this equation it is possible to relate change in temperature to a change in the equilibrium constant for a given temperature which in this case is the plateau pressure for hydrogen evolution. Plotting the natural log of plateau pressure against the reciprocal of temperature results in a straight line whose gradient is equal to ΔH (the heat of formation) divided by R (the ideal gas constant) which allows the determination of ΔH. ΔS (the standard entropy change of a system) can be determined from the y-intercept which is equal to ΔS divided by R. T is the temperature and K is the equilibrium constant. ΔG is the Gibbs free energy of the system.

$$\Delta G = \Delta H - T\Delta S \qquad\qquad \textbf{Eq. 4.5.1}$$

$$\Delta G = -RT \ln K \qquad\qquad \textbf{Eq. 4.5.2}$$

$$\Rightarrow \ln K = -\frac{\Delta H}{RT} + \frac{\Delta S}{R} \qquad\qquad \textbf{Eq. 4.5.3}$$

Figure 4.5.1 depicts isotherm measurements performed on an IGA for Aldrich MgH_2. Traditionally (and correctly) the central point of the plateau in pressure is used to determine ΔH. However, the observed plateaux were found to deviate significantly from the vertical, in particular at lower temperatures. This results from slow kinetics and leads to inaccurate values for the plateau pressure. Under these circumstances the onset pressure of the plateau is a more reliable indicator of the thermodynamic properties of the sample and may be used

instead. In fact, the true ΔH lies between the values obtained by using the onset temperatures of absorption and desorption[1]. Unfortunately, desorption measurements were not obtained due to restrictions on equipment time.
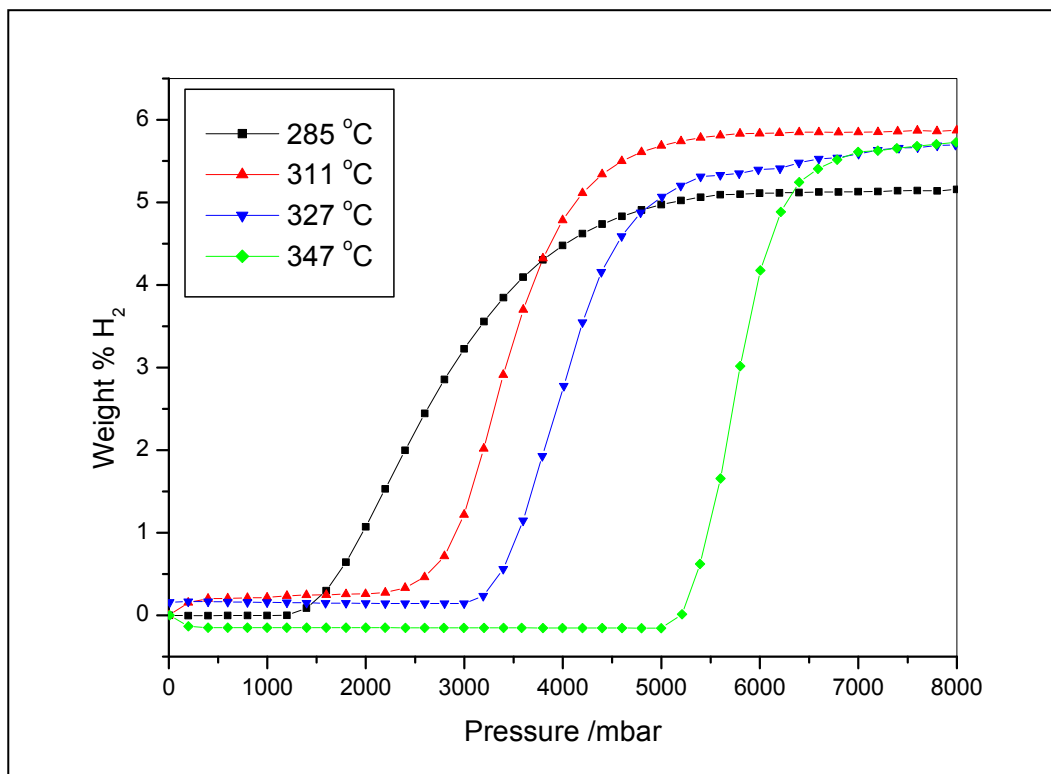

Figure 4.5.1 : Isothermal absorption traces performed on an IGA for MgH$_2$ (Aldrich)

Figure 4.5.2 shows the isotherm measurements performed on a sample of MgH$_2$ + LiBH$_4$ (90:10) under similar conditions. Although the kinetics of this sample were quicker the plateau pressures were still not vertical and, for direct comparison with the method used for as-received MgH$_2$, the onset pressure of each plateau was again used.

Interestingly, the onset pressure for MgH$_2$ + LiBH$_4$ was higher at each temperature point, except for 347°C, than for pure MgH$_2$ (figure 4.5.3) which would suggest that addition of LiBH$_4$ increases the H$_2$ plateau pressure at temperatures around 300°C and thus destabilises MgH$_2$ at these temperatures.

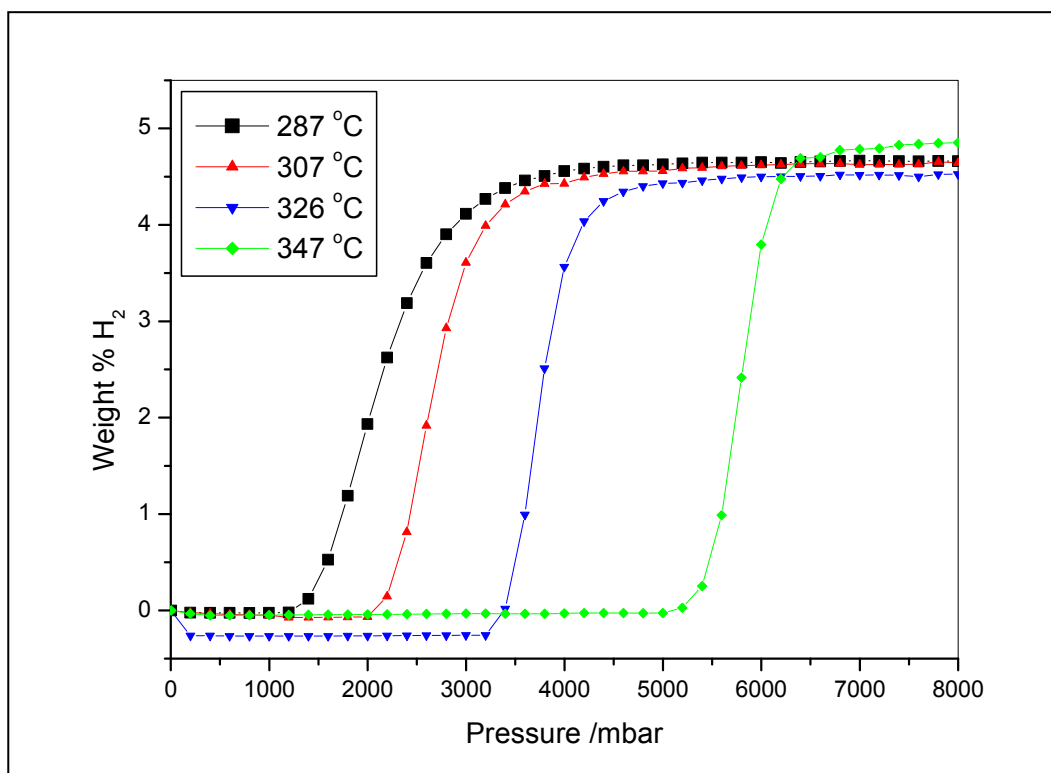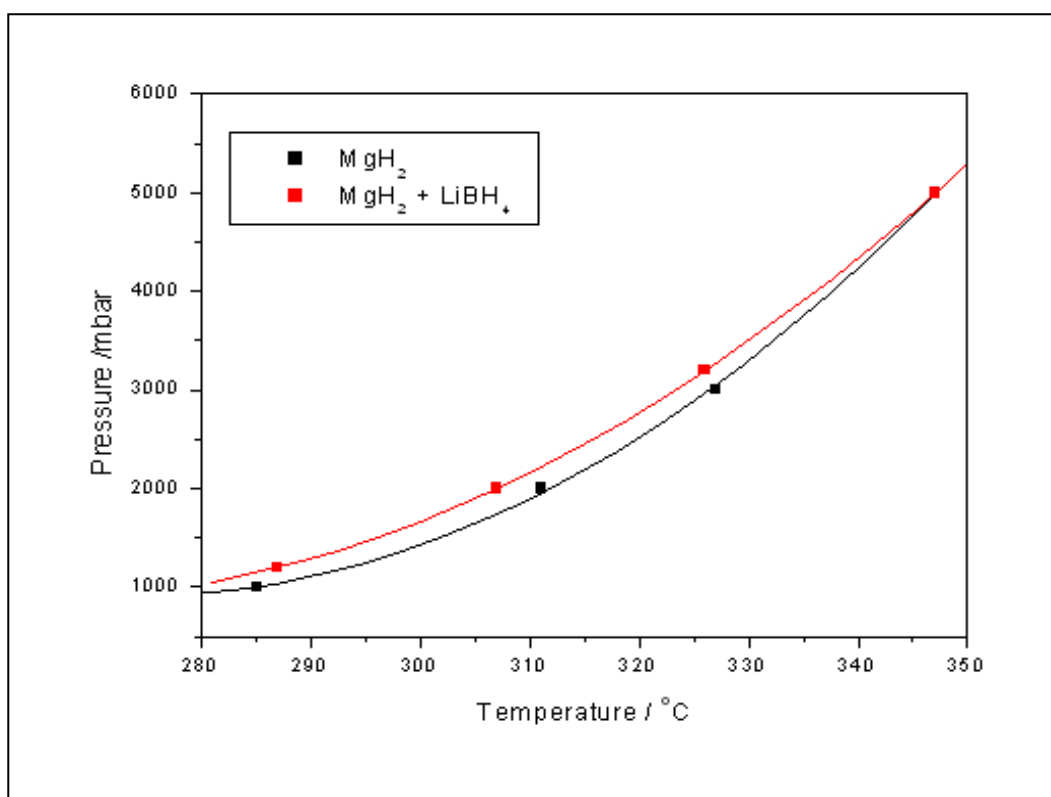**Figure 4.5.2 : Isothermal absorption traces performed on an IGA for MgH$_2$ + LiBH$_4$ (90:10)**

Figure 4.5.3 : Absorption onset pressures plotted against temperature for MgH$_2$ and MgH$_2$ + LiBH$_4$ during isotherm measurements

Figure 4.5.4 shows Van't Hoff plots for MgH_2 and MgH_2 + $LiBH_4$ (90:10). The gradients of the fitted lines give $\Delta H_f[MgH_2] = -75.3\ (\pm 5.1)$ kJmol^{-1} and $\Delta H_f[MgH_2 + LiBH_4\ (90:10)] = -71.9\ (\pm 2.1)$ kJmol^{-1}. Unfortunately, the observed difference was within the margins of error.
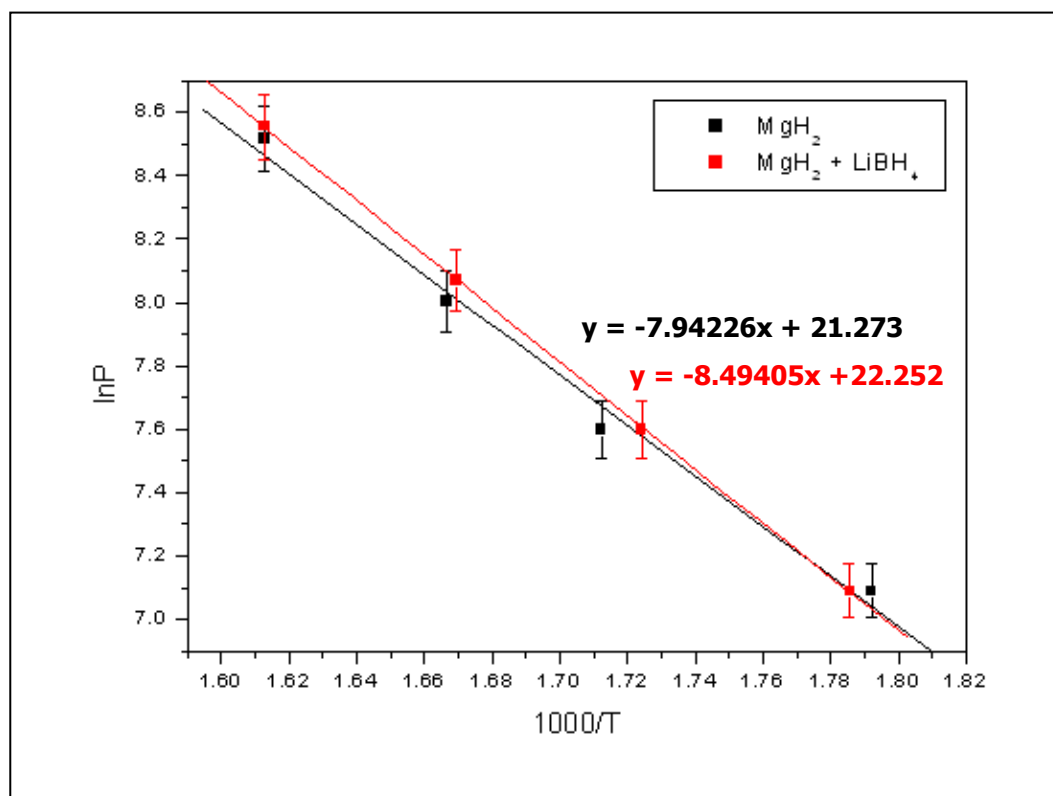

Figure 4.5.4 : Van't Hoff plot for MgH$_2$ and MgH$_2$ + LiBH$_4$ (90:10) isotherms performed on an IGA

4.5 (b) HTP Study

In an attempt to corroborate the data from the IGA, a sample was investigated using a volumetric system (HTP – described in chapter 3). Instead of measuring the mass change, the system takes note of the gas absorbed by the sample at a static pressure. A sample of Aldrich MgH_2 + $LiBH_4$ (90:10) was loaded inertly onto the HTP system and cycling of the material was performed under a hydrogen atmosphere – absorption cycles were performed at 300°C and 10 bar H_2, while desorption cycles were performed at 300°C and 10 mbar H_2 – to

simulate the processing on an IGA that led to improved hydrogen sorption kinetics. Isothermal absorptions and desorptions were then performed on the sample.

Figure 4.5.5 shows the obtained isotherms for hydrogen cycled Aldrich MgH$_2$ + LiBH$_4$ (90:10). The mid-point of each pressure plateau was used to determine the heat of formation for absorption and desorption.
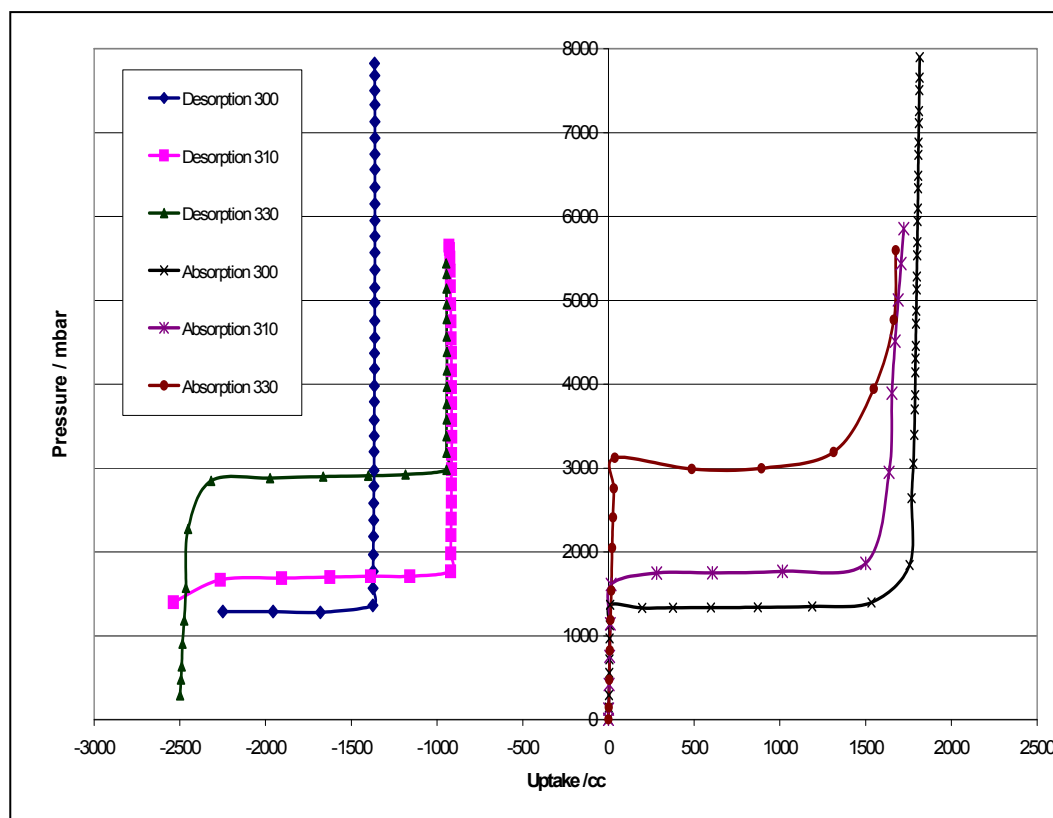

Figure 4.5.5 : Desorption and absorption isothermal traces for MgH$_2$ (Aldrich) + LiBH$_4$ (90:10) performed on an HTP apparatus

Figure 4.5.6 shows the Van't Hoff plot for Aldrich MgH$_2$ + LiBH$_4$ (90:10). The gradient of the line for the absorption isotherms gives ΔH$_f$[MgH$_2$ + LiBH$_4$ (90:10)] = −77.2 (± 1) kJmol^{-1} and −77.5 (± 1) kJmol^{-1} for the desorption isotherms. This result lies within the range of values reported in literature for MgH$_2$[3].
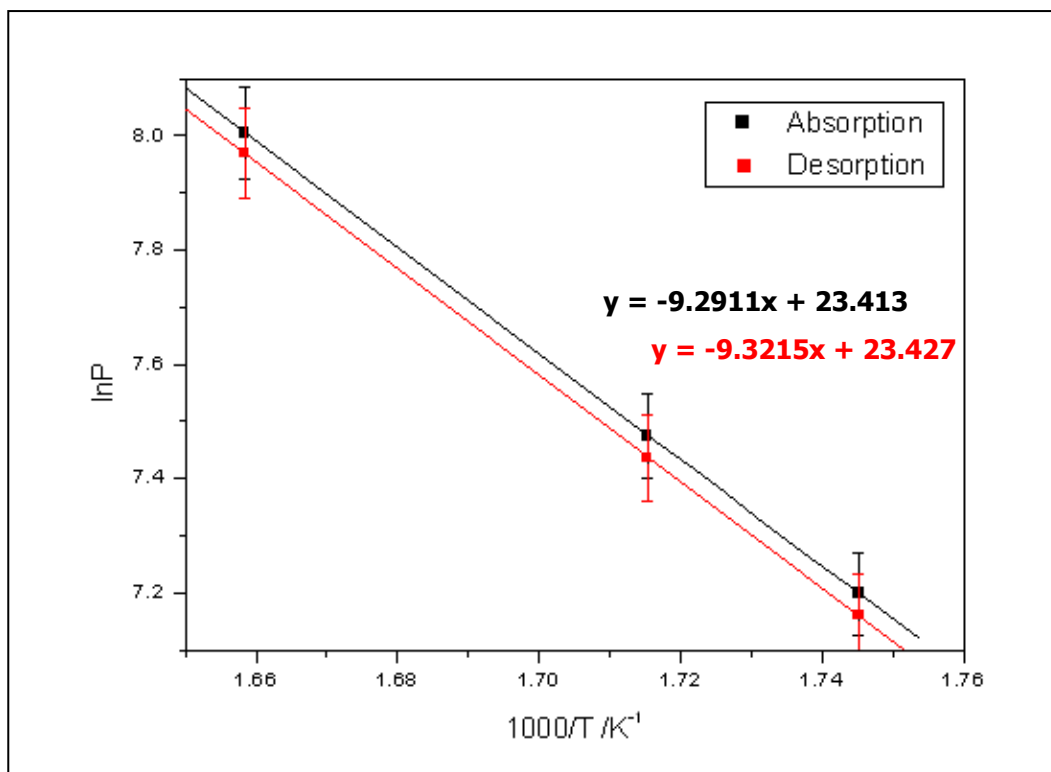
Figure 4.5.6 : Van't Hoff plot for MgH$_2$ + LiBH$_4$ (90:10) desorption and absorption isotherms performed on a HTP

4.5 (c) DSC Study

Differential scanning calorimetry is one of the most common techniques used to obtain the heat of formation for compounds. This can be done by performing isobar measurements against a standard of known heat capacitance. For most structural changes in compounds, ΔH is derived from the integrated area under the curve for the specific transition corresponding to the work done (ΔQ) from the equilibrium temperature (T_{eq}). However, due to the slow kinetics of hydrogen absorption and desorption for magnesium-based systems, the equilibrium temperature is difficult to obtain accurately from the DSC trace due to the difference in onset temperatures for the two changes in phase (Figure 4.5.7).

Rongeat et al. reported that it was possible to use kinetic measurements to obtain an accurate ΔH by approximating the T_{eq}^{abs} and T_{eq}^{des} using the onset temperatures over

multiple isobar measurements in an analogous way to isotherms[1]. As stated by Rongeat, the true ΔH_f lies between the two values obtained for ΔH_{abs} and ΔH_{des}; this method is a quick way of determining ΔH for compounds where kinetic factors outweigh thermodynamic in limiting the rate of reaction.
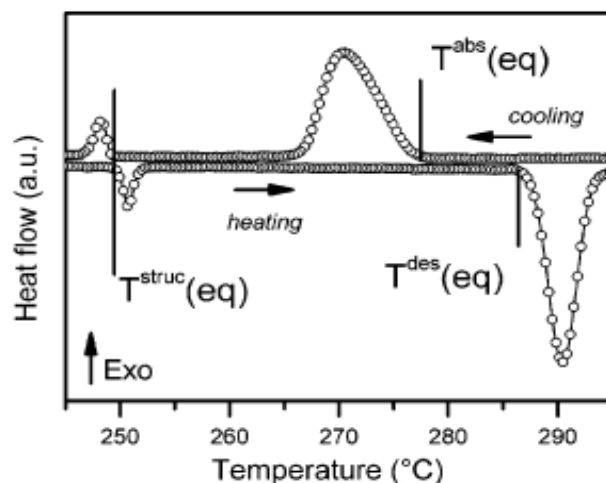

Figure 4.5.7 : Diagram showing the difficulty in obtaining equilibrium temperatures for hydrogen desorption and absorption[1]

Using the method described by Rongeat et al. samples of Goldschmidt MgH_2, 5 hour ball milled Goldschmidt MgH_2 and Strem Mg were analysed via DSC: samples were heated from room temperature to 500°C at a rate of 2°C/min under a flow of hydrogen held at constant pressure.

Figures 4.5.8 – 10 show the observed endothermic peaks during desorption of hydrogen performed in a sequential manner (absorption traces are shown in Figures 4.5.12 – 14). The shape of the desorption traces of Goldschmidt MgH_2, milled MgH_2 and hydrided magnesium are well understood and reported in the literature[6, 7]. Single, well defined peaks correspond with the decomposition of a single phase of MgH_2 and indicate an even particle size. The double peak, or peaks with a shoulder, are attributed to a distribution in particle size[7] and the resultant increase in kinetics and a reduction in activation energy. Metastable phases, such as γ-MgH_2, can also result in multiple peaks and lowered onset temperatures[7] though

Figure 4.5.8 : DSC traces showing desorption endotherms for samples of Goldschmidt, milled Goldschmidt (5hrs), magnesium and hydrogen cycled MgH₂ + 10% LiBH₄ (5 absorption cycles) at a) 3 bar and b) 10 bar H₂

none of these were observed during X-ray diffraction and are unlikely to be a consideration in this study. The sharp peak at 449°C is an impurity on the measurement plate and is not part of the sample itself.

In comparison, the MgH_2 + 10% $LiBH_4$ phase has a more interesting evolution in peak shape and number with the change in pressure. In every isothermal desorption trace there is a small exothermic peak that possibly corresponds to the phase transition of $LiBH_4$ (~120°C)[8]
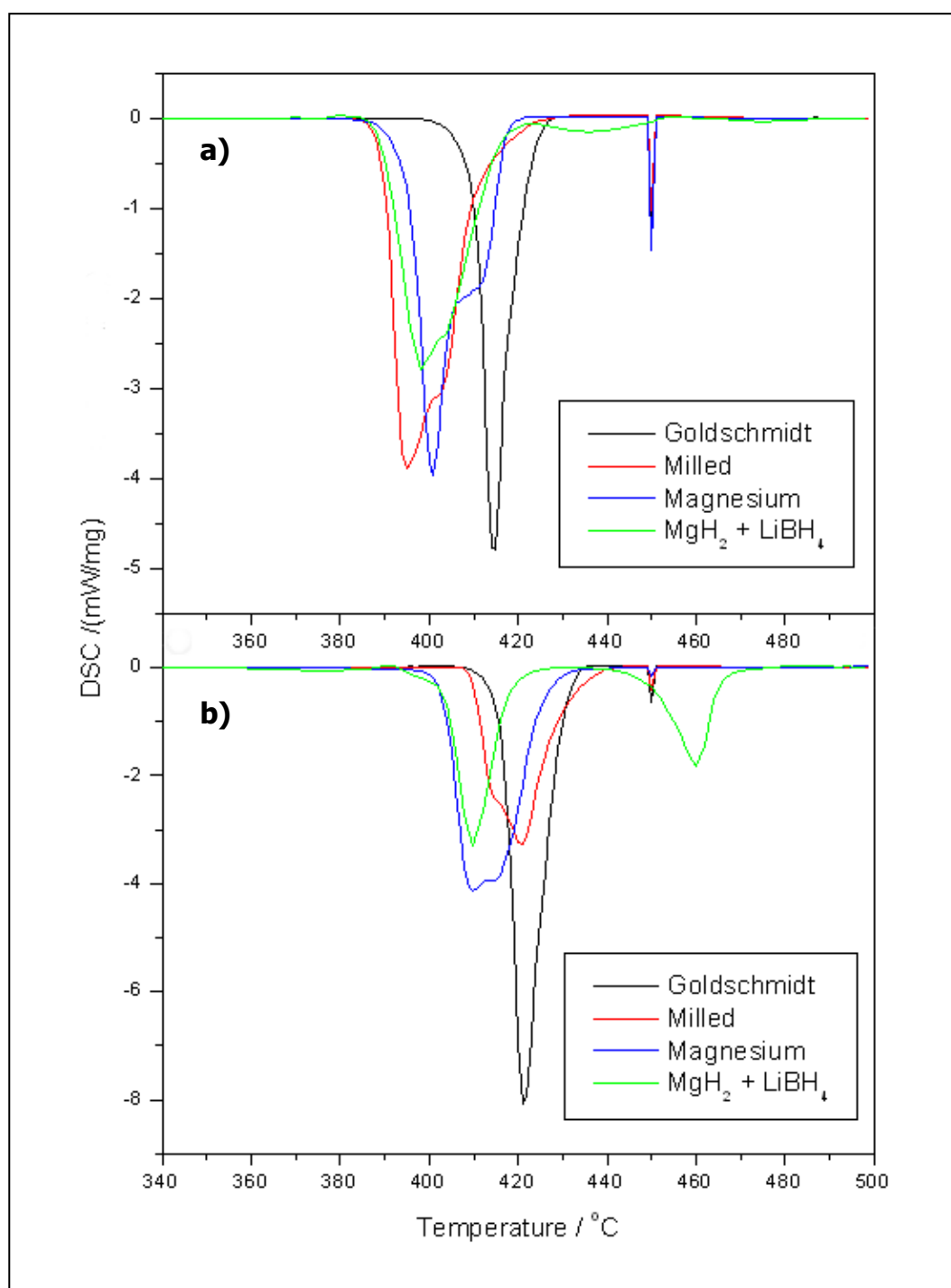

Figure 4.5.9 : DSC traces showing desorption endotherms for samples of Goldschmidt, milled Goldschmidt (5hrs), magnesium and hydrogen cycled MgH_2 + 10% $LiBH_4$ (5 absorption cycles) at a) 15 bar and b) 20 bar H_2

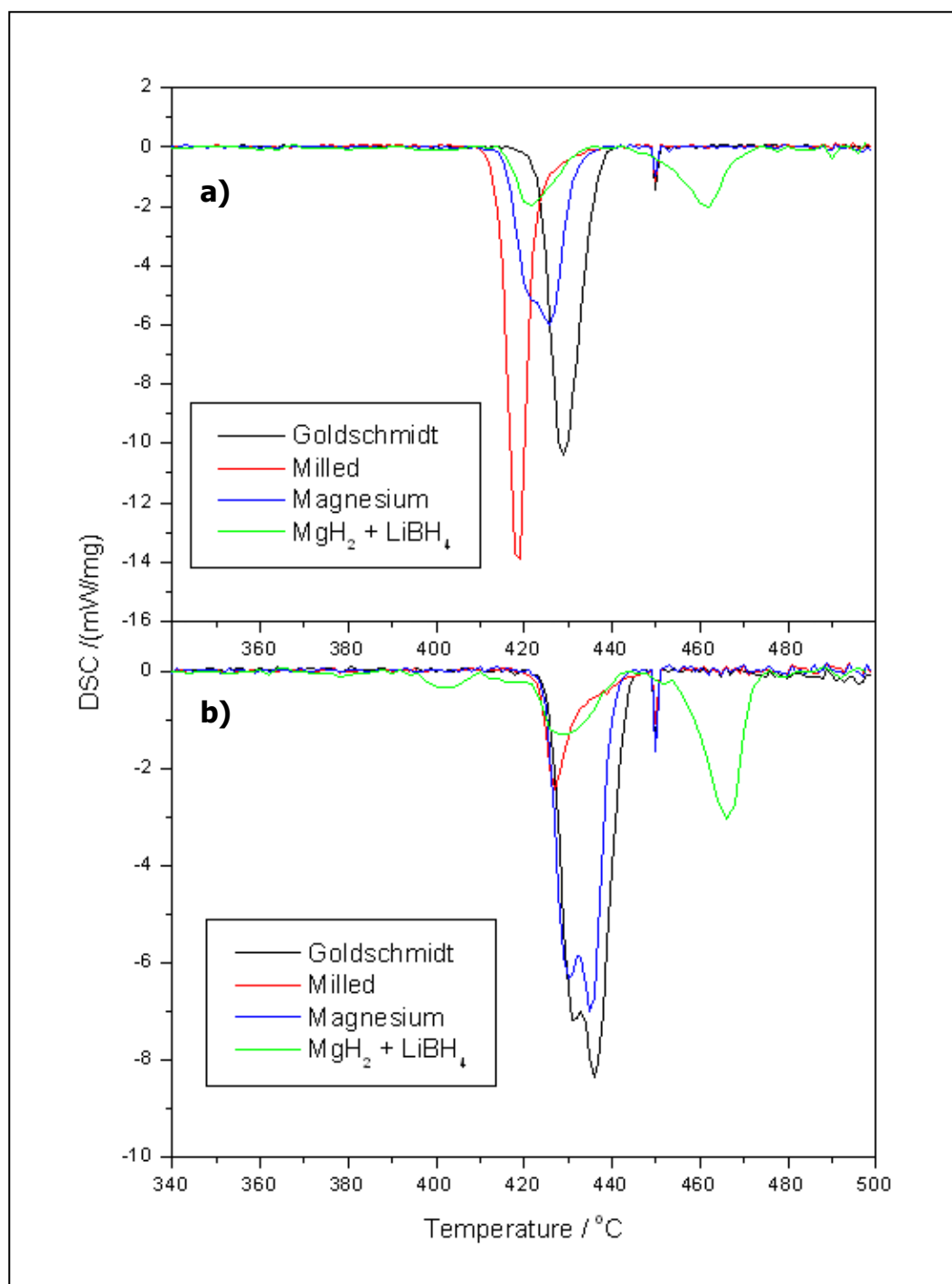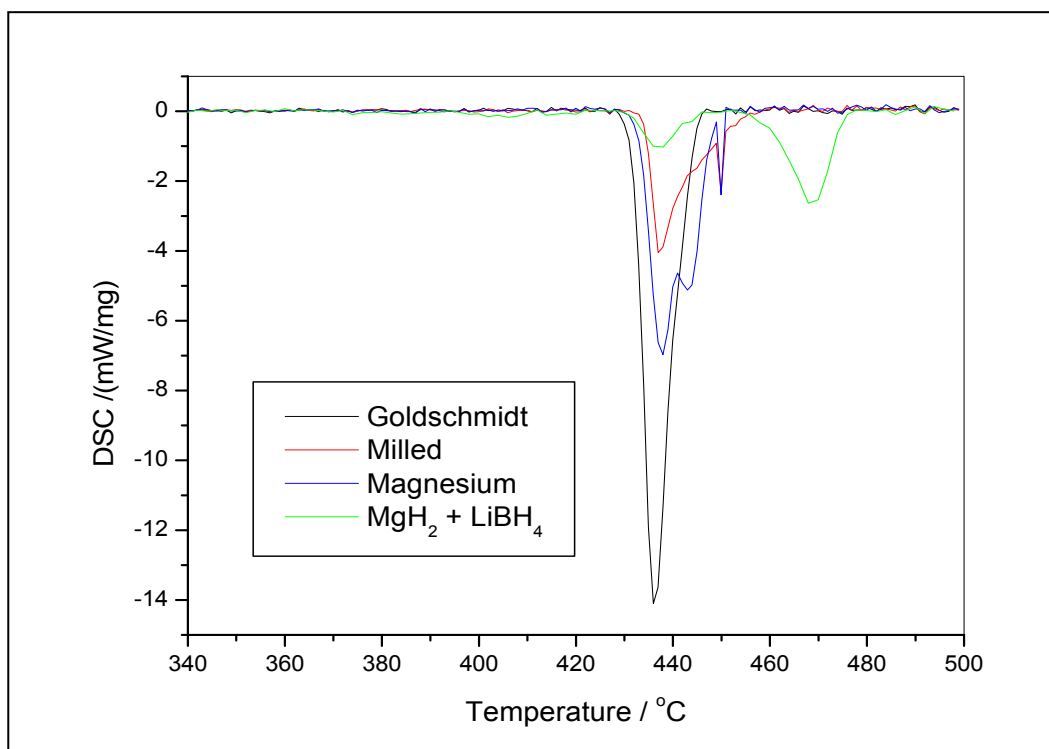**Figure 4.5.10 : DSC traces showing desorption endotherms for samples of Goldschmidt, milled Goldschmidt (5hrs), magnesium and hydrogen cycled MgH$_2$ + 10% LiBH$_4$ (5 absorption cycles) at 25 bar H$_2$**

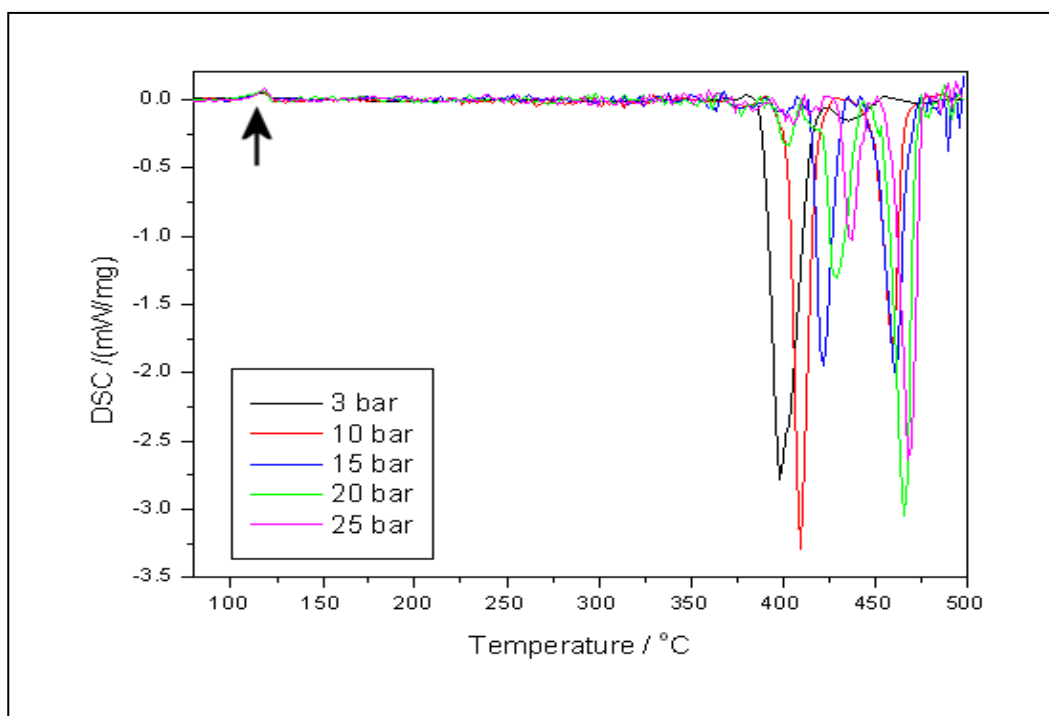**Figure 4.5.11 : DSC isothermal traces showing the phase transformation indicative of LiBH$_4$ for a sample of hydrogen cycled MgH$_2$ + 10% LiBH$_4$ (5 absorption cycles) at various pressures**

which is observed at approximately 116°C (Fig. 4.5.11) despite no $LiBH_4$ phase being observed in powder synchrotron X-ray diffraction after hydrogen cycling. However, there was no peak which would correspond to the melting point of $LiBH_4$ as observed by Bösenberg et al. at approximately 270°C[8]. There are various observed[9] and theoretical[10] intermediate compounds during the heating and decomposition of $LiBH_4$ no conclusive evidence was seen via XRD that any of these were formed during the reaction with MgH_2 – though the exothermic peak might be indicative of such a transition or reaction of one of those phases with MgH_2.

The MgH_2 + 10% $LiBH_4$ DSC isothermal traces showed a series of complex endothermic events depending on pressure. Two dominant peaks (one of which corresponds to the MgH_2 desorption and overlaps the other samples' peaks) were observed and, as pressure was increased, the relative intensity of the two peaks became reversed. Table 4.5.1 lists the onset temperatures observed for all endothermic events. The 3 bar trace shows the first had an onset temperature of ~380°C which corresponds to the comparable decomposition of MgH_2 as observed in the other samples, though there was also a small secondary peak that had an onset temperature of ~425°C. This second peak possibly corresponds to decomposition of $LiBH_4$ which is reported to occur between approximately 327°C and 427°C[11] for pure $LiBH_4$ under 1 bar H_2. Orimo et al. also reported the dehydriding process starting at 427°C with a peak at 577°C during thermal gravimetric analysis at atmospheric pressure. They also observed a 30°C reduction in desorption temperature in the presence of 10 at% of Mg to Li content which demonstrates the destabilisation that can be caused by additives.

Two endothermic peaks were also observed in the 10 bar trace, however, at 15 bar and above three endothermic peaks were observed; the first peak at 25 bar was ill-defined and so it is difficult to determine the onset temperature for that event. It remains unknown what causes these secondary peaks to appear, though at higher pressures, the third peak became the largest. Due to the experiments being performed under a hydrogen environment there is no associated mass spectrum data to determine whether hydrogen is released during the two

	Goldschmidt MgH2	5hr milled Goldschmidt	Magnesium	MgH$_2$ + 10% LiBH$_4$ (5 H$_2$ cycles)
3 bar	395-430	381-436	384-421	*380-421*
				425-455
10 bar	406-437	404-445	393-436	*390-429*
				440-480
15 bar	415-442	405-439	409-439	390-407
				413-435
				441-473
20 bar	420-446	414-450	419-444	395-409
				419-443
				448-475
25 bar	427-446	430-461	427-450	n/a
				427-445
				452-477

Table 4.5.1 : Onset temperatures (±2°C) and end-point temperatures (±5°C) for endothermic events during desorption isotherms for various samples performed via DSC. Known endothermic events that produce hydrogen for the MgH$_2$ + 10% LiBH$_4$ are marked with asterisks

extra endothermic events or if they are phase transitions or chemical reactions that do not result in the evolution of hydrogen. What is apparent is that the known hydrogen desorption event for the MgH$_2$ + 10% LiBH$_4$ sample coincides within error with those of the Goldschmidt MgH$_2$, milled Goldschmidt and Magnesium samples. It is seen that at lower pressures (3 and 10 bar) kinetic effects have a larger influence on the onset temperature with Goldschmidt having the largest particle size: <100µm compared with <90µm for the Strem Mg sample and <30µm for the milled sample. At higher pressures kinetic effects become less important and the known hydrogen desorption endothermic events overlap across the four samples.

Figures 4.5.12 – 14 show the exothermic events for absorption over a range of temperatures; 3, 10, 15, 20 and 25 bar. The large peaks at ~441°C are due to an impurity on the measurement place and do not affect the samples measured. Interestingly, there was only

Figure 4.5.12 : DSC traces showing absorption exotherms for samples of Goldschmidt, milled Goldschmidt (5hrs), magnesium and hydrogen cycled MgH$_2$ + 10% LiBH$_4$ (5 absorption cycles) at a) 3 bar and b) 10 bar H$_2$ whilst undergoing cooling

one exothermic event at each pressure for each sample that was associated with hydrogen absorption. This implies that the LiBH$_4$ is either reformed or partially rehydrided at the same time as MgH$_2$. It was also seen that each exothermic event corresponding to the absorption

of hydrogen in the MgH_2 + 10% $LiBH_4$ was much sharper and covered a shorter temperature range than those in the samples containing MgH_2 only. This would imply that the presence of $LiBH_4$ (whether fully or partially hydrided) increases the uptake of H_2 in MgH_2 significantly.

An interesting feature of the 5hr milled MgH_2 sample is that, at 20 and 25 bar, the exothermic event has an unusual shape that is not reflected by the other samples. Though it is unknown what the cause of this feature is, the relative inhomogeneity of particle size in the sample might account for it (Figure 4.1.10).

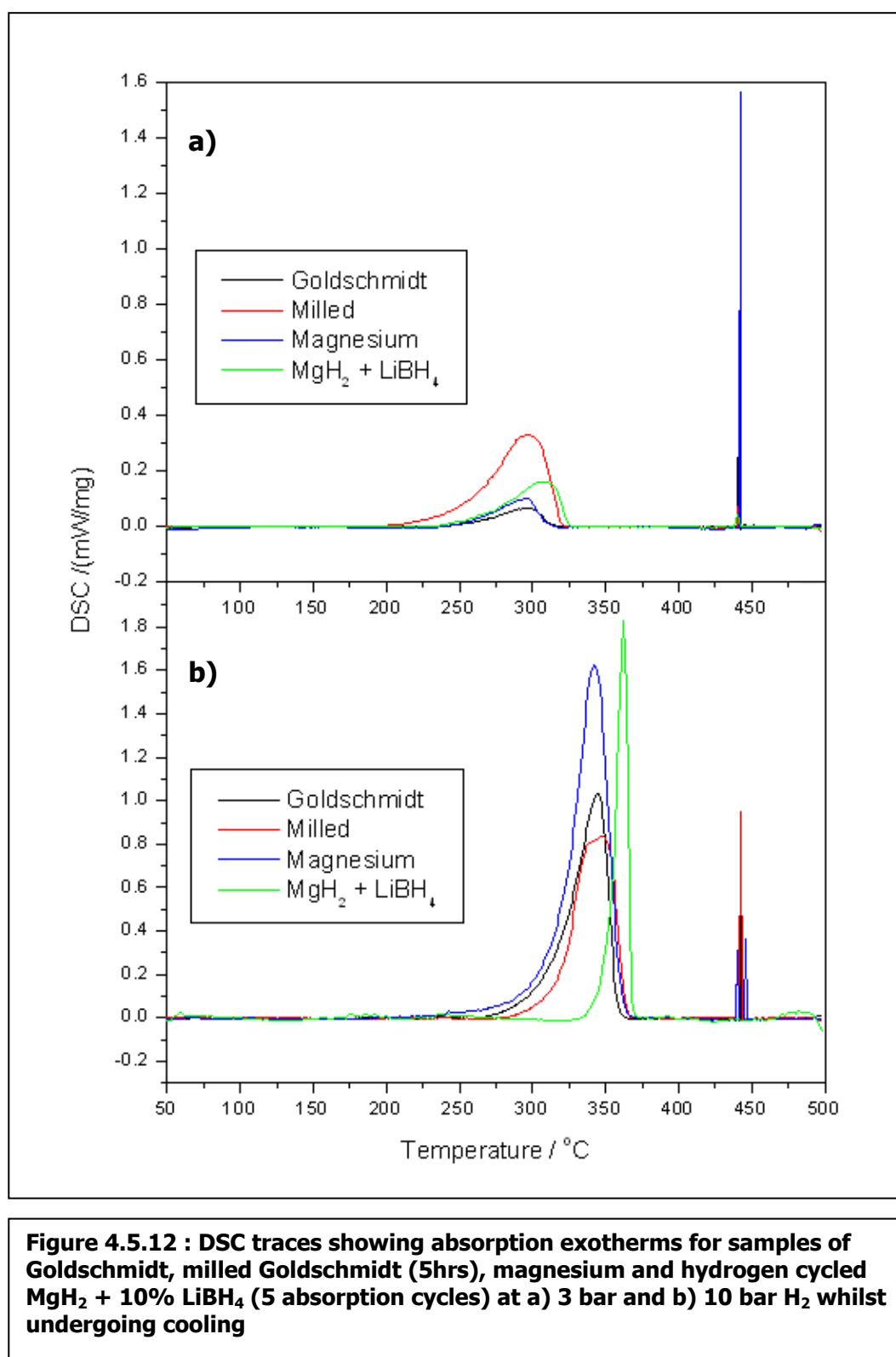**Figure 4.5.13 : DSC traces showing absorption exotherms for samples of Goldschmidt, milled Goldschmidt (5hrs), magnesium and hydrogen cycled MgH_2 + 10% $LiBH_4$ (5 absorption cycles) at 15 bar H_2 whilst undergoing cooling**

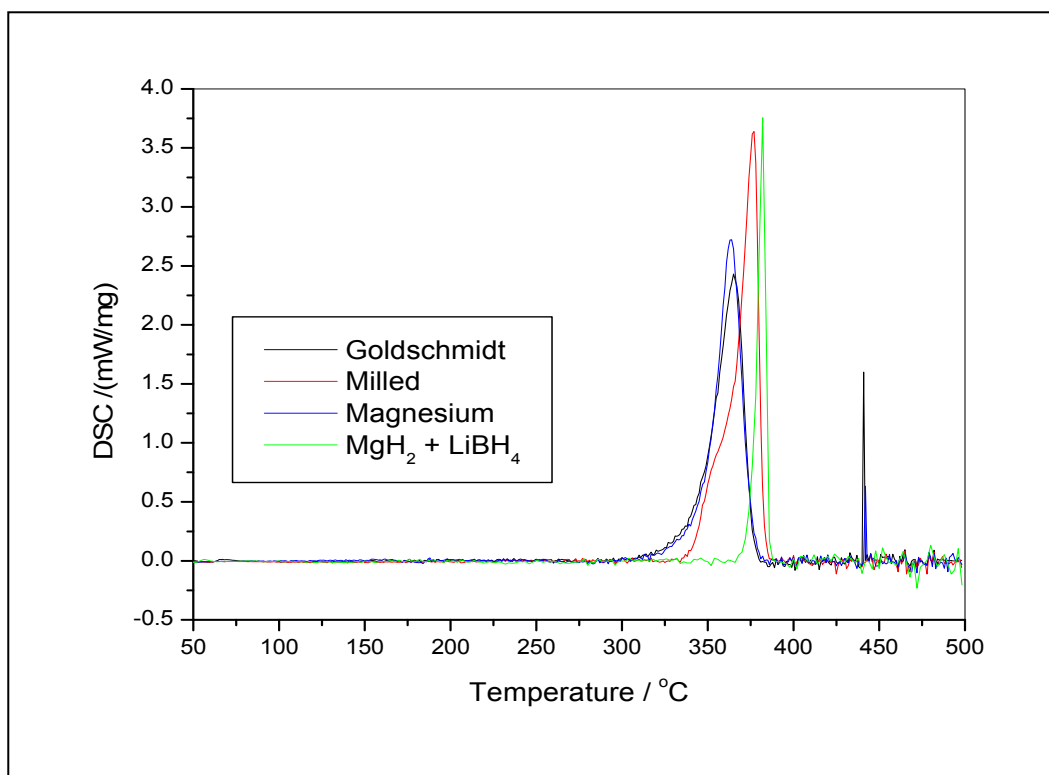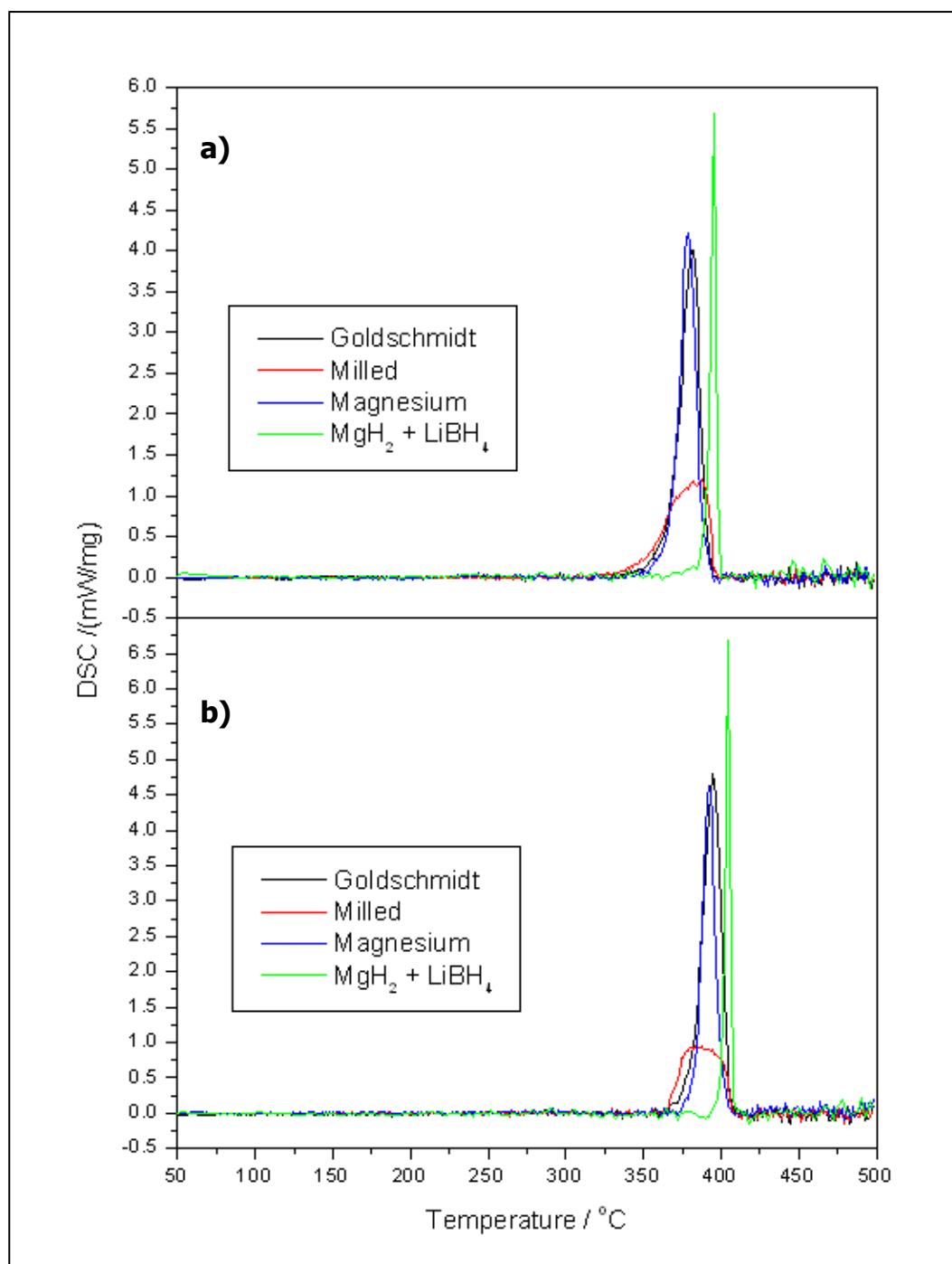**Figure 4.5.14 : DSC traces showing absorption exotherms for samples of Goldschmidt, milled Goldschmidt (5hrs), magnesium and hydrogen cycled MgH$_2$ + 10% LiBH$_4$ (5 absorption cycles) at a) 20 bar and b) 25 bar H$_2$ whilst undergoing cooling**

	Goldschmidt MgH2	5hr milled Goldschmidt	Magnesium	MgH$_2$ + 10% LiBH$_4$ (5 H$_2$ cycles)
3 bar	320-236	324-187	318-222	327-219
10 bar	365-263	365-275	364-263	369-333
15 bar	380-300	385-333	381-304	388-367
20 bar	395-330	398-310	395-344	400-386
25 bar	409-360	408-360	408-371	409-393

Table 4.5.2 : Onset temperatures (±2°C) and end-point temperatures (±5°C) for exothermic events during desorption isotherms for various samples performed via DSC

Figure 4.5.15 displays the Van't Hoff plots obtained using the onset temperatures of absorption. The gradients of the fitted lines give values of ΔH$_f$[MgH$_2$] = -76.1 (±0.6) kJmol^{-1}, -78.8 (±1.9) kJmol^{-1} and -80.0 (±0.5) kJmol^{-1} for the Goldschmidt, milled Goldschmidt and Strem samples respectively. Due to this method being affected by kinetic considerations, larger particle size is likely to play a part in determining the heat of formation. However, the observed results are within error.

A heated sample of Strem Mg + LiBH$_4$ (90:10) was also measured via this method and yielded a value of ΔH$_f$[MgH$_2$ + LiBH$_4$ (90:10)] = -83.2 (±0.2) kJmol^{-1}. Although this value is larger than previous samples, it is in line with the value observed for pure Strem Mg material.
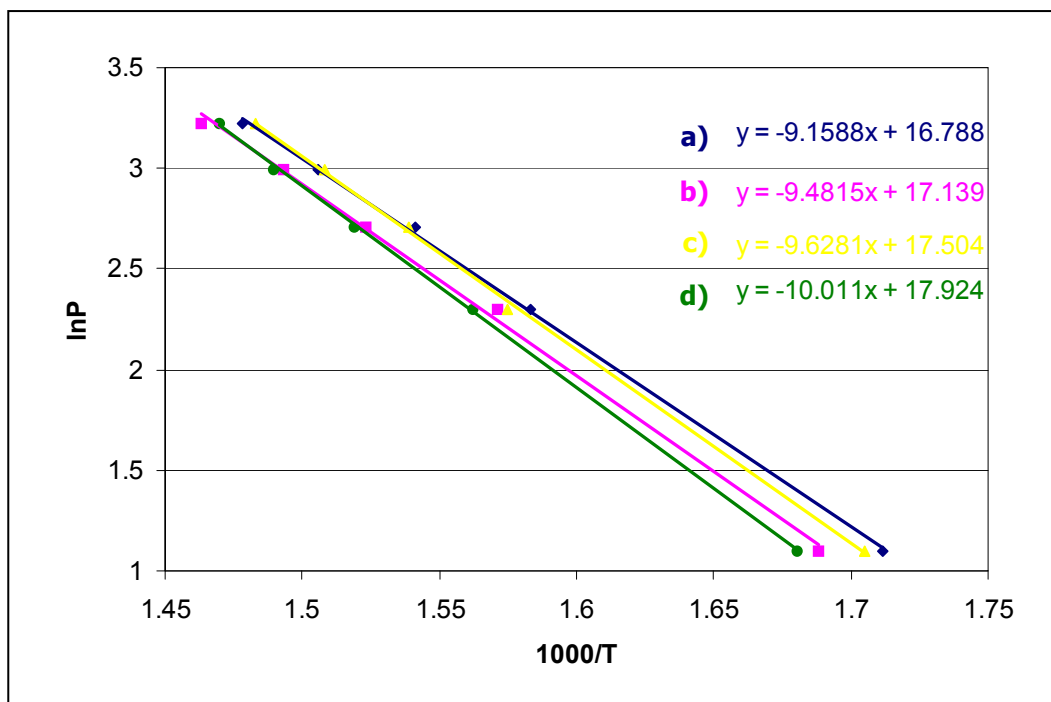
Figure 4.5.15 : Van't Hoff plots comparing desorption kinetic data for a) Goldschmidt MgH₂, b) Goldschmidt MgH₂ milled 5 hrs, c) Strem Mg and d) pre-heated Strem Mg + LiBH₄ (90:10)

This result reinforces the previous indication that $LiBH_4$ has little or no effect on the heat of formation of MgH_2.

4.4 (d) Thermodynamic Overview

The thermodynamic stability of MgH_2 is one of the reasons for its relatively high requirements for reversibility. However, this stability can be reduced through careful manipulation of the compound through it's reactions and interactions with other species and compounds[12-14]. MgH_2 is formed via an enthalpy of formation according to Eq. 4.5.4 and $LiBH_4$ is formed through the reaction detailed in Eq. 4.5.5.

$$Mg + H_2 \rightarrow MgH_2 \qquad \Delta H_f = -75 kJmol^{-1}H_2 \qquad \textbf{Equation 4.5.4}$$

$$LiH + B + \frac{3}{2}H_2 \rightarrow LiBH_4 \qquad \Delta H_f = 69 kJmol^{-1}H_2 \qquad \textbf{Equation 4.5.5}$$
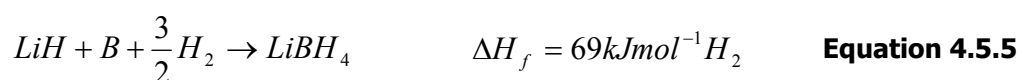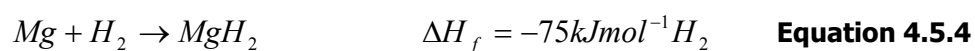
For the MgH_2 + $LiBH_4$ system there are a number of possible reported ways for the two to interact. First the decomposition via:

$$2LiBH_4 + MgH_2 \longleftrightarrow 2LiH + MgB_2 + 4H_2 \quad \Delta H_f = 46 kJmol^{-1}H_2 \text{ [14]}\textbf{Equation 4.5.6}$$
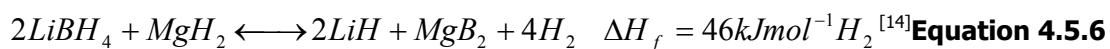
This path provides a much lower thermodynamic route for the decomposition of both reagents. Fang et al. have also reported a further decomposition between $Mg(BH_4)_2$ and $LiBH_4$ through the decomposition of both products via production of diborane (B_2H_6):

$$LiBH_4 \xleftrightarrow{1} \frac{1}{12}Li_2B_{12}H_{12} + \frac{5}{6}LiH + \frac{13}{12}H_2 \xleftrightarrow{2} LiH + B + \frac{3}{2}H_2 \text{ [15]} \quad \textbf{Equation 4.5.6}$$
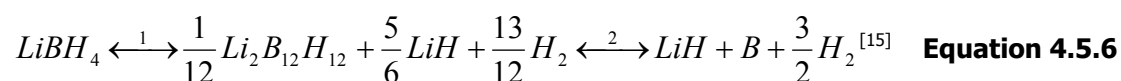
$$\Delta H_f = 56 kJmol^{-1}H_2$$

Since $Mg(BH_4)_2$ can be formed via reaction of B_2H_6, it seems logical that the formation of the $Li_2B_{12}H_{12}$ and $Li_2B_{10}H_{10}$ phases reported in the literature[16] via the decomposition of $LiBH_4$ through loss of B_2H_6 (reacting with itself) that there are many possibilities for the reduction of the heat of decomposition for the combination of MgH_2 and $LiBH_4$. Further study is needed on these compounds before all the possible reaction pathways between the two are found.

1. Rongeat C., Llamas-Jansa I., Doppiu S., Deledda S., Borgschulte A., Schultz L., and Gutfleisch O., *Determination of the heat of hydride formation/decomposition by high-pressure differential scanning calorimetry (HP-DSC).* J. Phys Chem. B., 2007. **111**(46): p. 13301.

2. *CRC Handbook of chemistry and Physics.* 73 ed, ed. Lide D.R. 1992-1993: CRC Press.

3. Dornheim M., Doppiu S., Barkhordarian G., Boesenberg U., Klassen T., Gutfleisch O., and Bormann R., *Hydrogen storage in magnesium-based hydrides and hydride composites.* Scr. Mater., 2007. **56**: p. 841.

4. Pedersen A.S., Kjoller J., Larsen B., and Vigeholm B., *Magnesium for hydrogen storage.* Int. J. Hydrogen Energy, 1983. **8**: p. 205.

5. Stampfer J.F., Holley C.E., and Suttle J.F., *The magnesium-hydogen system.* J. Am. Chem. Soc., 1960. **82**: p. 3504.

6.   Huot J., Liang G., Boily S., Van Neste A., and Schulz R., *Structural Study and hydrogen sorption kinetics of ball-milled magnesium hydride.* J. Alloy Cmpd., 1999. **293-295**: p. 495.

7.   Gennari F.C., Castro F.J., and Urretavizcaya G., *Hydrogen desorption behaviour from magnesium hydrides synthesized by reactive mechanical alloying.* J. Alloy. Compd., 2001. **321**: p. 46.

8.   Bösenberg U., Doppiu S., Mosegaard L., Barkhordarian G., Eigen N., Borgschulte A., Jensen T.R., Cerenius Y., Gutfleisch O., Klassen T., Dornheim M., and Bormann R., *Hydrogen sorption properties of MgH_2 - $LiBH_4$ composites.* Acta Mater., 2007. **55**: p. 3951.

9.   Mosegaard L., Møller B., Jørgensen J., Bösenberg U., Dornheim M., Hanson J.C., Cerenius Y., Walker G., Jakobsen H.J., Besenbacher F., and Jensen T.R., *Intermediate phases observed during decomposition of $LiBH_4$.* J. Alloy Cmpd., 2007. **446-447**: p. 301.

10.   Ohba N., Miwa K., Aoki M., Noritake T., Towata S., Nakamori Y., Orimo S., and Züttel A., *First-principles study on the stability of intermediate compounds of $LiBH_4$.* Phys. Rev. B, 2006. **74**: p. 075110.

11.   Orimo S., Nakamori Y., Kitahara G., Miwa K., Ohba N., Towata S., and Züttel A., *Dehydriding and rehydriding reactions of $LiBH_4$.* J. Alloy Cmpd., 2005. **404-406**: p. 427.

12.   Castro F.J., Yavari A.R., LeMoulec A., Ishikawa T.T., and Botta W.J., *Improving H-sorption in MgH_2 powders by addition of nanoparticles of transition metal fluoride catalysts and mechanical alloying.* J. Alloy Cmpd., 2005. **389**: p. 270.

13.   Grochala W. and Edwards P.P., *Thermal decomposition of the non-interstital hydrides for the storage and production of hydrogen.* Chem. Rev., 2004. **104**: p. 1283.

14.   Vajo J.J., Salguero T.T., Gross A.F., Skeith S.L., and Olson G.L., *Thermodynamic destabilization and reaction kinetics in light metal hydrides.* J. Alloy Cmpd., 2007. **446-447**: p. 409.

15.   Fang Z.-Z., Kang X.-D., Wang P., Li H.-W., and Orimo S., *Unexpected dehydrogenation behaviour of $LiBH_4/Mg(BH_4)_2$ mixture associated with the in situ formation of dual-cation borohydride.* J. Alloy. Compd., 2010. **491**: p. L1-L4.

16.   Friedrichs O., Remhof A., Hwang S.-J., and Züttel A., *Role of $Li_2B_{12}H_{12}$ for the formation and decomposition of $LiBH_4$.* Chem. Mater., 2010. **22**: p. 3265.

5.   Discussion and Conclusions

It has been seen that addition of $LiBH_4$ to MgH_2 and Mg improves the hydrogen absorption and desorption kinetics, though the exact nature of the interaction between the two is still unknown. It is clear that more than one effect is at play in the $MgH_2/LiBH_4$ system and it has been the subject of this investigation to examine the extent of those effects.

5 (a) The effect of contamination on the H_2 sorption kinetics of the $MgH_2/LiBH_4$ system

Shortly after the time allotted for experimentation had expired it was discovered that the oil seal around the bearing in the turbomolecular pump on the IGA had failed, allowing hydrocarbons to back-flush through the vacuum system into the main reactor chamber. The degradation of the seal happened slowly, over a long period of time, though we speculate that this started around the time that we switched to alternate sources of MgH_2 with their apparently slower kinetic properties. Evidence of the impact that this has had on reactive compounds such as MgH_2 and $LiBH_4$ can be seen in chapter 4.4. Although the chemical composition is identical to MgH_2 samples sourced from Aldrich, the performance of the Strem Mg + $LiBH_4$ (90:10) sample that had been hydrogen cycled independently before kinetic measurements were undertaken was much improved over the Strem Mg + $LiBH_4$ (90:10) sample cycled on the IGA. The final absorption for the sample processed on the TPD system was 2.8 times faster and the final desorption is 2.5 times faster than the sample processed on the IGA, and both values were almost equal to those obtained using Aldrich MgH_2.

While it would be incorrect to presume that all samples performed since the change of reagent should perform at least 2.5 times as fast as observed, the relative slowness of kinetics can, at least in part, be explained by this sample contamination. The IGA

experiments were performed with a liquid nitrogen trap on the H_2 pipeline inlet so, in theory, any contamination from O_2 or H_2O in the H_2 gas itself could be ruled out. It would also be unlikely that the poor kinetics, observed over a large number of samples and over a long period of time would have been consistently poor when combined with the fact that replacement of H_2 cylinders was a relatively common occurrence (every couple of months). So, if one sample had been contaminated due to bad management of the liquid N_2 trap or contamination from excessive impurities in a gas supply it would be quite apparent in comparison to the slight reduction in sorption kinetics for the MgH_2 + $LiBH_4$ samples. Other samples on other pieces of equipment were not reported to be adversely affected and that would indicate that the problem was not from the gas source.

It has also been observed that the combination of MgH_2 and $LiBH_4$ results in a mixture that is far more susceptible to oxidation. Section 4.3 (c) showed the difference between loading a sample under atmospheric conditions and loading it under an inert atmosphere such as argon. As reported elsewhere[1] oxide formation on the surface of the Mg/MgH_2 particles hinders hydrogen diffusion and this effect results in significantly reduced kinetics for the first absorption and desorption. It was found that inertly loading a sample of MgH_2 + $LiBH_4$ (90:10) allowed 4.7 wt% H_2 to be desorbed at 300°C in under 1000 minutes for the first hydrogen cycle whereas a sample loaded in atmosphere only desorbed 0.4 wt% H_2 in 2100 minutes at 300°C; this was achieved within 121 minutes for the inertly loaded sample which is an improvement of over 17 times.

It should be noted that some of the observed variation in the H_2 storage capacity between different samples could be, at least partially, explained by the introduction of contaminants to the mixture. This effect could be determined through measurement on a different set of apparatus or via a different gas supply.

The samples that are affected by this still exhibit faster kinetics than their non-reacted forms (i.e. pure MgH_2) which would suggest that there is still some benefit to be had from adding

LiBH$_4$ in situations where sample degradation might be a problem. It's possible that the reaction between MgH$_2$ + LiBH$_4$ is resistant to contaminants.

5 (b) Effect of particle size on the H$_2$ sorption kinetics of the MgH$_2$/LiBH$_4$ system

It is known that one of the main limiting factors governing the storage of hydrogen in the magnesium system is the diffusion of H$_2$ through MgH$_2$ regions of a particle[2]. While a reduction in particle size has no effect on the thermodynamics of the system[3], a smaller particle and grain size will result in faster diffusion of H$_2$. This aspect can manifest itself in the reduction of onset temperatures for hydrogen absorption and desorption (T$_{onset}$) resulting in a kinetically faster material for smaller grain and particle sizes as observed through the process of mechanical milling of Mg and MgH$_2$[4]. As the particle size becomes homogenous there is a single, fine desorption/absorption peak observed, however, if the particle size lies over a wide range (from the micrometer to nanometer scale) this peak will broaden or even split into several peaks whose bases overlap depending on the particle size distribution and their relative H$_2$ diffusion coefficients. Varin et al. noted that a reduction in grain/crystallite size is not as important as a reduction in particle size[4] and this has been confirmed by other research groups[3, 5, 6]. This also agrees with work carried out in this investigation where it has been noted that grain size increases during the formation of the Mg and MgH$_2$ phases upon hydrogen cycling (section 4.1, figure 4.1.9), but there is no observed reduction in the rate of hydrogen sorption, which in fact, tends to improve with hydrogen cycling due to decrepitation of particles, leading to a convergence in grain and particle size.

For the MgH$_2$/LiBH$_4$ system this reduction in particle size is an important aspect of the increase in kinetics. It can be seen that the interaction between MgH$_2$ and LiBH$_4$ results in an increased surface area with a very fine microstructure (Figure 4.2.10) which possibly results from an increased rate of decrepitation. Certainly, the propagation of the [BH$_4$]$^-$ complex and homogenisation of the sample over successive hydrogen cycles, as observed during Raman spectroscopy after successive absorption measurements had been taken (section 4.4 (d)),

and the observed diffusion of boron into the bulk magnesium 'cube' (section 4.4 (e)) might be linked to an improved or increased decrepitation process which results in the observed refinement of a highly porous microstructure of MgH_2 and the break-down of larger particles for samples of MgH_2 + $LiBH_4$ (90:10) (Figures 4.2.10 and 4.4.7).
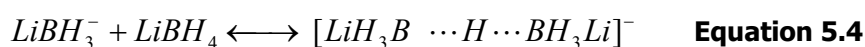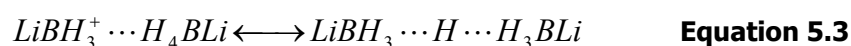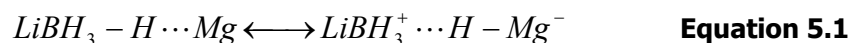
5 (c) The interaction of $LiBH_4$ with MgH_2

The MgH_2/$LiBH_4$ system has been investigated by a number of research groups, however the majority of studies have been performed on $LiBH_4$-rich ratios and/or at high temperature[7-12]. Studies by Vajo et al. showed that formation of MgB_2 and LiH at temperatures above 400°C destabilises MgH_2 and $LiBH_4$, thus providing a favourable decomposition product which effectively lowers the overall energy required to dissociate hydrogen from both Mg and the $LiBH_4$[10, 11]. Yu et al. reported the formation of two Li–Mg alloy phases above 440°C from the decomposition of LiH in the presence of Mg[8]. However, as discovered in this investigation (and confirmed by Mao et al.[9]) MgB_2 and LiH are not formed at temperatures between 300 and 350°C, and the presence of MgB_2 in a mixture with MgH_2 does not appreciably increase the reaction kinetics over pure MgH_2 over numerous hydrogen cycles at these temperatures.

While the refinement of the microstructure of MgH_2 is easily observed via SEM for MgH_2 + $LiBH_4$ samples (Figures 4.2.10, 4.4.10), the nature of the chemical interaction between the two compounds remains elusive. Vigeholm et al. observed a similar structural refinement over 31 H_2 cycles though it was much less pronounced[13]. The fact that a better structural refinement was achieved in only 6 H_2 cycles suggests that the improvement is definitely attributable to the interaction of $LiBH_4$ with MgH_2. Powder XRD data showed a slight reduction in MgH_2, Mg and $LiBH_4$ lattice structure over a range of Mg/MgH_2:$LiBH_4$ mixture ratios from Mg-rich to Li-rich. However, Goldschmidt unit cell volumes for heated samples were significantly smaller than those observed for Avocado, which might indicate a very small substitution of Li or B into the MgH_2 lattice – presumably not observed in the Avocado

samples due to the presence of magnesium oxide and hydroxide which might preferentially react with LiBH$_4$ as shown in section 4.3 (a). LiBH$_4$ reflections were visible after heating in the presence of MgH$_2$ under static vacuum but not after hydrogen cycling and additional peaks were observed both after heating and after hydrogen cycling but not with any consistency. Thermodynamic data suggests that if there is a reduction in the enthalpy of formation for MgH$_2$, then it is very small: ~5 kJmol^{-1}. This reduction – if a real effect – could give the appearance of faster desorption kinetics as it would mean that the formation of MgH$_2$ is destabilised slightly. However, the absorption kinetics are equally improved after reaction with LiBH$_4$ – this might be explained through the refinement in microstructure as diffusion of H$_2$ during absorption is the rate limiting step for materials with larger microstructure[2].
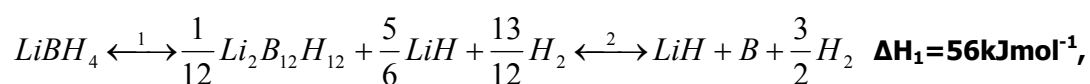
Mao et al. suggested that it is Li$^+$ in the form of LiBH$_4$ or LiH which catalyses the reaction of H$_2$ with Mg[9]. However, there is some evidence that LiBH$_4$ does have a chemical interaction with Mg. Infrared analysis shows a shift in absorptions from 1090 and 2302 cm^{-1} to higher wavenumber values: 1118 and 2357 cm^{-1} respectively. This might correspond to a strengthened B-H bonding arrangement from the interaction of Mg with LiBH$_4$ (Figure 4.3.15). This could result from the formation of an Mg–Li borohydride –analogous to Mg–Li–N–H compounds[14] – or through the transfer of hydrogen atoms between LiBH$_4$ and Mg (Eq. 5.1).

$$LiBH_3 - H \cdots Mg \longleftrightarrow LiBH_3^+ \cdots H - Mg^- \qquad \textbf{Equation 5.1}$$

$$HMg^- \cdots H - H_3BLi \longleftrightarrow MgH_2 + LiBH_3^- \qquad \textbf{Equation 5.2}$$

$$LiBH_3^+ \cdots H_4BLi \longleftrightarrow LiBH_3 \cdots H \cdots H_3BLi \qquad \textbf{Equation 5.3}$$

$$LiBH_3^- + LiBH_4 \longleftrightarrow [LiH_3B \cdots H \cdots BH_3Li]^- \qquad \textbf{Equation 5.4}$$

There is some evidence to support this process though it is unlikely that this process is happening due to the unfavourable nature of several of the species: No $LiBH_4$ is observed via XRD after H_2 cycling though both Li and B are known to be present from previous XPS studies[15]. Secondly, for mixtures of Mg + $LiBH_4$ heated at 300°C under static vacuum, MgH_2 was seen to be formed after heating for 12 hours and as $LiBH_4$ is a known reducing agent, direct transfer of hydrogen from the boron to the metal could be an obvious answer to the question of why the kinetics improve as much as they do with so few hydrogen cycles. This mechanism could possibly facilitate the porous microstructure growth of the material with $LiBH_4$ acting as a nucleation point for new MgH_2 particulates and phases. There is also the indication of a strengthened B–H bonding interaction seen via IR which might result from a slight hydrogen deficiency in the $LiBH_4$ lattice. Lastly, there was more evidence of a new bonding arrangement from Raman spectroscopy which was only observed for dehydrided samples after the cycling process had occurred (section 4.4 (d), figure 4.4.13). There was no evidence of $LiBH_4$ vibrational peaks at 1288 and 2296 cm^{-1}, instead new peaks at 757, 934, 1111, 1246 and 2493 cm^{-1} were observed, however, for the equivalent hydrided sample only MgH_2 and $LiBH_4$ vibrational stretches were seen.

Johnson et al. reported that ^{11}B NMR showed a single peak before hydrogen cycling but, after MgH_2 and $LiBH_4$ were heated together this changed to having multiple peaks after the first desorption and subsequent absorptions and desorptions[15] which would suggest that the boron environment had become more complex. Four separate ^{11}B NMR peaks were observed, one corresponding to a slightly down-shifted $LiBH_4$ environment (−43 ppm) and three up-shifted peaks at 12.7, 0.9 and −16 ppm. An up-shift in ppm usually corresponds to a change in the bonding around the boron atom: BR_4 has a higher ppm than BH_4, where R is any alkyl group, usually around −15 to −22 ppm. Partially dehydrided $LiBH_4$ phases or new bonding arrangements with Mg might be the cause some of these aspects of the Raman, IR and NMR results.

However there is also another possible theory on the nature of the interaction between MgH_2 and $LiBH_4$. The reported compounds, $Li_2B_{12}H_{12}$ and $Li_2B_{10}H_{10}$, formed from the partial decomposition of $LiBH_4$ when held at temperatures above 150°C, might play a role in the fast kinetics of MgH_2[16-18]. The Raman shifts reported in literature by Orimo et al. and Reed et al. correspond closely to those observed for dehydrided samples of MgH_2 + $LiBH_4$ (90:10)[16, 19]. The Raman peaks for $Li_2B_{12}H_{12}$ are observed at 580, 760, 920 and 2500 cm^{-1} while in the Raman study of MgH_2 + $LiBH_4$ in section 4.4 (d), peaks at 566, 745, 939 and 2504 cm^{-1} were observed after the third desorption. Furthermore, after the fifth desorption previously unseen Raman shifts were observed, suggesting that there is a chemical evolution occurring upon sequential H_2 cycling. Interestingly, the Raman spectra obtained after absorption were relatively uninteresting – mainly being composed of MgH_2 (as would be expected). However, the disparity between the features observed after desorption and not observed after absorption might point to the interaction between $LiBH_4$ and Mg being more important than that of the hydrided phase. It might also lend more credence to the idea that $LiBH_4$ lowers the enthalpy of formation for MgH_2 as this decomposition is more thermodynamically stable than the direct decomposition of $LiBH_4$ to LiH and B (Eq.5.5) by 20 $kJmol^{-1}$[16](Eq. 5.6).

$$LiBH_4 \longleftrightarrow LiH + B + \frac{3}{2}H_2 \qquad \textbf{Equation 5.5}$$

$$LiBH_4 \xleftrightarrow{1} \frac{1}{12}Li_2B_{12}H_{12} + \frac{5}{6}LiH + \frac{13}{12}H_2 \xleftrightarrow{2} LiH + B + \frac{3}{2}H_2 \quad \textbf{ΔH}_1\textbf{=56kJmol}^{-1}\textbf{,}$$
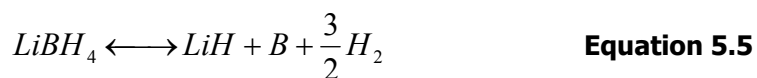
$$\textbf{Equation 5.6}$$

Considering the lower enthalpy for the first step in Eq. 5.6 and the Raman evidence that there is still a large possibility of a partially hydrided Li-complex within the sample it might be

possible to propose a different reaction scheme to the one outlined in Eq.s 5.1 – 5.4 centred around a stabilisation reaction of $Li_2B_{12}H_{12}$ or $Li_2B_{10}H_{10}$ with Mg. Especially because $Li_2B_{12}H_{12}$ takes the form of $2\{Li^+[B_{12}H_{12}]^-\}$, it would not be unlikely that Mg^{2+} was able to substitute for $2Li^+$. In fact, Fang et al. reported that a dual-cation borohydride was formed through mechanical milling of $Mg(BH_4)_2$ with $LiBH_4$ through the decomposition of both compounds through release of diborane[Fang Z.-Z., 2010 #21] – the same route that is suggested for the formation of both $Li_2B_{12}H_{12}$ and $Li_2B_{10}H_{10}$. There is also the suggestion of the reverse reaction being true during H_2 absorption measurements for samples of $MgH_2 + LiBH_4$ as the $[BH_4]^-$ unit appears to be reformed (Figure 4.4.13) as usually $LiBH_4$ is not reversible at temperatures of 300°C and 10 bar.

If $LiBH_4$ is a nucleation site for the formation of MgH_2 then the observed inhomogeneity during early hydrogen cycles in the Raman samples may be the reason why successive hydrogen cycles are required to propagate the $LiBH_4$ and activate the MgH_2 samples. Indeed, the importance of the initial heating step before cycling (Figure 4.2.16) suggests that being held at 300°C allows the dispersal of the $LiBH_4$ throughout the Mg/MgH_2 material which otherwise must be achieved during hydrogen cycling.

Whether or not the above proposed mechanism is taking place, what seems to be certain from the available information is that $LiBH_4$ interacts primarily with Mg and not MgH_2 and that hydriding may be catalysed by the reduction of Mg by $LiBH_4$. Indeed, while DSC desorption events were similar to those of Goldschmidt MgH_2, 5hr milled Goldschmidt MgH_2 and Strem Mg (though there were unknown extra endothermic events observed at temperatures below and above the main H_2 desorption peak) were seen for $Mg + LiBH_4$ (section 4.5 (c)) the absorption peaks occurred at higher temperatures and had a smaller area under the curve due to the narrowness of the event – suggesting the absorption reaction was completed much more quickly (and therefore with faster kinetics) than for MgH_2.

5 (d) The effect of increased LiBH$_4$ content on the sorption kinetics of MgH$_2$

It has also been observed that an increase in LiBH$_4$ content results in an associated improvement in hydrogen sorption kinetics over samples with a lower MgH$_2$:LiBH$_4$ ratio. A sample of MgH$_2$ + LiBH$_4$ (9:3) performed 1.6 times faster on absorption than a sample with a ratio of 9:1 and 2.1 times faster on desorption (section 4.3 (e)). This result suggests that the optimum ratio of Mg:LiBH$_4$ for an Mg-rich mixture lies at somewhere between a MgH$_2$:LiBH$_4$ ratio of 1:1 and 9:1.

The observation of new phases arising in samples of various ratios for heated samples of Mg and LiBH$_4$ between the ratios of 1:1 and 9:1 (section 4.4 (b)) also points to this conclusion. It might be important to note that LiBH$_4$ unit cell volumes appear to increase on increasing content of Mg towards the unit cell volume of pure LiBH$_4$ – a small amount of Mg present in a sample of LiBH$_4$ appears to slightly reduce the unit cell size (Figure 4.4.5).

6   Further work and experimentation

A new reaction mechanism has been proposed for the interaction of Mg and LiBH$_4$ at temperatures of 300–350°C under 10 mbar of H$_2$ via the reduction of Mg to possibly form an Mg-Li complex. While it is still unclear what form this interaction ultimately takes, it is possible that the decomposition of LiBH$_4$ to one of its stable intermediates, Li$_2$B$_{12}$H$_{12}$ or Li$_2$B$_{10}$H$_{10}$ might be an important step towards a lowered enthalpy for the combined system.

MgH$_2$ and LiBH$_4$ have been combined to produce samples that have vastly improved H$_2$ sorption kinetics, however, the optimum reaction ratio is not yet known. Several investigations to understand the exact interaction can be undertaken:

- Perform the reaction of Mg + LiBH$_4$ at 300°C under flowing argon and monitor the exhaust with a residual gas analyser. This would help determine whether H$_2$ is desorbed from the LiBH$_4$ at lower temperatures than usual through interaction with Mg (as proposed for the interaction between the lone pair of electrons from NH$_3$ and LiH for the LiNH$_2$/LiH system) or if the hydrogen is donated to the Mg directly.

- X-ray diffraction studies on hydrogen cycled-Mg/MgH$_2$ + LiBH$_4$ in its dehydrided state. This would show any new phases resulting from the interaction of LiBH$_4$ and Mg over successive H$_2$ cycles – as observed through Raman spectroscopy.

- Perform a thorough ^{11}B NMR analysis over the full range of Mg/MgH$_2$ + LiBH$_4$ ratios after heating and after hydrogen cycling. Further clarification of the boron environment at each step of the process might lead to a better understanding of the reaction mechanism.

- Exploration of the effects of pressure on the possible hindrance of nucleation for MgH$_2$ and whether the highly porous agglomeration of particles observed for samples of H$_2$ cycled MgH$_2$ + LiBH$_4$ are resistant to this reported effect.

- Re-analysis of Avocado and Goldschmidt MgH_2 + 10% $LiBH_4$ with refurbished equipment or through H_2 cycling on the flowing TPD system and then transferring the sample to the IGA for gravimetric analysis.

- Determine if $Li_2B_{12}H_{12}$ can be formed in the presence of MgH_2 by mirroring the reaction conditions that are shown to generate the compound[16, 17].

- Perform SEM on a range of H_2 cycled Mg + $LiBH_4$ ratios to observe if the microstructure is altered by different concentrations of $LiBH_4$ in the sample.

- DSC experiments on cycled Mg + $LiBH_4$ under a flow of argon to determine whether the same variety of endothermic peaks are observed during desorption coupled with a mass spectrum analysis to look for the evolution of H_2 and diborane at those events.

1.   Chen C.P., Liu B.H., L. Z.P., and Wang Q.D., *The activation mechanism of Mg-based hydrogen storage alloys.* Z. Phys. Chem., 1993. **181**: p. 259.

2.   Vigeholm B., Jensen K., Larsen B., and Schroder-Pedersen A., *Elements of hydride formation mechanisms in nearly spherical magnesium powder particles.* J. Less Common Met., 1987. **131**: p. 133.

3.   Huot J., Liang G., Boily S., Van Nesteb A., and Schulz R., *Structural study and hydrogen sorption kinetics of ball-milled magnesium hydride.* J. Alloy. Compd., 1999. **293-295**: p. 495.

4.   Varin R.A., Czujko T., Chiu Ch., and Wronski Z., *Particle size effects on the desorption properties of nanostructured magnesium dihydride (MgH_2) synthesized by controlled reactive mechanical milling (CRMM).* J. Alloy. Compd., 2006. **424**(1-2): p. 356.

5.   Hanada N., Ichikawa T., Orimo S., and Fuji H., *Correlation between hydrogen storage properties and structural characteristics in mechanically milled magnesium hydride MgH_2.* J. Alloy. Compd., 2004. **366**(1-2): p. 269.

6.   Fátay D., Révész Á., and Spassov T., *Particle size and catalytic effect on the dehydriding of MgH_2.* J. Alloy. Compd., 2005. **399**: p. 237.

7.   Vajo J.J., Skeith S.L., and Mertens F., *Reversible storage of hydrogen in destabilized $LiBH_4$.* J. Phys. Chem. B, 2005. **109**: p. 3719.

8.   Yu X.B., Grant D.M., and Walker G.S., *A new dehydrogenation mechanism for reversible multicomponent borohydride systems - The role of Li-Mg alloys.* Chem. Commun., 2006: p. 3906.

9.   Mao J.F., Wu Z., Chen T.J., Weng B.C., Xu N.X., Huang T.S., Guo Z.P., Liu H.K., Grant D.M., Walker G.S., and Yu X.B., *Improved hydrogen storage of $LiBH_4$ catalyzed magnesium.* J. Phys. Chem. C, 2007. **111**(33): p. 12495.

10.   Vajo J.J. and Olson G.L., *Hydrogen storage in destabilized chemical systems.* Scripta Mater., 2007. **56**: p. 829.

11.   Vajo J.J., Skeith S.L., and Mertens F., *Reversible storage of hydrogen in destabilized $LiBH_4$.* J. Phys. Chem. B Letters, 2005. **109**(9): p. 3719.

12.   Bösenberg U., Doppiu S., Mosegaard L., Barjhordarian G., Eigen N., Borgschulte A., Jensen T.R., Cerenius Y., Gutfleisch O., Klassen T., Dornheim M., and R. Bormann, *Hydrogen sorption properties of MgH_2-$LiBH_4$ composites.* Acta. Mater., 2007.

13.   Vigeholm B., Køller J., Larsen B., and Pedersen A.S., *Formation and decomposition of magnesium hydride.* J. Less Common Met., 1983. **89**: p. 135.

14.   Xiong Z., Hu J., Wu G., Chen P., Luo W., Gross K., and Wang J., *Thermodynamic and kinetic investigations of the hydrogen storage in the Li-Mg-N-H system.* J. Alloy. Compd., 2005. **398**: p. 235.

15.   Johnson S.R., Anderson P.A., Edwards P.P., Gameson I., Prendergast J.W., Al-Mamouri M., Book D., Harris I.R., Speight J.D., and Walton A., *Chemical activation of MgH_2; a new route to superior hydrogen storage materials.* Chem. Commun., 2005: p. 2823.

16. Orimo S., Nakamori Y., Ohba N., Miwa K., Aoki M., and Towata S., *Experimental studies on intermediate compound of LiBH₄.* Appl. Phys. Lett., 2006. **89**: p. 021920.

17. Mosegaard L., Møller B., Jørgensen J., Bösenberg U., Dornheim M., Hanson J.C., Cerenius Y., Walker G.S., Jakobsen H.J., Besenbacher F., and Jensen T.R., *Intermediate phases observed during decomposition of LiBH₄.* J. Alloy. Compd., 2007. **446-447**: p. 301.

18. Friedrichs O., Remhof A., Hwang S.-J., and Züttel A., *Role of Li₂B₁₂H₁₂ for the formation and decomposition of LiBH₄.* Chem. Mater., 2010. **22**: p. 3265.

19. Reed D. and Book D., *In-situ raman study of the thermal decomposition of LiBH₄.* Mater. Res. Soc. Symp. Proc., 2010. **1216**(1216-W06-05).